Dissertation

Moisture-Induced Dynamics of Tilted Tropical Cyclones

Tom Dörffel

2022

eingereicht am

Fachbereich für Mathematik und Informatik
der Freien Universität Berlin

zur Erlangung des Grades eines
Doktors der Naturwissenschaften

Abstract

The following dissertation examines the asymptotic model, initially derived and published by Päschke et al. (2012), that describes the tropospheric flow above the boundary layer of a strongly tilted tropical cyclone (TC)-like vortex in vertical wind shear and under the influence of diabatic heating.

Beginning with re-deriving the reduced model equations following essential steps of Päschke et al.'s (2012) asymptotic analysis, we show a straight-forward extension that accounts for smaller storms in the not originally anticipated cyclostrophic regime. In a next step we conduct analytical examinations of the leading-order equations that govern the motion of a TC-like vortex. Based on these findings, we make statements about the energetics and structural changes of the TC in the context of intensity changes due to symmetric and asymmetric diabatic heating. Furthermore, we analyze the structural properties of the equations that allow us to construct an adapted numerical scheme to efficiently and robustly solve the asymptotic equations by means of finite-volume methods. Special attention is paid to the semi-implicit second-order time integration of the coupled system.

The remaining part of this dissertation is dedicated to presenting the results of numerical experiments that examine mechanisms, either in isolated or combined fashion, that, as we suggest, play a crucial role in the context of rapid intensification (RI) and rapid weakening (RW). These experiments are conducted based on both, the asymptotic model equations and the full three-dimensional equations of atmospheric fluid dynamics, to make statements about the validity and accuracy of the reduced model equations. We present possible pathways of intensity changes that are based on a combined interaction of external wind shear and symmetric-asymmetric diabatic heating. It is found particularly interesting how diabatic heating interacts with the storms structure causing both, intensity and structural changes. Implications towards the applicability of the asymptotic theory in the context of the open research question of RI/RW are discussed as a final contribution of this dissertation.

Contents

List of Figures

List of Figures

List of Tables

Symbols

H	Hilbert space
$T(I)$	Torus over interval
$(\cdot, \cdot), \langle \cdot, \cdot \rangle$	Scalar product
$\lvert\lvert \cdot \rvert\rvert$	Norm
$\boldsymbol{v}$	Three-dimensional velocity
$\boldsymbol{u}, \boldsymbol{u}_\parallel$	Two-dimensional components of horizontal velocity
w	Vertical velocity
ρ	Mass density
p	Pressure
Θ	Potential temperature
$\boldsymbol{x}$	Three-dimensional coordinate vector $\boldsymbol{x} = (x, y, z)$
$\boldsymbol{x}_\parallel$	Two-dimensional horizontal coordinate vector $\boldsymbol{x}_\parallel = (x, y)$
z	Vertical coordinate
t	Time coordinate
r	Radial coordinate
θ	Azimuthal coordinate
$\boldsymbol{i}, \boldsymbol{j}, \boldsymbol{k}$	Cartesian unit vectors ($\boldsymbol{x} = x\boldsymbol{i} + y\boldsymbol{j} + z\boldsymbol{k}$)
$\boldsymbol{e}_r, \boldsymbol{e}_\theta$	Polar unit vectors ($\boldsymbol{x} = r\boldsymbol{e}_r + z\boldsymbol{k}$)
$\dfrac{\partial}{\partial \xi}, \partial_\xi$	Partial derivative w.r.t. ξ
$\dfrac{d}{d\xi}$	Total derivative w.r.t. ξ
$\boldsymbol{\nabla}$	Three-dimensional gradient operator
$\boldsymbol{\nabla}_\parallel$	Two-dimensional horizontal gradient operator
$\overline{(\cdot)}$	Background state variable
$(\cdot)'$	Perturbation variable
ι	Imaginary unit
$\hat{H}$	Hamiltonian linear differential operator
$\mathcal{A}$	Advection operator
$\hat{R}_\phi$	Two-dimensional rotation operator (rotation about the angle ϕ)
ε	Small scale parameter ($\varepsilon^3 = \mathrm{Ma}^2$)
Ma	Mach number
Fr	Froude number
Ro	Rossby number
Da	Damköhler number
$\delta(x)$	Delta (Dirac) distribution
$\otimes$	Tensor product ($(\boldsymbol{a} \otimes \boldsymbol{b})\boldsymbol{c} := \boldsymbol{a}(\boldsymbol{b}, \boldsymbol{c})$)

List of Acronyms

AMR	adaptive mesh refinement
APE	available potential energy
CB	convective burst
CFL	Courant-Friedrichs-Lewy
CIN	convection inhibition layer
CISK	convective instability of the second kind
ECMWF	European Centre for Medium-Range Weather Forecast
EQB	equivalent barotropic
EULAG	Eulerian-Lagrangian model
IFS	integrated forecast system
MPDATA	multidimensional positive definite advection transport algorithm
MPI	maximum potential intensity
NWP	numerical weather prediction
ODE	ordinary differential equation
PBL	planetary boundary layer
PDE	partial differential equation
QG	quasi-geostrophic
RI	rapid intensification
RMW	radius of maximum wind
RW	rapid weakening
SHARPIE	Scheme for Hamiltonian-Advection equations on Radial geometry by Pseudo-linear Implicit-Explicit integration
SLO	Sturm-Liouville operator
TC	tropical cyclone
TPE	total potential energy
TVD	total variation diminishing
VRW	vortex Rossby wave
WISHE	wind-induced surface heat exchange
WTG	weak temperature gradient

1. Introduction

Tropical cyclones (TCs) are among to the most powerful weather systems on our planet. Yet, understanding the dynamics of the underlying physical processes belongs to the key challenges of modern meteorology. Originating typically far offshore close to the equator, they travel long distances over the open ocean before they potentially make landfall. When and where a TC makes landfall, however, hundreds of kilometers of coastline are affected, and adjacent infrastructure is threatened to be devastated. The cost of rebuilding amounts to billions of USD per year[1], not to mention the risk TCs pose to human life. In the highly urbanized coastlines of North America or Asia civil protection often requires large-scaled evacuation schemes that involve the full available capacity of road infrastructure to bring people to safety in time. A misguided forecast is therefore not only a threat to those who remain in regions that are directly affected by the strongest winds and high precipitation. The blockage of escape routes additionally endangers those who are trapped. The success of such operations relies on precisely knowing where, when, and at which strength a storm will make landfall. Reliable predictions are therefore of utmost importance.

The problem of TC forecast accuracy essentially splits into two parts, *track* and *intensity* forecast. Track forecast lead time improved dramatically over the last decades (Yu et al. 2021). The reason for that may be found in higher-quality data sources with increased availability of satellite observations, station-based measurements and those conducted aboard of airplanes and ships. This data is assimilated into improved and fine-tuned numerical models. Through increased computing power and improved theoretical understanding of the guiding physical processes, this led to closer and closer resemblance of the true large-scale environmental state in which TCs are embedded and with which they evolve over time (Magnusson et al. 2021). Better spatio-temporal localization has helped to prevent casualties, but there are still plenty of cases where predicted track ensembles do not capture the actual track (Tang et al. 2021), eventually leaving the local population unprepared.

In contrast, the prediction of intensity and especially the prediction of sudden intensity changes, often referred to in the literature as rapid intensification (RI) and rapid weakening (RW), is less well understood. It is, however, just as important to know the intensity as it is to know the precise location to prepare coordinated safety precautions. Both, RI and RW, pose an enormous challenge to theoretical and numerical model development since the physical processes involved stretch above orders of spatial and temporal scales. The rich body of literature published in the recent years demonstrates the effort that is put into this research question (Callaghan 2017; Ryglicki et al. 2018; Rogers et al. 2015, to name just a few).

The crucial issue consists in the theoretical understanding of cloud physical processes that bridge scales from cloud droplet formation to turbulent mixing and finally the

---

[1] `https://coast.noaa.gov/states/fast-facts/hurricane-costs.html`

aero-thermodynamical interaction of cloud systems with the meso- and synoptic scale environment. The role of cloud convective processes is comprehensively reviewed by Houze (2010) in the light of TCs, but as being a universal research target in meteorology, many more studies have been conducted trying to understand the dynamics that is triggered on the smallest scales (W. Grabowski and Smolarkiewicz 1996; Rogers et al. 2015; Wadler et al. 2021).

Cloud convective processes happen typically on scales much smaller than those on which small scale processes accumulate into organized large-scale flow patterns. It is therefore to bridge a vast range of scales, or speaking in terms of numerical modelling, enormous computing power is required to explicitly resolve the microphysical and turbulent processes and still cover the whole domain of a TC. Efforts in that direction have been made recently by the HD(CP)^2 collaboration that endeavored to resolve cloud processes in climate (*i.e.*, global) scale simulations (Stevens et al. 2020). Yet, it is still necessary to put further developments into such high-resolution models to render them efficient and scalable for the deployment in numerical weather prediction (NWP). Until it is possible to explicitly resolve cloud microphysics and turbulence, if feasible at all, numerical models rely on the parametrization of subgrid-scale processes and fine-tuning of parameters; a procedure that itself requires a certain intuition of the processes involved.

Climate change will further challenge these efforts. Since TCs are crucially determined by the state of the large-scale environment in which they are embedded and under whose influence they evolve, a climatological drift of large-scale conditions will inevitably affect where and how often TCs emerge, and under which conditions they change their intensity (IPCC 2021). Furthermore, parametrization of NWP models that are tuned to the present climatology of the atmospheric state may not keep their accuracy with changing climate due to global warming. Understanding the underlying physical processes of TC dynamics are therefore key in adapting to a changing climate, and with that universal mechanisms that are responsible for vortex motion and intensity change.

Pioneering work on the modeling of TC intensification has been conducted by Charney and Eliassen (1964), Eliassen (1952), and Ooyama (1964, 1969, 1982) and later extended by a series of seminal papers of Emanuel (1986, 1991), Hack and Schubert (1986), Rotunno and Emanuel (1987), and Schubert and Hack (1982, 1983). Emanuel's (1986) maximum potential intensity (MPI) theory is based on the notion of TCs being heat engines and provides an upper estimate of the maximum wind speed based on the environmental conditions such as ocean surface and upper outflow temperature. In an axisymmetric model a theoretical balance between diabatic and frictional forcing is constructed and delivers a handle on the intensity a TC *can* reach based on thermodynamic considerations. Typically, these estimates are rarely met but provide a reasonable indicator to assess the potential risk (Persing and Montgomery 2003; Rousseau-Rizzi et al. 2021; Smith et al. 2008). By their simplicity, the MPI and related models do not capture the time resolved dynamics and thus do not give much insight in the timing of an intensification event (Montgomery and Smith 2017a).

Later studies further deepened the picture of a tropical cyclone as a thermodynamic cycle converting latent, sensible and radiative heat into mechanical work (Pauluis and Zhang 2017). Bhalachandran et al. (2020), on the other hand, analyzed the energetic pathways in the spirit of Lorenz (1955) and computed transitions rates between azimuthal wavenumbers of available potential energy (APE) and kinetic energy. RI and RW were

found to show characteristic signals in the transitions rates hinting towards the important role of asymmetries in the process of sudden intensity changes.

The feedback between the boundary layer and the bulk flow is found to be essential in understanding intensity changes. The bulk flow preconditions the boundary layer in which convective processes are initiated that feed back energy into the bulk flow. It is, however, disputed whether frictionally induced convergence or the preconditioning of the atmosphere with a high level of saturation by evaporation through surface drag is responsible for triggering deep convection. The first concept is labeled *convective instability of the second kind (CISK)* and traces back to Charney and Eliassen (1964) and Ooyama (1964) while the latter is called *wind-induced surface heat exchange (WISHE)* and was coined by Emanuel (1986). It is still not fully understood, what are the exact feedback mechanisms necessary for maintaining and increasing the intensity of TCs. While some later studies are in favor for the WISHE concept (Craig and Gray 1996), others disagree and prefer CISK (Lee and Frisius 2018).

Nonetheless, axisymmetric models have successfully described essential features of TC dynamics, especially in case of stronger, convectively more organized storms (Montgomery and Smith 2017a,b). Over the past three decades, however, the role of shear and asymmetries in the context of shear resiliency and rapid intensification moved into focus. Dunkerton et al. (2009), Marks, Black, et al. (2008), and Marks, Houze, et al. (1992) argued in observational studies that substantial tilt may be characteristic for a TC flow field. The horizontal displacement throughout the depth of the troposphere is found to be in the same order of magnitude as the horizontal extent of the vortex core, *i.e.*, in the order of several hundred kilometers.

Asymmetries in the flow field may as a consequence affect the structure of convection patterns as observations show (Alvey et al. 2015; Callaghan 2017; Frank and Ritchie 1999; Rios-Berrios 2020, among others). The control asymmetries of the flow field have on the boundary layer and the resulting presence of asymmetric convection, however, are associated to events of rapid intensity change (Callaghan 2017; Rios-Berrios 2020; Stevenson et al. 2014; Wadler et al. 2021). In an observational study, Hazelton, Hart, et al. (2017) and Hazelton, Rogers, et al. (2017) found pronounced asymmetries in the distribution of strong convective bursts (CBs) in the eyewall and that the rate of CB events is connected with periods of sustained intensification. There are also studies examining explicitly this feedback between asymmetries in the flow field and asymmetric convection pointing towards the role injections of low potential temperature into the boundary layer play (Li and Dai 2020; Riemer et al. 2010, and references therein). On the other hand, asymmetric convection is able to lead to structural changes in the symmetry of the flow field (Davis et al. 2008). The tight interconnection between asymmetric structures and rapid intensification has also been investigated by means of high-resolution non-idealized simulations (H. Chen and Gopalakrishnan 2015; Leighton et al. 2018).

Jones (1995, 2000, 2004) used idealized three-dimensional simulation to examine the response of idealized vortices to externally imposed shear. In a series of publications, Reasor, Montgomery, Marks, et al. (2000), Reasor and Montgomery (2001), Schecter, Montgomery, and Reasor (2002), Schecter and Montgomery (2003), and Reasor, Montgomery, and Grasso (2004) studied by means of observational and theoretical approaches how asymmetries develop and evolve under the presence of shear and found that in their linearized equivalent barotropic (EQB) model radiation of vortex

Rossby waves (VRWs) act as an intrinsic mechanism to stabilize the vortex against externally imposed shear. The ability of self-alignment is coupled to the existence of a critical layer where circulation and precession frequency are synchronous (Schecter and Montgomery 2004; Schecter 2015). Further analysis added the influence of moist convection (Schecter and Montgomery 2007). In an idealized ensemble simulation, Miyamoto and Nolan (2018) examined the timing between vertical alignment and RI. A different approach was followed by Nolan and Montgomery (2002) and Nolan and Grasso (2003) who analyzed the growth rate of linear perturbations from a symmetric reference state in terms of azimuthal and vertical wavenumbers.

Many of the aforementioned approaches have in common that they describe the problem in cylindrical coordinates and tilt is represented as the deviation from an unperturbed vertically aligned (axisymmetric) reference state. Hence, a tilted vortex will show signals in azimuthal wavenumbers 1 and higher. In that tilt is indistinguishable from genuine asymmetries in the flow field, at least without further analysis. Already mentioned by Marks, Houze, et al. (1992), TCs often exhibit a center of rotation that varies vertically and evolves over time. Following a long-standing concept in the theory of slender vortex filaments (Callegari and Ting 1978; Ling and Ting 1988), it was finally investigated by Päschke et al. (2012) to what extent a TC under the influence of external shear and diabatic heating can be described by a tilted *centerline*. Based on this, an asymptotic theory was derived.

There is a rich body of literature in which asymptotic analysis was used to simplify model equations in a variety of fields ranging from pure partial differential equation (PDE) analysis to applications in the natural and engineering science. Under the framework of asymptotic analysis, a powerful collection of tools was established that help to reduce the complexity of the governing equations with the ultimate goal of rendering them more tractable in terms of analytical and numerical solutions strategies (cf. Eckhaus 1979, for a recent reference). In many cases, the process of model reduction helps to gain deeper insights into the dominant driving forces that — under the prerequisites set carefully in advance of the asymptotic analysis — guide the dynamics of a process under consideration.

Päschke et al. (2012) (see also the dissertations of Mikusky (2007, Päschke's maiden name) and Marschalik (2015)) presented the results of a matched two-scale asymptotic analysis on the flow field of a TC that possesses an axisymmetric primary circulation, organized level-by-level around a tilted *centerline*, and that is exposed to the influence of externally imposed shear and diabatic heating. Their model provides two tendency equations, one for the leading-order tangential velocity and a second one for the centerline position, and essentially captures the interaction of the vortex core structure with the embedding large-scale quasi-geostrophic (QG) flow. By asymptotic matching the vortex core structure reduced to a slender vortex filament that is steered by the QG flow, but also feeds back by self-induced motions. As a result of that analysis, Päschke et al. (2012) found special cases where analytical solutions exist. *E.g.*, for a Boussinesq flow with vertically uniform primary circulation, there exist precessing eigensolutions for the tilted centerline. They further found an asymmetric pathway to control the tangential velocity, in addition to the well established mechanism based on symmetric radial inward motions of (conserved) angular momentum (Schubert and Hack 1982). Essentially, as we will further elude in this work, the asymmetric pathway to

intensification (and attenuation) results from the correlation of tilt and vertical velocity asymmetries (or diabatic heating).

The present work takes up on these results and adds further refinements to the asymptotic analysis. The aim of this procedure is to consistently demonstrate the validity of the original theory of Päschke et al. (2012) through scaling regimes that involve Rossby numbers higher than 1, *i.e.*, in general stronger storms, which were not originally captured. By doing so, we naturally reproduce Päschke et al.'s (2012) theory, highlight the adaptions necessary to extend towards more intense TCs, and we give some intuition of the limitations of the presented approach. The essentials of these findings are published by Dörffel et al. (2021).

On the quest of better understanding pathways to TC intensification, we examine the energetic properties of the asymptotic theory. That allows us, by finding connections to Lorenz's (1955) APE concept, to trace back both, symmetric and asymmetric intensification pathways, to the correlation of potential temperature perturbations and vertical velocity structures. In other words, it is the thermodynamic adjustment to the flow structure, that interacts with coordinated vertical motions that can be induced by diabatic heating, or, more likely in nature, by vertical mass ejection of the boundary layer. A related study on reanalysis data has been conducted recently by Bhalachandran et al. (2020) but symmetries and higher-order wavenumber perturbation were assessed in a cylindrical, *i.e.*, vertically aligned coordinate system not explicitly taking the tilted structure into account.

On the other hand, our aim is to deepen the understanding of the analytical structure of the leading-order asymptotic equations. By tracing back substructures of the centerline equations to a coupled advection–Sturm-Liouville problem, we are able to construct (abstract) solutions of the centerline equation that form the basis for the subsequent numerical treatment. Through careful analysis of the individual subdivisions of the nonlinearly coupled PDE problem, we identify prototypical sub-problems that can readily be solved by standard methods developed in the context of atmospheric fluid dynamics and quantum mechanics. We construct a trapezoidal time integration scheme that allows to consistently integrate the coupled system of equations up to second order in time and space, yet achieving a high degree of stability to cope with the nonlinearity of the equations. This procedure poses a natural extension of methods that have been successfully used to integrating the three-dimensional equations of atmospheric fluid dynamics (Benacchio and Klein 2019; Smolarkiewicz, Kühnlein, and W. W. Grabowski 2017).

In the spirit of preceding studies (Frank and Ritchie 1999; Jones 1995, 2000, 2004; Schecter, Montgomery, and Reasor 2002; Wang and Holland 1996), we perform three-dimensional simulations to test the theory's predictions. The presented work directly builds upon the dissertation of Papke (2017) who performed a first series of experiments to test the response of a tilted vortex to purely asymmetric diabatic heating. To this end, we also make use of the well established Eulerian-Lagrangian model (EULAG) (Smolarkiewicz, Kühnlein, and W. W. Grabowski 2017) that integrates the equations of atmospheric fluid dynamics with the semi-implicit second-order accurate scheme. As we will demonstrate, asymmetric diabatic heating directly affects tilt precession frequency and/or amplitude, depending on the relative orientation of tilt vector and heating dipole. We make further use of the simulation data and analyze the energetic

transition from heating via APE to kinetic energy. This shall validate the asymptotic results on the energy budget.

The structure of this thesis is the following. In chapter 2 we will present many of the derivation steps that lead to the model originally presented by Mikusky (2007) and Päschke et al. (2012). Chapter 3 will discuss the dynamics and energetics of the forcing mechanisms induced by diabatic heating and external wind shear. More thorough insights into the structure of the leading-order asymptotic equations will be provided that help to construct the numerical scheme as presented in chapter 4. In chapter 5 we will outline the needed ingredients for performing three-dimensional simulations that help to validate the asymptotic model. In chapter 6, we will show the results of a series of numerical experiments deploying both, the asymptotic model implementation and three-dimensional reference simulations. This thesis will be summarized in chapter 7 where also an outlook to future work will be given.

2. Asymptotic Analysis of Tropical Cyclones

In this chapter we will give motivation and an overview of the methods of Päschke et al. (2012) and their findings regarding a leading-order set of equations governing the dynamics of a tilted atmospheric vortex. Further, we highlight possible extensions to this theory with the aim of enlarging the field of possible applications.

In principle, there is no need for deriving specialized equations for describing the flow of an atmospheric vortex since the *atmospheric equations of fluid dynamics* (cf. eqs. (2.1)) already provide a mathematical framework that governs the motion not only of vortices but of a variety of phenomena across a wide range of scales in space and time. However, these equations have proven to pose one of the most challenging problems in modern applied mathematics when it comes to deriving analytical solutions. In the most general setting, *i.e.*, in three spatial dimensions with generic initial data and boundary conditions, next to the fact, that solutions cannot be handled analytically, there is still ongoing research about existence, uniqueness and regularity of solutions (Farwig 2014; Robinson 2020). This circumstance may be considered as an artifact of the wide range of applicability of these equations uniformly describing small-scale turbulent motions up to the largest scales of planetary flows (Pope 2011).

Nevertheless, it is common practice that solutions are approximated numerically, and it is not only since the advent of digital computers that sophisticated numerical methods have been established, which form the backbone of today's weather forecasting. Continuous efforts in comparing predictions with observations have proven that numerical solutions, at least to a certain degree of accuracy, represent reality and allow for weather forecasts up to several days. It is for this very reason that mispredictions sometimes come at a surprise and reveal the actual lack of understanding of the underlying physical processes. So it happened for the integrated forecast system (IFS), developed at the European Centre for Medium-Range Weather Forecast (ECMWF) and one of the most accurate medium-range forecast models, that its prediction score with respect to tropical cyclones was below that of competitors that usually have a lower score in terms of global predictions (J.-H. Chen et al. 2019).

It is obvious, that the source of errors is a lack of accuracy in representing the driving physical processes. That can be caused either by under-resolved fluid structures (on a numerical level) that — in reality — emerge on small scale and accumulate to effects on a larger scale, or (on an analytical level) by the fact that often physical processes are approximated through *surrogate models* that exceed their respective scope of validity.

It is less obvious, however, which particular processes need better representations. The structure of the governing equations (2.1) does not allow a priori for much more insight on an analytical level than what the archetype of the equations suggests: mass continuity, and balances of momentum and internal energy (Klein 2017). Phrasing it a little differently, they are based on *first principles* far beyond the scope of atmospheric

fluid dynamics. The particular processes, in our case, guiding the motion of a tropical cyclone, are hidden in the universality of the atmospheric equations of fluid dynamics.

A possible remedy to the above problems may be increasing the resolution until small scale structures are resolved sufficiently to drive motions at the larger scale (of interest). Even with the capabilities of modern high-performance computing, this approach is limited since scales, separated by orders of magnitude, may interact with each other, and it remains unclear which processes and thus scales are involved in detail (until a sufficiently accurate solution is obtained). In light of missing insights on regularity bounds, it is even questionable if there are analytical solutions for generic settings of initial data and boundary conditions and if the numerical solution converges towards the analytical one.

Next to advanced numerical computing techniques such as adaptive mesh refinement (AMR) (Berger and Oliger 1984), *scale asymptotic methods* are a powerful family of tools to construct simplified equations with solutions approximating those of the original equations (Eckhaus 1979; Klein 2004, 2009, 2017; Kutz 2020). Not only do they allow for deriving simplified equations which are often easier to solve, both analytically and numerically, but the structure of these simplified equations may reveal dominant interactions of physical processes while neglecting less important ones. These interactions usually cover multiple scales in space and time. By applying *multiscale* or *matched asymptotic* methods it may be possible to find a closed set of equations combining leading-order effects across two or more scales. In conjunction with appropriate coordinate choices, asymptotic methods further reveal leading-order symmetries and help to lower the effective dimensionality of the mathematical description. As we will see in the present case, a three-dimensional atmospheric vortex can be effectively described by two independent spatial coordinates (radial and vertical) in the reduced model equations, yet describing a fully three-dimensional flow field. Altogether, these insights, gained during deriving a reduced model, may ultimately help to understand the mechanisms of intensity changes of tropical cyclones and guide the future development of NWP models.

For reference and following Mikusky (2007) and Päschke et al. (2012), in section 2.1, we will present the governing equations of atmospheric fluid dynamics and condition them for the subsequent asymptotic analysis. In sections 2.2 and 2.3 we highlight details of the asymptotic methods to be applied to the example of a tropical cyclone in section 2.4, and show how the scaling approach of Päschke et al. (2012) can be uniformly extended to vortices of different size and strength (*i.e.*, deviating from the gradient-wind towards the cyclostrophic regime). Finally, in section 2.5 we demonstrate the extension towards the circulation-free limit. This renders the theory applicable to "stronger-than-incipient" TCs which typically exhibit flow structures not allowing to assume a finite circulation throughout the whole depth of the atmosphere.[1] These extensions are partially published by Dörffel et al. (2021).

---

[1]TCs are always topped by an anticyclonic outflow layer at altitudes near the tropopause (not only to compensate for the frictional inflow near the ocean surface). While at lower and mid level altitudes, the flow typically has a positive (cyclonic) circulation on the Northern Hemisphere, this essentially means that the outflow layer has a circulation with negative sign, hence, assuming continuity throughout the vertical depth, there must be a zero-crossing, *i.e.*, there exists a height-level of vanishing circulation.

2.1. The Governing Equations

Gravitational acceleration	g	=	9.81	$\mathrm{m\,s^{-2}}$
Coriolis parameter	$f_{\mathrm{ref}} = f\vert_{\phi=30°}$	=	$7.3 \cdot 10^{-5}$	$\mathrm{s^{-1}}$
Beta parameter	$\beta_{\mathrm{ref}} = df/dy\vert_{\phi=30°}$	=	$2 \cdot 10^{-11}$	$\mathrm{m^{-1}\,s^{-1}}$
Pressure	p_{ref}	=	$1 \cdot 10^{5}$	$\mathrm{kg\,m^{-1}\,s^{-2}}$
Temperature	T_{ref}	=	300	K
Dry air gas constant	R	=	287	$\mathrm{m^2\,s^{-2}\,K^{-1}}$
Adiabatic exponent	γ	=	1.4	

Table 2.1.: Independent parameters characterizing the atmospheric flow. Adopted from Klein (2010)

The point of departure for the subsequent asymptotic analysis are the compressible inviscid equations of fluid dynamics on a rotating beta plane. As systematically outlined in Klein (2010, 2017), our goal is to highlight the derivation of a *reduced model* for TCs (the one presented by Päschke et al. 2012) from a more general *first-principle law*[2]. In an earth-relative coordinate system (zonal, meridional and vertical coordinates (x, y, z) with corresponding unit vectors $(\boldsymbol{i}, \boldsymbol{j}, \boldsymbol{k})$) the governing equations read

$$\frac{\partial \rho}{\partial t} + \boldsymbol{\nabla}_{\parallel} \cdot \rho \boldsymbol{u} + \frac{\partial \rho w}{\partial z} = 0, \tag{2.1a}$$

$$\frac{\partial \boldsymbol{u}}{\partial t} + \boldsymbol{u} \cdot \boldsymbol{\nabla}_{\parallel} \boldsymbol{u} + w \frac{\partial \boldsymbol{u}}{\partial z} + \frac{1}{\rho} \boldsymbol{\nabla}_{\parallel} p + f \boldsymbol{k} \times \boldsymbol{u} = 0, \tag{2.1b}$$

$$\frac{\partial w}{\partial t} + \boldsymbol{u} \cdot \boldsymbol{\nabla}_{\parallel} w + w \frac{\partial w}{\partial z} + \frac{1}{\rho} \frac{\partial p}{\partial z} = -g, \tag{2.1c}$$

$$\frac{\partial \Theta}{\partial t} + \boldsymbol{u} \cdot \boldsymbol{\nabla}_{\parallel} \Theta + w \frac{\partial \Theta}{\partial z} = Q_{\Theta}, \tag{2.1d}$$

$$p = p_{\mathrm{ref}} \left(\frac{R\rho\Theta}{p_{\mathrm{ref}}} \right)^{\gamma}. \tag{2.1e}$$

ρ is the (dry) mass density, $\boldsymbol{u}$ the two horizontal and w the vertical components of the velocity vector. $\boldsymbol{\nabla}_{\parallel}$ are the horizontal components of the three-dimensional gradient operator $\boldsymbol{\nabla}$, i.e., $\boldsymbol{\nabla}_{\parallel} = \boldsymbol{i}\partial_x + \boldsymbol{j}\partial_y$ and $\boldsymbol{\nabla} = \boldsymbol{\nabla}_{\parallel} + \boldsymbol{k}\partial_z$. p (p_{ref}) is the (reference) pressure, $f = f_{\mathrm{ref}} + \beta_{\mathrm{ref}} y$ the Coriolis parameter in the *beta-plane approximation* with β_{ref} the linearized slope of f at the latitude ϕ_0. Finally, g is the gravitational acceleration. For more details on the parameters, see table 2.1.

2.1.1. Non-Dimensionalization and Dimensionless Numbers

To the end of simplifying eqs. (2.1) in the regime of a TC towards a more tractable set of equations, we seek for justification of omitting terms which are small relative to

---

[2]The term *first-principle law* has rather a "relative" meaning. *E.g.*, while the Navier-Stokes equations act as a first-principle law for many applications in meteorology (amongst others), yielding a number of reduced models to be valid on a certain spatial and temporal scale (Ekman layer, Boussinesq, weak temperature gradient (WTG), QG, etc., see Klein (2010)), they are themselves the limit of large particle numbers of the Boltzmann equation.

Density	ρ_{ref}	$=$	$\dfrac{p_{\text{ref}}}{RT_{\text{ref}}}$	$\approx$	1	$\text{kg\,m}^{-3}$
Pressure scale height	h_{sc}	$=$	$\dfrac{p_{\text{ref}}}{g\rho_{\text{ref}}}$	$\approx$	10^4	m
Synoptic length scale	L_{syn}	$=$	$\dfrac{N_{\text{ref}}h_{\text{sc}}}{f_{\text{ref}}}$	$\approx$	1200	km
Var. of pot. temp.	$\Delta\Theta$	$=$	$\dfrac{T_{\text{ref}}h_{\text{sc}}N_{\text{ref}}^2}{g}$	$\approx$	30	K
Velocity	u_{ref}	$=$	$\dfrac{2}{\pi}\tan\phi\dfrac{N_{\text{ref}}^2}{f_{\text{ref}}^2}\beta h_{\text{sc}}^2$	$\approx$	10	$\text{m\,s}^{-1}$
Time	t_{ref}	$=$	$\dfrac{h_{\text{sc}}}{u_{\text{ref}}}$	$\approx$	10^3	s
Speed of sound	c_{ref}	$=$	$\sqrt{\dfrac{p_{\text{ref}}}{\rho_{\text{ref}}}}$	$\approx$	300	$\text{m\,s}^{-1}$

Table 2.2.: Further reference quantities derived from table 2.1. Adopted from Klein (2010)

others and find expressions which are transparent with respect to the involved physical processes. In the literature of meteorology and fluid dynamics, techniques of simplifying the fundamental equations of fluid dynamics towards equations which are suited to the special regime under consideration have a long-standing tradition (Bannon 1996; Barenblatt 1996; Durran 1989; Eckhaus 1979; Holton 2004; Klein 2008). Although they all follow the idea of identifying problems (equations) whose solutions are close to those of the original problems yet easier to find, they essentially differ in the physical intuition necessary to justify the individual steps of derivation and require different levels of mathematical rigor.

Simplification essentially means to compare the magnitude of quantities as a proxy to neglect terms, and therefore it involves *measures*. Hence, we inevitably have to deal with concept of *units*, *i.e.*, *physical dimensions*. Assigning a concrete numerical value to a quantity involves the notion of a unit, *i.e.*, a reference quantity that comes along with a reproducible measuring procedure.[3] *Physical dimensions*, on the other hand, define a relation between physical quantities in the sense that quantities with the same dimension can be directly compared to each other (*commensurability*). This means in particular that they can be converted to the same units and then be compared by their numerical value. In summary, a dimensional quantity ϕ can be written as

$$\phi = \phi^*\phi_{\text{ref}}\,, \tag{2.2}$$

where ϕ^* is the (non-dimensional) numerical value with respect to the unit expressed by ϕ_{ref}. Although a bit of a stretch, it is precisely this property that we need for an assessment of relative smallness in the further course.

---

[3]If, say, a certain object has the length of 2.4 m we compared it with a *unit* measure of 1 m and concluded that it was 2.4 times longer. If taken the unit measure of 1 yd, wee would have ended up with the measurement of 2.62 yd.

For completeness, we mention that considerations about the dimensionality of physical quantities are far more powerful than outlined here. So can the sole fact of a set of parameters having units lead to governing equations (at least up to a multiplicative constant). More details on the so-called *dimensional analysis* are covered by Barenblatt (1996).

Although there exist several established systems of units (with the *International System of Units (SI)* the most prominent amongst them) we are free to define our own problem-adapted set of units and call them *reference quantities* (cf. tables 2.1 and 2.2). It may be intuitively clear, that all the independent parameters describe characteristic properties of the system under consideration, including those associated to initial data, boundary conditions and external forcing.

From a purely mathematical point of view, it appears beneficial to select these reference quantities such that the numerical value of a quantity becomes close to unity. To accommodate for this circumstance, it may be necessary to define several reference quantities of the same dimension to account for quantities that possess distinctively different magnitudes, since, *e.g.*, the vertical scale $h_{sc} \approx 10^4$ m differs from the horizontal synoptic length scale $L_{syn} \approx 10^6$ m.

$$
\begin{array}{rlll}
\text{Strouhal number} & \text{Sr} & = \dfrac{h_{sc}}{t_{ref}\, u_{ref}} & = 1 \\[2em]
\text{Mach number} & \text{Ma} & = \sqrt{\dfrac{u_{ref}}{c_{ref}}} & \approx 0.03 \\[2em]
\text{Rossby number} & \text{Ro} & = \dfrac{u_{ref}}{h_{sc} f_{ref}} & \approx 10 \\[2em]
\text{(barotropic) Froude number} & \text{Fr} & = \dfrac{u_{ref}}{\sqrt{g h_{sc}}} \equiv \text{Ma} & \approx 0.03 \\[2em]
\text{Non-dimensional beta-parameter} & \hat{\beta} & = \dfrac{\beta_{ref}\, h_{sc}}{f_{ref}} & \approx 3 \cdot 10^{-3} \\[2em]
\text{Damköhler number} & \text{Da} & = \dfrac{Q_{\Theta,ref}\, t_{ref}}{T_{ref}} & = 1
\end{array}
$$

Table 2.3.: Dimensionless characteristic numbers.

Buckingham's π theorem — as a consequence of the algebraic property of dimensional quantities — states that for a number of m given reference quantities that in total possess n independent dimensions, there are $m - n$ independent *dimensionless numbers* that uniquely describe the system up to a similarity transformation (cf. Barenblatt 1996; Klein 2017). These dimensionless numbers, however, are not uniquely determined by a given set of parameters, as, *e.g.*, the product of two dimensionless numbers results in a third one. In fluid dynamics in general, and meteorology in particular, a common set of these numbers has been established to characterize a physical system. For our purposes, we defined a set of them in table 2.3 along the choice of our reference parameters.

In many situations it may be possible to find reference quantities which are inherently defined by the physical setting (Klein 2017). For systems that exhibit scale interactions, however, reference quantities are not unique. *E.g.*, different processes may act on

individual length and/or time scales. Conversely, this means selecting a certain reference scale will emphasize processes on that particular scale. Hence, the choice of the reference parameters ultimately depends on the targeted process(es). Intuition about the scaling of physical processes cannot be overrated when seeking to discover simplified theories by asymptotic analysis.

Performing the process of *non-dimensionalization* (following Klein 2010), *i.e.*, inserting eq. (2.2) for each quantity into eqs. (2.1) and taking into account the reference quantities given in tables 2.1 and 2.2, we end up with the non-dimensional set of governing equations:

$$\frac{\partial \rho^*}{\partial t^*} + \nabla^*_\parallel \cdot \rho^* \boldsymbol{u}^* + \frac{\partial \rho^* w^*}{\partial z^*} \qquad\qquad = 0, \qquad (2.3a)$$

$$\frac{\partial \boldsymbol{u}^*}{\partial t^*} + \boldsymbol{u}^* \cdot \nabla^*_\parallel \boldsymbol{u}^* + w^* \frac{\partial \boldsymbol{u}^*}{\partial z^*} + \frac{1}{\mathrm{Ma}^2} \frac{1}{\rho^*} \nabla_\parallel p^* + \frac{1}{\mathrm{Ro}}(1 + \hat{\beta} y^*) \boldsymbol{k} \times \boldsymbol{u}^* = 0, \qquad (2.3b)$$

$$\frac{\partial w^*}{\partial t^*} + \boldsymbol{u}^* \cdot \nabla^*_\parallel w^* + w^* \frac{\partial w^*}{\partial z^*} + \frac{1}{\mathrm{Ma}^2} \frac{1}{\rho^*} \frac{\partial p^*}{\partial z^*} \qquad\qquad = -\frac{1}{\mathrm{Fr}^2}, \qquad (2.3c)$$

$$\frac{\partial \Theta^*}{\partial t^*} + \boldsymbol{u}^* \cdot \nabla^*_\parallel \Theta^* + w^* \frac{\partial \Theta^*}{\partial z^*} \qquad\qquad = Q^*_\Theta, \qquad (2.3d)$$

$$p^* = (\rho^* \Theta^*)^\gamma \quad (2.3e)$$

Note that differential operators ∂_t, $\nabla_\parallel$, and ∂_z involve the notion of *dimensional* coordinates which themselves need to be rescaled. By applying the chain rule, the trivial connection between dimensional and non-dimensional differential operators is given by

$$\frac{\partial}{\partial \xi} = \frac{d\xi^*}{d\xi} \frac{\partial}{\partial \xi^*} = \frac{1}{\xi_{\mathrm{ref}}} \frac{\partial}{\partial \xi^*} \qquad (2.4)$$

for a coordinate ξ. Hence, $\nabla^*_\parallel$ is to be understood as $\boldsymbol{i}\partial_{x^*} + \boldsymbol{j}\partial_{y^*}$. We will, however, from here on drop the superscript * for the sake of streamlining the notation. Further, note that for now all spatial coordinates are rescaled with the same length h_{sc} and all velocity components with u_{ref}. This will change in sections 2.4.3 and 2.4.4.

Let us finalize this section with the following observation: The definition of the reference quantities (tables 2.1 and 2.2) yield the characteristic dimensionless numbers, defined in table 2.3, which determine the *flow regime*, provided that the reference quantities are chosen such that the resulting non-dimensional quantities are of order unity. Klein (2017) alludes on this in the following sense: There are physical systems that differ in the set of determining reference quantities. However, they may lead to the same set of characteristic numbers, and in that they lead to the same non-dimensional set of equations. Hence, provided same (non-dimensional) initial data and boundary conditions, they have the same non-dimensional solution, although their physical solutions may vary by orders of magnitude.

There is an ambiguity in the literature: On the one hand, Klein (2004, 2005, 2017), amongst others, refers to *distinguished limits* as a scale-independent property of the physical system under consideration (*e.g.*, the resulting rescaled equations of atmospheric fluid dynamics by using Earth-characteristic parameters and coupling the non-dimensional parameters to a small-scale parameter ε, Klein 2010, cf.). *Flow* or *scaling regimes*, in that sense, emerge from rescaling the independent variables of the system (*i.e.*, the coordinates) by powers of the small-scale parameter ε. Sensible choices

of coordinate rescaling reveal non-trivial balances that are dominant on that particular scale. Sometimes they are called *rich limits* (Klein 2022).

Kutz (2020), on the other hand, uses a slightly different nuance of the term *distinguished limit*. In the context of given equations including a small-scale parameter ε (*i.e.*, the definition of distinguished limits from above), *distinguished limits* are introduced as dominant balances that arise from various choices of coordinate rescalings. Along this line of thoughts, distinguished limits are constructed from identifying dominant balances, thus the latter give rise to the former. This is in contrast to Klein, who identifies dominant balances as the result of a particular coordinate scaling.

These two different view point meet once the effective length and time scales of a particular multiscale system are considered as system properties (and therefore scale independent). This is a rather philosophical consideration, and for realistic applications, it may not be of practical use as the majority of physically relevant systems exhibit a wide range of scaling cascades comprising separated and continuous scales. Throughout the remainder of this thesis, however, we will refer to the nomenclature of Kutz (2020).

It is the set of characteristic non-dimensional numbers (cf. table 2.3) that describes the (flow) regime. In other words, in the space of reference quantities, there are sub-manifolds characterized by a specific choice of non-dimensional characteristic numbers that describe a specific regime. All solutions on a sub-manifold are distinct in that the dimensional variables of the solution may take different values. The ratio between a solution quantity and its reference value, *i.e.*, the non-dimensional solution, however, is constant. These considerations are essentially the result of *Buckingham's (1914) theorem*, which traces this issue back to the over-determined system of equations determining non-dimensional quantities expressed by the dimensional reference quantities (see Klein (2017) for more details).

2.1.2. Scale Analysis

The result of the previous section was the set of equations (2.3) which is parametrized by the dimensionless numbers given in table 2.3. For the sake of completeness, we want to illustrate at the example of eqs. (2.3) how *scale analysis* is applied, and we will see later how this method compares to *asymptotic analysis*.

By the very definition of the corresponding reference quantities that we used during non-dimensionalization we conclude that the order of every term in eqs. (2.3) is determined by the value of the pre-factorial characteristic numbers. The ratio of the prefactors reveals which terms interact with each other *at leading order*, *i.e.*, prefactors with ratio 1 correspond to interacting terms. However, since every quantity ϕ can be composed of a large-scale contribution $\overline{\phi}$ (which may exhibit certain symmetries) and a small scale perturbation ϕ' (with $|\overline{\phi}| \gg |\phi'|$), it is only possible to make estimates on the largest appearing prefactors, *i.e.*, the *leading-order*. So are, *e.g.*, all terms of the continuity equation (2.3a) equipped with the prefactor 1, hence all terms are of order unity and there is no simplification obvious.[4] The same is true for the potential temperature equation (2.3d).

This is different for the horizontal and vertical momentum equations (2.3b) and (2.3c): With the prefactors $1/\text{Ma}^2 \equiv 1/\text{Fr}^2 \approx 1000$ and $1/\text{Ro} \approx 0.1$, there is a clear dominance

---

[4]This is the result of setting the *Strouhal number* to 1, *i.e.*, identifying the reference and the advection timescale.

of the pressure gradient and gravity terms involving the Mach and Froude numbers Ma and Fr. There are no other terms to balance them, so the leading-order balances become

$$\nabla_{\parallel}\overline{p} = 0 \quad \text{and} \quad \frac{\partial \overline{p}}{\partial z} = -\overline{\rho} \,. \tag{2.5}$$

Hence, in the regime set by the dimensionless numbers of table 2.3, the pressure is horizontally homogeneous and vertically hydrostatic (at leading order!). Despite the fact that this approximation is well established in the literature (Holton 2004), it is unclear how to find higher-order corrections by that approach. Although we are on a horizontal scale of $O(10\,\text{km})$, horizontal pressure gradients may play a role as a driver for horizontal motions. There are ways to refine this analysis, but they involve a certain degree of physical intuition and cannot be justified with mathematical rigor, alone. Asymptotic analysis offers various tools and techniques to rigorously derive simplified models along the mathematical properties of the governing equations.

It should be mentioned here that authors from different fields different opinions on the distinction between scale analysis and asymptotics. In the spirit of Kruskal (1963), both fall under the umbrella of "Asymptotology" making use of the scale separation of processes acting in a physical system. Nonetheless, *asymptotic analysis* can be considered as a systematic and rigorous way of analyzing dominant (and subdominant) balances within governing equations.

In the subsequent parts of this chapter we will see how we are able to find expression for next-to-leading-order correction terms by the means of *asymptotic analysis* that will help us to gain more insights into the dynamics of TCs.

2.1.3. Distinguished Limits

With eqs. (2.3) we derived a parametrized version of the dimensional eqs. (2.1) involving the characteristic numbers outlined in table 2.3. *Scale analysis*, as consulted in the previous section, provides a fundamental way of assessing the orders of magnitude of the individual terms of the governing equations. By exploiting the relative smallness of prefactors in eqs. (2.3) over one another, we described a way to cancel terms that are of subordinate importance. The *distinguished limit*, *i.e.*, the set of dimensionless numbers dictated the relative ordering of the terms of the governing equations. Comparing the prefactors to order 1 we can decide whether a term is considered *small* or *large* (*i.e.*, inversely small).

It is tempting to approximate the solution, to be considered as a function that depends in some unknown non-linear way on the non-dimensional numbers (parameters), by a multidimensional Taylor expansion at a certain limiting point where the parameters are small. A limiting process for each parameter independently, as it is well known from multidimensional calculus, can depend on the path, *i.e.*, if performed consecutively, on the order in which each parameter is passed to its limit.[5] For this approach to be generally valid, the solution needs to exhibit a certain regularity at the limiting point that involved higher-order derivatives with respect to the parameters (Klein 2017).

---

[5]In fact, by selecting the Euler equations over the Navier-Stokes equations we implicitly passed to the limit of vanishing viscosity. This choice is based on a well-established assumption of meteorology and valid for large-scale flows. This assumption, however, could also be derived from an asymptotic analysis.

Ultimately, this approach would require a priori the very information on the solution which we seek to unravel by the asymptotic analysis.

A further aspect, that is important when considering such a limiting process, is that the ordering of the individual terms of eqs. (2.3), that is established by the non-dimensional numbers, should be maintained throughout the limiting process! (Otherwise, we would depart from the given flow regime.) This consideration gives rise to the concept of *distinguished limits*.

Thinking about a *path* through the multidimensional space of non-dimensional numbers, *i.e.*, a single-parameter function for each non-dimensional number

$$(\mathrm{Sr}, \mathrm{Ma}, \mathrm{Ro}, \mathrm{Fr}, \mathrm{Da}) = \boldsymbol{F}(\varepsilon) \tag{2.6}$$

we need to maintain the ordering established by the numerical values of the particular set of non-dimensional numbers (cf. table 2.3) when passing to the limit $\varepsilon \to 0$. If one non-dimensional number is large in comparison to another one at a given $\varepsilon > 0$, then it must not become smaller than the second one in the limiting process. For $0 < \varepsilon \ll 1$ this behavior can be ensured by coupling the non-dimensional numbers to powers of a small number ε.

In a series of articles, Klein (2000, 2004, 2008, 2009, 2010) studied how this *distinguished limit* can be established in the context of atmospheric flows such that the subsequent asymptotic analysis reveals leading-order equations that correspond to reduced model equation well-known in the literature of atmospheric fluid dynamics. Following these studies, we fix the small scale parameter ε by the Mach number such that $\mathrm{Ma}^2 = \varepsilon^3$, *i.e.*, $\varepsilon \approx 0.1$. The remaining non-dimensional numbers are then set to equate a power of ε times a constant of $O(1)$ (independent of ε):

$$\mathrm{Fr} = \mathrm{Ma} =: \varepsilon^{3/2} \tag{2.7a}$$

$$\mathrm{Ro} =: \frac{1}{\varepsilon f_0} \tag{2.7b}$$

$$\hat{\beta} =: \varepsilon^3 \beta \tag{2.7c}$$

$$\mathrm{Da} = \mathrm{Sr} = 1 \tag{2.7d}$$

The distinguished limit (2.7) transforms eqs. (2.3) into

$$\frac{\partial \rho}{\partial t} + \boldsymbol{\nabla}_{\parallel} \cdot \rho \boldsymbol{u} + \frac{\partial \rho w}{\partial z} = 0 \,, \tag{2.8a}$$

$$\frac{\partial \boldsymbol{u}}{\partial t} + \boldsymbol{u} \cdot \boldsymbol{\nabla}_{\parallel} \boldsymbol{u} + w\frac{\partial \boldsymbol{u}}{\partial z} + \frac{1}{\varepsilon^3}\frac{1}{\rho}\boldsymbol{\nabla}_{\parallel}p + \varepsilon(f_0 + \varepsilon^3 \beta y)\boldsymbol{k} \times \boldsymbol{u} = 0 \,, \tag{2.8b}$$

$$\frac{\partial w}{\partial t} + \boldsymbol{u} \cdot \boldsymbol{\nabla}_{\parallel} w + w\frac{\partial w}{\partial z} + \frac{1}{\varepsilon^3}\frac{1}{\rho}\frac{\partial p}{\partial z} = -\frac{1}{\varepsilon^3} \,, \tag{2.8c}$$

$$\frac{\partial \Theta}{\partial t} + \boldsymbol{u} \cdot \boldsymbol{\nabla}_{\parallel}\Theta + w\frac{\partial \Theta}{\partial z} = Q_{\Theta} \,. \tag{2.8d}$$

Note, that this set of equations is fully equivalent to its initial form given in eqs. (2.1) through the definitions of tables 2.1 to 2.3 and eqs. (2.7). With the formulation of eqs. (2.8), however, we have transformed the multi-parametrical eqs. (2.3) into equations depending on a single small parameter ε that ensures to maintain the flow regime throughout the limiting process, a property that naturally transfers to the solution.

The *distinguished limit* of eqs. (2.8) (in the spirit of Kutz (2020)) is based on the particular choice of reference parameters. Switching to another set of reference parameters, *e.g.*, by rescaling the coordinates, as we will see in sections 2.4.3 and 2.4.4, will modify eqs. (2.8) yielding a different *distinguished limit*.

In section 2.4, we make use of this single-parameter description and seek for solutions that approximate the atmospheric equations of fluid dynamics in the setting of a TC-like vortex. To this end, in the next two sections we discuss the methods of perturbation theory, *i.e.*, we analyze the asymptotic behavior of solution (leading- and higher-order) in the limit of $\varepsilon \to 0$. In addition to that, we show how by rescaling we are able to enter different scaling regimes and how to construct theories that span across multiple scale.

2.2. Regular Perturbation Theory and Asymptotic Expansions

In the previous section we prepared the set of governing equations (2.1) and constructed a single-parameter family of equations (2.7) involving a small parameter $0 < \varepsilon \ll 1$. As a consequence, solutions depend parametrically on ε, but in some unidentified way. Throughout the history of theoretical and mathematical physics (and related fields of science) it was and is common practice to analyze such problems involving small parameters[6] by means of *perturbation theory* hoping to find "nearby problems" that are of simpler structure and easier to solve. In the subsequent summary of the notions of *regular perturbation theory* we refer to the seminal publications of Eckhaus (1979), Erdélyi (1956), and Kruskal (1963). We follow in particular the notation of van Dyke (1975). This is typically accomplished by representing the solution ϕ by a *perturbation series expansion*

$$\phi(x; \varepsilon) = \phi^{(0)}(x) + \sum_{i=1}^{n} \varepsilon^i \phi^{(i)}(x) + o(\varepsilon^n) \tag{2.9}$$

i.e., a power series[7] in ε, and analyzing the limit $\varepsilon \to 0$. $\phi^{(0)}$ corresponds to the *leading-order solution*, *i.e.*, the solution ϕ in the limit $\varepsilon \to 0$, subject to the *leading-order problem*. $\{\phi^{(i)}\}_{i=1}^{n}$ are the *expansion coefficients* or *expansion modes* corresponding to the order $O(\varepsilon^i)$ and — by construction — independent of ε. n is called the *truncation order* of the series expansion resulting in the *error term* $o(\varepsilon^n)$ (below, we will give the latter symbol a more meaningful definition). This essentially means, that the summation of n terms approximates $\phi(x; \varepsilon)$ such that the error can be estimated by the final order ε^n.[8]

For non-zero perturbations we urge to have control over the correction terms, *i.e.*, the size of the error introduced by $n < \infty$, *i.e.*, restricting to the approximate problem.

---

[6] The methodology is not limited to small parameters. By introducing $\mu = 1/\varepsilon$, we can also analyze large parameters by converting the problem back to one of a small parameter.

[7] Mind the formal relation to the Taylor series: $\partial^n \phi(x; \varepsilon) / \partial \varepsilon^n |_{\varepsilon=0} = n! \phi^{(n)}(x)$.

[8] Note, that this does not necessarily mean convergence as $n \to \infty$, hence the series does not necessarily converge to ϕ. In fact, often perturbation (asymptotic) series diverge for large n. In the same way the convergence of a Taylor series may be impeded by a lack of higher-order differentiability, the dependency of ϕ on ε determines if for a given n the error term can be estimated by the final order function. However, for sufficiently regular ϕ there is always an optimal truncation order $n^* > 0$ up until the eq. (2.9) is valid, and the error term is under control.

To this end, it is necessary to set the terms $\varepsilon^i \phi^{(i)}$, $i = 1, 2, \ldots$ for a given i into relation to the other terms, especially to $\phi^{(0)}$. In other words, we seek for a notion of relative smallness of two expressions involving functions of ε in the vicinity of $\varepsilon = 0$. Following Eckhaus (1979) and van Dyke (1975), the *Landau symbols* provide a formal way of doing that by the following relations:

$$f(\varepsilon) := O(g(\varepsilon)) \qquad \Leftrightarrow \qquad \lim_{\varepsilon \to 0} \frac{f(\varepsilon)}{g(\varepsilon)} = c \quad \text{with} \quad |c| < \infty \qquad (2.10a)$$

$$f(\varepsilon) := o(g(\varepsilon)) \qquad \Leftrightarrow \qquad \lim_{\varepsilon \to 0} \frac{f(\varepsilon)}{g(\varepsilon)} = 0 \qquad (2.10b)$$

$$f(\varepsilon) := O_s(g(\varepsilon)) \qquad \Leftrightarrow \qquad f(\varepsilon) := O(g(\varepsilon)) \quad \text{and} \quad g(\varepsilon) := O(f(\varepsilon)) \quad (2.10c)$$

Note that the choice of the $\phi^{(i)}(x)$ independent of ε in eq. (2.9) is a particular one and may lead to limited success when apply to construct asymptotic approximations. A more general ansatz is constructed by asymptotic expansion modes that depend on ε and behave like

$$\phi^{(i)}(x; \varepsilon) = O_s(1) \quad \forall i < n \in \mathbb{N} \qquad (2.11)$$

This condition ensures that the powers of ε in eq. (2.9) determine the asymptotic order of each of the summation terms (in a decreasing manner) and hence, the resulting error term due to the truncation. It is, however, not necessary to ensure eq. (2.11) for the limit $n \to \infty$. Often, insightful results can be obtained by truncating the asymptotic series after the first few expansion modes. Thus, it may not be necessary for higher-order expansion modes to fulfill eq. (2.11), yet the approximation of eq. (2.9) behaves regular in the limit $\varepsilon \to 0$. In fact, practical applications often exhibit diverging behavior for higher-order terms due to the dependency of the solution on ε and the lack of higher-order differentiability w.r.t. ε.

Perturbation theory deals with the limiting behavior of ϕ when $\varepsilon \to 0$. To this end, the ansatz (2.9) is inserted into the governing equation and, by passing to the limit $\varepsilon \to 0$ we can find a constituting equation for $\phi^{(0)}$. This so obtained equation can be subtracted from the governing equation, and again by passing to the limit $\varepsilon \to 0$, we get a constituting equation for $\phi^{(1)}$, and so on. We end up with a hierarchy of equations for the expansion modes $\phi^{(i)}$.

Several branches of science have invented, re-invented and extended this methodology to their respective needs, each coining a particular methodology and terminology. In celestial mechanics, *e.g.*, the orbit of the moon around the earth in the gravitational field of earth and sun (a three-body problem without closed analytic solution) has been analyzed in terms of departures from the Keplerian orbit (solutions of the leading-order two-body problem) to find corrections that correspond to the three-body interaction (Gutzwiller 1998). In atmospheric fluid mechanics, this approach led to a number of *low Mach* model equations that exclude sub-dominant effects such as acoustic waves from the equations and by that increase the efficiency of numerical integration (Bannon 1996; Boussinesq 1897; Durran 1989; Klein 2010).

Pioneering work on asymptotic methods was conducted by Eckhaus (1979), Erdélyi (1956), Friedrichs (1955), Kruskal (1963), and van Dyke (1975), not only in systematizing the methodological framework of "Asymptotology [...] the art of dealing with applied mathematical systems in limiting cases" (Kruskal 1963). So is the choice of

powers of ε in eq. (2.9) rather arbitrary. For the sake of generalizing towards more complex problems, Erdélyi (1956) and later Kruskal (1963) discussed the limitations of a power series ansatz and introduced a more general form of eq. (2.9) called *asymptotic expansion*, essential for the methodology of *asymptotic analysis* or *asymptotics*, involving an *n*-term series with respect to the previously defined small scale parameter ε called *asymptotic series*:

$$\phi(x; \varepsilon) = \sum_{i=0}^{n} \epsilon_i(\varepsilon) \phi^{(i)}(x; \varepsilon) + o(\epsilon_n(\varepsilon)) \tag{2.12}$$

Here, we introduced the *order functions* $\epsilon_n(\varepsilon)$ satisfying $\epsilon_{n+1}(\varepsilon) = o(\epsilon_n(\varepsilon))$ as $\varepsilon \to 0$. Hence, the *perturbation series expansion* is a special case of the *asymptotic expansion* and *asymptotics* a superset of *perturbation theory*. *Asymptotology*, however, "at best a quasi-science" (Kruskal 1963), encompasses a rich body of theoretical and empirical findings that come handy when dealing with actual problems.

Although, there are studies on the general theory of the regularity of asymptotic analysis with respect to the truncation order *n* and the choice of $\{\epsilon_n\}_n$ (Eckhaus 1979), there is, unfortunately, no formal way of deciding which choice suits a particular problem best and ensures regularity. Often, either a related problem has proven to be tractable following a certain strategy, or it is trial and error.

By providing consistent results, Päschke et al. (2012) have given reason to an ansatz of a *regular asymptotic expansion* (see Eckhaus (1979) for details)

$$\phi(x; \varepsilon) = \sum_{i=0}^{n} \epsilon_i(\varepsilon) \phi^{(i)}(x) + o(\epsilon_n(\varepsilon)) \ , \tag{2.13}$$

i.e., assuming that expansion modes do not depend on ε, and restricting to order functions $\epsilon_n(\varepsilon) = \varepsilon^{\alpha(n-n_0)}$. The general form of the asymptotic expansion used later on reads

$$\phi(x; \varepsilon) = \sum_{i=0}^{n} \varepsilon^{\alpha(i-n_0)} \phi^{(i)}(x) + o(\varepsilon^i) \ . \tag{2.14}$$

With $\alpha \in \mathbb{Q}$ and $n_0 \in \mathbb{Z}$ we allow for non-integer powers of ε and for starting the series with powers other that ε^0. As we will see in the subsequent sections, with this approach we are able to reproduce the findings of Päschke et al. (2012) and generalize them to other scaling regimes.

2.3. Singular Perturbations and Multiple Scales

Problems in nature often occur on multiple scales that interact with each other. Usually, small-scale processes are guided by large-scale background states and eventually feed back to it. Examples are boundary layer-type problems that are common in the context of fluid dynamics. A fluid system is driven by a substantially different dynamics near a wall due to friction than it is in the free bulk flow. Other problems involve the interaction of fast and slow (or small and large) scale structures such as the interaction of small-scale convective cloud towers embedded into a larger-scale flow field (Hittmeir and Klein 2017; Klein and Majda 2006) or the aforementioned hierarchical three-body

problem moon-earth-sun. All of these problems involve a *scale separation*. The physics (and the mathematical structure of the governing equations) changes depending on the characteristic scale under consideration. Loosely speaking, looking through microscope will alter the view on the problem (as does the view through a telescope).

On a mathematical level, *scales* appear as small parameters in the governing equations that balance the different order differential terms and determine the importance of certain forces over other ones. In the definition of distinguished limits we agreed upon for this thesis, scales are the characteristic coordinate scales that appear when balancing certain differential terms at leading-order. Going from one scale to another by rescaling coordinates by powers of the small-scale parameter ε, one will potentially change the dominant balances (*i.e.*, switch to another distinguished limit) since prefactorial to the (differential) terms in the governing equation (*i.e.*, the powers of ε) are affected due to the explicit or implicit occurrence of the coordinates (*e.g.*, by differential operators).[9] Rescaling effectively means re-weighting the terms. These relative weight differences are what turns asymptotics into a powerful framework of simplifying equations since it allows ruling out certain terms in the leading-order equations and delegate them to higher order. Moreover, by coupling high-order modes with lower order modes, simple solutions of the low (leading) orders can be considered as given sources in the higher-order equations. A systematic analysis of eqs. (2.8) in terms of different spatial and temporal scales leads to a family of approximate PDEs accounting for the various single scale regimes apparent in the atmosphere (cf. Klein 2010).

The advantages of asymptotic analysis, however, come at a price. By rescaling, the structure and type of the leading-order, *i.e.*, the *limiting problem* can substantially differ from the original problem. In a PDE, *e.g.*, some differential terms may be dropped, and the problem changes its overall characteristic.[10] In that so-called *singular limit*, initial and/or boundary conditions may not be consistently applicable, anymore. The next two subsections will discuss strategies to tackle problems of that type.

2.3.1. Multiscale Asymptotics

One method to account for processes where two or more scales are interacting with each other is called *multiscale analysis*. The asymptotic ansatz (2.14) is modified such that

$$\phi(x;\varepsilon) := \sum_{i=0}^{n} \varepsilon^i \phi^{(i)}(\dots,\varepsilon^{-1}x,x,\varepsilon x,\dots;\varepsilon) + o\left(\varepsilon^i\right) , \qquad (2.18)$$

---

[9]In fact, a rescaling of coordinates that does not affect the distinguished limit falls under the category of similarity transformations.

[10]Think of the (hyperbolic) wave equation

$$\partial_t^2 \phi + \partial_x^2 \phi = 0 . \qquad (2.15)$$

When rescaling the spatial coordinate, $x \to \varepsilon x$, *i.e.*, focusing on smaller scales, we get the rescaled problem

$$\varepsilon^2 \partial_t^2 \phi + \partial_x^2 \phi = 0 . \qquad (2.16)$$

At leading order, we have the approximate balance

$$\partial_x^2 \phi^{(0)} = 0, \qquad (2.17)$$

resembling an elliptic equation, since the second time derivative couples at $O\left(\varepsilon^2\right)$, at first.

i.e., the expansion modes are treated as functions of variables, each representing an accordingly scaled coordinate. This approach results in PDEs in the respective coordinates to be solved hierarchically.

Multiscale asymptotics is of particular interest in situations where small-scale features coexists with large-scale features everywhere in the domain (*e.g.*, small oscillations on a slowly varying (even static) background). The large and the small-scale solution structures may interact with each other.

Although a powerful tool, multiscale asymptotics requires substantial input from physical intuition since assumptions are made on the structure of the solution. Equation (2.18), *e.g.*, requires a priori inputs on the separation between the interacting scales under consideration (number and ratio in terms of powers of ε of individually scaled coordinates that are treated as independent variables). Even in situations where it is technically possible to rigorously derive structural properties of the solution functions, restricting the solution structure a priori may help to substantially simplify the calculations (cf. Klein 2004, sec. 3.4). The high level of experience and intuition necessary to excel in this methodology could be one of the reasons why until now this method has been only rarely applied to investigate scale interactions in meteorological scenarios (Grooms, Julien, and Fox-Kemper 2011; Hittmeir and Klein 2017; Majda and Grooms 2014; Klein and Majda 2006; Owinoh et al. 2011; Pedlosky 1984, to name a few). See also Grooms and Julien (2018) for a recent review.

2.3.2. Matched Asymptotic Analysis

In scenarios where a restricted subdomain is interacting with the rest of the solution domain, *matched asymptotic analysis* can be considered to derive approximate solutions. In the context of fluid dynamics, one often analyzes the structure and interaction of a boundary layer (subdomain) with the bulk of the fluid flow (solution domain). Those derivations lead to successful models for describing fluid flows around obstacles such as air foils (Veldman 2001), but also gave insight into the flow structure of the planetary boundary layer (PBL) near the surface where the atmosphere interacts with land or ocean (Holton 2004).

A slightly different situation arises when studying TCs, that is a vortex core at small scale extent embedded into a larger-scale flow field. The notions of smallness of coordinates obviously requires an adapted choice of coordinates. As we will go more into details later in section 2.4.3, Päschke et al. (2012) considered a radial distance from the vortex core and derived a model based on two distinct scaling regimes with respect to the radial coordinate.

The matching procedure involves finding *matching conditions*, *i.e.*, boundary conditions in the overlap region between two individually scaled solution. To this end, we introduce the notation $\phi(x)$ for a function that approximates the solution on the outer (larger) scale and $\hat{\phi}(\hat{x})$ on the inner (smaller) scale. The basic idea is that the large-scale limits of a small-scale solution function shall coincide (up to truncation order) with the small-scale limit of the large scale solution:

$$\lim_{x \to 0} \phi(x) \simeq \lim_{\hat{x} \to \infty} \hat{\phi}(\hat{x}) = \phi_M \,. \tag{2.19}$$

Hence, rescaling to a common set of coordinates (possibly at intermediate scale and where both regimes hold approximately true) provides the matching boundary term ϕ_M.
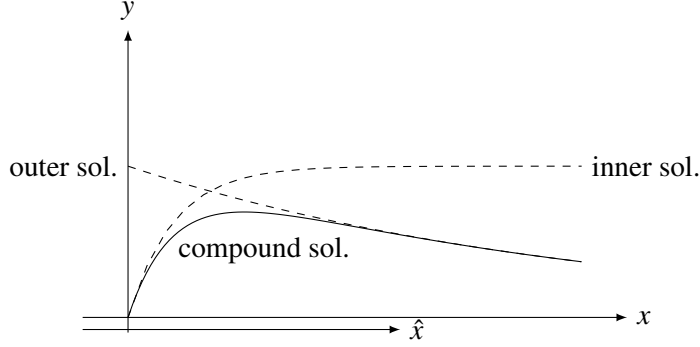
Figure 2.1.: Schematics of asymptotic matching. On the two different scales (inner and outer) individual solutions are found by single-scale asymptotics (dashed curves). By applying the method of asymptotic matching a compound solution is found (solid curve).

The compound approximation of the solution on the whole domain reads

$$\phi(x) + \hat{\phi}(\hat{x}) - \phi_M \tag{2.20}$$

The principle of the matching procedure is visualized in fig. 2.1. More details can be found in Eckhaus (1979), Klein (2004, 2017), and Kutz (2020), and will be given directly on the example of a TC in section 2.4.5.

A slightly different approach was introduced with van Dyke's (1975) matching principle: Assume we have outer and inner solutions $\phi(x)$ and $\hat{\phi}(\hat{x})$ given in terms of asymptotic series expansions, symbolized by

$$\phi(x) = E^{(m)}\phi(x) + o(\epsilon_n(\varepsilon)) := \sum_{n=0}^{m} \epsilon_n(\varepsilon)\phi^{(n)}(x) + o(\epsilon_n(\varepsilon)) \,, \tag{2.21a}$$

$$\hat{\phi}(\hat{x}) = \hat{E}^{(m)}\hat{\phi}(\hat{x}) + o(\hat{\epsilon}_n(\varepsilon)) := \sum_{n=0}^{m} \hat{\epsilon}_n(\varepsilon)\hat{\phi}^{(n)}(\hat{x}) + o(\hat{\epsilon}_n(\varepsilon)) \,. \tag{2.21b}$$

$E^{(m)}\phi(x)$ and $\hat{E}^{(m)}\hat{\phi}(\hat{x})$ stand for the outer and inner m-term expansion. Further, let us define the transformation operation

$$(T\phi)(\hat{x}) = \hat{\phi}(\hat{x}) = \phi(T^{-1}(\hat{x})) \,, \tag{2.22}$$

i.e., T being the conversion between the respectively scaled coordinate of the inner and outer regime. The coordinate x itself shall transform as $Tx = \hat{x} = \varepsilon^{\alpha-1}x$, with $0 < \alpha < 1$, in our specific case (cf. section 2.4.3). The actual matching then is performed by (Eckhaus 1979; Marschalik 2015; Päschke et al. 2012)

$$\hat{E}^{(m_i)}TE^{(m_o)}\phi = \hat{E}^{(m_i)}TE^{(m_o)}T^{-1}\hat{E}^{(m_i)}\hat{\phi}(\hat{x}) \,. \tag{2.23}$$

The left-hand side symbolizes the asymptotic expansion of the outer solution $E^{(m_o)}\phi(x)$, given as an asymptotic series up to order m_o, transformed to inner coordinates and expanded up to order m_i. Due to the smallness of ε, the leading-order terms of the resulting expansion correspond to the limit $x = \varepsilon^{1-\alpha}\hat{x} \to 0$. Conversely, on the

right-hand side, the solution given as the expansion $\hat{E}^{(m_i)} \hat{\phi}(\hat{x})$ is transformed to the outer coordinates and expanded into an asymptotic series up to order m_o. Again due to the smallness of ε, this procedure corresponds to the limiting process $\hat{x} = \varepsilon^{\alpha-1} x \to \infty$. Finally, for the sake of comparing with the small-scale expansion of the outer solution, the result is back-transformed to inner coordinates and once again expanded to order m_i. Both sides of the equation yield asymptotic expansions that can now be compared order-by-order to find matching terms. The procedure becomes more transparent with the direct example given in section 2.4.5.

2.4. Two-Scale Asymptotics of Tropical Cyclones

Here, we will recapture the essential results originally derived by Päschke et al. (2012) and show how to extend their findings, initially restricted to weak TCs in *gradient-wind balance*, towards the cyclostrophic regime. Hence, we introduce a more generalized scaling regime for the inner core solution and demonstrate in which way conclusions of the original derivation hold true through the regime transition.

From a methodological point of view, Päschke et al. (2012) made use of a two-scale matched asymptotics scheme to find a set of reduced equations. To this end, the governing equations are approximated on an *inner core* region, for which solutions are then matched to that of the *quasi-geostrophic* regime at large radii.

2.4.1. Azimuthal Fourier Modes 0 and 1

In the course of the following chapters we will make extensive use of the notion of *azimuthally symmetric* structures as well as *Fourier-1 modes*, *i.e.*, dipolar patterns of physical fields. Albeit a bit apart from the usual conventions but helpful in streamlining the notation, we will make the following definitions: For a scalar field given in polar coordinates $(r, \theta) \in \mathbb{R}_+ \times T([0, 2\pi])$ we have

$$\phi_0(r) := \frac{1}{2\pi} \int_0^{2\pi} \phi(r, \theta) \, d\theta \,, \tag{2.24a}$$

$$\phi_{11}(r) := \frac{1}{\pi} \int_0^{2\pi} \phi(r, \theta) \cos\theta \, d\theta \,, \tag{2.24b}$$

$$\phi_{12}(r) := \frac{1}{\pi} \int_0^{2\pi} \phi(r, \theta) \sin\theta \, d\theta \,. \tag{2.24c}$$

We further define the *dipole vector* $\boldsymbol{\phi}_1$ as

$$\boldsymbol{\phi}_1 := \begin{pmatrix} \phi_{11} \\ \phi_{12} \end{pmatrix} \tag{2.25}$$

This notation enables us to employ vector algebraic conventions. A dipolar field can be represented by the regular scalar product

$$\phi = \phi_{11} \cos\theta + \phi_{12} \sin\theta \equiv \boldsymbol{\phi}_1 \cdot \boldsymbol{e}_r \tag{2.26}$$

with the radial unit vector $\boldsymbol{e}_r = (\cos\theta, \sin\theta)$, and the azimuthal correlation of two dipolar fields reads

$$\frac{1}{2\pi} \int_0^{2\pi} (a_1 \cos\theta + a_2 \sin\theta)(b_1 \cos\theta + b_2 \sin\theta) \, d\theta \equiv \frac{1}{2} \boldsymbol{a} \cdot \boldsymbol{b} \,. \tag{2.27}$$
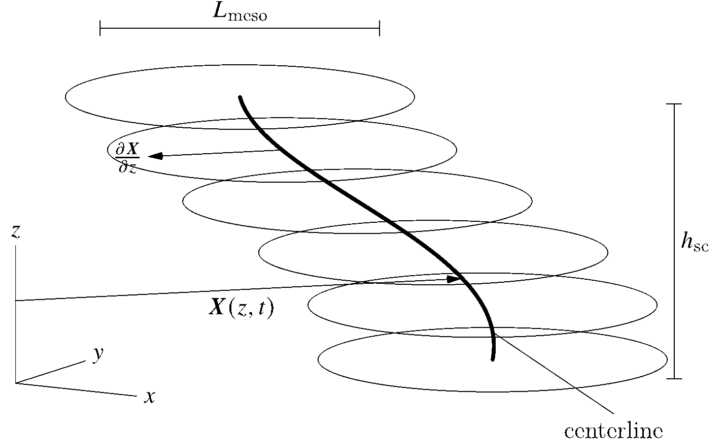
Figure 2.2.: Schematic structure of an idealized TC (based on Päschke et al. 2012).

Finally, by identifying the Fourier-1 mode of a dipolar field with a two-vector, we have a handle on the orientation of the field: For a given r, the vector $\boldsymbol{\phi}_1(r)$ points towards the direction of the maximum of the field.

Formally, this construction is nothing else than identifying the complex plane $\mathbb{C}$ with $\mathbb{R}^2$, since the real and imaginary parts of Fourier coefficients of real-valued functions correspond to the sine and cosine modes above. We will make use of the following correspondence:

$$\boldsymbol{\phi}_1 = \begin{pmatrix} \phi_{11} \\ \phi_{12} \end{pmatrix} \in \mathbb{R}^2 \qquad \Leftrightarrow \qquad \phi_1 = \phi_{11} + \iota \phi_{12} \in \mathbb{C}, \qquad (2.28)$$

where ι is the imaginary unit. This duality will help us to seamlessly switch between the vectorial and complex representation of dipolar structures when appropriate.

2.4.2. Co-Moving Centerline Coordinate

Before entering the scaling regime of the inner-core vortex flow, we transform the coordinates by defining centerline-relative coordinates $\boldsymbol{x}^{\text{rel}}$:

$$\boldsymbol{x}_{\parallel} =: \boldsymbol{X}(z,t) + \boldsymbol{x}^{\text{rel}} \quad \text{with} \quad \boldsymbol{x}^{\text{rel}} = r\boldsymbol{e}_r(\theta) . \qquad (2.29)$$

$\boldsymbol{x}_{\parallel}$ are the horizontal components of the Earth-relative coordinates. The definition of these *tilted polar coordinates* follows the choice of the mesoscale, *i.e.*, it depends on α to be defined in eq. (2.33). As a consequence, due to the functional dependency of the coordinate center w.r.t. z and t, differential operators transform accordingly:

$$\boldsymbol{\nabla}_{\parallel} = \boldsymbol{e}_r \frac{\partial}{\partial r} + \boldsymbol{e}_\theta \frac{1}{r}\frac{\partial}{\partial \theta} , \qquad (2.30a)$$

$$\left.\frac{\partial}{\partial z}\right|_{t,x,y} = \left.\frac{\partial}{\partial z}\right|_{t,r,\theta} - \frac{\partial \boldsymbol{X}}{\partial z} \cdot \boldsymbol{\nabla}_{\parallel} , \qquad (2.30b)$$

$$\left.\frac{\partial}{\partial t}\right|_{t,x,y} = \left.\frac{\partial}{\partial t}\right|_{t,r,\theta} - \frac{\partial \boldsymbol{X}}{\partial t} \cdot \boldsymbol{\nabla}_{\parallel} . \qquad (2.30c)$$

Finally, we define the storm-relative horizontal velocity according to

$$\boldsymbol{u} = \frac{\partial \boldsymbol{X}}{\partial t} + u_r \boldsymbol{e}_r + u_\theta \boldsymbol{e}_\theta \, . \tag{2.31}$$

Ultimately, eqs. (2.8) transform in the following way:

• Continuity:

$$\left. \frac{\partial \rho}{\partial t} \right|_{r,\theta,z} + \left(\frac{1}{r} \frac{\partial \rho u_r r}{\partial r} + \frac{1}{r} \frac{\partial \rho u_\theta}{\partial \theta} \right) + \left. \frac{\partial \rho w}{\partial z} \right|_{r,\theta,t} -$$
$$- \left(\frac{\partial \boldsymbol{X}}{\partial z} \cdot \boldsymbol{e}_r \frac{\partial \rho w}{\partial r} + \frac{\partial \boldsymbol{X}}{\partial z} \cdot \boldsymbol{e}_\theta \frac{1}{r} \frac{\partial \rho w}{\partial \theta} \right) = 0 \tag{2.32a}$$

• Radial momentum:

$$\left. \frac{\partial u_r}{\partial t} \right|_{r,\theta,z} + \left(u_r \frac{\partial u_r}{\partial r} + \frac{u_\theta}{r} \frac{\partial u_r}{\partial \theta} - \frac{u_\theta^2}{r} \right) + \left. w \frac{\partial u_r}{\partial z} \right|_{r,\theta,t} +$$
$$+ \left. \frac{\partial}{\partial t} \frac{\partial \boldsymbol{X}}{\partial t} \right|_{r,\theta,z} \cdot \boldsymbol{e}_r + \left. w \frac{\partial}{\partial z} \left(\frac{\partial \boldsymbol{X}}{\partial t} \cdot \boldsymbol{e}_r \right) \right|_{r,\theta,t} -$$
$$- \left(w \frac{\partial \boldsymbol{X}}{\partial z} \cdot \boldsymbol{e}_r \frac{\partial u_r}{\partial r} + w \frac{\partial \boldsymbol{X}}{\partial z} \cdot \boldsymbol{e}_\theta \frac{1}{r} \frac{\partial u_r}{\partial \theta} - w \frac{\partial \boldsymbol{X}}{\partial z} \cdot \boldsymbol{e}_\theta \frac{u_\theta}{r} \right) +$$
$$+ \frac{1}{\varepsilon^3} \frac{1}{\rho} \frac{\partial p}{\partial r} - \varepsilon \left(f_0 + \varepsilon^3 \beta y \right) \left(u_\theta + \frac{\partial \boldsymbol{X}}{\partial t} \cdot \boldsymbol{e}_\theta \right) = 0 \tag{2.32b}$$

• Tangential momentum:

$$\left. \frac{\partial u_\theta}{\partial t} \right|_{r,\theta,z} + \left(u_r \frac{\partial u_\theta}{\partial r} + \frac{u_r u_\theta}{r} + \frac{u_\theta}{r} \frac{\partial u_\theta}{\partial \theta} \right) + \left. w \frac{\partial u_\theta}{\partial z} \right|_{r,\theta,t} +$$
$$+ \left. \frac{\partial}{\partial t} \frac{\partial \boldsymbol{X}}{\partial t} \right|_{r,\theta,z} \cdot \boldsymbol{e}_\theta + \left. w \frac{\partial}{\partial z} \left(\frac{\partial \boldsymbol{X}}{\partial t} \cdot \boldsymbol{e}_\theta \right) \right|_{r,\theta,t} -$$
$$- \left(w \frac{\partial \boldsymbol{X}}{\partial z} \cdot \boldsymbol{e}_r \frac{\partial u_\theta}{\partial r} + w \frac{\partial \boldsymbol{X}}{\partial z} \cdot \boldsymbol{e}_\theta \frac{u_r}{r} + w \frac{\partial \boldsymbol{X}}{\partial z} \cdot \boldsymbol{e}_\theta \frac{1}{r} \frac{\partial u_\theta}{\partial \theta} \right) +$$
$$+ \frac{1}{\varepsilon^3} \frac{1}{\rho r} \frac{\partial p}{\partial \theta} + \varepsilon \left(f_0 + \varepsilon^3 \beta y \right) \left(u_r + \frac{\partial \boldsymbol{X}}{\partial t} \cdot \boldsymbol{e}_r \right) = 0 \tag{2.32c}$$

• Vertical momentum:

$$\left. \frac{\partial w}{\partial t} \right|_{r,\theta,z} + \left(u_r \frac{\partial w}{\partial r} + \frac{u_\theta}{r} \frac{\partial w}{\partial \theta} \right) + \left. w \frac{\partial w}{\partial z} \right|_{r,\theta,t} -$$
$$- \left(w \frac{\partial \boldsymbol{X}}{\partial z} \cdot \boldsymbol{e}_r \frac{\partial w}{\partial r} - w \frac{\partial \boldsymbol{X}}{\partial z} \cdot \boldsymbol{e}_\theta \frac{1}{r} \frac{\partial w}{\partial \theta} \right) + \frac{1}{\varepsilon^5} \frac{1}{\rho} \frac{\partial p}{\partial z} - \frac{1}{\varepsilon^5} \frac{1}{\rho} \frac{\partial \boldsymbol{X}}{\partial z} \cdot \boldsymbol{\nabla}_{\|} p = -\frac{1}{\varepsilon^5} \tag{2.32d}$$

• Potential temperature:

$$\left. \frac{\partial \Theta}{\partial t} \right|_{r,\theta,z} + \left(u_r \frac{\partial \Theta}{\partial r} + \frac{u_\theta}{r} \frac{\partial \Theta}{\partial \theta} \right) + \left. w \frac{\partial \Theta}{\partial z} \right|_{r,\theta,t} -$$
$$- \left(w \frac{\partial \boldsymbol{X}}{\partial z} \cdot \boldsymbol{e}_r \frac{\partial \Theta}{\partial r} - w \frac{\partial \boldsymbol{X}}{\partial z} \cdot \boldsymbol{e}_\theta \frac{1}{r} \frac{\partial \Theta}{\partial \theta} \right) = Q_\Theta \tag{2.32e}$$

2.4.3. Inner Core Flow

We came to the conclusion that independently of the actual defining reference parameters, the non-dimensional eqs. (2.3) govern the same general family of problems as the original eqs. (2.1). In case of the reference parameters being characteristic for the system, however, the non-dimensional coordinates and solution variables take values of the order unity, and the small parameters ε imposes an ordering system in size of the individual terms.

In section 2.1.3, we discussed how to rescale coordinates in order to capture scaling regimes other than approached directly by construction of the distinguished limits as outlined in section 2.1.3 and based on the original reference parameters (see tables 2.1 and 2.2). Since we are in non-dimensional coordinates, re-scaling means multiplying with an appropriate prefactor. We want to maintain the relative ordering of coordinate scales (*e.g.*, coordinate x being larger than z), throughout the limiting process, hence the re-scaling factor has to be in terms of powers of the small scale parameter ε. Together with the distinguished limit of the dimensionless characteristic numbers[11], rescaling the coordinates by ratios in terms of powers of ε leads to rebalancing of the constituting terms of the governing equation(s), the particular *distinguished limit* or *dominant balance*. Meaningful dominant balances, in that sense, justify the choice of the rescaling factor and therefore manifest a scaling regime. Although the numerical value of the ratio will change through the limiting process, z, transformed back to a dimensional coordinate, will be assured to be about the factor ε smaller than x.

All spatial coordinate in eqs. (2.8) are uniformly scaled with respect to the pressure scale height, *i.e.*, $h_{sc} \approx 10\,\text{km}$. Time is scaled with respect to corresponding advection timescale h_{sc}/u_{ref}.

Here, we revisit the findings of Päschke et al. (2012), and enter the *inner core regime* by rescaling horizontal and time coordinates of eqs. (2.8) accordingly:

$$\boldsymbol{x}_\| \to \frac{1}{\varepsilon^{1+\alpha}}\boldsymbol{x}_\| \tag{2.33a}$$

$$t \to \frac{1}{\varepsilon^{2+\alpha-\delta}}t \tag{2.33b}$$

The centerline $\boldsymbol{X}$ is rescaled consistently with $\boldsymbol{x}_\|$. With the parameter $\alpha \geq 0$ we allow for a more flexible scaling of the inner core size. $\alpha = 0$ corresponds to a horizontal scaling of $O(100\,\text{km})$ while $\alpha > 0$ enlarges this scale by a factor of $\varepsilon^{-\alpha}$. For the sake of reducing complexity, however, we allow for half-integer values of α, only. Moreover, the outer QG scale induces an upper bound at $\alpha = 1$ (cf. section 2.4.4), hence the values 0 and 1/2 are admissible. Along the lines of Päschke et al. (2012) we chose the *vortex core evolution timescale* as being by a factor ε^{-1} larger than the vortex turnover time:

$$t_{VC} = \frac{t_{to}}{\varepsilon} = \frac{L_{meso}}{\varepsilon u_{VC}} = \frac{h_{sc}}{\varepsilon^{2+\alpha-\delta}u_{ref}} = \frac{1}{\varepsilon^{2+\alpha-\delta}}t_{ref} \tag{2.34}$$

Similarly to α, we introduced the parameter $\delta \geq 0$ that settles the leading-order magnitude of the vortex-core maximum wind speed u_{VC}. $\delta = 0$ implies maximum wind speed of $u_{VC} = u_{ref} = O(10\,\text{m s}^{-1})$ and $\delta = 1/2$ is equivalent to $u_{VC} = O(30\,\text{m s}^{-1})$.

---

[11]Note, that we denote the distinguished limit of an equation the coupled limit of the dimensionless parameters of the equation(s) including ratios of coordinate rescalings.

Below we will explore the dependency of the structure of the leading-order equations on the scalings induced by α and δ. In particular, this will help to unveil the leading-order equations for both, the cyclostrophic and the gradient-wind regime and the structural similarities through these regimes.

The above stretching transformation recasts eqs. (2.32) into the distinguished limit equations of the vortex core:

- Continuity:

$$
\frac{1}{\varepsilon^\delta} \left.\frac{\partial \rho}{\partial t}\right|_{r,\theta,z} + \frac{1}{\varepsilon} \left(\frac{1}{r}\frac{\partial \rho u_r r}{\partial r} + \frac{1}{r}\frac{\partial \rho u_\theta}{\partial \theta} \right) + \frac{1}{\varepsilon^{2+\alpha}} \left.\frac{\partial \rho w}{\partial z}\right|_{r,\theta,t} -
$$
$$
- \frac{1}{\varepsilon^{2+\alpha}} \left(\frac{\partial \boldsymbol{X}}{\partial z} \cdot \boldsymbol{e}_r \frac{\partial \rho w}{\partial r} + \frac{\partial \boldsymbol{X}}{\partial z} \cdot \boldsymbol{e}_\theta \frac{1}{r}\frac{\partial \rho w}{\partial \theta} \right) = 0 \quad (2.35a)
$$

- Radial momentum:

$$
\frac{1}{\varepsilon^\delta} \left.\frac{\partial u_r}{\partial t}\right|_{r,\theta,z} + \frac{1}{\varepsilon} \left(u_r \frac{\partial u_r}{\partial r} + \frac{u_\theta}{r}\frac{\partial u_r}{\partial \theta} - \frac{u_\theta^2}{r} \right) + \frac{1}{\varepsilon^{2+\alpha}} w \left.\frac{\partial u_r}{\partial z}\right|_{r,\theta,t} +
$$
$$
+ \varepsilon^{1-2\delta} \left.\frac{\partial}{\partial t}\frac{\partial \boldsymbol{X}}{\partial t}\right|_{r,\theta,z} \cdot \boldsymbol{e}_r + \frac{1}{\varepsilon^{1+\delta+\alpha}} w \frac{\partial}{\partial z}\left.\left(\frac{\partial \boldsymbol{X}}{\partial t} \cdot \boldsymbol{e}_r \right)\right|_{r,\theta,t} -
$$
$$
- \frac{1}{\varepsilon^{2+\alpha}} \left(w\frac{\partial \boldsymbol{X}}{\partial z} \cdot \boldsymbol{e}_r \frac{\partial u_r}{\partial r} + w\frac{\partial \boldsymbol{X}}{\partial z} \cdot \boldsymbol{e}_\theta \frac{1}{r}\frac{\partial u_r}{\partial \theta} - w\frac{\partial \boldsymbol{X}}{\partial z} \cdot \boldsymbol{e}_\theta \frac{u_\theta}{r} \right) +
$$
$$
+ \frac{1}{\varepsilon^4}\frac{1}{\rho}\frac{\partial p}{\partial r} - \left(\frac{1}{\varepsilon^{1+\alpha}} f_0 + \varepsilon^{-2\alpha}\beta y \right)\left(u_\theta + \varepsilon^{1-\delta}\frac{\partial \boldsymbol{X}}{\partial t} \cdot \boldsymbol{e}_\theta \right) = 0 \quad (2.35b)
$$

- Tangential momentum:

$$
\frac{1}{\varepsilon^\delta} \left.\frac{\partial u_\theta}{\partial t}\right|_{r,\theta,z} + \frac{1}{\varepsilon} \left(u_r \frac{\partial u_\theta}{\partial r} + \frac{u_r u_\theta}{r} + \frac{u_\theta}{r}\frac{\partial u_\theta}{\partial \theta} \right) + \frac{1}{\varepsilon^{2+\alpha}} w \left.\frac{\partial u_\theta}{\partial z}\right|_{r,\theta,t} +
$$
$$
+ \varepsilon^{1-2\delta} \left.\frac{\partial}{\partial t}\frac{\partial \boldsymbol{X}}{\partial t}\right|_{r,\theta,z} \cdot \boldsymbol{e}_\theta + \frac{1}{\varepsilon^{1+\delta+\alpha}} w \frac{\partial}{\partial z}\left.\left(\frac{\partial \boldsymbol{X}}{\partial t} \cdot \boldsymbol{e}_\theta \right)\right|_{r,\theta,t} -
$$
$$
- \frac{1}{\varepsilon^{2+\alpha}} \left(w\frac{\partial \boldsymbol{X}}{\partial z} \cdot \boldsymbol{e}_r \frac{\partial u_\theta}{\partial r} + w\frac{\partial \boldsymbol{X}}{\partial z} \cdot \boldsymbol{e}_\theta \frac{u_r}{r} + w\frac{\partial \boldsymbol{X}}{\partial z} \cdot \boldsymbol{e}_\theta \frac{1}{r}\frac{\partial u_\theta}{\partial \theta} \right) +
$$
$$
+ \frac{1}{\varepsilon^4}\frac{1}{\rho r}\frac{\partial p}{\partial \theta} + \left(\frac{1}{\varepsilon^{1+\alpha}} f_0 + \varepsilon^{-2\alpha}\beta y \right)\left(u_r + \varepsilon^{1-\delta}\frac{\partial \boldsymbol{X}}{\partial t} \cdot \boldsymbol{e}_r \right) = 0 \quad (2.35c)
$$

- Vertical momentum:

$$
\frac{1}{\varepsilon^\delta} \left.\frac{\partial w}{\partial t}\right|_{r,\theta,z} + \frac{1}{\varepsilon} \left(u_r \frac{\partial w}{\partial r} + \frac{u_\theta}{r}\frac{\partial w}{\partial \theta} \right) + \frac{1}{\varepsilon^{2+\alpha}} w \left.\frac{\partial w}{\partial z}\right|_{r,\theta,t} -
$$
$$
- \frac{1}{\varepsilon^{2+\alpha}} \left(w\frac{\partial \boldsymbol{X}}{\partial z} \cdot \boldsymbol{e}_r \frac{\partial w}{\partial r} - w\frac{\partial \boldsymbol{X}}{\partial z} \cdot \boldsymbol{e}_\theta \frac{1}{r}\frac{\partial w}{\partial \theta} \right) + \frac{1}{\varepsilon^{7+\alpha}}\frac{1}{\rho}\frac{\partial p}{\partial z} -
$$
$$
- \frac{1}{\varepsilon^{7+\alpha}}\frac{1}{\rho}\frac{\partial \boldsymbol{X}}{\partial z} \cdot \boldsymbol{\nabla}_\| p = -\frac{1}{\varepsilon^{7+\alpha}}
$$
$$
(2.35d)
$$

• Potential temperature:

$$\frac{1}{\varepsilon^\delta} \left.\frac{\partial \Theta}{\partial t}\right|_{r,\theta,z} + \frac{1}{\varepsilon}\left(u_r \frac{\partial \Theta}{\partial r} + \frac{u_\theta}{r}\frac{\partial \Theta}{\partial \theta}\right) + \frac{1}{\varepsilon^{2+\alpha}}w \left.\frac{\partial \Theta}{\partial z}\right|_{r,\theta,t} -$$
$$-\frac{1}{\varepsilon^{2+\alpha}}\left(w\frac{\partial X}{\partial z}\cdot e_r \frac{\partial \Theta}{\partial r} - w\frac{\partial X}{\partial z}\cdot e_\theta \frac{1}{r}\frac{\partial \Theta}{\partial \theta}\right) = \frac{1}{\varepsilon^{2+\alpha}}Q_\Theta$$

(2.35e)

The asymptotic expansion of the physical field reads

$$p = p_0(z) + \varepsilon p_1(z) + \varepsilon^2 \left(p^{(2)}(r,\theta,z,t) + p_2(z)\right) + o\left(\varepsilon^2\right) \tag{2.36a}$$

$$\rho = \rho_0(z) + \varepsilon \rho_1(z) + \varepsilon^2 \left(\rho^{(2)}(r,\theta,z,t) + \rho_2(z)\right) + o\left(\varepsilon^2\right) \tag{2.36b}$$

$$\Theta = \Theta_0(z) + \varepsilon \Theta_1(z) + \varepsilon^2 \left(\Theta^{(2)}(r,\theta,z,t) + \Theta_2(z)\right) + o\left(\varepsilon^2\right) \tag{2.36c}$$

$$u_r = \frac{1}{\varepsilon^\delta}\left(\qquad \varepsilon u_r^{(1)}(r,\theta,z,t) + o(\varepsilon)\right) \tag{2.36d}$$

$$u_\theta = \frac{1}{\varepsilon^\delta}\left(u_\theta^{(0)}(r,z,t) + \varepsilon u_\theta^{(1)}(r,\theta,z,t) + o(\varepsilon)\right) \tag{2.36e}$$

$$w = \frac{1}{\varepsilon^\delta}\left(\qquad \varepsilon w^{(1)}(r,\theta,z,t) + o(\varepsilon)\right) \tag{2.36f}$$

$$X = \frac{1}{\varepsilon^{1-\alpha}}X_0 + X^{(0)} + o(1) \tag{2.36g}$$

We made the same symmetry and scaling assumption for the leading-order tangential wind $u_\theta^{(0)}$ as Päschke et al. (2012). Only, we avoid an intermediate asymptotic mode $u_\theta^{(1/2)}$ as it turns out to be superfluous. From table 2.3 we recall that the Rossby number is based on the involved length scale and reference velocity. Our approach, in fact, leads to an effective or *vortex core Rossby number*

$$\mathrm{Ro_{VC}} = \varepsilon^{1+\alpha-\delta}\underbrace{\frac{u_{\mathrm{ref}}}{h_{\mathrm{sc}}f_{\mathrm{ref}}}}_{\mathrm{Ro}=O\left(\varepsilon^{-1}\right)} = O\left(\varepsilon^{\alpha-\delta}\right), \tag{2.37}$$

characterizing the flow regime in the vortex core region. If $\alpha = \delta$, $\mathrm{Ro_{VC}} = O(1)$, and we are in the *gradient wind regime*. With $\delta > \alpha$ we enter the *cyclostrophic regime*. For our following considerations we abandon the case of $\alpha > \delta$, i.e., the *geostrophic flow regime*.

Inserting eqs. (2.36) into eqs. (2.32), we obtain the following hierarchy of asymptotic equations guiding the motions of tropical storms:

First, we get the *cyclostrophic* or *gradient-wind balance* for the leading-order radial force depending on the choice of δ:

$$\frac{1}{\rho_0}\frac{\partial p^{(3-2\delta)}}{\partial r} = \frac{\left(u_\theta^{(0)}\right)^2}{r} + f_0 u_\theta^{(\alpha-\delta)} = \begin{cases}\dfrac{\left(u_\theta^{(0)}\right)^2}{r}, & \delta > \alpha \\[3mm] \dfrac{\left(u_\theta^{(0)}\right)^2}{r} + f_0 u_\theta^{(0)}, & \delta = \alpha\end{cases} \tag{2.38}$$

27

Moreover, due to the symmetry of $u_\theta^{(0)}$, $p^{(3-2\delta)}$ is axisymmetric as well:

$$\frac{\partial p^{(3-2\delta)}}{\partial \theta} = 0 \,. \tag{2.39}$$

This balance settles the order $\varepsilon^{3-2\delta}$ at which the pressure is horizontally balancing the circular motions. We find that the horizontal averages of the at horizontal pressure modes up to at least $O(\varepsilon^2)$ follow the *hydrostatic balance*:

$$\frac{\partial p_i}{\partial z} = -\rho_i \,, \quad i = 0, 1, 2 \tag{2.40a}$$

In addition to that, the non-trivial contribution due to eq. (2.38) is hydrostatic as well:

$$\frac{\partial p^{(3-2\delta)}}{\partial z} - \frac{\partial X^{(0)}}{\partial z} \cdot e_r \frac{\partial p^{(3-2\delta)}}{\partial r} = -\rho^{(3-2\delta)} \tag{2.40b}$$

According to the *equation of state* we get[12]

$$\frac{p^{(3-2\delta)}}{\gamma p_0} = \frac{\rho^{(3-2\delta)}}{\rho_0} + \frac{\theta^{(3-2\delta)}}{\theta_0} \tag{2.41}$$

and for the involved mode of potential temperature we find a modified version of the *weak temperature gradient approximation*:

$$\frac{u_\theta^{(0)}}{r} \frac{\partial \Theta^{(3-2\delta)}}{\partial \theta} + w^{(3+\alpha-2\delta)} \frac{d\Theta_1}{dz} = Q_\Theta^{(4+\alpha-3\delta)} \tag{2.42}$$

$w^{(3+\alpha-2\delta)}$ is the leading-order mode of vertical velocity that takes into account that the pressure perturbations due to the gradient-wind (cyclostrophic) balance (2.38) lead to a modulation of the density and ultimately a perturbation in the potential temperature (c.f. eqs. (2.40b) and (2.41)). As a result of the tilt, the horizontal pressure gradient translates into a Fourier-mode 1 perturbation of the density and consequently of the potential temperature (c.f. eq. (2.40b)). This thermodynamic adjustment leads to a dipolar deformation of surfaces of constant entropy (potential temperature) which adiabatic fluid parcels are required to follow, and hence we observe an adiabatic dipolar perturbation of the vertical velocity (c.f. eq. (2.42)).

Since $w^{(i)} d\Theta_1/dz = Q^{(1-\delta+i)}$ for $i < 3 + \alpha - 2\delta$, we are at liberty to set the heating $Q^{(j)} \equiv 0$ for $j < 4 + \alpha - 3\delta$. The corresponding mode of the vertical velocity is balanced by the *anelastic constraint*:

$$\frac{1}{r} \frac{\partial u_r^{(2-2\delta)} r}{\partial r} + \frac{1}{r} \frac{\partial u_\theta^{(2-2\delta)}}{\partial \theta} + \frac{1}{\rho_0} \frac{\partial \rho_0 w^{(3+\alpha-2\delta)}}{\partial z} = \frac{\partial X^{(0)}}{\partial z} \cdot \nabla_\parallel \left(w^{(3+\alpha-2\delta)} \right) \tag{2.43}$$

Due to the above order restriction of vertical velocity, all modes of horizontal velocity of order larger than $O(\varepsilon^{2-2\delta})$ are horizontally divergence-free, *i.e.*,

$$\frac{1}{r} \frac{\partial \rho_0 u_r^{(i)} r}{\partial r} + \frac{1}{r} \frac{\partial \rho_0 u_\theta^{(i)}}{\partial \theta} = 0 \quad \text{for} \quad i < 2 - 2\delta \,. \tag{2.44}$$

---

[12]$(\gamma - 1)/\gamma =: \Gamma^{**}\varepsilon = 2/7$ as $\varepsilon \to 0$, with $\Gamma^{**} = O(1)$, is considered small (*Newtonian Limit*). See the discussion of eq. (21) in Klein and Majda (2006). For more reference, also see Lipps and Hemler (1982) and Parkins et al. (2000).

From axisymmetry of $u_\theta^{(0)}$ follows $u_r^{(0)} \equiv 0$. For the radial momentum at order $O(\varepsilon^{-2\delta})$ we get

$$\frac{u_\theta^{(0)}}{r}\frac{\partial u_r^{(1)}}{\partial \theta} - 2\frac{u_\theta^{(0)} u_\theta^{(1)}}{r} + \frac{1}{\rho_0}\frac{\partial p^{(4-2\delta)}}{\partial r} - \frac{\rho_1}{\rho_0^2}\frac{\partial p^{(3-2\delta)}}{\partial r} -$$

$$-f_0\left(u_\theta^{(1+\alpha-\delta)} + \frac{\partial \boldsymbol{X}^{(\alpha-\delta)}}{\partial t}\cdot \boldsymbol{e}_\theta\right) - \beta y u_\theta^{(2\alpha-\delta)} = 0 \qquad (2.45)$$

In addition to these diagnostic equations, we find a prognostic equation for the dynamics of the leading-order tangential wind speed. Equation (2.42) settles the leading-order of vertical velocity to $w^{(\alpha^*)}$ with $\alpha^* = 3 + \alpha - 2\delta$ for abbreviation, and we arrive at

$$\frac{\partial u_\theta^{(0)}}{\partial t} + u_r^{(1)}\frac{\partial u_\theta^{(0)}}{\partial r} + \frac{u_r^{(1)}}{r}u_\theta^{(0)} + \frac{u_\theta^{(0)}}{r}\frac{\partial u_\theta^{(1)}}{\partial \theta} + w^{(\alpha^*)}\frac{\partial u_\theta^{(2\delta-1)}}{\partial z} -$$

$$-w^{(\alpha^*)}\frac{\partial \boldsymbol{X}^{(1-2\delta)}}{\partial z}\cdot \boldsymbol{e}_r\frac{\partial u_\theta^{(0)}}{\partial r} + \frac{1}{\rho_0 r}\frac{\partial p^{(4-2\delta)}}{\partial \theta} + f_0\left(u_r^{(1+\alpha-\delta)} + \frac{\partial \boldsymbol{X}^{(\alpha-\delta)}}{\partial t}\cdot \boldsymbol{e}_r\right) = 0\,.$$

$$(2.46)$$

For symmetry reasons ($\partial_\theta u_\theta^{(0)} = 0$), eq. (2.46) further simplifies to

$$\frac{\partial u_\theta^{(0)}}{\partial t} + u_{r,0}^{(1)}\frac{\partial u_\theta^{(0)}}{\partial r} + \frac{u_{r,0}^{(1)}}{r}u_\theta^{(0)} + w_0^{(\alpha^*)}\frac{\partial u_\theta^{(2\delta-1)}}{\partial z} =$$

$$\frac{\partial u_\theta^{(0)}}{\partial r}\left(w^{(\alpha^*)}\frac{\partial \boldsymbol{X}^{(1-2\delta)}}{\partial z}\cdot \boldsymbol{e}_r\right)_0 - f_0 u_{r,0}^{(1+\alpha-\delta)} \qquad (2.47)$$

The subscript $(\cdot)_0$ refers to the Fourier-0 mode according to eq. (2.24a). We may argue here, that the regime $\delta = 0$ does not comply with the observations. With eq. (2.38) we found that the leading-order pressure perturbation (that deviates from horizontal homogeneity) scales with $\varepsilon^{3-2\delta}$, i.e., for $\delta = 0$ that would correspond to pressure perturbation of the order $O(\varepsilon^3 p') = 1$ hPa, much too weak for a tropical cyclone. For transparency, however, we keep δ wherever it appeared in the derivations but may use the circumstance that it is fixed to $\delta = 1/2$. Especially for the above equation that helps us to argue that the coupling $w^{(\alpha^*)}\partial_z \boldsymbol{X}^{(1-2\delta)}$ can be dropped, which nicely resembles the result of Päschke et al. (2012) and leads us to the conclusion that this equation is preserved in its structure also in the regime of $\alpha = 0$.

Equation (2.43) yields a relation between the mean radial inflow $u_{r,0}^{(2-2\delta)}$ and the vertical velocity Fourier modes 0 and 1 (cf. section 2.4.1):

$$\frac{1}{r}\frac{\partial r\rho_0 u_{r,0}^{(2-2\delta)}}{\partial r} + \frac{\partial \rho_0 w_0^{(\alpha^*)}}{\partial z} = \frac{1}{2}\frac{\partial \boldsymbol{X}^{(0)}}{\partial z}\cdot \frac{\partial \rho_0 \boldsymbol{w}_1^{(\alpha^*)}}{\partial r} \qquad (2.48)$$

Without friction there is no other driver for radial inflow except vertical mass fluxes, hence this equation gives the leading-order radial velocity. In particular, the term $u_{r,0}^{(1+\alpha-\delta)}$ of eq. (2.47) vanishes for $\alpha = 0$, as assumed by eq. (2.36d). It is driven by both, Fourier modes 0 and 1 of vertical velocity. Together with the symmetrized radial

flux components

$$u_{r,*}^{(2-2\delta)} := \frac{1}{2}\frac{\partial X^{(0)}}{\partial z}\cdot w_1^{(\alpha^*)}, \tag{2.49a}$$

$$u_{r,00}^{(2-2\delta)} := u_{r,0}^{(2-2\delta)} - u_{r,*}^{(2-2\delta)}, \tag{2.49b}$$

we obtain

$$u_{r,00}^{(2-2\delta)} = -\frac{1}{r}\int_0^r \frac{r'}{\rho_0}\frac{\partial}{\partial z}\left(\rho_0 w_0^{(\alpha^*)}\right)dr'. \tag{2.50}$$

By projecting eq. (2.42) onto Fourier modes 0 and 1, *i.e.*,

$$w_0^{(\alpha^*)}\frac{d\Theta_1}{dz} = Q_{\Theta,0}^{(\alpha^*+1-\delta)} \tag{2.51a}$$

$$\frac{u_\theta^{(0)}}{r}\hat{R}_{-\pi/2}\Theta_1^{(3-2\delta)} + w_1^{(\alpha^*)}\frac{d\Theta_1}{dz} = Q_{\Theta,1}^{(\alpha^*+1-\delta)} \tag{2.51b}$$

Taking advantage of the projections of eqs. (2.40b) and (2.41) onto the Fourier 1 mode we end up with the perturbation potential temperature dipole induced by the centerline tilt:

$$\frac{\Theta_1^{(3-2\delta)}}{\Theta_0} = -\frac{1}{\rho_0}\frac{\partial p^{(3-2\delta)}}{\partial r}\frac{\partial X^{(0)}}{\partial z} \tag{2.52}$$

Equation (2.51b) transforms into

$$w_1^{(\alpha^*)} = \frac{1}{d\Theta_1/dz}\left(Q_{\Theta,1}^{(\alpha^*+1-\delta)} + \hat{R}_{-\pi/2}\frac{\Theta_0}{\rho_0}\frac{u_\theta^{(0)}}{r}\frac{\partial p^{(3-2\delta)}}{\partial r}\frac{\partial X^{(0)}}{\partial z}\right) \tag{2.53}$$

where the vertical velocity dipole takes a contribution due to diabatic heating and one that is caused by and perpendicular to the centerline tilt.

The above derivations lead us to the conclusion that the radial influx splits into a contribution ($u_{r,00}^{(2-2\delta)}$) due to symmetric diabatic heating (eq. (2.50)) and another one ($u_{r,*}^{(2-2\delta)}$) traced back to the projection of the vertical velocity dipole $w_1^{(\alpha^*)}$ onto the tilt vector $\partial_z X^{(0)}$ (cf. eq. (2.49a)). Since the vertical velocity contribution attributed to a dipolar potential temperature perturbation is perpendicular to the tilt, it vanished in the projection of eq. (2.49a) and the only projecting moment comes from the diabatic heating dipole:

$$u_{r,*}^{(2-2\delta)} = \frac{1}{2}\frac{\partial X^{(0)}}{\partial z}\cdot\frac{Q_{\Theta,1}^{(\alpha^*+1-\delta)}}{d\Theta_1/dz} \tag{2.54}$$

We shall emphasize that the attribution of diabatic heating to vertical velocity is an artifact of the equations (2.1) that model atmospheric flows by dry dynamics. In atmospheric fluid dynamics including moist thermodynamics as well as friction, vertical motions can have different origin. Nevertheless, it is ultimately the projection (*i.e.*, the orientation) of asymmetric vertical motions relative to the centerline tilt that causes an azimuthally mean radial inflow $u_{r,*}^{(2-2\delta)}$ additionally to the classical inflow due to symmetric heating. We will come back to this discussion later.

In section 2.4.4, we will outline the construction of a leading-order solution to eqs. (2.1) by an approximation to the streamfunction ψ. For the sake of matching

the inner-core and quasi-geostrophic outer solution (in section 2.4.5) we introduce the streamfunction for the inner-core as well, but due to the presence of diabatic heating, we cannot assume the flow to be horizontally divergence-free on the expansion order at which the inner solution is matched to the outer one.

At $O(\varepsilon^1)$, radial and tangential components of the relative horizontal velocity are expressed by the *Helmholtz-Hodge decomposition* in polar coordinates:

$$u_r^{(1)} = \frac{1}{r}\frac{\partial \psi^{(1)}}{\partial \theta} + \frac{\partial \phi^{(1)}}{\partial r}, \tag{2.55a}$$

$$u_\theta^{(1)} = -\frac{\partial \psi^{(1)}}{\partial r} + \frac{1}{r}\frac{\partial \phi^{(1)}}{\partial \theta}. \tag{2.55b}$$

ψ is the streamfunction and ϕ is the velocity potential associated to the relative horizontal velocity. In analogy with Päschke et al. (2012), by cross-differentiation eqs. (2.45) and (2.46) and projecting to the Fourier-1 mode we find the elliptic equations

$$\left(\frac{\partial^2}{\partial r^2} + \frac{1}{r}\frac{\partial}{\partial r} - \left(\frac{\partial_r \zeta^{(0)}}{u_\theta^{(0)}} + \frac{1}{r^2}\right)\right)\psi_1^{(1)} = \frac{1}{u_\theta^{(0)}}\boldsymbol{k} \times (\mathcal{H} + \mathcal{I} + \mathcal{J} + \boldsymbol{Q})$$

$$\equiv \frac{1}{u_\theta^{(0)}}\boldsymbol{k} \times \mathcal{K} \tag{2.56}$$

and

$$\left(\frac{\partial^2}{\partial r^2} + \frac{1}{r}\frac{\partial}{\partial r} - \frac{1}{r^2}\right)\boldsymbol{\phi}_1^{(1)} = -\frac{1}{\rho_0}\frac{\partial\left(\rho_0 \boldsymbol{w}_1^{(\alpha^*)}\right)}{\partial z} + \frac{1}{2}\frac{\partial X^{(0)}}{\partial z}\frac{\partial w_0^{(\alpha^*)}}{\partial r}$$

$$\equiv \boldsymbol{R}_1 \tag{2.57}$$

The definitions of $\mathcal{H}$, $\mathcal{I}$, $\mathcal{J}$, and $\boldsymbol{Q}$ are given by

$$\mathcal{H} = \partial_r\left(r w_1^{(\alpha^*)}\partial_z u_\theta^{(2\delta-1)}\right), \tag{2.58a}$$

$$\mathcal{I} = r\left(\zeta^{(0)} + 2\alpha f_0\right)\boldsymbol{W}_1, \tag{2.58b}$$

$$\mathcal{J} = \left(\frac{\partial \boldsymbol{\phi}_1^{(1)}}{\partial r}\right)\left(r\frac{\partial \zeta^{(0)}}{\partial r}\right), \tag{2.58c}$$

$$\boldsymbol{Q} = \left(w_0^{(\alpha^*)}\frac{u_\theta^{(0)}}{r} - \frac{\partial}{\partial r}\left(r w_0^{(\alpha^*)}\partial_r u_\theta^{(0)}\right)\right)\frac{\partial X^{(1-2\delta)}}{\partial z} \tag{2.58d}$$

in conjunction with the definitions

$$\boldsymbol{W}_1 = -\frac{1}{\rho_0}\partial_z(\rho_0 \boldsymbol{w}_1^{(\alpha^*)}) \tag{2.59a}$$

$$\zeta^{(0)} = \frac{1}{r}\frac{\partial(r u_\theta^{(0)})}{\partial r}. \tag{2.59b}$$

By radial integration and variation of constants we have integral expressions for $\boldsymbol{\psi}^{(1)}$ and $\boldsymbol{\phi}_1^{(1)}$:

$$\boldsymbol{\phi}_1^{(1)} = -r \int\limits_r^\infty \frac{1}{(r')^3} \int\limits_0^{r'} \bar{r}^2 \boldsymbol{R}_1 \, d\bar{r} \, dr' \,, \tag{2.60}$$

$$\boldsymbol{\psi}_1^{(1)} = \boldsymbol{k} \times \left(u_\theta^{(0)} \int\limits_0^r \frac{1}{r' \left(u_\theta^{(0)} \right)^2} \int\limits_0^{r'} \bar{r} \left(\mathcal{H} + \mathcal{I} + \mathcal{J} + \boldsymbol{Q} \right) d\bar{r} \, dr' \right). \tag{2.61}$$

The latter equation for the streamfunction is essential for the matching procedure as outlined in section 2.3.2 and the result of which presented in section 2.3.2. Physically speaking, the large-scale limit determines how the vortex core couples to the QG flow which is guided at leading order solely by the streamfunction.

2.4.4. Large-Scale Quasi-Geostrophic Flow

To the end of entering the *quasi-geostrophic* regime, ubiquitously present in the meteorological literature (Holton 2004), that resolves advective motions on horizontal distances comparable to the synoptic scale, we rescale horizontal and time coordinates, as given through the definitions of table 2.2, according to

$$\boldsymbol{x}_\| \rightarrow \frac{1}{\varepsilon^2} \boldsymbol{x}_\| \,, \tag{2.62}$$

$$t \rightarrow \frac{1}{\varepsilon^2} t \,. \tag{2.63}$$

This choice corresponds to a timescale that is by a factor $\varepsilon^{\alpha-\delta}$ longer compared to the turnover timescale of the vortex core (cf. eq. (2.33)). The horizontal scale, however, is fixed to be of order $h_{\mathrm{sc}}/\varepsilon^2 \approx 1000\,\mathrm{km}$ at subtropical latitudes.

Starting with eqs. (2.7) and transforming the coordinates according to eqs. (2.8), the resulting equations are

$$\frac{\partial \rho}{\partial t} + \boldsymbol{\nabla}_\| \cdot \rho \boldsymbol{u} + \frac{1}{\varepsilon^2} \frac{\partial \rho w}{\partial z} = 0 \,, \tag{2.64a}$$

$$\frac{\partial \boldsymbol{u}}{\partial t} + \boldsymbol{u} \cdot \boldsymbol{\nabla}_\| \boldsymbol{u} + \frac{1}{\varepsilon^2} w \frac{\partial \boldsymbol{u}}{\partial z} + \frac{1}{\varepsilon^3} \frac{1}{\rho} \boldsymbol{\nabla}_\| p + \frac{1}{\varepsilon} (f_0 + \varepsilon \beta y) \boldsymbol{k} \times \boldsymbol{u} = 0 \,, \tag{2.64b}$$

$$\frac{\partial w}{\partial t} + \boldsymbol{u} \cdot \boldsymbol{\nabla}_\| w + \frac{1}{\varepsilon^2} w \frac{\partial w}{\partial z} + \frac{1}{\varepsilon^5} \frac{1}{\rho} \frac{\partial p}{\partial z} = -\frac{1}{\varepsilon^5} \,, \tag{2.64c}$$

$$\frac{\partial \Theta}{\partial t} + \boldsymbol{u} \cdot \boldsymbol{\nabla}_\| \Theta + \frac{1}{\varepsilon^2} w \frac{\partial \Theta}{\partial z} = \frac{1}{\varepsilon^2} Q_\Theta \,. \tag{2.64d}$$

Note, that the modified length scale corresponds to an adjusted Rossby number $\mathrm{Ro}_{\mathrm{syn}} = O(\varepsilon)$.

Following Päschke et al. (2012), the asymptotic expansion scheme for the variables reads

$$p = p_0(z) + \varepsilon p_1(z) + \varepsilon^2 \left(p^{(2)}(\boldsymbol{x}, z, t) + p_2(z) \right) + o\left(\varepsilon^2\right), \qquad (2.65a)$$

$$\rho = \rho_0(z) + \varepsilon \rho_1(z) + \varepsilon^2 \left(\rho^{(2)}(\boldsymbol{x}, z, t) + \rho_2(z) \right) + o\left(\varepsilon^2\right), \qquad (2.65b)$$

$$\Theta = \Theta_0(z) + \varepsilon \Theta_1(z) + \varepsilon^2 \left(\Theta^{(2)}(\boldsymbol{x}, z, t) + \Theta_2(z) \right) + o\left(\varepsilon^2\right), \qquad (2.65c)$$

$$\boldsymbol{u} = \boldsymbol{u}^{(0)} + \varepsilon \boldsymbol{u}^{(1/2)} + \varepsilon \boldsymbol{u}^{(1)} + o(\varepsilon), \qquad (2.65d)$$

$$w = w^{(0)} + \varepsilon w^{(1)} + \varepsilon^2 w^{(2)} + \varepsilon^3 w^{(3)} + o\left(\varepsilon^3\right). \qquad (2.65e)$$

In the same fashion, we denote horizontally homogeneous static background states by $(p_i, \rho_i, \Theta_i)(z)$ and dynamical modes by $(p^{(i)}, \rho^{(i)}, \Theta^{(i)}, \boldsymbol{u}^{(i)}, w^{(i)})$. Here, we introduced the general assumption that for an atmospheric state the thermodynamic fields are static up to higher order. Furthermore, the potential temperature is constant at leading order ($\Theta_0 = $ const) and vertical variation enter at next-to-leading order ($d\Theta_1/dz \neq 0$) (Klein 2004, 2010).

Inserting the series expansions of eqs. (2.65) into eqs. (2.64) we reproduce the findings of Päschke et al. (2012) that essentially resemble the quasi-geostrophic model equations:

$\bullet$ $O\left(\varepsilon^{i-5}\right)$:

$$\frac{\partial (p^{(i)} + p_i)}{\partial z} = -\rho^{(i)} - \rho_i \quad \text{for } i = 0, \cdots, 5 \qquad (2.66)$$

$\bullet$ $O\left(\varepsilon^{-2}\right)$:

$$\frac{\partial \rho_0 w^{(0)}}{\partial z} = 0 \quad \Rightarrow w^{(0)} = 0 \qquad (2.67)$$

$w^{(0)}$ vanished due to the choice of boundary conditions $w|_{z=0} = 0$.

$\bullet$ $O\left(\varepsilon^{-1}\right)$:

$$\frac{\partial \rho_0 w^{(1)}}{\partial z} + \frac{\partial \rho_1 w^{(0)}}{\partial z} = 0 \quad \Rightarrow w^{(1)} = 0 \qquad (2.68)$$

$$\frac{1}{\rho_0} \boldsymbol{\nabla}_{\parallel} p^{(2)} + f_0 \boldsymbol{k} \times \boldsymbol{u}^{(0)} = 0 \qquad (2.69)$$

$\bullet$ $O\left(\varepsilon^0\right)$:

$$\boldsymbol{\nabla}_{\parallel} \cdot \left(\rho_0 \boldsymbol{u}^{(0)} \right) + \frac{\partial \left(\rho_0 w^{(2)} \right)}{\partial z} = 0 \qquad (2.70)$$

$$\frac{\partial \boldsymbol{u}^{(0)}}{\partial t} + \boldsymbol{u}^{(0)} \cdot \boldsymbol{\nabla}_{\parallel} \boldsymbol{u}^{(0)} + w^{(2)} \frac{\partial \boldsymbol{u}^{(0)}}{\partial z} + \frac{1}{\rho_0} \boldsymbol{\nabla}_{\parallel} p^{(3)} - \frac{\rho_1}{\rho_0^2} \boldsymbol{\nabla}_{\parallel} p^{(2)} +$$

$$+ \beta y \boldsymbol{k} \times \boldsymbol{u}^{(0)} + f_0 \boldsymbol{k} \times \boldsymbol{u}^{(1)} = 0 \qquad (2.71)$$

• $O\left(\varepsilon^1\right)$:

$$\boldsymbol{\nabla}_\parallel \cdot \left(\rho_0 \boldsymbol{u}^{(1)}\right) + \frac{\partial\left(\rho_0 w^{(3)}\right)}{\partial z} = 0 \tag{2.72}$$

$$w^{(2)} \frac{d\Theta^{(1)}}{dz} = Q_\Theta^{(3)} = 0 \quad \Rightarrow w^{(2)} = 0 \tag{2.73}$$

• $O\left(\varepsilon^2\right)$:

$$\frac{\partial\Theta^{(2)}}{\partial t} + \boldsymbol{u}^{(0)} \cdot \boldsymbol{\nabla}_\parallel \Theta^{(2)} + w^{(3)}\frac{d\Theta^{(1)}}{dz} = Q_\Theta^{(4)} = 0 \tag{2.74}$$

We draw conclusions for the expansion modes $w^{(0)}$, $w^{(1)}$, and $w^{(2)}$ from the assumption that corresponding modes of diabatic heating vanish. This is in line with the scaling of section 2.4.3.

These expressions resemble some well-known properties of atmospheric flows in the QG regime: The flow is *hydrostatic*, *i.e.*, vertical pressure gradient is balanced by mass density up to at least $O\left(\varepsilon^5\right)$ (eq. (2.66)). Equation (2.69) directly constitutes the asymptotic formulation of the *geostrophic balance*. We find that the horizontal flow is essentially divergence-free since eq. (2.70) together with eq. (2.73) yields

$$\boldsymbol{\nabla}_\parallel \cdot \boldsymbol{u}^{(0)} = 0 \,. \tag{2.75}$$

Defining $\psi^{(0)} = -\frac{p^{(2)}}{f_0\rho_0}$ and applying the cross product with $\boldsymbol{k}$, we get from eq. (2.69)

$$\boldsymbol{u}^{(0)} = -\boldsymbol{k} \times \boldsymbol{\nabla}_\parallel \psi^{(0)} \,, \tag{2.76}$$

hence, we identify ψ as the *streamfunction*. As a result of eq. (2.72), the flow is anelastic at next-to-leading order.

For reproducing the findings of Päschke et al. (2012) that are essential to the construction of the asymptotic TC model, we introduce the *relative vorticity* $\zeta = \boldsymbol{k} \cdot (\boldsymbol{\nabla}_\parallel \times \boldsymbol{u})$ obtaining the governing equation

$$\frac{\partial(\zeta^{(0)} + \beta y)}{\partial t} + \boldsymbol{u}^{(0)} \cdot \boldsymbol{\nabla}_\parallel (\zeta^{(0)} + \beta y) + f_0\boldsymbol{\nabla}_\parallel \cdot \boldsymbol{u}^{(1)} = 0 \tag{2.77}$$

at leading order from eq. (2.71). *QG Potential vorticity* is defined as

$$q^{(0)} = \zeta^{(0)} + \beta y + \frac{f_0}{\rho_0}\frac{\partial}{\partial z}\left(\frac{\rho_0\Theta^{(2)}}{d\Theta_1/dz}\right) \tag{2.78}$$

which, since diabatic heating couples at higher than fourth order, is constant along horizontal trajectories:

$$\frac{\partial q^{(0)}}{\partial t} + \boldsymbol{u}^{(0)} \cdot \boldsymbol{\nabla}_\parallel q^{(0)} = 0 \,. \tag{2.79}$$

Päschke et al. (2012) continues the derivation with the elliptic equation

$$(\boldsymbol{\nabla}_\parallel^2 + \mathcal{L}_z)\psi^{(0)} = -q_{\mathrm{rel}}^{(0)} := q^{(0)} - \beta y \tag{2.80}$$

for the *relative potential vorticity* q_{rel} introducing the second-order differential operator

$$\mathcal{L}_z(\cdot) = \frac{f_0^2}{\rho_0} \frac{\partial}{\partial z} \left(\frac{\rho_0}{d\Theta_1/dz} \frac{\partial}{\partial z} \cdot \right) \tag{2.81}$$

These expressions are the result of eq. (2.76) and eq. (2.78). Relative potential vorticity is not necessarily regular, *i.e.*, may only be defined by means of distributions. As we outlined in section 2.4.3, the inner core region is resolved by a separate asymptotic regime constituted on a horizontal length scale which is by a factor $\varepsilon^{1-\alpha}$, $\alpha \geq 0$, smaller than the present synoptic scale. Since we require the asymptotic approximation to converge as $\varepsilon \to 0$, the very idea of asymptotic analysis, the scale separation becomes infinite, yet leaving the large-scale behavior of the inner-core solution unchanged, hence core structures shrink to a singularity. For an analytical treatment, it is thus beneficial to split q_{rel} into *singular* (inner core) and *regular* (QG) parts,

$$q_{\text{rel}} = q_s + q_r , \tag{2.82}$$

where the singular part representing the point vortex is expressed by *Dirac delta distribution* focused at the *centerline position* $\boldsymbol{X}(z,t)$:

$$q_s(\boldsymbol{x}, z, t) = \Gamma(t, z)\delta_2(\boldsymbol{x} - \boldsymbol{X}(z,t)) \tag{2.83}$$

with the expansion for the total circulation Γ and the centerline position $\boldsymbol{X}$

$$\Gamma = \Gamma^{(0)} + \varepsilon\Gamma^{(1)} + o(\varepsilon) \tag{2.84a}$$

$$\boldsymbol{X} = \boldsymbol{X}_0(t) + \varepsilon^{1-\alpha}\boldsymbol{X}^{(0)}(z,t) + o\left(\varepsilon^{1-\alpha}\right) . \tag{2.84b}$$

$\boldsymbol{X}$ induces a tilted polar coordinates system (r, θ, z) with

$$r := \|\boldsymbol{x} - \boldsymbol{X}\| \quad \text{and} \quad \tan\theta := \frac{(\boldsymbol{x} - \boldsymbol{X}) \cdot \boldsymbol{j}}{(\boldsymbol{x} - \boldsymbol{X}) \cdot \boldsymbol{i}} . \tag{2.85}$$

As solution to eq. (2.80), Päschke et al. (2012) constructed the following streamfunction which we employ as an ansatz adapted to our scaling:

$$\psi = -\frac{\Gamma(z,t)}{2\pi} \ln r + M_0 r^2(\ln r - 1) + \varepsilon^{1-\alpha}M_1 r \ln r - \varepsilon^{2-2\alpha}M_2 + \psi_2^* \tag{2.86}$$

with the abbreviations

$$M_0 = \frac{1}{8\pi} \frac{f_0^2}{\rho_0} \frac{\partial}{\partial z} \left(\frac{\rho_0}{d\Theta_1/dz} \frac{\partial\Gamma}{\partial z} \right) , \tag{2.87a}$$

$$M_1 = -\frac{f_0^2}{4\pi\rho_0\Gamma} \frac{\partial}{\partial z} \left(\frac{\rho_0\Gamma^2}{d\Theta_1/dz} \frac{\partial\boldsymbol{X}^{(0)}}{\partial z} \right) \cdot \boldsymbol{e}_r = -\boldsymbol{M}_1 \cdot \boldsymbol{e}_r , \tag{2.87b}$$

$$M_2 = \frac{f_0^2\Gamma}{8\pi d\Theta_1/dz} \left(\left(\boldsymbol{e}_\theta \cdot \frac{\partial\boldsymbol{X}^{(0)}}{\partial z} \right)^2 - \left(\boldsymbol{e}_r \cdot \frac{\partial\boldsymbol{X}^{(0)}}{\partial z} \right)^2 \right) . \tag{2.87c}$$

Owing to that, the singular part of ψ has an explicit representation while the regular part ψ_2^* is governed by

$$\left(\nabla_\|^2 + \mathcal{L}_z \right) \psi_2^* = -\mathcal{L}_z\psi_1^{2d} - q_r , \tag{2.88}$$

where

$$\psi_1^{2d} = M_0 r^2(\ln r - 1) + \varepsilon^{1-\alpha}M_1 r \ln r - \varepsilon^{2-2\alpha}M_2 , \tag{2.89}$$

and can be solved by numerical means.

2.4.5. Matching of Inner and Outer Solution

During the derivations of sections 2.4.3 and 2.4.4 we observed that the inner vortex core solution takes the centerline position, its time and vertical derivatives into account, that encodes the large-scale structure of the storm. The outer synoptic-scale solution couples to the inner core flow by the large-r tail of the horizontal velocity. For the sake of clarity, here we use $\hat{r}$ and $\hat{t}$ as coordinates scaled to the inner core flow, whereas we remain with r and t scaled to the QG regime, *i.e.*, $r = \varepsilon^{1-\alpha}\hat{r}$ and $t = \varepsilon^{\delta-\alpha}\hat{t}$.

Without further assumption, following Päschke et al. (2012), we have

$$
\begin{aligned}
\hat{E}^{(1-\alpha)}TE^{(1-\alpha)}\boldsymbol{u} &= \hat{E}^{(1-\alpha)}TE^{(1-\alpha)}\left(-\boldsymbol{k}\times\boldsymbol{\nabla}_{\|}\psi\right) \\
&= \boldsymbol{u}_0^{(0)} + \varepsilon^{1-\alpha}\left(\boldsymbol{u}_0^{(1-\alpha)} + \boldsymbol{X}^{(0)}\cdot\left(\boldsymbol{\nabla}_{\|}\boldsymbol{u}\right)_0^{(0)}\right) + \\
&\quad + \left(\frac{1}{\varepsilon^{1-\alpha}}\frac{\Gamma}{2\pi\hat{r}} - \varepsilon^{1-\alpha}M_0\hat{r}\left(2\ln\hat{r} - 1 + 2\ln\varepsilon^{1-\alpha}\right)\right)\cdot\boldsymbol{e}_\theta + \\
&\quad + \varepsilon^{1-\alpha}\hat{r}\boldsymbol{e}_r\cdot\left(\boldsymbol{\nabla}_{\|}\boldsymbol{u}\right)_0^{(0)} + \\
&\quad + \varepsilon^{1-\alpha}\left(\left(\ln\hat{r} - \ln\frac{1}{\varepsilon^{1-\alpha}}\right)\boldsymbol{k}\times\boldsymbol{M}_1 + (\boldsymbol{M}_1\cdot\boldsymbol{e}_r)\boldsymbol{e}_\theta\right) \qquad (2.90)
\end{aligned}
$$

for the near-field limit of the QG velocity. $\boldsymbol{M}_1$ is defined by eq. (2.87b) and $\boldsymbol{u}_0$ accounts for the regular QG flow $-\boldsymbol{k}\times\boldsymbol{\nabla}_{\|}\psi_2^*$ evaluated at the coordinate center $\boldsymbol{x} = r\boldsymbol{e}_r + \boldsymbol{X} = 0$. Expressions involving $\left(\boldsymbol{\nabla}_{\|}\boldsymbol{u}\right)_0^{(0)}$ resemble the first-order terms of the Taylor approximation.

We now have to find corresponding expressions of the far-field behavior of the inner-core flow at the individual orders. To this end, we generalize Päschke et al.'s (2012) eq. (5.8) to

$$
\hat{E}^{(1-\alpha)}T\boldsymbol{u} = \hat{E}^{(1-\alpha)}\left(\frac{\partial\boldsymbol{X}}{\partial\hat{t}} + u_r\boldsymbol{e}_r + u_\theta\boldsymbol{e}_\theta\right) \tag{2.91a}
$$

$$
\begin{aligned}
&= \varepsilon^{\alpha-\delta}\frac{d\boldsymbol{X}_0}{d\hat{t}} + \varepsilon^{1-\delta}\frac{\partial\boldsymbol{X}^{(0)}}{\partial\hat{t}} + \\
&\quad + \varepsilon^{1-\delta}u_r^{(1)}\boldsymbol{e}_r + \frac{1}{\varepsilon^\delta}\left(u_\theta^{(0)} + \varepsilon u_\theta^{(1)}\right)\boldsymbol{e}_\theta + o\left(\varepsilon^{1-\delta}\right)
\end{aligned} \tag{2.91b}
$$

$$
\begin{aligned}
&= \varepsilon^{\alpha-\delta}\frac{d\boldsymbol{X}_0}{d\hat{t}} + \varepsilon^{1-\delta}\frac{\partial\boldsymbol{X}^{(0)}}{\partial\hat{t}} + \\
&\quad + \frac{1}{\varepsilon^\delta}u_\theta^{(0)}\boldsymbol{e}_\theta + \varepsilon^{1-\delta}\left(\hat{\boldsymbol{\nabla}}\phi^{(1)} - \boldsymbol{k}\times\hat{\boldsymbol{\nabla}}\psi^{(1)}\right) + o\left(\varepsilon^{1-\delta}\right)\,. \tag{2.91c}
\end{aligned}
$$

Same as Päschke et al. (2012), we assume the diabatic heating to be localized such that we can conclude that the velocity potential vanished in the far-field limit:

$$
\lim_{\hat{r}\to\infty}\hat{\boldsymbol{\nabla}}\phi^{(1)} = 0 \tag{2.92}
$$

Further, we examine the asymptotic behavior of the solenoidal contribution $-\boldsymbol{k}\times\hat{\boldsymbol{\nabla}}\psi^{(1)}$. Expressing $\psi^{(1)}$ in terms of its Fourier-modes, we have

$$
-\boldsymbol{k}\times\hat{\boldsymbol{\nabla}}\psi^{(1)} = u_{\theta,0}^{(1)} - \boldsymbol{k}\times\frac{\boldsymbol{\psi}_1^{(1)}}{\hat{r}} - \hat{r}\boldsymbol{e}_\theta\frac{\partial}{\partial\hat{r}}\left(\frac{\boldsymbol{k}\times\boldsymbol{\psi}_1^{(1)}}{\hat{r}}\right)\cdot\boldsymbol{e}_\theta - \boldsymbol{k}\times\hat{\boldsymbol{\nabla}}\psi_2^{(1)}\,. \tag{2.93}
$$

Here, $-\partial_r \psi_0^{(1)} \equiv u_{\theta,0}^{(1)}$. Subscripts to $\psi^{(1)}$ refer to the corresponding Fourier modes. For $\psi_1^{(1)}$, we found the solution by eq. (2.61) for which we now want to derive the far-field limit. To this end, we define the integral operator

$$
L[\mathcal{K}] := \lim_{r \to \infty} \left[\frac{u_\theta^{(0)}}{r} \int_0^r \frac{1}{r' \left(u_\theta^{(0)}\right)^2} \int_0^{r'} \bar{r} \mathcal{K}(\bar{r}) \, d\bar{r} \, dr' \right]
$$

$$
= \frac{\pi}{\Gamma^{(1-\alpha-\delta)}} \int_0^\infty r \mathcal{K}(r) \, dr \, , \tag{2.94}
$$

The latter equality uses L'Hôspital's rule and the fact that $u_\theta^{(0)} \to \Gamma^{(1-\alpha-\delta)}/2\pi\hat{r}$ for $\hat{r} \to \infty$. This is a direct result of matching the inner-core axisymmetric tangential velocity to the point vortex limit of the outer QG solution:

$$
\lim_{\hat{r} \to \infty} u_\theta = \frac{1}{\varepsilon^{1-\alpha}} \frac{\Gamma}{2\pi\hat{r}} \left(1 + o(1)\right)
$$

$$
= \frac{1}{\varepsilon^\delta} \left(u_\theta^{(0)} + \varepsilon u_{\theta,0}^{(1)} + o(\varepsilon) \right) \tag{2.95}
$$

Note, that for scaling of Päschke et al. (2012) with $\alpha = \delta = 1/2$, we reproduce the correspondence of $u_\theta^{(0)}$ and $\Gamma^{(0)}$. For the scaling with $\alpha = 0$ and $\delta = 1/2$, however, the leading-order of the circulation enters at $O(\varepsilon^{1/2})$. In particular, this implies $\Gamma^{(0)} = 0$.

In the original derivations, substantial effort was spent on the limiting behavior of eq. (2.94). Particularly, the term $L[\mathcal{I}]$ (with $\mathcal{I}$ defined through eq. (2.58b)) needed special treatment in that the logarithmic tail was split off:

$$
L[\mathcal{I}] = L[\tilde{\mathcal{I}}] + 2\alpha \ln r \, \boldsymbol{k} \times \boldsymbol{M}_1 \tag{2.96}
$$

The term proportional to $\boldsymbol{M}_1$ is the result of the Coriolis term present in the pressure gradient eq. (2.38) for the gradient-wind regime ($\alpha = \delta = 1/2$). In case of $\alpha = 0$, this term is relegated to higher orders and so is the logarithmic tail. We account for this circumstance by introducing the factor α (in eq. (2.33)) that acts as a switch between the two scaling regimes. Hence, we can elegantly summarize both regimes and end up with

$$
\psi^{(1)} \to r \left(\boldsymbol{\Psi} - 2\alpha \ln r \, \boldsymbol{M}_1 \right) \quad \text{as} \quad r \to \infty. \tag{2.97a}
$$

where

$$
\boldsymbol{\Psi} := \boldsymbol{k} \times L[\mathcal{H} + \tilde{\mathcal{I}} + \mathcal{J} + \mathcal{Q}] \tag{2.97b}
$$

$\boldsymbol{\Psi}$ as the definite integral w.r.t. $\hat{r}$ is independent of it. In summary, for the far-field limit of the inner-core solution we get

$$
\hat{E}^{(1-\alpha)} \boldsymbol{Tu} E^{(1-\alpha)} T^{-1} \hat{E}^{(1-\alpha)} \boldsymbol{Tu} = \frac{d\boldsymbol{X}_0}{d\hat{t}} + \varepsilon^{1-\delta} \frac{\partial \boldsymbol{X}^{(0)}}{\partial \hat{t}} + \varepsilon^{-\delta} \left(u_\theta^{(0)} + \varepsilon u_{\theta,0}^{(1)} \right) \boldsymbol{e}_\theta -
$$

$$
- \varepsilon^{1-\delta} \boldsymbol{k} \times \boldsymbol{\Psi} - \varepsilon^{1-\delta} \boldsymbol{k} \times \hat{\boldsymbol{\nabla}} \psi_2^{(1)} +
$$

$$
+ 2\alpha \varepsilon^{1-\delta} \left(\ln \hat{r} \, \boldsymbol{k} \times \boldsymbol{M}_1 + (\boldsymbol{M}_1 \cdot \boldsymbol{e}_r) \boldsymbol{e}_\theta \right) \, . \tag{2.98}
$$

For the final matching, we again recognize that $\boldsymbol{M}_1$ effectively vanishes in case of $\alpha = 0$ (by being of $O(\varepsilon^{1/2})$ due to $u_\theta^{(0)} \to \Gamma^{(1/2)}/2\pi\hat{r}$). This allows us to cancel the last line of eq. (2.90). That, together with the original derivation of Päschke et al. (2012) for $\alpha = 1/2$, we end up with the generalized *centerline equation* of motion

$$\frac{\partial \boldsymbol{X}^{(0)}}{\partial t} = \boldsymbol{u}_0^{(1-\alpha)} + \boldsymbol{X}^{(0)} \cdot (\boldsymbol{\nabla}_\| \boldsymbol{u})_0^{(0)} + \alpha \ln(\varepsilon)(\boldsymbol{k} \times \boldsymbol{M}_1) + \boldsymbol{k} \times \boldsymbol{\Psi} \,. \qquad (2.99)$$

Remark. In fact, the above reasoning for matching the circulation allows for another conclusion: If we consider the inner-core regime with $\alpha = 0$ and $\delta = 1$, the inner-core leading-order tangential velocity u_θ becomes $O(\varepsilon^{-1})$ that again leads to the far-field limit $u_\theta \to \Gamma/2\pi\hat{r}$. We find that at an intermediate scale of $\varepsilon^{-1/2}L_{\text{meso}} = O(300\,\text{km})$, *i.e.*, the inner-core scale of Päschke et al. (2012), $u_\theta = O(\varepsilon^{-1/2})$, that is already accounted for by the original theory, only that the higher core velocities need to be matched by larger centerline velocities, which is covered by the rescaled inner-core timescale (cf. eq. (2.34)). Hence, there is a trivial extension to even stronger storms, the details of which we leave to future work.

2.5. Circulation-Free Meso-Vortices Embedded in QG Far-Field

The matched asymptotic analysis of section 2.4 revealed that the inner core solution couples to the large-scale flow via the streamfunction that is induced by the inner core's *circulation*. We found the limiting expression for the integral operator L in eq. (2.94) that enters the definition of $\boldsymbol{\Psi}$ in eq. (2.97b) provided the circulation Γ is finite. Not only for the sake of the physical relevance of the scenario, we now want to deal with the situation of vanishing circulation. In general, diabatic heating can lead, at least locally, to such a solution, and we need a special treatment in this limit to maintain stability of the numerical integration scheme presented in chapter 4.

It is trivial to show that the terms M_0, M_1, and M_2 vanish with $\Gamma \to 0$ (cf. eqs. (2.87) and use L'Hôspital's rule). The remaining term of the streamfunction is

$$\psi = \psi_2^* \,. \qquad (2.100)$$

Together with eq. (2.88), we find that with vanishing circulation Γ the streamfunction solely depends on the *regular* distribution of large-scale potential vorticity q_r (ψ_1^* vanishes with M_0, M_1, and M_2). When matching the outer solution of $\psi = \psi_2^*$ to the inner core solution we find no corresponding term since in the limit $r \to \infty$ the circulation and with that the streamfunction vanishes.

We conclude that in the limit of a circulation-free meso-vortex embedded into a large-scale QG flow the terms in eq. (2.99) proportional to $\boldsymbol{M}_1$ and $\boldsymbol{\Psi}$ vanish. The centerline equation becomes

$$\frac{\partial \boldsymbol{X}^{(0)}}{\partial t} = \boldsymbol{u}_0^{(0)} + \boldsymbol{X}^{(0)} \cdot (\boldsymbol{\nabla}_\| \boldsymbol{u})_0^{(0)} \,. \qquad (2.101)$$

The vortex is completely driven by external forcing and does not feed back to the QG flow! With Γ being a function of z and t, however, this statement is valid only locally. For the numerical treatment in chapter 4, the implementation of eq. (2.99) is adapted to use eq. (2.101) wherever Γ becomes small.

3. Analysis of Leading-Order Equations

In chapter 2 we revisited the derivation of the asymptotic model equations for a tilted TC under the influence of diabatic heating and vertical wind shear. So far, the insights gained by the two-scale matched asymptotic analysis was on a purely mathematical level. Next to further analytical understanding, we now want to focus on the physical interpretation of the revealed mechanisms and provide some qualitative explanations of the dynamics of vortex structure and intensity. These examinations serve as a basis for the subsequent construction of numerical solution strategies (chapter 4) as well as for the design of the experiments presented in chapters 5 and 6.

3.1. Principles of TC Intensification by Diabatic Heat Release

The foremost goal of our investigation on the asymptotic theory on tilted TCs is to understand how diabatic heating, as a model for the actual physical processes related to heat exchange, is driving the dynamics of the structure and the intensity of a TC. To this end, we will analyze how both, the centerline equation (2.99) and the tangential wind equation (2.47) behave under the influence of diabatic heat release. In the following subsections we will focus on the model's prediction in terms of linear and angular momentum as well as kinetic energy balances and establish relations to existing theories.

3.1.1. Linear Momentum Balance

The possibly most valuable predictive feature of the present theory is given in the form of the tangential wind equation (2.47). Converted back to an equation with physical dimensions we have the leading-order equation

$$\frac{\partial u_\theta}{\partial t} + u_{r,00}\frac{\partial u_\theta}{\partial r} + w_0\frac{\partial u_\theta}{\partial z} = -(u_{r,00} + u_{r,*})\left(\frac{u_\theta}{r} + f\right) . \tag{3.1}$$

$u_{r,00}, u_{r,*}$, and w_0 follow the definition of their non-dimensional asymptotic counterparts (cf. eqs. (2.49) and (2.51a)).

First, we focus on the symmetric contributions of diabatic heating to the secondary circulation which are encoded in $u_{r,00}$ and w_0. The latter is the — in the tilted polar coordinate system — azimuthally averaged vertical velocity, *i.e.*, the azimuthal Fourier-0 mode of the vertical velocity field w, and result of $Q_{\Theta,0}$, the Fourier-0 mode of diabatic heating. As exemplified in fig. 3.1, due to mass conservation (2.43), $u_{r,00}$ is tied to w_0: The mass displacement by upward moving air parcels is compensated by radial motions. While w_0 and $u_{r,00}$ on the left-hand side of eq. (3.1) resemble the axisymmetric advective motion of air parcels in the r-z-plane, the source term proportional to $u_{r,00}$ on the right-hand side is responsible for acceleration and accounts for conservation of angular
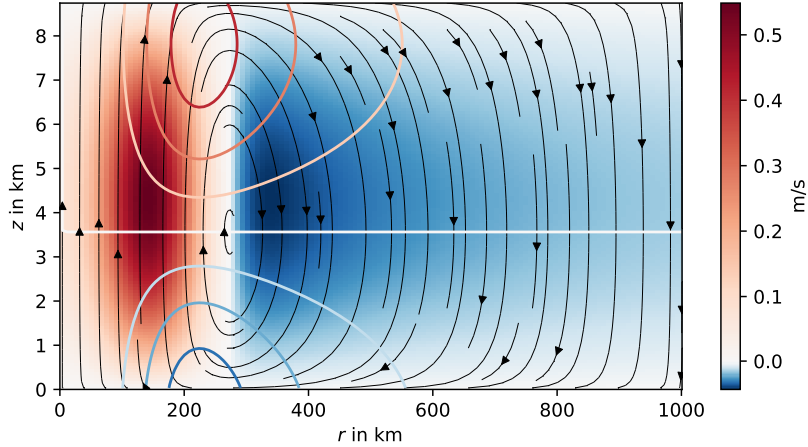
Figure 3.1.: Schematic secondary circulation induced by symmetric vertical velocity. Streamlines of the resulting flow in the r-z-plane are displayed in black whereas vertical and radial components of the flow are shown in color shades and contour lines. Negative and positive contributions are shown in blue and red, respectively. Quantities are shown in arbitrary units. Note, however, the strong exaggeration of the negative part of vertical velocity.

momentum (cf. section 3.1.2). This coupling of diabatic heating to the dynamics of an atmospheric vortex essentially resembles the secondary circulation accounted for the TC intensification throughout the literature (for a summary of the recent understanding, consult Montgomery and Smith 2017b, and references therein). Since the vertical velocity is the result of an externally imposed diabatic heating, however, and no explicit closure is provided on how the vertical velocity depends on the solution $(\boldsymbol{X}, u_\theta)$, there is no further connection to the notions of CISK (Charney and Eliassen 1964) or WISHE (Emanuel 1991), that hypothesize on the causality between radial surface inflows and vertical updrafts.

$u_{r,*}$ on the other hand is the result of the projection of the vertical velocity Fourier-1 mode $\boldsymbol{w}_1$ onto the tilt vector $\partial_z \boldsymbol{X}$ (cf. eq. (2.49a)). Figure 3.2 demonstrates the origin of this radial velocity component: Due to the tilt of the vortex, a vertical velocity dipole may cause a net outflow (inflow) of mass through the boundaries of the tilted control volume given by a radius r and infinitesimal height Δz. Leading-order mass conservation (2.43) ensures that an equally sized radial mass influx (outflux) must compensate it. Radial mass flux, however, means tangential acceleration (deceleration) of air parcels along their trajectory due to angular momentum conservation. It is thus the orientation of the vertical velocity Fourier-1 mode relative to the tilt vector that determines whether the storm (locally) intensifies or attenuates.

We now focus on the effect of diabatic heating on the centerline motion. In section 2.4.3, we found that for a tilted vortex the vertical velocity possesses an adiabatic contribution in the form of a dipolar field that is perpendicular to the tilt vector, hence it does not contribute to intensity changes. It is, however, the full vertical velocity dipole, *i.e.*, the sum of diabatic and adiabatic contributions, that induces Fourier-1 modes of radial and tangential velocity. In the far-field limit these velocity components
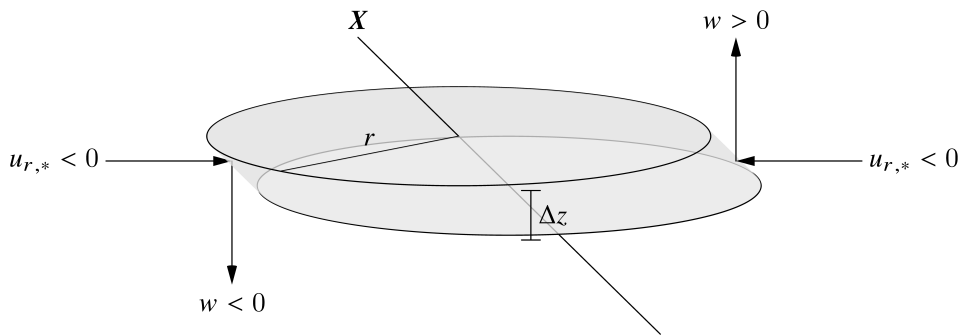
Figure 3.2.: Mass flux through boundary of control volume. In the present example, the antiparallel orientation of vertical velocity dipole and tilt vector causes mass to leave the control volume. Radial influx ($u_{r,*} < 0$) compensates for the mass deficit while transporting angular momentum to smaller radii which leads to acceleration.
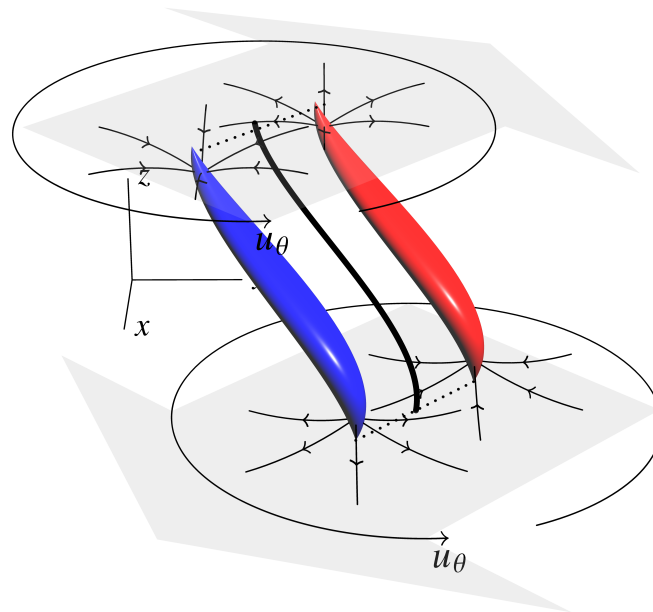
Figure 3.3.: Horizontal motions induced by dipolar vertical velocity. Next to the centerline (thick black line in the center), red and blue structures depict regions of up- and downdrafts, here in the configuration of an adiabatic, tilted vortex, that draw in air either on the bottom (updraft) or the top (downdraft) and eject it on the top or bottom, respectively (streamlines indicated by black arrows). The resulting net flow on top and bottom is depicted by the large gray arrows.

accumulate to

$$\boldsymbol{u}_{\text{ff}} = -\boldsymbol{k} \times \boldsymbol{\Psi} + 2\alpha \ln r \boldsymbol{k} \times \boldsymbol{M}_1 + 2\alpha \left((\boldsymbol{k} \times \boldsymbol{M}_1) \cdot \boldsymbol{e}_\theta\right) \boldsymbol{e}_\theta \,, \qquad (3.2)$$

which are given in the coordinate system attached to the centerline position. As discussed during the matching procedure (cf. section 2.4.5), this velocity field has to be matched to the outer QG solution given in earth-relative coordinates. In the matching procedure of section 2.4.5, we concluded that the last terms of eq. (3.2) finds a counterpart in the (earth-relative) near-field limit of the QG solution; similarly the second term has a counterpart in the QG solution and, due to the coordinate rescaling, degenerates to the logarithmic term in the centerline equation (2.99). Hence, eq. (3.2), posing the flow relative to the centerline, is reinterpreted in earth-relative coordinates to the centerline motion plus the near-field limit of the QG flow. As we will see in section 3.2, $\boldsymbol{\Psi}$ essentially depends on contributions of symmetric and asymmetric diabatic heat release. Concentrating on the latter one and discarding symmetric heating for the moment, we can conclude that it is the vertical velocity dipole that induces centerline-relative motions encoded in the far-field limit of the streamfunction $\psi^{(1)}$ in the centerline coordinate system. In earth-relative coordinates, these relative motions translate into the centerline motion in terms of precession, tilting/aligning or a linear superposition of that.

A bit more intuitive explanation of eq. (3.2) is given with fig. 3.3. Each (positive and negative) column of vertical velocity along the centerline causes inflow into the column where the vertical gradient of w is positive and outflow in the negative gradient case. Figure 3.3 demonstrates a simplified setting where tilt direction is constant and tilt amplitude maximal in the middle layers. Near the bottom the "positive" (red) column draws air in while the "negative column" (blue) pushes air out. Both effects partially compensate each other in the inner region between the two columns by forming a closed circuit, *i.e.*, mass outflux from the negative column equals the mass influx into the positive column. There is, however, a net effect due to the inflow from larger radii into the positive column and outflow from the negative column towards larger radii that have the same direction. This effect causes air to enter the vortex on one side and exit on the opposite side. In total, as this description was conducted from the viewpoint relative to the centerline coordinates, the net motion of air in the co-moving frame must be compatible with a motion in an earth-relative coordinate description. If we assume the vortex to be embedded into an environment at rest[1], this can only mean that the vortex *itself* is moving with a velocity of same magnitude and opposite sign. Combining these considerations with the analogous finding for the top region where the net motions have opposite sign (due to the inverse sign of the vertical gradients of w) the motion of the three-dimensional structure resembles — for the adiabatic case where $\boldsymbol{w}_1$ is rotated $-90°$ relative to the tilt vector — the precession of the centerline.

Diabatic heating alters this picture in that it may add a component to the vertical velocity that projects onto the Fourier-1 mode. In comparison to the adiabatic motion, the net effect may be a rotation (and change in amplitude) of the resulting vertical velocity dipole which — analogous to the discussion above — leads to a net horizontal velocity at top and bottom of the vortex, cf. fig. 3.4. Since in this setting the vertical velocity dipole does not necessarily have to be orthogonal to the tilt vector, diabatic
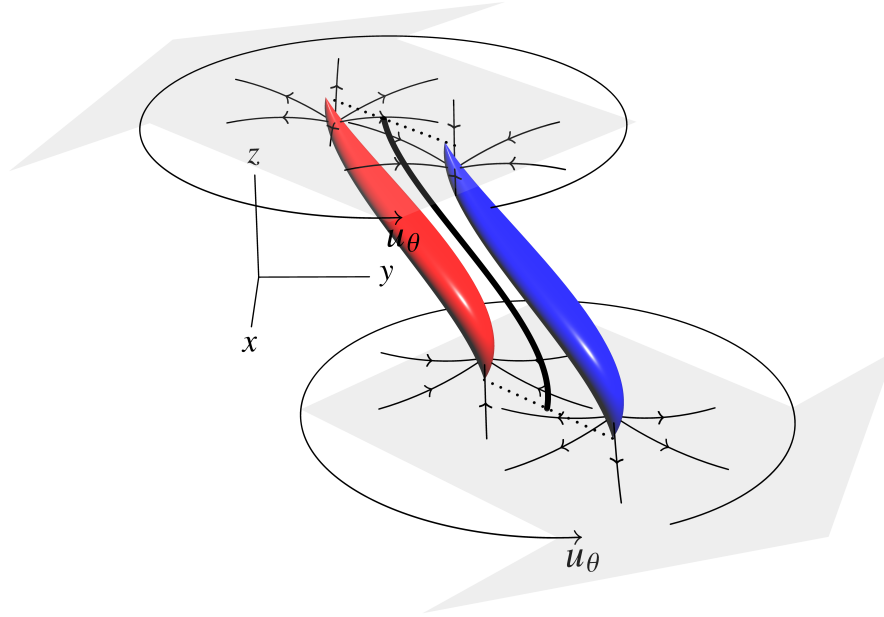
---

[1]Which is true for $\alpha = 0$

Figure 3.4.: Same as fig. 3.3 but vertical velocity dipole is rotated due to contribution from diabatic heating.

heating can induce far-field motions that are parallel/antiparallel to the tilt vector leading to further tilting or vertical alignment of the centerline.

We conclude that heating *downtilt*, *i.e.*, a configuration where the tilt and diabatic heating dipole vectors are parallel to each other leads to a superposition of precession and vertical alignment while the opposite orientation (*uptilt* heating) causes a further tilting of the centerline in conjunction with precession. (In both situations, precession is the result of the adiabatic vertical velocity dipole.) Together with the conclusion drawn from eq. (3.1) we can associate vertical alignment with decreasing intensity. Asymmetric diabatic heating that leads to intensification, however, goes along with the stretching (misalignment) of the centerline.

3.1.2. Angular Momentum Balance

With the definition of specific angular momentum (Schubert and Hack 1983),

$$M := ru_\theta + \frac{1}{2}fr^2 \tag{3.3}$$

we find from eq. (3.1) the specific *angular momentum balance*

$$\frac{\partial M}{\partial t} + u_{r,00}\frac{\partial M}{\partial r} + w_0\frac{\partial M}{\partial z} = -u_{r,*}(u_\theta + fr)\,. \tag{3.4}$$

It reveals that in the tilted polar coordinate system, purely symmetric diabatic heating (*i.e.* $u_{r,*} \equiv 0$) causes redistribution of angular momentum, only. Local intensification of tangential wind speed is thus due to the replacement of fluid parcels of lower angular momentum by such of higher angular momentum. Whether the vortex gets accelerated
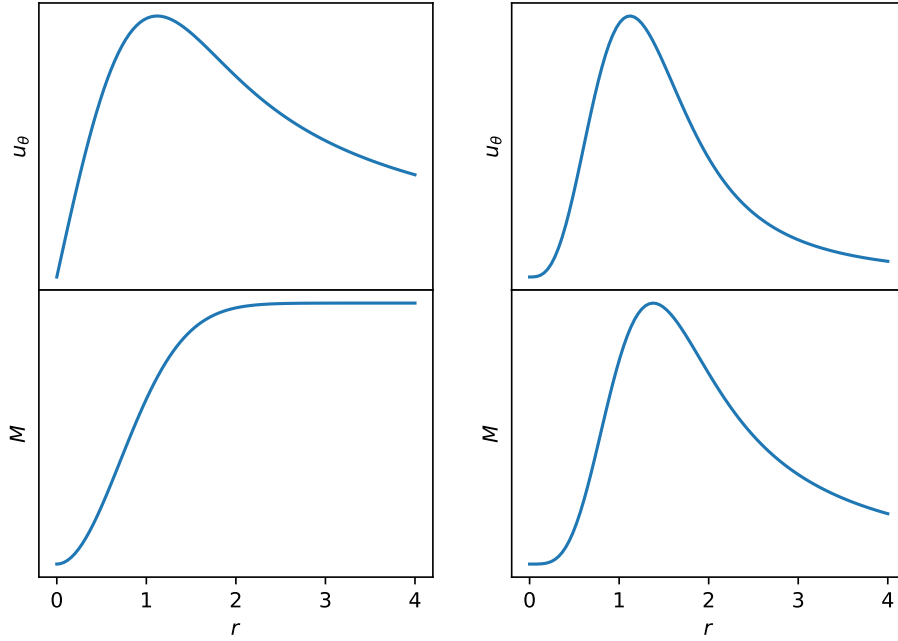
Figure 3.5.: Two different radial profiles of tangential velocity and resulting angular momentum. Top left panel shows $u_\theta \sim 1/r$ as $r \to \infty$ and bottom left panel the corresponding angular momentum in the cyclostrophic regime ($f \equiv 0$). Top and bottom right panels show tangential velocity with $u_\theta \sim 1/r^3$ as $r \to \infty$ and corresponding angular momentum. All quantities are in arbitrary units.

by symmetric diabatic heating depends on the radial profile of tangential velocity. The left panels of Figure 3.5 demonstrate that for typical radial velocity profiles with long-range tail $\sim 1/r$, the resulting angular momentum is a monotonously increasing function of r and inward moving air parcels near the bottom transport high angular momentum inwards and with that accelerate in tangential wind speed. If the tangential velocity profile differs (see right panels of fig. 3.5), it is possible that the angular momentum is not monotonous anymore, at least in the cyclostrophic limit (where f is vanishing). In that case, it depends on the positioning of the heating whether inward motions higher or lower the local value of angular momentum.

The asymmetric component of diabatic heating, encoded by $u_{r,*}$, however, introduces a source term on the right-hand side of eq. (3.4), *i.e.*, along the trajectories of the secondary circulation, that is proportional to the scalar product of w_1 and $\partial_z X$. With the negative sign on the right-hand side of eq. (3.4) and $u_\theta + fr$ being positive for cyclonic motions on the Northern Hemisphere[2], intensification corresponds to a negative sign of $u_{r,*}$.

At first glance, it appears to be unphysical that angular momentum can be created. The explanation can be found in the geometry of the fluid structure and the choice of centerline-adapted coordinates: Following Noether's (1918) theorem, every conserved

---

[2]The theory is of course also valid on the Southern Hemisphere. In this case, both, u_θ and M are negative and intensification is associated to a positive sign of $u_{r,*}$.
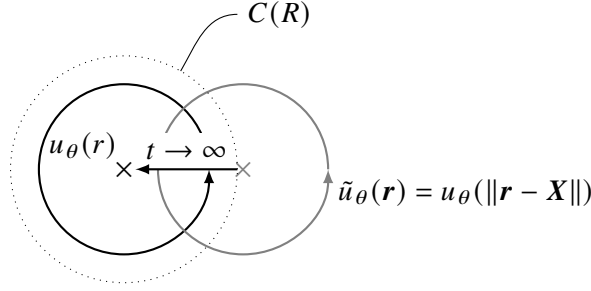
Figure 3.6.: Misalignment of an axisymmetric vortex (Two-dimensional projection). Shown are two example streamlines (solid) of a centered (black) and an off-centered (gray) flow field of circular structure. The angular momentum is computed as the integral of fluid elements contained within the cylinder $C(r)$ (dotted).

quantity is associated to a symmetry of the system. In case of angular momentum the corresponding symmetry would be with respect to rotations about the center of the coordinate system. As long as the vortex is upright, *i.e.*, $\partial_z X \equiv 0$, the centerline prescribes a cylindrical coordinate system and the rotation symmetry is maintained. In fact, in this situation $u_{r,*} \equiv 0$ independently of the orientation of w_1. (Hence, there exists no orientation of w_1 for which the vortex changes its intensity!)

A tilted vortex, however, breaks this very symmetry and thus angular momentum is not a conserved quantity in the tilted coordinate system, anymore. Angular momentum can be extracted from or injected to the system by a suitable alignment of w_1 relative to the tilt vector. The picture becomes more comprehensive when considering the vortex to be embedded into a larger system in which angular momentum is a conserved quantity.[3] Total angular momentum then consists of the vortex' contribution (in centerline coordinates) and another one that accounts for the embedding of the whole vortex into environment, *i.e.*, the precession of the centerline (and earth's rotation). In that context vortex intensification means decreasing the angular momentum of the embedding and increasing it for the vortex. In fact, intensification of u_θ goes along with increasing the centerline tilt.

A slightly less abstract but equivalent explanation is found in considering an axisymmetrically circulating flow field: In a cylindrical coordinate system the vertical component of (relative) angular momentum of the fluid bulk is given by the radius-weighted volume integration of azimuthal momentum over a cylinder with radius R and height Z:

$$L = \boldsymbol{k} \cdot \int\limits_{C(R,Z)} \rho(\boldsymbol{r})\boldsymbol{r} \times \boldsymbol{u}(\boldsymbol{r})\, d^3r = \int\limits_0^R \int\limits_0^{2\pi} \int\limits_0^Z \rho(\boldsymbol{r}) r^2 u_\theta\, dr\, d\theta\, dz \tag{3.5}$$

This situation is illustrated in fig. 3.6. If an axisymmetric flow field is centered in the coordinate origin the velocity completely projects onto the azimuthal component (in

---

[3]To a higher degree the whole earth in a coordinate frame relative to the fixed stars is such a system. Considering the cyclostrophic regime, the background in the Coriolis-free limit is approximately rotationally invariant.

that coordinate system). An off-centered flow field, however, partially projects onto the azimuthal and the radial components with mixed sign, ultimately diminishing the integral measure compared to the centered flow field. If the off-centered flow field were to be shifted towards the center of the cylindrical coordinate system without changing its structure this would mean an increase in angular momentum. Conservation of angular momentum (without applying external torque) requires the increase of angular momentum, caused by the shift of the circulation center, to be compensated by decreasing velocity of the flow field that projects onto the azimuthal coordinate direction. Hence, neglecting the effects of symmetric diabatic heating and the resulting global transport of angular momentum by the secondary circulation, vertical alignment of a tilted vortex by purely asymmetric heating must coincide with the reduction of intensity and vice versa.

Schecter, Montgomery, and Reasor (2002) reason similarly, yet in a different flavor, in that they state that "any increase in the (PV weighted) mean square radius[4] of the skirt requires a decrease in the mean square radius of the core", which means that the core angular momentum increases at the cost of the skirt's angular momentum.

The break in symmetry of the fluid flow allows for the extraction of energy from the asymmetric component of vertical velocity that is in general associated to unorganized convection and store it into kinetic energy of the symmetric component of the primary circulation (see also the next section), and therefore in its angular momentum, by favorable alignment of the vortex asymmetric structure, *i.e.*, the tilt, and the asymmetric heating. This is a remarkable example of the ability of atmospheric flows to self-organize by channeling energy released in asymmetric patters into symmetric flow structures!

3.1.3. Energetic Balance

Now, we make use of the analytical findings of the asymptotic theory presented in chapter 2. As we will see there is a strong connection to Lorenz's (1955) theory on available potential energy (APE) that will help us to understand intensity changes due to diabatic heating on a deeper level. To this end we will derive a leading-order energy balance equation from the tangential momentum equation (3.1) and further set it into relation to the expression given by Lorenz (1955).

In Lorenz's (1955) seminal work on the energetics of (global) atmospheric motions, he claimed that kinetic energy is the result of imbalanced atmospheric states which lead to redistribution of air masses, hence to their acceleration. What he coined total potential energy (TPE) is the sum of the system's potential energy (within the gravitational field of the earth) and thermal energy. Due to hydrostatic balance, which is satisfied to very high order in a regular atmosphere, these two energy forms are maintained in constant ratio to each other and can be combined.

For every given atmospheric state at rest, there exists a state of minimal TPE that can be attained by redistributing air parcels adiabatically. Hence, there is no atmospheric state possible with lower TPE (when maintaining total mass and chemical composition). That is the atmospheric state achieved after friction diminished all motions. The difference between the system's actual TPE and the minimal one is called APE and

---

[4]The term *PV weighted mean square radius* is used synonymously with canonical angular momentum, *i.e.*, with eq. (3.5).

accounts for the energy available for conversion into kinetic energy. Lorenz (1955) derived the balance relations

$$\frac{d\bar{A}}{dt} = G - C \tag{3.6a}$$

$$\frac{d\bar{K}}{dt} = C - D \tag{3.6b}$$

accounting for the rate of change of APE, denoted by A, and the kinetic energy K. For the generation of APE, G, and the conversion rate to kinetic energy, C, he provided the integral expressions

$$G = \frac{1}{g} \int_0^{p_s} \frac{\Gamma_d}{\Gamma_d - \bar{\Gamma}} \frac{\overline{T'Q'}}{\bar{T}} \, dp \tag{3.7a}$$

$$C = -\frac{R}{g} \int_0^{p_s} \frac{1}{p} \overline{T\omega} \, dp \, . \tag{3.7b}$$

$\bar{(\cdot)}$ indicates the average of a quantity over a constant-pressure surface, and $(\cdot)'$ refers to its deviation from that average. R and g are the dry air gas constant and gravitational acceleration as given in table 2.1, $\Gamma = \partial_z \bar{T}$ is the lapse rate of mean temperature and $\Gamma_d = g/c_p$ the dry-adiabatic lapse rate. The specific heat is given by $Q = c_p \pi Q_\Theta$ with the Exner pressure $\pi = T/\Theta$. $\omega = dp/dt$ is the vertical velocity in pressure coordinates (*i.e.*, the pressure change along flow trajectories). Although essential for global-scale flows on climatological time scales, friction is neglected in our case, and so we set the term D in eqs. (3.6) to zero.

Let us continue our discussion by presenting the leading-order kinetic energy equation resulting from eq. (3.1) and the anelastic constraint (2.43):

$$\frac{\partial e_{\mathrm{kin}}}{\partial t} + \frac{1}{r} \frac{\partial}{\partial r} \left(r u_{r,00} h_{\mathrm{kin}} \right) + \frac{\partial}{\partial z} \left(w_0 h_{\mathrm{kin}} \right) = \frac{\rho}{\Theta \partial_z \Theta} \left(\Theta_0' Q_{\Theta,0} + \frac{1}{2} \boldsymbol{\Theta}_1' \cdot \boldsymbol{Q}_{\Theta,1} \right) . \tag{3.8}$$

We introduced $e_{\mathrm{kin}} = \frac{1}{2} \rho_0 u_\theta^2$, $h_{\mathrm{kin}} = e_{\mathrm{kin}} + p'$, and by neglecting higher-order Fourier modes, we arrive at the conclusion that the right-hand side term in parentheses is the azimuthal mean of $\Theta' Q_\Theta$. Therefore, with the volume integral $K = \int_V e_{\mathrm{kin}} \, dV$, we get

$$\frac{dK}{dt} = C = \int_V \frac{g\rho}{\Theta \partial_z \Theta} \Theta' Q_\Theta \, dV + \mathrm{h.o.t.} \tag{3.9a}$$

$$= \int_V g\rho w \frac{\Theta'}{\Theta} \, dV + \mathrm{h.o.t.} \tag{3.9b}$$

Taking eqs. (2.51) into account, we can replace the term $Q_\Theta/(\partial_z \Theta)$ with w since the adiabatic component of w is 90° rotated relative to the dipole of the potential temperature perturbation, and thus the product vanishes under the integral rendering only the diabatic contribution $w_{\mathrm{dia}} = Q_\Theta/(\partial_z \Theta)$ important for the generation of kinetic energy.

We seek to compare the above expression of kinetic energy conversion with both, G and C, as defined in eqs. (3.7). Lorenz's (1955) formulation takes averages and

perturbations on constant-pressure surfaces into account while eq. (3.9) is expressed in regular Cartesian coordinates. To meet at common ground and to have a reference for analyzing the simulation results of chapter 6 we reformulate eqs. (3.7) in terms of Cartesian coordinates.

First, addressing to Lorenz's (1955) notation where

$$q(x, y, p, t) = \bar{q}(p, t) + q'(x, y, p, t),\tag{3.10}$$

i.e., a three-dimensional variable q, given in pressure coordinates, is expressed by an average $\bar{q}$ on a surface of constant pressure, and the perturbation q'. Consequently, we have

$$Q = \bar{Q} + Q' = c_p \pi (\bar{Q}_\Theta + Q'_\Theta),\tag{3.11}$$

and with $T'/\bar{T} = \Theta'/\bar{\Theta}$ and assuming hydrostatic balance we obtain

$$\bar{\Gamma} = -\pi \overline{\frac{\partial \Theta}{\partial z}} + \Gamma_d.\tag{3.12}$$

Finally, G transforms to

$$G = \int\limits_0^{p_s} \frac{1}{\overline{\partial_z \Theta}} \frac{\overline{\Theta' Q'_\Theta}}{\bar{\Theta}} \, dp.\tag{3.13}$$

The above expression is to be understood as the integration of constant-p averages. Except for a constant factor accounting for the surface, it resembles a volume integral expressed in the pressure-coordinate system. To compare it, however, with the Cartesian integral of eq. (3.9), it is necessary to convert the average expression on pressure surfaces into Cartesian coordinates. To this end, we introduce the following notation: Let a quantity q be expressed by $q_z(x, y, z, t)$ in Cartesian and by $q_p(x, y, p, t)$ in pressure coordinates. In particular, the height z is a function $z_p(x, y, p, t)$ of pressure. Similarly, pressure is a function $p_z(x, y, z, t)$ of height. As a consequence, for fixed (x, y, t), p_z and z_p are inverse functions:

$$p_z(x, y, z, t) = z_p^{-1}(x, y, z, t)\tag{3.14a}$$

$$z_p(x, y, p, t) = p_z^{-1}(x, y, p, t)\tag{3.14b}$$

Hence, for a quantity given in pressure coordinates we derive the following relation[5]

$$
\begin{aligned}
q = q_p(p) &= q_z(z_p(p)) \\
&= q_z(\bar{z}_p(p) + z'_p(p)) \\
&= q_z(\bar{z}_p(p)) + \left.\frac{\partial q_z}{\partial z}\right|_{z=\bar{z}_p(p)} (z_p(p) - \bar{z}_p(p)) + O\left(z'_p(p)^2\right) \\
&= q_z(\bar{z}_p(p)) + \left.\frac{\partial q_z}{\partial z}\right|_{z=\bar{z}_p(p)} \frac{p - p_z(\bar{z}(p))}{\partial_z p_z|_{z=\bar{z}_p(p)}} + O\left(p'_z(z)^2\right) \\
&= q_z(\bar{z}_p(p)) - \left.\left(\frac{p'}{g\rho}\frac{\partial q_z}{\partial z}\right)\right|_{z=\bar{z}_p(p)} + O\left(p'_z(z)^2\right)
\end{aligned}\tag{3.15}
$$

---

[5]For the sake of clarity we drop the explicit coordinate dependency on (x, y, t).

Thus, we are able to approximate the average over a pressure surface by an average over a surface of constant height:

$$\overline{q_P(x,y,p,t)} \approx \frac{1}{|A|} \int_A q_z(x,y,\overline{z_P(x,y,p,t)},t)\,dx\,dy\,, \tag{3.16}$$

where $A \subset \mathbb{R}^2$ is the two-dimensional surface area of the integration domain. By doing so, we introduce an error of $O(q\varepsilon^2)$ that is about 1% of the magnitude of q. Substituting the differential by using the hydrostatic balance, $dp = -g\rho\,dz$, G can now be expressed in terms of Cartesian coordinates:

$$G = \int_V \frac{g\rho}{\partial_z\Theta}\frac{\Theta' Q'_\Theta}{\Theta}\,dV + O(\varepsilon^2)\,. \tag{3.17}$$

Note that Θ' and Q'_Θ are still to be understood as perturbations with respect to averages on pressure surfaces.

For the transformation of C (cf. eq. (3.7b)) we first need to deal with the vertical velocity in pressure coordinates, $\omega := dp/dt$, *i.e.*, the pressure change along fluid trajectories. From a numerical point of view (given data on a Cartesian grid with limited temporal resolution), this expression is rather hard to handle, and so we seek for a replacement better suited to achieve sufficient accuracy:

$$C = -\frac{1}{|A|} \int_A \int_0^{p_s} \frac{dp}{dt}\frac{dp}{g\rho}\,dx\,dy \tag{3.18a}$$

$$= -\frac{1}{|A|} \int_A \int_0^{\infty} \left(\frac{\partial p}{\partial t} + \boldsymbol{u}\cdot\boldsymbol{\nabla}_\parallel p + w\frac{\partial p}{\partial z}\right)dz\,dx\,dy \tag{3.18b}$$

$$= -\frac{1}{|A|} \int_V \left(\frac{\partial}{\partial t}\int_z^{\infty} g\rho\,dz' + \boldsymbol{u}\cdot\boldsymbol{\nabla}_\parallel p - wg\rho\right)dV \tag{3.18c}$$

$$= -\frac{1}{|A|} \int_V \left(-g\int_z^{\infty}\left(\boldsymbol{\nabla}_\parallel\cdot(\rho\boldsymbol{u}) + \frac{\partial\rho w}{\partial z'}\right)dz' + \boldsymbol{u}\cdot\boldsymbol{\nabla}_\parallel p - wg\rho\right)dV \tag{3.18d}$$

$$= -\frac{1}{|A|} \int_V \boldsymbol{u}\cdot\boldsymbol{\nabla}_\parallel p\,dV \tag{3.18e}$$

We used the definition of ω, the convective derivate $\frac{d}{dt} = \partial_t + \boldsymbol{u}\cdot\boldsymbol{\nabla}_\parallel + w\partial_z$, the integral form of the hydrostatic balance and the continuity equation (in that order from (a) to (d)). The last step is justified by canceling the second and fourth term in (d) and Gauß' theorem assuming that the mass flux $\rho\boldsymbol{u}$ can be neglected through the lateral boundaries.[6] The integrand of eq. (3.18) now is local in time and involves only the horizontal gradient of pressure.

We want to close this section by drawing some intermediate conclusions:

---

[6]That is a rather strong assumption. With global mass conservation, however, there must be a domain large enough to ensure this property to be satisfied. We can therefore fulfill this requirement by enlarging the domain size.

(i) The asymptotic theory yields the energy budget (*i.e.*, the kinetic energy conversion rate C) derived in eq. (3.9), that follows the same analytic expression as the *APE generation* term G in Cartesian coordinates, given in eq. (3.17), provided the horizontal mean diabatic heating vanishes.

(ii) Although we considered diabatic heating as the driving force for vertical motions, it is the configuration of symmetric and asymmetric vertical motions relative to the storm's centerline (and tilt), that is important for the intensity and structural changes. By the leading-order WTG approximation valid for the flow regime of a TC, diabatic heating and vertical velocity have a direct correspondence, however.

(iii) Up to leading order, APE, generated by the energy input of diabatic heating, is directly converted to kinetic energy (for mean-zero heating). Hence, APE is accumulated only at higher-than-leading orders.

In chapter 6 we will continue this discussion by analyzing the energy transition rates of three-dimensional simulation data and draw further conclusions from that.

3.2. Substructure of the Centerline Equation of Motion

Identifying sub-structural components of eq. (2.99), *i.e.*, the terms corresponding to individual physical mechanisms, allows for both, insights into the driving mechanisms of tilted vortex motion under the influence of diabatic or shear-induced forcing and designing numerical strategies according to the properties of the (rather generic) building blocks of the couples set of equations. To this end, we particularly analyze eqs. (2.58) on the basis of distinguishing between diabatic and adiabatic effects. From eq. (2.42) we know that the Fourier-1 mode w_1 of vertical velocity is a linear superposition

$$w_1 = w_{1,\mathrm{dia}} + w_{1,\mathrm{ad}} , \tag{3.19a}$$

of contributions due to diabatic heat release,

$$w_{1,\mathrm{dia}} := \frac{1}{\Theta'_1} Q_{\Theta,1} , \tag{3.19b}$$

and those which are induced by the tilted geometry of the centerline,

$$w_{1,\mathrm{ad}} := \frac{1}{\Theta'_1} W \hat{R}_{-\pi/2} \partial_z X = \hat{R}_{-\pi/2} \hat{w} X . \tag{3.19c}$$

$W = (\Theta_0/\rho_0)(u_\theta^{(0)}/r)\partial_r p^{(3-2\delta)}$ and, as introduced earlier, $\hat{R}_{-\pi/2}$ is the two-dimensional $-90°$-rotation matrix. We will show that the expression Ψ, given in eq. (2.97b), due to linearity, splits into three subdivisions which exhibit different analytical properties.

In the further course we will make use of the notational convention that operator-valued entities are indicated by a hat symbol, *e.g.*, $\hat{w}$ is defined by

$$\hat{w} = \frac{W}{\Theta'_1} \frac{\partial}{\partial z} . \tag{3.20}$$

We further analyze the components of $\mathbf{\Psi}$ given in eqs. (2.58). For $\mathcal{H}_1$ we get

$$\mathcal{H} = \mathcal{H}_{\text{dia}} + \hat{R}_{-\pi/2}\hat{\mathcal{H}}X \tag{3.21a}$$

with the definitions

$$\mathcal{H}_{\text{dia}} := \frac{\partial}{\partial r}\left((r\boldsymbol{w}_{1,\text{dia}})\frac{\partial u_\theta}{\partial z}\right), \tag{3.21b}$$

$$\hat{\mathcal{H}}X := \frac{\partial}{\partial r}\left((r\hat{w}X)\frac{\partial u_\theta}{\partial z}\right). \tag{3.21c}$$

In analogy with eqs. (3.19), $\boldsymbol{W}_1$ subdivides into

$$\boldsymbol{W}_1 = \boldsymbol{W}_{1,\text{dia}} + \hat{R}_{-\pi/2}\hat{W}X, \tag{3.22a}$$

$$\boldsymbol{W}_{1,\text{dia}} := -\frac{1}{\rho_0}\partial_z(\rho_0\boldsymbol{w}_{1,\text{dia}}), \tag{3.22b}$$

$$\hat{W}X := -\frac{1}{\rho_0}\partial_z(\rho_0\hat{w}X), \tag{3.22c}$$

which allows reformulating $\mathcal{I}$:

$$\mathcal{I} = \mathcal{I}_{\text{dia}} + \hat{R}_{-\pi/2}\hat{\mathcal{I}}X \tag{3.23a}$$

$$\mathcal{I}_{\text{dia}} := r\left(\zeta + f_0\right)\boldsymbol{W}_{\text{dia}} \tag{3.23b}$$

$$\hat{\mathcal{I}}X := r\left(\zeta + f_0\right)\hat{W}X. \tag{3.23c}$$

Together with

$$\boldsymbol{M}_1 = \frac{f^2}{4\pi\rho_0\Gamma}\frac{\partial}{\partial z}\left(\frac{\rho_0\Gamma^2}{\Theta_1'}\frac{\partial X}{\partial z}\right) =: \hat{M}X \tag{3.24}$$

we get the following split for $\tilde{\mathcal{I}}$:

$$\tilde{\mathcal{I}} = \mathcal{I}_{\text{dia}} + \hat{R}_{-\pi/2}\hat{\mathcal{I}}X + H_s(r-1)\frac{1}{r^2}\frac{\Gamma}{2\pi}\hat{R}_{-\pi/2}\hat{M}X \tag{3.25}$$

$$=: \mathcal{I}_{\text{dia}} + \hat{R}_{-\pi/2}\hat{\tilde{\mathcal{I}}}X \tag{3.26}$$

$\boldsymbol{\phi}_1$ involves the expression $\boldsymbol{R}_1$, which is assembled as

$$\boldsymbol{R}_1 = \boldsymbol{W}_{1,\text{dia}} + \hat{R}_{-\pi/2}\hat{W}X + R_{Q,0}\partial_z X, \tag{3.27a}$$

$$R_{Q,0} := \frac{1}{2}(\partial_r w_0). \tag{3.27b}$$

We proceed with

$$\boldsymbol{\phi}_1 = \boldsymbol{\phi}_{1,\text{dia}} + \hat{R}_{-\pi/2}\hat{\phi}X + \phi_{Q,0}\partial_z X \tag{3.28a}$$

$$\boldsymbol{\phi}_{1,\text{dia}} := -r\int_r^\infty \frac{1}{\bar{r}^3}\int_0^{\bar{r}}\bar{\bar{r}}^2\boldsymbol{W}_{1,\text{dia}}\,d\bar{\bar{r}}\,d\bar{r} \tag{3.28b}$$

$$\hat{\phi}X := -r\int_r^\infty \frac{1}{\bar{r}^3}\int_0^{\bar{r}}\bar{\bar{r}}^2\hat{W}X\,d\bar{\bar{r}}\,d\bar{r} \tag{3.28c}$$

$$\phi_{Q,0} := -r\int_r^\infty \frac{1}{\bar{r}^3}\int_0^{\bar{r}}\bar{\bar{r}}^2 R_{Q,0}\,d\bar{\bar{r}}\,d\bar{r} \tag{3.28d}$$

giving rise to the formulation for $\mathcal{J}_1$:

$$\mathcal{J} = \mathcal{J}_{\mathrm{dia}} + \hat{R}_{-\pi/2}\hat{\mathcal{J}}X + \mathcal{J}_{Q,0}\partial_z X \,. \tag{3.29a}$$

$$\mathcal{J}_{\mathrm{dia}} := \partial_r(\boldsymbol{\phi}_{1,\mathrm{dia}})(r\partial_r\zeta) \tag{3.29b}$$

$$\hat{\mathcal{J}}X := \partial_r(\hat{\phi}X)(r\partial_r\zeta) \tag{3.29c}$$

$$\mathcal{J}_{Q,0} := (\partial_r\phi_{Q,0})(r\partial_r\zeta) \tag{3.29d}$$

Ultimately, we have

$$Q_1 = \left(w_0\frac{u}{r} - \partial_r(rw_0\partial_r u)\right)\frac{\partial X}{\partial z} =: Q_0\frac{\partial X}{\partial z} \,. \tag{3.30}$$

All together, we can summarize

$$\begin{aligned}
\boldsymbol{\Psi} &= \hat{R}_{\pi/2}L[\mathcal{K}] = \hat{R}_{\pi/2}L[\mathcal{H} + \tilde{\mathcal{I}} + \mathcal{J} + \mathcal{Q}] \\
&= \hat{R}_{\pi/2}L[\tilde{\mathcal{K}}_{\mathrm{dia}}] + \hat{R}_{\pi/2}L[\mathcal{J}_{Q,0}\partial_z X + Q_0\partial_z X] + L[\hat{\mathcal{H}} + \hat{\tilde{\mathcal{I}}} + \hat{\mathcal{J}}]X \,,
\end{aligned} \tag{3.31}$$

where we identify (so far unspecified) terms due — and proportional — to the diabatic Fourier-mode 1 contributions to w_1, first-order differential terms due to symmetric diabatic heat release and rotated (generally second-order) differential expression acting on X. In eq. (3.31), we introduced the definitions of $\tilde{\mathcal{K}}_{\mathrm{dia}} := \mathcal{H}_{\mathrm{dia}} + \mathcal{I}_{\mathrm{dia}} + \mathcal{J}_{\mathrm{dia}}$.

Most of the evaluations presented so far involve elements of $\mathbb{R}^2$, denoted by bold-face symbols. We now make the transition to complex-valued expressions. Formally, this is done by identifying elements of $\mathbb{R}^2$ with $\mathbb{C}$ which we will symbolically represent by plain symbols, *e.g.*,

$$X := \boldsymbol{X} \cdot \boldsymbol{i} + \iota \boldsymbol{X} \cdot \boldsymbol{j} \tag{3.32}$$

ι canonically represents the *imaginary unit*.

In this setting we can formulate the *complex* eq. (2.99) as

$$\begin{aligned}
\iota(\partial_t X + L[(\mathcal{J}_{Q,0} + Q_0)\partial_z X]) = &-\alpha\ln(\varepsilon)\hat{M}X - L[\hat{\mathcal{H}} + \hat{\tilde{\mathcal{I}}} + \hat{\mathcal{J}}]X+ \\
&+ \iota u_s - \iota L[\mathcal{H}_{\mathrm{dia}} + \mathcal{I}_{\mathrm{dia}} + \mathcal{J}_{\mathrm{dia}}] \,,
\end{aligned} \tag{3.33}$$

or, in a more compact form,

$$\iota(\partial_t X + A\partial_z X) = \hat{H}X + \iota Q + \iota u_s \,, \tag{3.34}$$

with straight-forward abbreviation terms as appearing in eq. (3.33). This matches our previously set goal to split eq. (2.99) into components with different properties: $A\partial_z$ imposes the one-dimensional advection equation, $\hat{H}$ is a linear second-order differential operator (further analyzed in section 3.3) and therefore imposes a *Schrödinger-like* equation. Q collects all terms due to asymmetric diabatic heat release (proportional to w_1). All the quantities A, $\hat{H}$ and Q depend on the solution (X, u), where $\hat{H}$ explicitly depends only on u and the coordinates r and z. A, as a function of symmetric diabatic heat contributions w_0, may in general depend on X as well, imposing a non-linear advection problem. u_s represents externally imposed background wind shear as function

of z and t only. Note, that we neglected the term $\boldsymbol{X}^{(0)} \cdot \boldsymbol{\nabla}_{\parallel}(\boldsymbol{u})_0^{(0)}$ of eq. (2.99).[7] By doing so, we assume that the geostrophic wind is horizontally uniform.

The outlined analysis gives reason for further examination with respect to the properties of the sub-equation imposed by each contribution. Analytical findings will be presented in the remainder of this chapter. A numerical approach of solving eq. (3.34) together with eq. (3.1) however, will be discussed in detail in chapter 4.

3.3. Sturm-Liouville Theory on the Centerline Hamiltonian

In their section 6, Päschke et al. (2012) pointed out that for exponential or constant background density profile there exist precessing solutions of the adiabatic centerline equation. For that specialized case they derived an explicit solution to eq. (2.99). For more realistic scenarios the assumption on the background density might be too strong. However, in the following examination we will clarify that precessing solution exist for a wider range of environmental conditions and are a consequence of the spectral properties of the time evolution operator of the adiabatic centerline equation.

In section 3.2 we identified those contributions to the centerline motion which do not dependent on diabatic heat release. Also neglecting forcing by background wind we end up with a *Schrödinger-type* equation[8]

$$\iota \partial_t X = \hat{H} X \,. \tag{3.35}$$

These findings revealed that $\hat{H}$ as a linear operator acting on X depends on u_θ which is time-independent in the adiabatic case. Hence, $\hat{H}$ is time-independent in that case as well.

Problems of the type of eq. (3.35) are typically treated in the context of quantum mechanics, where X is considered an element of the *Hilbert space* $(H, \langle \cdot, \cdot \rangle)$ with elements being functions $\psi : \Omega \to \mathbb{C}$ and equipped with the scalar product $\langle \cdot, \cdot \rangle$.

We motivate the following analysis by assuming that $\hat{H}$ exhibits a spectrum $\{\lambda_k\}_{k=1,\dots,d}$ with eigenvectors solving

$$\hat{H} \psi_k = \lambda_k \psi_k \tag{3.36}$$

and forming a complete orthonormal basis $\{\psi_k \in H_X : \langle \psi_l, \psi_k \rangle = \delta_{lk}\} \,\forall k, l = 1, \dots, d$ with $d \in \mathbb{N} \cup \infty$ such that we can construct solutions as linear superposition of eigenvectors

$$X(t, z) = \sum_k^d c_k(t) \psi_k(z) \,. \tag{3.37}$$

---

[7]This simplification serves the purpose of highlighting the symplectic structure of the centerline equation of motion and to avoid the inconvenient notation of $\boldsymbol{X} \cdot \boldsymbol{\nabla}_{\parallel}(\boldsymbol{u})_0^{(0)}$ in terms of complex-valued solutions. Including the shear-term would in fact not alter the general property of the resulting equation, *i.e.*, not affect the Sturm-Liouville property of the Hamiltonian, since $\boldsymbol{X} \cdot \boldsymbol{\nabla}_{\parallel}(\boldsymbol{u})_0^{(0)} = \left(\boldsymbol{\nabla}_{\parallel} \otimes (\boldsymbol{u})_0^{(0)}\right) \boldsymbol{X}$ is linear in $\boldsymbol{X}$, cf. section 3.3.

[8]We use the term *Schrödinger-type* as the regular notion involves a Hamiltonian which is supposed to be self-adjoint under the regular inner product $\langle f.g \rangle := \int_\Omega \bar{f} g \, d\Omega$ whereas here we have to make use of weighted scalar products $\langle f, g \rangle_w = \int_\Omega w \bar{f} g \, d\Omega$. Nonetheless, is it straightforward to generalize the Schrödinger equation accordingly.

$c_k(t) \in \mathbb{C}$ are time-dependent coefficients, consistently defined as

$$c_k(t) := \langle \psi_k(z), X(z,t) \rangle, \tag{3.38}$$

and, inserting eq. (3.37) into eq. (3.35) we get a set of linear ordinary differential equations (ODEs):

$$\frac{dc_k}{dt} = -\iota \lambda_k c_k, \quad k = 1, \dots, d. \tag{3.39}$$

Each eigenmode c_k decouples from the rest and takes only the (constant) eigenvalue λ_k into account. We immediately arrive at the solution given as

$$c_k(t) = c_k(0) e^{-\iota \lambda_k t}, \tag{3.40}$$

i.e., eigenmodes precess in the complex plane if λ_k is real, and grow (decay) if λ_k has a negative (positive) imaginary part.

Now, as we pointed out that the properties of the spectrum of $\hat{H}$, if well-posed, determine the evolution of the eigenmodes and therefore of the overall solution $X(z,t)$, we need to make statements about these spectral properties of $\hat{H}$. To this end, we have to characterize the solutions of the eigenvalue problem eq. (3.36).

Since $\hat{H}$ is a one-dimensional linear second-order differential operator we can treat eq. (3.36) as a *Sturm-Liouville problem* of the form

$$\frac{d}{dz}\left(p(z)\frac{d\psi}{dz}\right) + q(z)\psi = -\lambda w(z)\psi \quad \text{in} \quad \Omega = [a,b] \subset \mathbb{R}, \tag{3.41}$$

$$0 = \alpha_1 p(a)\psi'(a) + \alpha_2 \psi(a)$$
$$0 = \beta_1 p(b)\psi'(b) + \beta_2 \psi(b)$$

The coefficients of homogeneous boundary conditions have to satisfy $\alpha_1^2 + \alpha_2^2 > 0$ and $\beta_1^2 + \beta_2^2 > 0$. Sturm-Liouville theory (Teschl 2012) states that eq. (3.41) with coefficient functions

$$p \in C^1(\Omega, \mathbb{R}), \tag{3.42a}$$

$$q \in C^0(\Omega, \mathbb{R}), \tag{3.42b}$$

$$w \in C^0(\Omega, \mathbb{R}), \tag{3.42c}$$

$p, w > 0 \; \forall z \in \Omega$ is called *regular Sturm-Liouville problem* and possesses a discrete real spectrum of eigenvalues. We thus have to show that $\hat{H}$ in eq. (3.36) takes the form

$$\hat{H}\psi = -\frac{1}{w(z)}\left(\frac{d}{dz}\left(p(z)\frac{d\psi}{dz}\right) + q(z)\psi\right). \tag{3.43}$$

In that case, $\hat{H}$ is called a *Sturm-Liouville operator*. Together with the boundary conditions of eq. (3.41) the operator is *self-adjoint* and possesses real eigenvalues (Teschl 2012). Eigenmodes of eq. (3.36) would then be precessing solutions of eq. (3.35). The remaining question is whether $\hat{H}$ as defined in eqs. (3.33) and (3.34) and thus the problem (3.36) is of the form of eq. (3.41) and satisfies the requirements (3.42). For the sake of validating the above statements, we make the following considerations:

Lemma 3.1. *The boundary value problem*

$$\hat{H}\psi \equiv P\psi'' + Q\psi' + R\psi = \lambda\psi \tag{3.44}$$

is equivalent to eq. (3.41) provided the same boundary conditions.

Proof[9]. With the conditions (3.42) satisfied, eq. (3.41) can be expressed as

$$p\psi'' + p'\psi' + q\psi = -\lambda w\psi . \tag{3.45}$$

We hence identify

$$P = -\frac{p}{w} , \tag{3.46a}$$

$$Q = -\frac{p'}{w} , \tag{3.46b}$$

$$R = -\frac{q}{w} . \tag{3.46c}$$

By solving

$$w = \exp\left(\int \frac{Q - P'}{P}\, dz\right) , \tag{3.47a}$$

$$p = -P \exp\left(\int \frac{Q - P'}{P}\, dz\right) , \tag{3.47b}$$

$$q = -R \exp\left(\int \frac{Q - P'}{P}\, dz\right) , \tag{3.47c}$$

assuming that $P \neq 0$ we have traced eq. (3.44) to the form of eq. (3.41). $\qquad\square$

Lemma 3.2. *The sum of two Sturm-Liouville operators is a Sturm-Liouville operator.*

Proof. Let $\hat{H}_1$ and $\hat{H}_2$ be Sturm-Liouville operators that are expressed as

$$\hat{H}_{1,2}\psi = -\frac{1}{w_{1,2}}\left(\frac{d}{dz}\left(p_{1,2}\frac{d\psi}{dz}\right) + q_{1,2}\psi\right) . \tag{3.48}$$

Then

$$\hat{H}\psi = \hat{H}_1\psi + \hat{H}_2\psi ,$$
$$= -\frac{1}{w_1}\left(\frac{d}{dz}\left(p_1\frac{d\psi}{dz}\right) + q_1\psi\right) - \frac{1}{w_2}\left(\frac{d}{dz}\left(p_2\frac{d\psi}{dz}\right) + q_2\psi\right) ,$$
$$= -\left(\frac{p_1}{w_1} + \frac{p_2}{w_2}\right)\psi'' - \left(\frac{p_1'}{w_1} + \frac{p_2'}{w_2}\right)\psi' - \left(\frac{q_1}{w_1} + \frac{q_2}{w_2}\right)\psi ,$$
$$\equiv P\psi'' + Q\psi' + R\psi , \tag{3.49}$$

which is of the form of eq. (3.44) and therefore can be traced back to eq. (3.41). $\qquad\square$

---

[9]Proof adapted from `https://en.wikipedia.org/wiki/Sturm_Liouville_theory#Application_to_inhomogeneous_second-order_boundary_value_problems`, accessed on 11/24/2021.

With that statement, we can treat each of the constituents of $\hat{H}$ individually, as defined in eq. (3.33), and find that all but one term follow the form of eq. (3.43). The only attention has to be paid to the expression $\hat{\mathcal{H}}$, which is a first-order differential operator. However, we have the following

Lemma 3.3. *The sum of a Sturm-Liouville operator and a first-order differential operator is a Sturm-Liouville operator.*

Proof. Let $\hat{H}$ be a Sturm-Liouville operator. Then

$$\hat{H}\psi + \tilde{Q}\psi' = P\psi'' + (Q + \tilde{Q})\psi' + R\psi \tag{3.50}$$

Which is again of the form of eq. (3.44), hence a Sturm-Liouville operator. $\qquad\square$

Lemma 3.4. *In case of $q \equiv 0$ and $p, w > 0$, the operator $\hat{H}$, defined through eq. (3.43), possesses a positive spectrum.*

Proof. To show, that the spectrum of $\hat{H}$ has a definite sign, it suffices to show that $\hat{H}$ is definite. We consider the scalar product

$$\langle \psi, \hat{H}\psi \rangle_w = -\int_a^b \bar{\psi}(p\psi')'\, dz$$

$$= -\bar{\psi}p\psi'\big|_a^b + \int_a^b \bar{\psi}'p\psi'\, dz$$

$$= \int_a^b |\psi'|^2\, p\, dz > 0 \tag{3.51}$$

The first term in the second line of eq. (3.51) is omitted due to the assumption of homogeneous boundary conditions together with the operator $\hat{H}$.[10] If ψ is an eigenvector of $\hat{H}$, it follows that

$$\langle \psi, \hat{H}\psi \rangle_w =: \lambda \|\psi\|_w^2 \tag{3.52}$$

with $\|\cdot\|_w$ the norm induced by the scalar product $\langle \cdot, \cdot \rangle_w$. From eqs. (3.51) and (3.52) follows the positive sign of λ. $\qquad\square$

With the statements of lemmas 3.1 to 3.4, it is now trivial to conclude that the sum of first and second-order differential operators that resemble $\hat{H} \equiv -L[\hat{\mathcal{H}} + \hat{\tilde{\mathcal{I}}} + \hat{\mathcal{J}}] - \alpha \ln(\varepsilon)\hat{M}$ forms a Sturm-Liouville operator, provided the boundary conditions of the problem are set to satisfy those of eq. (3.41). For practical applications, in chapter 6 we are bound to Neumann boundary conditions $X'(0) = X'(z_\top) = 0$ due to the assumption of rigid lids at $z = 0$ and $z = z_\top$.

Remark. A complete proof of the sign of p and w within the definition of the operator $\hat{H}$, assembled by eq. (3.33), remains open to future work. Empirically, however, it is evident through the experiments of chapter 6 that the eigenspectrum of $\hat{H}$ is purely

---

[10]This is a reasonable assumption as rigid-lid conditions ($w|_{z=z,z_t op} = 0$) induce $\partial_z X|_{z=0,z_\top} = 0$ in the adiabatic case.

negative leading to counterclockwise precession of eigenmodes. In section 2.5, however, we already discussed the scenario where Γ vanishes (either locally or globally). Since this quantity appears in the definition of $L[\cdot]$ (cf. eq. (2.94)) as a divisor, the above condition on w cannot be assumed anymore, and we have to deal with an *irregular Sturm-Liouville problem*.

To meet the requirement that $\hat{H}$ possesses a real spectrum, which is what we need for the statement of the existence of precessing eigenmodes, however, it suffices to satisfy *Lagrange's identity*

$$\int_a^b w(\bar{\phi}\hat{H}\psi - (\hat{H}\bar{\phi})\psi)\,dx = 0 \tag{3.53}$$

at least in an improper sense.[11] Without further proof, we assume this to be true, since we argued in section 2.5 that in the circulation-free limit the operator $\hat{H}$ still is well-defined throughout in integration domain, and the expression $\hat{H}\psi$ becomes 0 at the critical points.

With that being stated, we conclude that under a wide range of conditions the adiabatic centerline equation possesses counterclockwise precessing eigenmode solutions.

3.4. Dynamical Properties of the Vortex Centerline

After examining the adiabatic behavior of the centerline equation of motion, in this section we will discuss the response of the centerline to forcings that arise from external wind shear or diabatic heat release.

3.4.1. Motion under the Influence of Shear

Shear, *i.e.*, the vertical gradient of a large-scale external wind field the vortex is embedded into, is encoded in the leading-order asymptotic equations as external forcing on the centerline motion, cf. eq. (3.34). Neglecting all other effects than external wind, the centerline equation of motion reads

$$\iota\frac{\partial X}{\partial t} = \hat{H}X + \iota u_s \,. \tag{3.54}$$

The leading-order circumferential velocity relative to the centerline, on the other hand, is not affected by externally imposed shear. In fact, both, self-induced motions and externally imposed background wind, transport the leading-order tangential velocity field as being "attached to the centerline" as the latter one evolves.

Equation (3.54) can be formally solved by projecting onto the eigenspace of $\hat{H}$ (following section 3.3): Defining the coefficients c_k according to eq. (3.37), the eigenmodes decouple, and we obtain

$$\iota\frac{dc_k}{dt} = \lambda_k c_k + \iota u_k \tag{3.55}$$

---

[11]Here, *improper* is meant in the sense of an *improper integral*, *i.e.*, eq. (3.53) may possess an unbounded integration interval or the integrand may be ill-posed somewhere in the integration interval.

Trivially, by variation of constants, we can solve this ODE and find the general solution

$$c_k(t) = e^{-\imath\lambda_k t}\left(c_k(0) + \int_0^t e^{\imath\lambda_k t'} u_k(t')\,dt\right). \tag{3.56}$$

We note, that the value of λ_k determines the character of the equation and its solutions: For the lowest eigenmode with $\lambda_0 = 0$, we obtain the solution

$$c_0(t) = c_0(0) + \int_0^t u_0(t)\,dt \tag{3.57}$$

that resembles uniform translation due to mean horizontal wind. Shear is covered by eigenmodes with $k \geq 1$.

For the specialized case of constant-in-time external wind, we can further simplify and have

$$c_k(t) = \tilde{c}_k e^{-\imath\lambda_k t} - \imath\frac{u_k}{\lambda_k} \tag{3.58}$$

with the constant $\tilde{c}_k$ fixed by the initial condition $c_k(0) = \tilde{c}_k - \imath\frac{u_k}{\lambda_k}$.

Equation (3.55) reveals that for $u_k(t) = \imath\lambda_k c_k(0)(= \text{const})$ stationary solutions exist. Physically speaking, these solutions correspond to shear that cancels the proper motion of the adiabatic centerline precession. Nonetheless, this setting requires the background wind shear to be tuned to the initial data of tangential velocity (via the value λ_k), a rather unlikely scenario.

Reasor, Montgomery, and Grasso (2004), on the other hand, demonstrated, that an initially barotropic vortex can indeed tend towards a configuration where the tilt direction and amplitude become stationary, and they argue that damping of the tilt mode by VRWs causes this behavior. Though not directly incorporated into the asymptotic theory, we can encode VRW damping by introducing a linear damping term $-\imath d\,c_k$, with $d \in \mathbb{R}_+$, such that we have the governing ODE

$$\imath\frac{dc_k}{dt} = (\lambda_k - \imath d)c_k + \imath u_k . \tag{3.59}$$

In analogy to the previous calculations we have the general solution

$$c_k(t) = \tilde{c}_k e^{-(\imath\lambda_k + d)t} - \imath\frac{u_k}{\lambda_k + \imath d} \tag{3.60}$$

that, in the limit $t \to \infty$ tends to

$$c_k(t) \to \frac{u_k}{\imath\lambda_k - d} \quad \text{as} \quad t \to \infty . \tag{3.61}$$

Hence, with active damping through VRWs in the presence of vertical wind shear the solution settles towards a constant tilt configuration. This solution is qualitatively in line with Reasor, Montgomery, and Grasso (2004), yet, the damping constant d is not derived on the basis of VRW damping and can only be estimated from quantitative comparison.

Remark. Here, we chose a scalar damping coefficient d, that induces *Rayleigh damping*, *i.e.*, a damping term proportional to the amplitude $X = \sum c_k \psi_k$. Damping could also be proportional to the second derivative manifesting in the term $-\iota d \, \partial^2 X / \partial z^2$ on the right-hand side of eq. (3.54). Then, in eq. (3.59), d would be formally replaced by $\mathscr{d}_k$, the correction term that arises by transitioning the eigenvalue problem $\hat{H}\psi = \lambda\psi$ to

$$\left(\hat{H} + \iota d \frac{\partial^2}{\partial z^2} \right) \psi = (\lambda + \iota \mathscr{d}_k)\psi \,. \tag{3.62}$$

The qualitative statement of eq. (3.61) yet remains valid.

3.4.2. Motion under the Influence of Symmetric Diabatic Heat Release

Under purely symmetric convection, both, centerline and tangential wind equations are composed of advection operators on the left-hand side and source terms on the right-hand side:

$$\iota \left(\frac{\partial X}{\partial t} + A \frac{\partial X}{\partial z} \right) = \hat{H}X \tag{3.63a}$$

$$\frac{\partial u_\theta}{\partial t} + u_{r,00} \frac{\partial u_\theta}{\partial r} + w_0 \frac{\partial u_\theta}{\partial z} = -u_{r,00} \left(\frac{u_\theta}{r} + f_0 \right) \tag{3.63b}$$

Via the couplings $A = A(u_\theta, w_0)$ and $\hat{H} = \hat{H}(u_\theta)$ the equations are genuinely nonlinear. Note that diabatic heating can add to the nonlinearity via the parameterizations $w_0 = w_0(u_\theta, X)$ and $u_{r,00} = u_{r,00}(w_0)$. As we have seen in eq. (3.4), angular momentum is conserved along trajectories of the secondary circulation in the r-z-plane in the absence of tilt and heating asymmetries. In this case, eq. (3.1) is equivalent to

$$\frac{\partial M}{\partial t} + u_{r,00} \frac{\partial M}{\partial r} + w_0 \frac{\partial M}{\partial z} = 0 \,. \tag{3.64}$$

Previous studies on vortex intensity are based on this equation and from those we know that the underlying intensification mechanism is associated with the secondary circulation that drags air masses inwards, forces them to raise in the eyewall region and ejects them on top (Montgomery and Smith 2017b; Vigh and Schubert 2009). The angular momentum transported inwards is essentially what accelerates the vortex. Montgomery and Smith (2017b, and references therein) also acknowledge the difficulty in understanding the role of the boundary layer. At issue is whether turbulent friction causes the tangential wind to decrease towards the sea surface not balancing the pressure gradient and ultimately leading to an inflow. By conditioning the stability of the atmosphere convection is then triggered (CISK hypothesis by Charney and Eliassen (1964)). Alternatively, the WISHE hypothesis (Emanuel 1991) postulates that it is the surface wind drag that causes turbulent mixing of the atmosphere and convection is the consequence of the lifting of air parcels. The latter theory seems to be more favorable as the underlying mechanism for symmetric vortex intensification (Craig and Gray 1996).

In the process of the secondary circulation, however, also the centerline is guided by vertical advection that accounts for the vertical transport of the vortex structure, *i.e.*, the centerline position. For typical heating patterns, we empirically found that the advection velocity is positive. Depending on the lower boundary conditions, as we will see in chapter 6, vertical alignment by symmetric diabatic heating proves to be very efficient.

3.4.3. Motion under the Influence of Asymmetric Diabatic Heat Release

The derivation of eq. (3.34) was based on the fact that the vertical velocity and in particular its Fourier-1 mode splits into two contributions, one due to diabatic heating and a second one due to the potential temperature perturbation induced by the tilted vortex. The more explicit formulation eq. (3.33) points to the relation between the terms HX and iQ of eq. (3.34): The diabatic contribution to the centerline motion Q takes all the Fourier-1 modes of vertical velocity into account that are due to diabatic heating. To discuss the dynamics of asymmetric diabatic heating, we start by setting $w_0 = 0$. With eq. (2.50), the immediate consequence is $u_{r,00} \equiv 0$, and the tendency equation for the tangential wind speed reduces to

$$\frac{\partial u_\theta}{\partial t} = -u_{r,*} \left(\frac{u_\theta}{r} + f \right) . \tag{3.65}$$

With $w_{1,\mathrm{dia}} = -w_{1,\mathrm{ad}}$, *i.e.*, $w_1 \equiv 0$, the relation between $\hat{H}X$ and Q becomes

$$
\begin{aligned}
\iota Q|_{w_{1,\mathrm{dia}}=-w_{1,\mathrm{ad}}} &= -\iota \, L[\mathcal{H}_{\mathrm{dia}} + \mathcal{I}_{\mathrm{dia}} + \mathcal{J}_{\mathrm{dia}}]\big|_{w_{1,\mathrm{dia}}=-w_{1,\mathrm{ad}}} \\
&= \iota \lim_{r\to\infty} \frac{\pi}{\Gamma} \int_0^r r' \, (\mathcal{H}_{\mathrm{dia}} + \mathcal{I}_{\mathrm{dia}} + \mathcal{J}_{\mathrm{dia}})\big|_{w_{1,\mathrm{dia}}=w_{1,\mathrm{ad}}} \, dr' \\
&= L[\hat{\mathcal{H}} + \hat{\hat{\mathcal{I}}} + \hat{\mathcal{J}}]X - 2\alpha \lim_{r\to\infty} \ln(r)\hat{M}X \\
&= -\hat{H}X - \alpha \lim_{r\to\infty} (2\ln(r) + \ln(\varepsilon))\hat{M}X .
\end{aligned}
\tag{3.66}
$$

The term $-2\alpha \lim_{r\to\infty} \ln(r)\hat{M}X$ accounts for the unbounded integration of the Coriolis term in the asymmetric WTG equation (2.42). At this point, we realize the difficulty that arises with the condition $w_{1,\mathrm{dia}} = -w_{1,\mathrm{ad}}$ for the scaling regime with $\alpha = 1/2$: The logarithmic part arising from the diabatic heating constructed in that way in the far-field limit of the core solution (cf. eq. (2.90)) does not match with a counterpart in the near-field limit of the outer solution. The compound solution becomes singular in that case. Note that this behavior is solely caused by the way the diabatic heating is constructed and does not interfere with the matching condition in the adiabatic case. In fact, Päschke et al. (2012) mentions this behavior by restricting diabatic heating to decay sufficiently rapid. A consistent asymptotic solution would involve a weak diabatic source in the QG far-field regime to match with the core solution such that the logarithmically diverging term of eq. (3.66) cancels. With Klein, Schielicke, et al. (2021) an asymptotic model for the QG regime is derived that could be matched to the present TC model. This work, however, is out of scope of this thesis.

To remedy this issue discussed above, we restrict to $\alpha = 0$ in the further course of this section and in setting up the initial data for the subsequent numerical experiments (cf. chapters 5 and 6) The singular effects, however, are only shifted to higher asymptotic orders. This, as we will see in section 6.3.1, eventually leads to long-term instabilities which are found under control for the purpose of the presented experiments.

The diabatic heating as constructed above under the scaling regime of $\alpha = 0$, and neglecting external wind shear, yields stationarity for the centerline equation of motion — at leading order:

$$\iota \frac{\partial X}{\partial t} = 0 \tag{3.67}$$

Until now, we have constructed a diabatic vertical velocity component such that the resulting vertical velocity dipole vanishes. We are at liberty to make different choices for w_{dia} such as rotated version of w_{ad} about an angle $\tilde{\theta}_0$. From eq. (2.42), we know that $\tilde{\theta}_0 = \theta_0 + \pi/2$, where θ_0 is the direction of the tilt vector. In the complex plane we can conveniently write

$$w_{1,\text{dia}} = \exp(\iota\tilde{\theta}_0)w_{1,\text{ad}} = \exp(\iota\theta_0)\hat{w}X \,. \tag{3.68}$$

Again we consider the forcing by asymmetric diabatic heating

$$\iota Q|_{w_{1,\text{dia}}=\exp(\iota\tilde{\theta}_0)w_{1,\text{ad}}} = \exp(\iota\tilde{\theta}_0)\hat{H}X \,. \tag{3.69}$$

Thus, the resulting centerline equation (neglecting forcing by external wind) poses a linear PDE in X:

$$\iota\frac{\partial X}{\partial t} = (1 + \exp(\iota\tilde{\theta}_0))\hat{H}X \tag{3.70}$$

The first term corresponds to a forcing induced by the sum of the adiabatic and diabatic vertical velocity dipoles. Without rigorous proof, but from numerical experiments we know that under regular conditions, $\hat{H}$ possesses a negative spectrum leading to counterclockwise precession. In the way the heating is constructed here, the above centerline equation of motion leads to a superposition of the adiabatic precessing motion and a contribution that has in general a complex spectrum (depending on $\exp(\iota\tilde{\theta}_0)$). Effectively the eigenvalues of $\hat{H}$ are modified by the prefactor $(1 + \exp(\iota\tilde{\theta}_0))$. Recalling the motion in the eigenspace (cf. eqs. (3.39) and (3.40)), a positive (negative) real part of $\exp(\iota\theta_0)$ leads to acceleration (deceleration) of the centerline motion, while a positive (negative) imaginary part of $\exp(i\theta_0)$ causes decay (growth) of the eigenmodes.

4. Numerical Methods for Solving the Leading-Order System

Chapter 3 served to identify structural properties of the leading-order asymptotic equations which govern the motion of TCs in both, the gradient-wind and the cyclostrophic regime. Along the lines of these properties we now seek to construct a numerical scheme which allows to integrate these equations forward in time in a sufficiently stable and accurate manner. As a reference we repeat the final result here in compact form:

$$\iota \left(\frac{\partial X}{\partial t} + A \frac{\partial X}{\partial z} \right) = \hat{H} X + \iota Q + \iota u_s \tag{4.1a}$$

$$\frac{\partial u}{\partial t} + u_{r,00} \frac{\partial u}{\partial r} + w_0 \frac{\partial u}{\partial z} = -u_{r,0} \left(\frac{u}{r} + f_0 \right) \tag{4.1b}$$

Since we will mainly focus on the mathematical structure rather than the physical interpretation, and for the sake of clarity we dropped the θ-indices indicating the primary circulation velocity u_θ. Note the general dependency of the coefficient functions on the solution state. Definitions of the occurring symbols are given in sections 3.1.1 and 3.2.

In the form of eqs. (4.1), we recognize three prototypes the system is composed of:

  i) (non-linear) advection,

 ii) linear Schrödinger equation,

iii) generally non-linear source terms.

Each of these items on their own poses a problem with a rich body of solution strategies existing in literature. The challenge consists in the coupled integration. To this end, we first construct a generic approach to solve for equations of that type, and subsequently, by splitting the integration process into quasi-independent sub-steps involving the trapezoidal rule and operator splitting, we apply well-established numerical methods to each of the arising prototype equations. This approach is different from the previous one by Weber (2011), where the whole system was discretized in space by a fourth-order finite difference method and the resulting time-dependent system of ODEs was integrated by generic time integration schemes. Despite the high order of accuracy and the resulting numerical efficiency, due to the nonlinearities, solutions suffered from spurious oscillations and resulting instabilities. The ultimate goal is to construct a stable numerical scheme achieving overall second-order accuracy in space and time.

4.1. Formal Time Integration of the Asymptotic Equations

We immediately see that the individual equations of eqs. (4.1) can be recast into the more abstract form

$$\frac{\partial \psi}{\partial t} + \mathcal{A} \psi = R(\psi, t) \,. \tag{4.2}$$

In the further course we will identify ψ either with X, u or (X, u), depending on the context. $\mathcal{A}$ is a first-order differential operator expressing the advection term of eq. (4.1a) or eq. (4.1b), *i.e.*, one-dimensional and two-dimensional advection for X and u, respectively. $R(\psi, t)$ collects all right-hand side terms which may depend, in general, non-linearly on the solution.

For the analysis of PDEs, we identify the solution ψ of eq. (4.2) with elements of a sufficiently regular[1] Hilbert space H, such that

$$\psi : [0, T] \to H(\Omega, F), \quad t \mapsto \psi(t) \quad \text{with} \quad \psi(t) : \Omega \to F \qquad (4.3)$$

Ω represents the spatial domain of functions $\phi = \psi(t)$ and F is its codomain, *i.e.*, $F = \mathbb{C}$, $F = \mathbb{R}$, or $F = \mathbb{C} \times \mathbb{R}$ depending on whether $\psi = X$, $\psi = u$, or $\psi = (X, u)$. In this formalism the operator $\mathcal{A}$ becomes an abstract linear operator on H:

$$\mathcal{A} : H \to H, \quad \psi \mapsto \mathcal{A}\psi \qquad (4.4)$$

As we derived in sections 3.1.1 and 3.2, advection, expressed by $\mathcal{A}$, is associated to Fourier mode-0 heating. Thus, the linear operator $\mathcal{A}$ itself is — in general — parametrized by the solution $\psi = (X, u)$ and time t. Usually[2], $\psi(x, t)$ can be expanded into orthonormal base vectors e_n of H

$$\psi(x, t) = \sum_n a_n(t) e_n(x), \quad \text{where} \quad a_n(t) = \langle e_n, \psi(t) \rangle \qquad (4.5)$$

with time-dependent coefficients $a_n(t) \in F$. $\langle \cdot, \cdot \rangle$ is the scalar product associated to H. With this construction eq. (4.2) is equivalent to the ODE

$$\frac{da_m(t)}{dt} + \sum_n (\hat{A}(\psi, t))_{mn} a_n(t) = R_m(\psi, t), \quad \forall m = 1, 2, \ldots \qquad (4.6)$$

where we have $(\hat{A})_{mn} = \langle e_m, \mathcal{A}e_n \rangle$ and $R_m(\psi, t) = \langle e_m, R(\psi, t) \rangle$. Note, that $(\hat{A})_{mn}$, again, in general depends on the solution. The rank of the matrix with elements $(\hat{A})_{mn}$ corresponds to the dimensionality of H, hence becomes infinite in our case. This formalism allows us to write eq. (4.2) as an abstract ODE

$$\frac{d\psi}{dt} + \mathcal{A}\psi(t) = R(\psi(t), t) \qquad (4.7)$$

with $d\psi/dt$ to be understood as the derivative of $\psi : t \mapsto \psi(t) \in \Omega$ along trajectories through H.

It is now possible to construct solutions of eq. (4.2) by first considering the homogeneous problem

$$\frac{d\psi_h}{dt} + \mathcal{A}\psi_h = 0 \qquad (4.8)$$

---

[1]Actual regularity constraints on ψ depend essentially on the source term R.

[2]The fact that we assume ψ to be expressed in terms of an orthogonal basis of H implies that we have a priori knowledge of H. It is the very task of PDE analysis to explore the properties of elements of H. Only for sufficiently simple problems this is possible. For the general and non-linear source terms R with which we deal here, however, the problem renders out of scope of the present work. We therefore consider eq. (4.5) as an ansatz.

with the formal solution

$$\psi_h(\tau) = e^{-\int_0^\tau \mathcal{A}(\psi(t),t)\,dt} \psi(0) =: e^{-\tau A^{(\tau)}} \psi(0) \tag{4.9}$$

with $\tau \in [0,T]$.[3]

We introduced the shorthand notation $A^{(\tau)}$ representing the mean of the differential operator $\mathcal{A}(\psi(t),t)$ along the trajectory $(\psi(t),t)$ with $t \in [0,\tau]$. Naturally, $\psi(0)$ is the initial solution state and $e^{-\tau A^{(\tau)}}$ represents the integral operator advecting the solution from $t=0$ to $t=\tau$. As exceeding the scope of the present work, we omit further details about the properties of $\mathcal{A}$ necessary to render the above construction well-posed. For now, we need to take care of the dependency of $\mathcal{A}$ on $\psi(t)$ and t, which prevents us from finding an explicit expression of $A^{(\tau)}$ in eq. (4.9). In section 4.2, however, we will argue how to linearize $e^{-\tau A^{(\tau)}}$ and solve eq. (4.8) by a finite-volume method.

Continuing with this formal approach, we now can integrate the inhomogeneity of eq. (4.2) by *variation of constants* using the ansatz

$$\psi_p(\tau) = e^{-\tau A^{(\tau)}} \psi_0(\tau) \tag{4.10}$$

for a *particular solution* which requires solving for $\psi_0(\tau)$. Inserted into eq. (4.2) we get

$$e^{-\tau A^{(\tau)}} \frac{d\psi_0}{d\tau} = R(\psi(\tau),\tau) \tag{4.11}$$

with the formal solution

$$\psi_0(\tau) = \int_0^\tau e^{t A^{(t)}} R(\psi(t),t)\,dt \tag{4.12}$$

The general solution then is

$$\psi(\tau) = \psi_h(\tau) + \psi_p(\tau) = e^{-\tau A^{(\tau)}} \left(\psi(0) + \int_0^\tau e^{t A^{(t)}} R(\psi(t),t)\,dt \right) \tag{4.13}$$

Note, that eq. (4.13) is formally the exact solution of eq. (4.2). However, the expression $A^{(\cdot)}$ and right-hand side R need information of the solution along the integral trajectory, hence rendering the integral expression of eq. (4.13) unfeasible to solve analytically.

4.2. Construction of Time Integration Schemes

In section 4.1 we transformed the original PDE problem eqs. (4.1) into the formal solution eq. (4.13), shifting the problem towards finding integral operators for $e^{-\tau A^{(\tau)}}$ and $\int_0^\tau \cdot\, dt$. In this section we will discuss a general approach to constructing approximate solution strategies and on that basis derive a closure for equation eq. (4.13). For further comprehension, we streamline notation by symbolically identifying $R(t)$ with the expression $R(\psi(t),t)$.

---

[3]We make the distinction between T and τ in that the former is a global time integration interval while the latter is merely interpreted as a time step in the sense of numerical time integration.

As generally dependent on $\psi(t)$, we cannot evaluate $R(t)$ without prior knowledge of the solution $\psi(t)$ for $t > 0$ and hence the integral in eq. (4.13) cannot be solved directly. However, literature provides a plethora of numerical quadrature schemes to solve integrals of the type $\int_a^b f(t)\,dt$. Rather generally, *n-point quadrature rules* take the form of a weighted sum

$$\int_{-1}^{1} f(t)\,dt \approx \sum_{i=0}^{n-1} \bar{w}_i f(t_i) \tag{4.14}$$

where the integrand f is evaluated at discrete nodes $t_i \in [-1, 1]$, $i = 0, \ldots, n - 1$, depending on the choice of the *interpolation polynomials* and the desired approximation order p. Typically, t_i are chosen such that a polynomial integrand f of order $2n - 1$ is integrated exactly. On a formal level, the integral in eq. (4.13) can be written as

$$\int_0^{\tau} e^{tA^{(t)}} R(t)\,dt = \tau \sum_{i=0}^{n-1} \bar{w}_i e^{t_i A^{(t_i)}} R(t_i) + O(\tau^p) \,, \tag{4.15}$$

transforming it into an implicit algebraic expression which approximates the exact solution up to an error of order p.

With this construction we now want to motivate a specific choice for the number and position of the nodes t_i as well as the weights w_i: Considering the *backward-advection* operator $e^{tA^{(t)}}$ it would be necessary to evaluate it multiple times over the integration interval $[0, \tau]$. This could pose a problem algorithmically as — in general — it appears to be a highly iterative process. Further, in case of $A^{(t)}$ depending on ψ, *i.e.*, nonlinear advection, shocks can form during forward integration, thus backward integration from $t > 0$ to 0 may be *non-unique*. There are, however, two points, $t_0 = 0$ and $t_1 = \tau$, at which this issue can be bypassed. At $t = 0$ the backward operator trivially becomes the identity operator, $e^{A^{(0)} \cdot 0} = \mathrm{id}$, and at $t = \tau$, $e^{\tau A^{(\tau)}}$ cancels with $e^{-\tau A^{(\tau)}}$, the forward advection operator in eq. (4.13).[4] Conveniently, together with the weights $w_0 = \frac{1}{2} = w_1$ this schemes turns into the *trapezoidal rule*

$$\int_0^{\tau} f(t)\,dt = \frac{\tau}{2}\left(f(0) + f(\tau)\right) + O\!\left(\tau^3\right) \tag{4.16}$$

which provides global second-order-in-time integration while being unconditionally stable (Süli and Mayers 2003) for linear ODE problems. Additional complexity arises, however, with an implicit solution step, *i.e.*, in general, a non-linear iteration. This procedure is well known in literature and provides additional energy conservation properties (Nandy and Jog 2014; Smolarkiewicz, Kühnlein, and Wedi 2014).

Summing up this discussion, eq. (4.13) is approximated by

$$\psi(\tau) = e^{-\tau A^{(\tau)}}\left(\psi(0) + \frac{\tau}{2}R(0)\right) + \frac{\tau}{2}R(\tau) + O\!\left(\tau^3\right) \,. \tag{4.17}$$

---

[4]We may note, however, that $e^{-\tau A^{(\tau)}}$ itself must be well-posed as well. It is therefore, without further proof, reasonable to assume that the above construction is well-posed only for limit time step sizes τ. Since the Courant-Friedrichs-Lewy (CFL) condition for the advection scheme needs to satisfied anyway, from a practical point of view we see no further restriction arising from that.

We are left with finding a suitable approximation of $e^{-\tau A^{(\tau)}}$ which itself requires time integration (cf. eq. (4.9)) along the trajectories $(\psi(t), t)$ of the solution. Following the *mean value theorem*, there exists a pair (ψ_m, t_m) such that

$$\int_0^\tau \mathcal{A}(\psi(t), t) \, dt = \mathcal{A}(\psi_m, t_m)\tau \tag{4.18}$$

is exactly satisfied, given that the map $(\psi, t) \mapsto \mathcal{A}(\psi(t), t)$ is sufficiently regular. By construction (cf. eq. (4.9)) we have $\mathcal{A}(\psi_m, t_m) \equiv A^{(\tau)}$. Approximating $A^{(\tau)}$ by $\mathcal{A}(\psi(\tau/2), \tau/2)$, *i.e.*, at the *midpoint* of the integration interval, introduces an error of $O(\tau^2)$, *i.e.*, leads to the approximation

$$\begin{aligned} e^{-\tau A^{(\tau)}}\psi &= e^{-\tau\left(\mathcal{A}(\psi(\tau/2), \tau/2) + O(\tau^2)\right)}\psi \\ &= \sum_{n=0}^\infty \frac{\left(-\tau\mathcal{A}(\psi(\tau/2), \tau/2) + O(\tau^3)\right)^n}{n!}\psi \\ &= e^{\tau\mathcal{A}(\psi(\tau/2), \tau/2)}\psi + O(\tau^3) \,, \end{aligned} \tag{4.19}$$

where the second line uses the definition of the operator exponential. $e^{-\tau\mathcal{A}(\psi(\tau/2), \tau/2)}$ is constant over the integration interval, *i.e.*, is independent of $(\psi(t), t)$, hence the integration of the advection term is approximated by a linear operator.

For approximating $\psi(\tau/2)$, there are several possible choices, among them the two-step linear extrapolation of the advection velocities as outlined in Smolarkiewicz (2006), or computing a first-order (explicit) *predictor* as proposed by Benacchio and Klein (2019). In the further course we will adopt and outline the latter.

The derivation of eq. (4.19) has shown, that we are free to approximate $\psi(\tau/2)$ with an error of $O(\tau^2)$ in the evaluation of $\mathcal{A}(\psi(\tau/2), \tau/2)$ to maintain an overall error of $O(\tau^3)$. With

$$\psi(\tau/2) = e^{-\mathcal{A}(\psi(0), 0)\tau}\left(\psi(0) + \frac{\tau}{2}R(0)\right) + O(\tau^2) \tag{4.20}$$

we can define an explicit *predictor* to $\psi(\tau/2)$, sufficient for the above condition. This choice, computing the midpoint value explicitly from values available at time $t = 0$, renders the overall integration scheme for the advection into the *explicit midpoint rule*. Technically, it is possible to make different approximations to $\psi(\tau/2)$, *e.g.*, using an *implicit Euler step* for the predictor instead (turning the overall integration scheme into the implicit midpoint rule). In summary, we have

$$e^{-\tau A^{(\tau)}} = e^{-\mathcal{A}(\psi^*, \tau/2)\tau} + O(\tau^3) \tag{4.21}$$

with the predictor

$$\psi^* = e^{-\mathcal{A}(\psi(0), 0)\tau}\left(\psi(0) + \frac{\tau}{2}R(0)\right) \tag{4.22}$$

It is worth mentioning that so far, there was no *operator splitting* involved in deriving the prototype solution of eq. (4.17). Independent integration of the sources R and the advection operator $\mathcal{A}$ is the result of solving an inhomogeneous ODE by varying the

constants of the homogeneous solution. An integration scheme emerges that is second-order accurate in time. In fact, if this equation was solved by integrating the individual terms via operator splitting, Strang (1968) splitting would have been necessary to achieve second-order in time with each integration stage being (at least) second-order-in-time. Here, however, the integration of the source term R is conducted via an explicit and an implicit step, each being first-order-in-time, yet leading to a second-order scheme. This corroborates the verbal statement of Benacchio and Klein (2019, sec. 3.b.2, last paragraph) and give a slightly different perspective to Smolarkiewicz and Margolin (1993).

4.3. Coupled Integration of the Leading-Order Asymptotic Equations

In the previous section we discussed how we can approach How we can approach the approximate integration of the prototype formula eq. (4.17). Now we want to apply these found results to eqs. (4.1) for each individual equation. In general, $\hat{H}$ changes over $[0, \tau]$ through its dependency on u. To this end, and thus complying with the formal time integration scheme as outlined in the previous section, we evaluate $\hat{H}$ at the starting point and at the end of the time interval and represent it with the symbols $\hat{H}^n$ and $\hat{H}^{n+1}$.

The semi-discrete form of eqs. (4.1) following eq. (4.17) reads:

$$u^{n+1} = e^{-\mathcal{A}_u \Delta t} \left(u^n - \frac{\Delta t}{2} u_{r,0}^n \left(\frac{u^n}{r} + f_0 \right) \right) -$$
$$- \frac{\Delta t}{2} u_{r,0}^{n+1} \left(\frac{u^{n+1}}{r} + f_0 \right) \tag{4.23a}$$

$$\left(1 + \frac{\iota \Delta t}{2} \hat{H}^{n+1} \right) X^{n+1} = e^{-\mathcal{A}_X \Delta t} \left(\left(1 - \frac{\iota \Delta t}{2} \hat{H}^n \right) X^n + \frac{\Delta t}{2} \left(Q^n + u_s^n \right) \right) +$$
$$+ \frac{\Delta t}{2} \left(Q^{n+1} + u_s^{n+1} \right) \tag{4.23b}$$

$\mathcal{A}_X$ and $\mathcal{A}_u$ represent the one- and two-dimensional advection terms acting on X and u in eqs. (4.1). This formulation involves expressions on both time level, t^n and t^{n+1}. It is important to keep in mind that the expressions $u_{r,0}^{n+1}$ and Q^{n+1} depend on the solution state (u^{n+1}, X^{n+1}) at time level t^{n+1}. By appropriately arranging the evaluation of sub-expressions advancing the solution (X, u) from t^n to t^{n+1} can be accomplished by the following steps:

Explicit step

$$u^* = u^n - \frac{\Delta t}{2} u_{r,0}^n \left(\frac{u^n}{r} + f_0 \right) \tag{4.24a}$$

$$X^* = \left(1 - \frac{\iota \Delta t}{2} \hat{H}^n \right) X^n + \frac{\Delta t}{2} \left(Q^n + u_s^n \right) \tag{4.24b}$$

Advective step

$$u^{**} = e^{-\mathcal{A}_u \Delta t} u^* \tag{4.25a}$$

$$X^{**} = e^{-\mathcal{A}_X \Delta t} X^* \tag{4.25b}$$

Implicit step To complete the time step the implicit part requires solving for the fixed-point induced through the dependency of Q^{n+1} and $u_{r,0}^{n+1}$ on the solution at final time (X^{n+1}, u^{n+1}). The iterative scheme takes the form

$$u^{n+1,\nu+1} = \frac{u^{**} r - \frac{1}{2} \Delta t u_{r,0}^{n+1,\nu} f_0 r}{r + \frac{1}{2} \Delta t u_{r,0}^{n+1,\nu}} \tag{4.26a}$$

$$\left(1 + \frac{\iota \Delta t}{2} \hat{H}^{n+1,\nu+1}\right) X^{n+1,\nu+1} = X^{**} + \frac{\Delta t}{2}(Q^{n+1,\nu} + u_s^{n+1}) \tag{4.26b}$$

with $\nu = 0, 1, \ldots$ and initial guesses $(X^{n+1,0}, u^{n+1,0}) = (X^{**}, u^{**})$. Each iteration cycle requires the solution of the linear problem for X^{n+1}. The iteration will be terminated once a prescribed accuracy goal is satisfied, *i.e.*, once the increments between $(X^{n+1,\nu+1}, u^{n+1,\nu+1})$ and $(X^{n+1,\nu}, u^{n+1,\nu})$ reaches a targeted precision goal, usually an l_∞ error of 10^{-13}. Note that depending on the order of solving eqs. (4.26a) and (4.26b) the iteration $u^{n+1,\nu+1}$ can be inserted in the equation for $X^{n+1,\nu+1}$ or vice versa. This may speed up convergence.

We shall mention that eqs. (4.26) pose generic non-linear optimization problems for which a vast number of black-box solvers are available. The software environments of NumPy (Harris et al. 2020) and SciPy (Virtanen et al. 2020) provide various solvers that can be used instead of the fixed-point iteration as suggested. Tests have shown, that benefits in terms of computational efficiency are apparent only for problem sizes (*i.e.* resolutions) beyond what is reasonable for our purposes. Hence, we make use of the iterations as suggested above.

4.4. Spatial Discretization of Hamiltonian and Source Terms

This section is dedicated to highlighting details of the spatial discretization. First, we recapture the derivation of the terms $\hat{H}X$ and iQ in eq. (4.1a) and realize that with eqs. (3.33) and (3.34) the following expression holds:

$$\hat{H}X = -\alpha \log(\varepsilon)\hat{M}X - L[\hat{\mathcal{H}} + \hat{\tilde{\mathcal{I}}} + \hat{\mathcal{J}}]X, \tag{4.27}$$

where $\hat{\tilde{\mathcal{I}}}$ originates from eq. (3.23c) and subtracting the non-integrable term that causes the logarithmic divergence (cf. eq. (3.25)) when passing the upper bound of the improper integral to the limit $r \to \infty$.

L is an integral operator in r on the domain $[0, \infty)$. This operator needs to be approximated in a numerical implementation by truncating the integration interval to $[0, r_\infty)$ with $r_\infty < \infty$. To this end, we define

$$\tilde{L}[\mathcal{K}] := \frac{\pi}{\Gamma} \int_0^{r_\infty} r\mathcal{K}(r) \, dr \tag{4.28}$$

and realize that

$$L[\hat{\mathcal{H}} + \hat{\hat{\mathcal{I}}} + \hat{\mathcal{J}}]X = \tilde{L}[\hat{\mathcal{H}} + \hat{\mathcal{I}} + \hat{\mathcal{J}}]X + 2\alpha \log(r_\infty)\hat{M}X + o(1) \quad \text{as} \quad r_\infty \to \infty. \quad (4.29)$$

Note, that the original operator L evaluates $\hat{\hat{\mathcal{I}}}X$, while the truncated operator $\tilde{L}$ uses $\hat{\mathcal{I}}$. This behavior arises from integrating $(\hat{\mathcal{H}} + \hat{\hat{\mathcal{I}}} + \hat{\mathcal{J}})X$ to a large but finite radius r_∞, where all integrated terms are sufficiently converged except the logarithmically decaying one[5], which is compensated for by the $\log(r_\infty)$-term in the above equation.

Additionally, we have $iQ(w_{\text{ad}}) = -L[\hat{\mathcal{H}} + \hat{\mathcal{I}} + \hat{\mathcal{J}}]X$, at least formally (cf. eqs. (3.33) and (3.34)), and together with eq. (4.29) we conclude that it is sufficient to discretize Q and $\hat{M}$. $\hat{\mathcal{H}}$ then is a superposition.

Starting with $w_{1,\text{ad}}$ requiring $\partial_z X$ we discretize[6]

$$\left.\frac{\partial X}{\partial z}\right|_{i+1/2} = \frac{1}{\Delta z}\left(X_{i+1} - X_i\right), \quad (4.30)$$

where integer indexes i stand for *cell-centered* grid points z_i and half-integer indexes for *face-centered grid points* $z_{i+1/2} = z_i + \Delta z/2$ in one dimension. Together with[7]

$$W_{(i+1/2,j+1/2)} = \frac{1}{2}\left(W_{(i,j+1/2)} + W_{(i+1,j+1/2)}\right), \quad (4.31)$$

W is defined through eqs. (3.19), we obtain

$$w_{1,\text{ad},(i+1/2,j+1/2)} = -\imath W_{(i+1/2,j+1/2)}\left.\frac{\partial X}{\partial z}\right|_{i+1/2}. \quad (4.32)$$

Hence, both, w and W, are stored on *nodal grid points*, *i.e.*, at points $(z_{i+1/2}, r_{j+1/2})$. Note that eq. (4.30) and eq. (4.31) represent the typical approach of converting cell-centered quantities to face-centered ones, either by computing the derivate or averaging.

With these discretizations at hand we can continue and straight-forwardly give expressions for the terms $\mathcal{H}$, $\mathcal{I}$, and $\mathcal{J}$ as defined through eq. (3.33).

$$\mathcal{H}_{i,j} = \frac{1}{\Delta r}\left(r_{j+1/2}w_{1,(i,j+1/2)}\left.\frac{\partial u}{\partial z}\right|_{i,j+1/2} - r_{j-1/2}w_{1,(i,j-1/2)}\left.\frac{\partial u}{\partial z}\right|_{i,j-1/2}\right) \quad (4.33)$$

$$R_{1,(i,j)} = \frac{1}{\Delta z}\frac{1}{\rho_{0,(i)}}\left(\rho_{0,(i+1/2)}w_{1,(i+1/2,j)} - \rho_{0,(i-1/2)}w_{1,(i-1/2,j)}\right) \quad (4.34)$$

$$\mathcal{I}_{i,j} = r_i\left(\zeta_{i,j} + f_0\right)R_{1,(i,j)} \quad (4.35)$$

For the next expressions a discretized integral operator needs to be defined. For the sake of generality, we define it as one-dimensional operator that applies to the desired coordinate direction for which we introduce the placeholder variable x. By employing the trapezoidal rule with extrapolated boundary conditions at $x = 0$, we get

$$\int_0^{x_i} g(x)\,dx \approx \mathbb{I}^x[g]_i := \Delta x\left(\sum_{k \le i} g_k - \frac{1}{2}g_i + \frac{1}{4}(g_0 - g_1)\right) \quad (4.36)$$

---

[5] For a detailed discussion on the limiting properties of the terms $L[\hat{\mathcal{H}}]X$, $L[\hat{\mathcal{I}}]X$, $L[\hat{\mathcal{J}}]X$, see Päschke et al. (2012, Appendix E).

[6] Mainly focusing on the spatial discretization we omit time indexes.

[7] Spatial indexes are put into parenthesis, where necessary, for disambiguation.

With this discrete formulation we achieve second-order-in-space integration of values at cell centers. The expression ϕ_1, needed for $\mathcal{J}$, is computed by

$$\phi_{1,i,j} = -r_j i_{i,j} \tag{4.37}$$

$$i_{i,j} = -\mathbb{I}^r \left[\frac{i_2}{r^3}\right]_{i,j} + \mathbb{I}^r \left[\frac{i_2}{r^3}\right]_{i,j_N} \tag{4.38}$$

where i_2

$$i_{2,(i,j)} = \mathbb{I}^r \left[r^2 R_1\right]_{i,j} \tag{4.39}$$

Instabilities potentially arising from dividing by small radii in eq. (4.38) are coped with by catching the divisor r^3 at small radii and setting the cell values to zero. This is legitimate due to the small-r limit of i_2 (cf. eq. (4.39)). With these ingredients we can find an approximation to $\mathcal{J}$ by

$$\mathcal{J}_{i,j} = r_j \left.\frac{\partial \zeta}{\partial r}\right|_{i,j} \left.\frac{\partial \phi_1}{\partial r}\right|_{i,j} \tag{4.40}$$

As an exception both, $\partial_r \zeta|_{i,j}$ and $\partial_r \phi_1|_{i,j}$, are discretized by a central second-order stencil:

$$\left.\frac{\partial \phi_1}{\partial r}\right|_{i,j} = \frac{1}{2\Delta r} \left(\phi_{1,(i,j+1)} - \phi_{1,(i,j-1)}\right) \tag{4.41}$$

$$\left.\frac{\partial \zeta}{\partial r}\right|_{i,j} = \frac{1}{2\Delta r} \left(\zeta_{i,j+1} - \zeta_{i,j-1}\right) \tag{4.42}$$

Altogether, Q then is computed as

$$Q_i = \frac{\pi}{\Gamma_i} \mathbb{I}^r_{\text{def}} \left[r(\mathcal{H} + \mathcal{I} + \mathcal{J})\right]_i \tag{4.43}$$

with the discrete approximation of the definite integral

$$\int\limits_0^\infty g(x)\,dx \approx \mathbb{I}^x_{\text{def}}[g] := \Delta x \sum_{k=0}^N g_k + \frac{\Delta x}{4}(g_0 + g_N) - \frac{\Delta x}{4}(g_1 + g_{N-1}) \tag{4.44}$$

and the circulation

$$\Gamma_i = 2\pi u_{i,j_N} r_{j_N}\,. \tag{4.45}$$

The remaining expression for $\hat{M}_1 X$ is given by

$$\left.\hat{M}X\right|_i = \frac{f_0^2}{4\pi \Gamma_i \rho_{0,(i)}} \frac{1}{\Delta z} \left(\gamma_{i+1/2} \left.\frac{\partial X}{\partial z}\right|_{i+1/2} - \gamma_{i-1/2} \left.\frac{\partial X}{\partial z}\right|_{i-1/2}\right) \tag{4.46}$$

with $\gamma_{i+1/2}$ a shorthand notation for

$$\gamma_{i+1/2} = \frac{1}{2} \left(\frac{\rho_{0,(i)}(\Gamma_i)^2}{\Theta'_{1,(i)}} + \frac{\rho_{0,(i+1)}(\Gamma_{i+1})^2}{\Theta'_{1,(i+1)}}\right). \tag{4.47}$$

4.5. Methods for the Quasi-Linear Advection Equation

In section 4.1 we found the linear advection equation eq. (4.8) to be the homogeneous equation to the general problem eq. (4.7) (and eq. (4.2), respectively). This circumstance is taken care of in section 4.2 in the time-discrete equation (4.23) by the *advection step* eq. (4.25) entering between the explicit and implicit integration of the source terms.

The integral operator $e^{-A^{(\Delta t)}\Delta t}$ needs to be approximated by a suitable numerical scheme. In case of the centerline equation (eq. (4.1a)) $\mathcal{A}_X$ forms a one-dimensional derivative operator,

$$\mathcal{A}_X X := A\frac{\partial X}{\partial z} \tag{4.48}$$

while for the time evolution of the tangential velocity u (eq. (4.1b)) the advection operator $\mathcal{A}_u$ becomes the two-dimensional directional derivative,

$$\mathcal{A}_u u := u_{r,00}\frac{\partial u}{\partial r} + w_0\frac{\partial u}{\partial z} =: \mathcal{A}_{u,r}u + \mathcal{A}_{u,z}u\,, \tag{4.49}$$

i.e., a combination of two one-dimensional advection operators acting on u.

Formally, the exact solution is given by eq. (4.9). For a numerical approximation $e^{-\tau A^{(\tau)}}$ needs to be discretized with a suitable numerical method. To comply with the second-order accuracy of the time discretization of the source terms, as presented in section 4.2, a candidate advection scheme should also be second-order in space and time.

Despite the plethora of methods available in literature, we will make use of the scheme outlined in (Benacchio and Klein 2019) comprising the combination of a robust one-dimensional advection scheme based on finite-volume shock-capturing techniques and Strang splitting (Strang 1968). However, there are other possible methods that can be used seamlessly instead (Dumbser and Munz 2005; Jiang and Shu 1996; Smolarkiewicz and Margolin 1993, 1998, to name just a few).

4.5.1. Strang Splitting

We deduced the initial problem (4.1b) to involve the solution of the equation

$$\frac{du}{dt} + \mathcal{A}_r u + \mathcal{A}_z u = 0\,, \tag{4.50}$$

which formally takes the exact solution

$$u(\tau) = e^{-(\mathcal{A}_r + \mathcal{A}_z)\tau}u(0)\,. \tag{4.51}$$

Following the approach of Strang (1968), solutions to this problem can be approximated by

$$u(\tau) = e^{-\frac{1}{2}\mathcal{A}_r\tau}e^{-\mathcal{A}_z\tau}e^{-\frac{1}{2}\mathcal{A}_r\tau}u(0) + O\left(\tau^3\right)\,, \tag{4.52a}$$

$$= e^{-\frac{1}{2}\mathcal{A}_z\tau}e^{-\mathcal{A}_r\tau}e^{-\frac{1}{2}\mathcal{A}_z\tau}u(0) + O\left(\tau^3\right)\,, \tag{4.52b}$$

i.e., by the successive integration of one-dimensional advection problems. In the actual implementation we alternate between eq. (4.52a) and eq. (4.52b) per time step.

4.5.2. One-Dimensional Advection

Solving the advection problem eq. (4.25) as part of the coupled integration of eqs. (4.1) is crucial to the overall stability and accuracy of the solution. As standard problem throughout the literature of hyperbolic PDEs (LeVeque 1992) we pose the prototype problem of one-dimensional advection with variable velocity as

$$\frac{\partial \psi}{\partial t}(x, t) + v(x, t) \frac{\partial \psi}{\partial x}(x, t) = 0 \tag{4.53}$$

with the solution defined as a map

$$\begin{aligned} \psi : \quad & \Omega \times \mathbb{R}_+ \to \mathbb{K} \\ & (x, t) \mapsto \psi(x, t) \end{aligned} \tag{4.54}$$

and initial and boundary conditions $\psi(x, 0) = \psi_0(x)$ and $\psi(x, t)|_{\partial\Omega} = g(x, t)$, respectively.

In literature, there is a plethora of schemes to solve equations of the type eq. (4.53), all with their own advantages and obstacles (consult LeVeque 1992; Tadmor 2012, among others for review). Among them, finite volume methods allow us to control integral balances of conserved quantities exactly, which is beneficial for both, accuracy and stability. In the following, we will adopt the notation and key ideas of the finite volume scheme presented by Benacchio and Klein (2019) and Smolarkiewicz, Kühnlein, and Wedi (2014) and show some modification to suit the problem presented here.

To this end, we will not solve eq. (4.53) directly, but first derive an equivalent conserved equation. Assume a strictly positive density-like quantity ρ following the continuity equation

$$\frac{\partial \rho}{\partial t}(x, t) + \frac{\partial \rho v}{\partial x}(x, t) = 0 \,. \tag{4.55}$$

Then for every quantity ψ obeying the advection equation (4.53) there is a conserved quantity $\rho\psi$ that satisfies the conservation law

$$\frac{\partial \rho \psi}{\partial t}(x, t) + \frac{\partial \rho v \psi}{\partial x}(x, t) = 0 \,. \tag{4.56}$$

By simultaneously solving eqs. (4.55) and (4.56) it is possible to solve eq. (4.53) by controlling a conserved quantity.

Defining the space-time grid cell $c_i^{n+1/2} = [x_{i-1/2}, x_{i+1/2}] \times [t^n, t^{n+1}]$ and introducing the notation $\psi_i^n \equiv \psi(x_i, t^n)$, a second-order discretization of the time derivative at the midpoint $(x_i, t^{n+1/2})$ of $c_i^{n+1/2}$ is given by

$$\left.\frac{\partial \rho \psi}{\partial t}\right|_i^{n+1/2} = \frac{1}{\Delta t}\left((\rho\psi)_i^{n+1} - (\rho\psi)_i^n \right) + O\left(\Delta t^2\right) \tag{4.57}$$

and the spatial discretization by

$$\left.\frac{\partial \rho v \psi}{\partial x}\right|_i^{n+1/2} = \frac{1}{\Delta x}\left((\rho v \psi)_{i+1/2}^{n+1/2} - (\rho v \psi)_{i-1/2}^{n+1/2} \right) + O\left(\Delta x^2\right) \,. \tag{4.58}$$
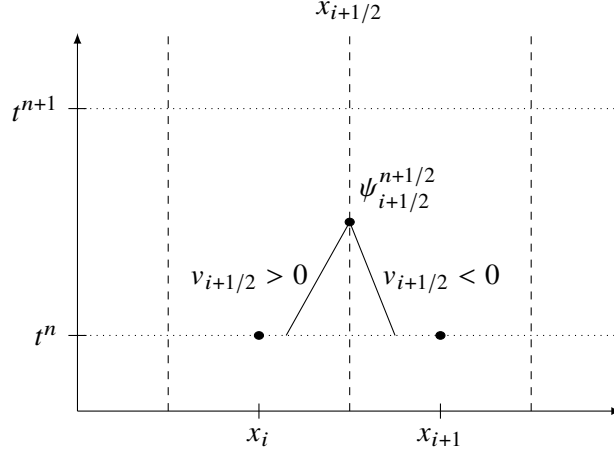
Figure 4.1.: Reconstruction of face values $\psi_{i+1/2}^{n+1/2}$.

We end up with the discrete formula

$$\psi_i^{n+1} = \frac{1}{\rho_i^{n+1}}\left((\rho\psi)_i^n + \frac{\Delta t}{\Delta x}\left((\rho v\psi)_{i-1/2}^{n+1/2} - (\rho v\psi)_{i+1/2}^{n+1/2}\right)\right) + O\left(\Delta t^3 + \Delta t \Delta x^2\right) . \quad (4.59)$$

Hence, we need to find an approximation of $(\rho v \psi)_{i+1/2}^{n+1/2}$ at the cell-face at half-time level.

Assuming for a moment $v(x,t)$ and $\rho(x,t)$ to be given functions up to first-order accuracy, we can treat the value $(\rho v)_{i+1/2}^{n+1/2}$ as given and the problem reduces to approximating $\psi_{i+1/2}^{n+1/2}$. Taylor series expansion of ψ at the point (x_i, t_n) gives

$$\begin{aligned}
\psi_{i+1/2}^{n+1/2} &= \psi_i^n + \frac{\Delta x}{2}\left.\frac{\partial\psi}{\partial x}\right|_i^n + \frac{\Delta t}{2}\left.\frac{\partial\psi}{\partial t}\right|_i^n + O\left((\Delta x + \Delta t)^2\right) \\
&= \psi_i^n + \frac{\Delta x}{2}\left.\frac{\partial\psi}{\partial x}\right|_i^n - \frac{\Delta t}{2}\left.\left(v\frac{\partial\psi}{\partial x}\right)\right|_i^n + O\left((\Delta x + \Delta t)^2\right) \\
&= \psi_i^n + \frac{\Delta x}{2}\left.\frac{\partial\psi}{\partial x}\right|_i^n\left(1 - \frac{\Delta t}{\Delta x}v_i^n\right) + O\left((\Delta x + \Delta t)^2\right) , \quad\quad (4.60a)
\end{aligned}$$

where we used eq. (4.53) to replace $\partial_t\psi$. Similarly, we can expand around (x_{i+1}, t^n) and find

$$\psi_{i+1/2}^{n+1/2} = \psi_{i+1}^n - \frac{\Delta x}{2}\left.\frac{\partial\psi}{\partial x}\right|_{i+1}^n\left(1 + \frac{\Delta t}{\Delta x}v_{i+1}^n\right) + O\left((\Delta x + \Delta t)^2\right) \quad\quad (4.60b)$$

From classical numerical analysis of hyperbolic PDEs (LeVeque 1992) we know that schemes solving the advection equation are unstable if the reconstruction is accomplished *downwind*. It is necessary to account for the information of the previous solution state in *upwind* direction (where the information is advected from). Therefore, depending on the sign of $v_{i+1/2}^{n+1/2}$ we either choose eq. (4.60a) or eq. (4.60b) for reconstructing $\psi_{i+1/2}^{n+1/2}$. The remaining issue is to approximate $\partial_x\psi|_i^n$.
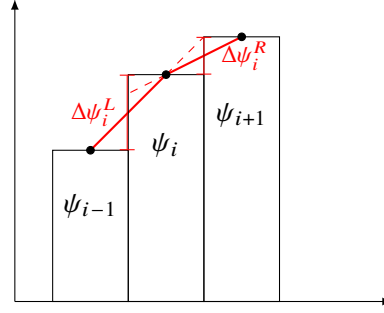
Figure 4.2.: Slope limiting.

A slightly different interpretation of eqs. (4.60) may be given by fig. 4.1. Depending on the sign of $v_{i+1/2}^{n+1/2}$ the advected quantity $\psi_{i+1/2}^{n+1/2}$ must originate from a position x_0 located either in the left or right neighboring cell:

$$x_{i+1/2}^0 = x_{i+1/2} - v_{i+1/2}^{n+1/2} \frac{\Delta t}{2} + O\left(\Delta t^2\right) \tag{4.61}$$

Advection interpreted as transport of ψ means that the half-time level face value $\psi_{i+1/2}^{n+1/2}$ is equal to this original value $\psi(x_{i+1/2}^0)$ which needs to be reconstructed *at time level t^n* (adding a slightly different flavor to the previous interpretation of a two-dimensional Taylor-series expansion). However, for the right-travelling wave we can approximate

$$
\begin{aligned}
\psi(x_{i+1/2}^0) &= \psi_i^n + \left.\frac{\partial \psi}{\partial x}\right|_i^n (x_{i+1/2}^0 - x_i) + O\left(\left(x_{i+1/2}^0 - x_i\right)^2\right) \\
&= \psi_i^n + \left.\frac{\partial \psi}{\partial x}\right|_i^n \frac{\Delta x}{2}\left(1 - \frac{\Delta t}{\Delta x} v_{i+1/2}^{n+1/2}\right) + O\left((\Delta x + \Delta t)^2\right) \tag{4.62}
\end{aligned}
$$

This matches the result for the left-sided reconstruction found in eq. (4.60a) except for the fact that v is evaluated at time $t^{n+1/2}$. Since $v^{n+1/2} = v^n + O(\Delta t)$, the difference of the two expression is submerged into the leading-order error term, thus the two expressions (4.60a) and (4.62) are equivalent in terms of the leading-order error, but the latter turns out to be numerically more stable.[8] With the same procedure we can find the right-sided reconstruction eq. (4.60b). This line of arguments shall strengthen the need for an *upwind* reconstruction of $\psi_{i+1/2}^{n+1/2}$.

The slope $\partial_x \psi|_i^n$ remains to be determined. Again we follow standard procedures of numerical analysis for hyperbolic PDEs and first find estimates of the slope by interpolating linearly between the local cell value and its left and right adjacent values, see fig. 4.2. To this end we define the left and right slopes

$$\Delta \psi_i^L := \psi_i - \psi_{i-1}, \quad \Delta \psi_i^R := \psi_{i+1} - \psi_i. \tag{4.63}$$

---

[8]The situation is similar to comparing the implicit and explicit midpoint rule. In the numerical implementation, $v_{i+1/2}^{n+1/2}$ is approximated by an explicit predictor step that estimated the face-centered mid-time-level advection velocities with first-order accuracy.
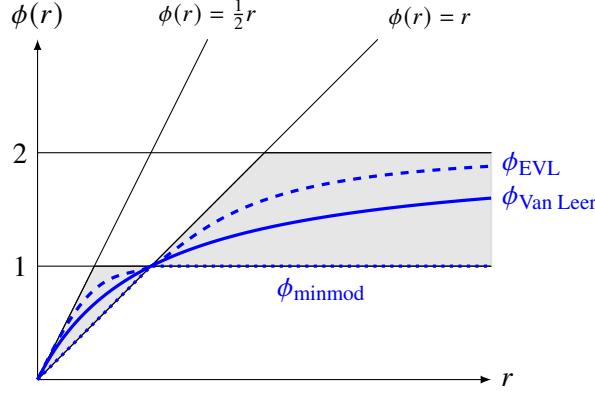
Figure 4.3.: Slope limiter functions. The second-order TVD area is shown in gray. Examples of slope limiter functions are given in blue.

Slope Limiting

The total variation diminishing (TVD) constraint

$$TV^{n+1} \leq TV^n \quad \text{with} \quad TV^n := \sum_i |\psi_i^n - \psi_{i+1}^n| \tag{4.64}$$

for stability of one-dimensional schemes for the linear advection equation (LeVeque 1992) requires the reconstruction of ψ within the cell by a local (linear) interpolant not to exceed (over- or undershoot) the neighboring values.

This problem is typically overcome by *slope limiting* which, given left-sided and right-sided slopes, sets the inter-cell slope $\Delta\psi_i = \psi_{i+1/2} - \psi_{i-1/2}$ to

$$\Delta\psi_i = \text{sign}(\Delta\psi_i^L)\text{Lim}(\Delta\psi_i^L, \Delta\psi_i^R) . \tag{4.65}$$

With this notation the TVD condition is expressed as

$$|\psi_{i+1} - \psi_i| = |\Delta\psi_i^R| \geq \frac{1}{2}\text{Lim}(\Delta\psi_i^L, \Delta\psi_i^R) \tag{4.66a}$$

$$|\psi_i - \psi_{i-1}| = |\Delta\psi_i^L| \geq \frac{1}{2}\text{Lim}(\Delta\psi_i^L, \Delta\psi_i^R) \tag{4.66b}$$

Defining the *slope ratio*[9]

$$r_i := \frac{\psi_{i+1} - \psi_i}{\psi_i - \psi_{i-1}} \tag{4.67}$$

we can introduce the *limiter function* ϕ_L, such that

$$\text{Lim}(\Delta\psi_i^L, \Delta\psi_i^R) = \phi(r_i)\Delta\psi_i^L . \tag{4.68}$$

For symmetry reasons it must follow

$$\text{Lim}(\Delta\psi_i^L, \Delta\psi_i^R) = \phi\left(\frac{1}{r_i}\right)\Delta\psi_i^R , \tag{4.69}$$

---

[9]Definitions in literature may vary in that the definition of r_i is inverse to that of eq. (4.67).

i.e.,

$$\phi\left(\frac{1}{r}\right) = \frac{1}{r}\phi(r) \, . \tag{4.70}$$

Together with eq. (4.66) the TVD region of $\phi(r)$ is limited by

$$\phi(r) \leq \frac{r}{2} \quad \text{and} \quad \phi(r) \leq 2 \, , \tag{4.71}$$

and in case $\Delta\psi_i^L = \Delta\psi_i^R$, *i.e.*, $r_i = 1$, $\text{Lim}(\Delta\phi_i^L, \Delta\psi_i^R) = \Delta\psi_i^L = \Delta\psi_i^R$, hence it must be $\phi(1) = 1$.

To gain deeper insight, we want to analyze the example of the first-order upwind scheme:

$$\psi_i^{n+1} = \psi_i^n + v_i^n \frac{\Delta t}{\Delta x} \left(\psi_{i-1}^n - \psi_i^n\right) \, . \tag{4.72}$$

In our framework this is equivalent to neglecting the local slope and setting $\psi_{i+1/2}^{n+1/2} = \psi_i^n$, thus, $\phi(r) = 0$ will yield the first-order upwind scheme. The question arises, if there are any other at least second-order methods fitting into this framework. By setting $\phi(r) = r$ we get

$$\psi_{i+1/2}^{n+1/2,\text{LW}} = \frac{1}{2}\left(1 - \frac{\Delta t}{\Delta x}v_n^i\right)\Delta\psi_i^L \tag{4.73}$$

Inserted into eq. (4.59) and setting $v = \text{const} = \rho$ gives

$$\psi_i^{n+1,\text{LW}} = \psi_i^n + \frac{v}{2}\frac{\Delta t}{\Delta x}\left(\psi_{i-1}^n - \psi_{i+1}^n\right) - \frac{v^2}{2}\frac{\Delta t^2}{\Delta x^2}\left(\psi_{i-1}^n - 2\psi_i^n + \psi_{i+1}^n\right) \, , \tag{4.74}$$

which is the second-order *Lax-Wendroff* scheme for the advection equation for $v > 0$ (LeVeque 1992). Similarly, by setting $\phi(r) = 1$ we get

$$\psi_i^{n+1,\text{BW}} = \psi_i^n + \frac{v}{2}\frac{\Delta t}{\Delta x}\left(-\psi_{i-2}^n + 4\psi_{i-1}^n - 3\psi_i^n\right) - \frac{v^2}{2}\frac{\Delta t^2}{\Delta x^2}\left(\psi_{i-2}^n - 2\psi_{i-1}^n + \psi_i^n\right) \, , \tag{4.75}$$

i.e., the scheme of Beam and Warming (1976) for $v > 0$.

Sweby (1984) concluded that weighted averages of both schemes again give a second-order scheme, one being *Fromm's* scheme.[10] However, we summarize our discussion with the comment that a second-order TVD scheme needs to satisfy the requirements

- $\phi(r) = \min(2r, 2)$

- $\min(r, 1) \leq \phi(r) \leq \max(r, 1)$

This matches with the shaded region of fig. 4.2. In literature, there is a plethora of choices for slope limiters, among them the *minmod* limiter,

$$\phi_{\text{minmod}}(r) = \max(0, \min(r, 1)) \, , \tag{4.76}$$

and the extended version of *Van Leer*'s limiter (Klein 2009):

$$\phi_{\text{EVL}}(r) = \frac{2r}{1+r}\begin{cases}\Xi(\min(r, 1/r)) \, , & r > 0 \\ 0 \, , & \text{else}\end{cases} \tag{4.77}$$

with

$$\Xi(r) = 1 + r(1 - r)(1 - r^k) \tag{4.78}$$

With $k = 0$ we obtain the classical formulation of Van Leer (1974).

---

[10] Due to the inverse definition $\tilde{r}_i = \frac{\Delta\phi_i^L}{\Delta\phi_i^R}$ of Sweby (1984) the identification of the schemes of Lax-Wendroff and Beam-Warming are interchanged.

Compressible Advection

So far, we assumed $\rho(x, t)$ and $v(x, t)$ to be given functions. The integration step eq. (4.59) is constructed to require $(\rho v)^{n+/1/2}$, ρ^n, and ρ^{n+1}. To this end, in the spirit of Smolarkiewicz, Kühnlein, and Wedi (2014), we write step from t^n to t^{n+1} as

$$\psi^{n+1} = \text{Adv}^{\Delta t}(\psi^n, (\rho v)^{n+1/2}, \rho^n, \rho^{n+1}) + O\left(\Delta t^3\right), \tag{4.79}$$

defining $\text{Adv}^{\Delta t}$ as the transport method to advect ψ for a time step of size Δt with the help of a primordial conservation law eq. (4.55) involving a *guiding density* ρ to be known at initial and final time as well as an approximation of the density fluxes $(\rho v_{i+1/2}^{n+1/2})$ at half-time on the cell faces.

In general, the time evolution of ρ is tied to $v(x, t)$ and therefore cannot assume to be known a priori. Nonetheless, trivially, we can integrate ρ in eq. (4.55) by

$$\rho^{n+1} = \text{Adv}^{\Delta t}(\rho^n, v^{n+1/2}, 1, 1) + O\left(\Delta t^3\right) =: \text{CAdv}^{\Delta t}(\rho^n, v^{n+1/2}) + O\left(\Delta t^3\right) \tag{4.80}$$

as we replace $\psi \to \rho$, $\rho v \to v$, and $\rho \to 1$. The conservative method $\text{CAdv}^{\Delta t}$ solely requires the information of $v_{i+1/2}^{n+1/2}$.

Equation (4.80) poses a method to solve the continuity eq. (4.55). Thus, replacing the conserved quantity ρ^n by $(\rho \psi)^n$ as the first argument of $\text{CAdv}^{\Delta t}$ yields the solution $(\rho \psi)^{n+1}$:

$$(\rho \psi)^{n+1} = \text{CAdv}^{\Delta t}((\rho \psi)^n, v^{n+1/2}) + O\left(\Delta t^3\right) \tag{4.81}$$

Together with the solution ρ^{n+1} we obtain ψ^{n+1}.

This approach has the advantage that, besides the uniform integration of ρ and $(\rho \psi)$, there is no need to reconstruct $v_{i+1/2}^{n+1/2}$ from $(\rho v)_{i+1/2}^{n+1/2}$ (given as the second argument to $\text{Adv}^{\Delta t}$ in eq. (4.79)) as needed during the reconstruction step for $\psi_{i+1/2}^{n+1/2}$ (see eqs. (4.60)) which would require $\rho_{i+1/2}^{n+1/2}$, *i.e.*, a sufficiently accurate approximation of the density at the half-time cell interfaces. So instead of constructing $(\rho v)_{i+1/2}^{n+1/2}$ or reconstructing $v_{i+1/2}^{n+1/2}$, one can also use $\text{CAdv}^{\Delta t}$ to solve the continuity equation (4.56).

During the construction of the advection scheme, we made use of the fact, that advective quantities are constant along flow trajectories. This is no longer true for conserved quantities transported by a divergent velocity field. Solving an advection equation instead of a continuity equation (desired for the reconstruction of $\psi_{i+1/2}^{n+1/2}$) we introduce an error that is due to the integration of the right-hand side of the continuity equation, written convective form:

$$\frac{1}{\rho}\frac{d\rho}{dt} = -\nabla \cdot \boldsymbol{v} \tag{4.82}$$

So takes the result of integrating ρ from t^n to $t^{n+1} = t^n + \Delta t$ along a flow trajectory $x_0(t)$ the form

$$\rho^{n+1}(x_0^{n+1}) = \rho_{\text{adv}}^{n+1}(x_0^{n+1})e^{-\int_{t^n}^{t^{n+1}} \nabla \cdot \boldsymbol{v} \, dt}, \tag{4.83}$$

with $\rho_{\text{adv}}^{n+1}(x_0^{n+1})$ the solution of eq. (4.82) with trivial right-hand side, *i.e.*, the advection equation. The exponential factor accounts for the expansion/compression along the

trajectory. We have $\rho^{n+1}_{\text{adv}}(x^{n+1}_0) = \rho^{n+1}_{\text{adv}}(x^n_0)$, since the solution of the advection equation is constant along flow trajectories.

Assuming a piece-wise linear-in-time velocity field, the above equation renders into

$$\rho^{n+1}(x^{n+1}_0) = \rho^{n+1}_{\text{adv}}(x^n_0)e^{-\nabla \cdot \boldsymbol{v}^{n+1/2} \Delta t} \ . \tag{4.84}$$

In fact, when considering ρ (or $\rho\psi$) alone, every time step introduces an error that is proportional to $1 - e^{-\nabla \cdot \boldsymbol{v}^{n+1/2} \Delta t}$. The fact, however, that we interested in $\psi^{n+1} = \frac{(\rho\psi)^{n+1}}{\rho^{n+1}}$ and that both, $(\rho\psi)$ and ρ, are integrated individually conveniently gives us the desired quantity ψ with the error term $e^{-\nabla \cdot \boldsymbol{v}^{n+1/2} \Delta t}$ canceled by the division. Hence, there is no need for a more complicated interface-time-centered reconstruction of $\boldsymbol{v}^{n+1/2}_{i+1/2}$ by means of $(\rho\boldsymbol{v})^{n+1/2}_{i+1/2}$ and $\rho^{n+1/2}_{i+1/2}$, especially since the latter is to be reconstructed up to first-order itself to maintain the overall order of the numerical scheme.

Note, that the problem to be solved does not necessarily provide *guiding density* variable ρ. However, we can always construct a *virtual* density with arbitrary initial value at the beginning of the time step, *e.g.*, $\rho^n = 1$. In that case, the solution ρ^{n+1} of eq. (4.55) accumulates the divergence of $\boldsymbol{v}^{n+1/2}_{i+1/2}$. Another scenario is that of a density that is governed by a divergence constraint, *e.g.*, the *anelastic constraint*, where ρ_0 is static ($\partial_t \rho_0 \equiv 0$), thus, $\rho_0\psi$ is conserved. Then, if $(\rho_0 v)^{n+1/2}_{i+1/2}$ is discretely divergence-free, $(\rho_0\psi)$ can be integrated by CAdv without the need for separately integrating ρ_0.

As a final remark, we want to emphasize that v itself can be an unknown variable and therefore subject to numerical integration (either by depending on ψ or governed by a PDE). To maintain overall second-order accuracy in space and time, $v^{n+1/2}_{i+1/2}$ must be at least first-order accurate (second-order error term in Δx and Δt). In case of v being transported by v itself (Burgers' equation), the most straightforward way (and the one suggested by Benacchio and Klein (2019)) is to use the method CAdv outlined above in eq. (4.81) to compute a first-order predictor $v^{n+1/2,*}_{i+1/2}$ by approximating the transport velocity $v^{n+1/4}_{i+1/4}$ by $v^n_{i+1/2}$. $v^{n+1/2,*}_{i+1/2}$ then is a first-order predictor to $v^{n+1/2}_{i+1/2}$ sufficient to maintain the desired accuracy.

4.6. Unitary Time Integration of the Schrödinger Equation

In section 4.2 we constructed the time integration scheme which led to the coupled integration scheme presented in section 4.3. A deeper motivational aspect of this construction was the fact that for numerical experiments testing various formulations of diabatic heating and externally imposed shear, the tilt $\partial_z X$ is a crucial quantity. A scheme for those kinds of experiments needs to ensure that both, locally and globally, tilt and henceforth X itself shall not be affected by spurious oscillations as well as non-linearly growing/damping modes. Tilt changes should be attributed to interactions with shear and diabatic heating, not the numerical scheme that accounts for the adiabatic precession. To this end, the numerical scheme is required to preserve certain invariants which we will discuss in the following section.

We outlined in the previous chapters that in the adiabatic case $((Q_{\Theta,0}, Q_{\Theta,1}) = (0,0))$ the leading-order tangential velocity is trivially constant (cf. eq. (3.1) with $u_{r,00} = w_0 = u_{r,*} = 0$). Therefore, the Hamiltonian $\hat{H}$ (defined in eqs. (3.33) and (3.34)) as well and the centerline tendency equation takes the form of eq. (3.35) which resembles a

one-dimensional Schrödinger Equation. In section 3.3 we gave heuristic justification that $\hat{H}$ possesses the properties of a (regular) Sturm-Liouville operator and therefore has a real spectrum of eigenvalues $\{\lambda_k \in \mathbb{R}\}_{1 \leq k \leq \text{rank}(\hat{H})}$. It was shown that this condition leads to the precession of eigenmodes:

$$\hat{H} X_k = \lambda_k X_k \quad \Rightarrow \quad X_k(t) = e^{-\imath \lambda_k t} X_k(0) \tag{4.85}$$

Note, that eigenmodes are determined up to a complex scalar prefactor.

We immediately conclude from eq. (4.85) that the norm[11] of a solution of eq. (3.35) is conserved:

$$\frac{d}{dt}||X||^2 = \frac{d}{dt}\sum_n |c_n|^2 = \bar{c}_n(-\imath\lambda_n c_n) + \imath\lambda_n \bar{c}_n c_n = 0, \tag{4.86}$$

where $c_n = \langle X_n, X \rangle$ and $\langle X_m, X_n \rangle = \delta_{mn}$.

A canonical approach in the numerical treatment of the Schrödinger equation is to construct the time-integration operator such that it fulfills the requirement of *unitarity*:

$$\hat{U}(t, t_0) : X(t) = \hat{U}(t, t_0)X(t_0) = e^{-\imath(t-t_0)\hat{H}}X(t_0) \tag{4.87}$$

We see that

$$\begin{aligned}
\langle X(t), X(t)) \rangle &= \langle \hat{U}(t, t_0)X(t_0), \hat{U}(t, t_0)X(t_0) \rangle \\
&= \langle e^{-\imath(t-t_0)\hat{H}}X(t_0), e^{-\imath(t-t_0)\hat{H}}X(t_0) \rangle \\
&= \langle X(t_0), e^{\imath(t-t_0)\hat{H}}e^{-\imath(t-t_0)\hat{H}}X(t_0) \rangle \\
&= \langle X(t_0), X(t_0)) \rangle,
\end{aligned} \tag{4.88}$$

i.e., the exact time evolution operator is unitary.

The time-discrete integration formalism of section 4.3 solving for the adiabatic centerline equation eq. (3.35) reduces to

$$\left(1 + \frac{\imath}{2}\Delta t \hat{H}\right) X^{n+1} = \left(1 - \frac{\imath}{2}\Delta t \hat{H}\right) X^n. \tag{4.89}$$

This integration step resembles the semi-implicit trapezoidal rule and has proven to preserve the square norm of the solution through its symplectic property (Hairer et al. 2006). Expanding the solution into eigenmodes at times t^n and t^{n+1} and multiplying eq. (4.89) we get for the amplitudes of the individual eigenmodes

$$c_k^{n+1}\left(1 + \frac{\imath}{2}\Delta t \lambda_k\right) = c_k^n\left(1 - \frac{\imath}{2}\Delta t \lambda_k\right) \tag{4.90}$$

hence,

$$|c_k^{n+1}|\sqrt{\left(1 + \frac{1}{4}\Delta t^2 \lambda_k^2\right)} = |c_k^n|\sqrt{\left(1 + \frac{1}{4}\Delta t^2 \lambda_k^2\right)}, \tag{4.91}$$

i.e., the norm with respect to each eigenmode and therefore the norm of the solution is constant under this time stepping scheme.

In summary, we have shown that the construction of the time stepping scheme of section 4.2 satisfies crucial properties to ensure that the forward-in-time integration does not spuriously affect the amplitude of the tilt by numerical instabilities originating from truncation errors.

---

[11]The norm $|| \cdot ||$ is induced by a scalar product: $||X|| := \langle X, X \rangle$.

5. Setup of Three-Dimensional Reference Simulations

In the previous chapters we discussed the derivation of an asymptotic model for tropical cyclones under the influence of vertical wind shear and diabatic heating as well as numerical strategies to solve the reduced model equations. As such, they are supposed to approximate solutions to eqs. (2.1) under the constraints set by parameters matching those of a tropical atmosphere (see tables 2.1 to 2.3). In the present chapter, we aim at outlining how to validate the asymptotic model and compare its solutions against those of the (unconstrained) governing equations. To this end, we present all the essential ingredients of the numerical algorithm used for solving eqs. (2.1) for general atmospheric scenarios, the setup of initial data as well as algorithmic components essential for conducting tests on the asymptotic theory.

5.1. Outline of the Numerical Scheme

The atmospheric flow equations given in eqs. (2.1) pose a set of PDEs which encompass a wide range of scenarios including, but not limited to, idealized[1] atmospheric physics (Prusa, Smolarkiewicz, and Wyszogrodzki 2008; Smolarkiewicz and Charbonneau 2013; Ziemiański et al. 2021). There is a plethora of suitable numerical models, all of which are more or less specialized for a particular application area. The range of scales, both space and time, determined by the physical problem under investigation, sets requirements towards the adopted numerical schemes and ultimately controls how efficient and stable a given numerical implementation is.

For the asymptotic analysis of chapter 2, it was examined how the motions of the vortex core on the *meso-scale* (here we choose ~100 km) affects the dynamics of the large-scale flow on the *synoptic length scales* (~1000 km). The timescale, however, is set by the inner-core flow (in fact, by being about a factor $1/\varepsilon$ larger than the vortex turnover timescale, *i.e.*, ~8 h). The results of Päschke et al. 2012 (summarized in chapter 2) revealed that for this regime relatively small-scale phenomena such as internal waves, acoustics and strong pressure oscillations do not play a dominant role. Moreover, the flow is essentially balanced due to hydrostatics induced by the gravitational force and due to the cyclostrophic (gradient-wind) balance.

Although — in theory — every numerical model solving for eqs. (2.1) could be deployed, it is a matter of efficiency and beneficial to design a numerical scheme to meet the dynamical degrees of freedom of the underlying problem. Throughout the literature of atmospheric fluid dynamics, it is commonly known that the hydrostatic background

---

[1]The term *idealized* is chosen to restrict to situations in which the fluid can be described as single-component ideal fluid without complicated parametrizations of boundary conditions, thermodynamic processes, etc.

is dominating the solution.[2] In fact, solving only for perturbations from that (constant or slowly varying) background state may lead to substantial improvements in terms of efficiency and stability.

However, dynamical modes of atmospheric motions cover several orders of magnitude in both, space and time, and exhibit a variety of wave-like phenomena with different characteristic wave speeds. Some of them are strong enough to take effect on the scale of interest (gravity waves), while others, such as acoustic waves, are orders of magnitude smaller in amplitude and have virtually no effect on the dynamics of an atmospheric flow. If resolved by the numerical model, they may, however, limit the time step size due to the CFL condition and the comparably high sonic wave speed (with ~300 m s^{-1} one order of magnitude larger than typical wind speeds). As a consequence, a rich body of literature was established to cope with this issue of *low Mach number flows*. While one strategy follows the idea of modifying the governing equations to eliminate acoustic waves (Bannon 1996; Durran 2008; Klein 2009), another approach is to construct time stepping scheme to integrate fast wave-like phenomena implicitly (Smolarkiewicz, Kühnlein, and Wedi 2014).

For the present study, the Eulerian-Lagrangian model (EULAG, Prusa and Smolarkiewicz (2003) and Smolarkiewicz, Kühnlein, and Wedi (2014)) was chosen as numerical framework as it provides the desired properties together with stable and efficient integration strategies and is furthermore well-tested throughout a considerable number of studies.

5.1.1. Conservative Time Integration

Similar to the basic time integration scheme presented in chapter 4[3], the scheme of EULAG starts by treating eqs. (2.1) as a set of equations of the form

$$\frac{\partial \rho \boldsymbol{\psi}}{\partial t} + \boldsymbol{\nabla} \cdot (\rho \boldsymbol{v} \otimes \boldsymbol{\psi}) = \rho \boldsymbol{R}(\boldsymbol{\psi}, t) \tag{5.1}$$

with the state vector $\boldsymbol{\psi} = (\boldsymbol{v}, \Theta)$ and the components

$$\boldsymbol{R_v} = -\frac{1}{\rho}\boldsymbol{\nabla} p - f \boldsymbol{k} \times \boldsymbol{u} + \boldsymbol{g} \, , \tag{5.2a}$$

$$R_\Theta = Q_\Theta \, , \tag{5.2b}$$

of the right-hand side vector $\boldsymbol{R} = (\boldsymbol{R_v}, R_\Theta)$. Together with the *continuity equation*

$$\frac{\partial \rho}{\partial t} + \boldsymbol{\nabla} \cdot (\rho \boldsymbol{v}) = 0 \, , \tag{5.3}$$

---

[2]For example, the strongest pressure variations are associated to the hydrostatic background, which range from 10^5 Pa at sea-level to $4 \cdot 10^4$ Pa for a typical vertical extent of 10 km. On the other hand, dynamical variations for the strongest atmospheric perturbations (such as TCs) are of the order of $5 \cdot 10^3$ Pa, *i.e.*, one order of magnitude smaller.

[3]In fact, the time integration scheme of chapter 4 is a formal extension based on the ideas presented in Smolarkiewicz, Kühnlein, and Wedi (2014).

the system of eqs. (5.1) and (5.3) is equivalent to eqs. (2.1) but in the generic form of a *balance law*[4]. The two eqs. (5.1) and (5.3) are equivalent to

$$\frac{d\boldsymbol{\psi}}{dt} = \boldsymbol{R} \tag{5.4}$$

with the *convective derivative* $\frac{d}{dt} = \partial_t + \boldsymbol{v} \cdot \boldsymbol{\nabla}$ meaning that $\boldsymbol{\psi}$ changes along streamlines with the rate $\boldsymbol{R}$.

Note that eq. (5.3) can be formally incorporated into the system (5.1) by adding $\psi_\rho \equiv 1$ and $R_\rho = 0$. However, its unique role as a *conservation law* becomes apparent through the discretization process: In section 4.2 we have justified the strategy of integrating equations of the type eq. (5.4) by making use of the trapezoidal rule for the right-hand side terms $\boldsymbol{R}$ and a conservative scheme to transport $\boldsymbol{\psi}$ along trajectories. These considerations again led to the formal construction of time stepping scheme for which the advection operator was integrated separately from the source terms encoded in $\boldsymbol{R}$. To this end, we first discretize eq. (5.1) for $\boldsymbol{R} \equiv 0$ on the time interval $[t^n, t^{n+1}]$ approximating the partial time derivative at $t^{n+1/2}$ by the midpoint rule and for a single component ψ:

$$\psi^{n+1} = \frac{\rho^n}{\rho^{n+1}} \left(\psi^n - \frac{\Delta t}{\rho^n} \left(\nabla \cdot \rho \boldsymbol{v} \psi \right)^{n+1/2} \right) + O\left(\Delta t^3 \right) \tag{5.5}$$

Although solving for an advective scalar ψ, this formulation allows to control the conservative fluxes for $\rho\psi$ composing a *conservative scheme*. $(\boldsymbol{\nabla} \cdot \rho \boldsymbol{v}\psi)^{n+1/2}$ can be interpreted as *conservative forcing* transporting ψ^n along trajectories from t^n to t^{n+1} (by the mass flux approximated up to first-order by $(\rho\boldsymbol{v})^{n+1/2}$) and is subject to a suitable second-order-in-time accurate advection method taking the generic form

$$\psi^{n+1} = \mathrm{Adv}^{\Delta t}\left(\psi^n, (\rho\boldsymbol{v})^{n+1/2}, \rho^n, \rho^{n+1} \right) + O\left(\Delta t^3 \right) . \tag{5.6}$$

Adv is the implementation of a suitable advection scheme; in the present case, the multidimensional positive definite advection transport algorithm (MPDATA) of (Smolarkiewicz 1984) is used. This formulation takes the prior knowledge of ρ^{n+1} at the final time into account which may need to be integrated on its own. By setting $\rho^n, \rho^{n+1} \to 1$, $\psi^n \to \rho^n$, and $(\rho\boldsymbol{v})^{n+1/2} \to \boldsymbol{v}^{n+1/2}$ we can make use of eq. (5.6) to solve for eq. (5.3).

EULAG's compound integration scheme for eq. (5.1) reads

$$\boldsymbol{\psi}^{n+1} = \mathrm{Adv}^{\Delta t}\left(\boldsymbol{\psi}^n + \frac{\Delta t}{2} \boldsymbol{R}^n, (\rho\boldsymbol{v})^{n+1/2}, \rho^n, \rho^{n+1} \right) + \frac{\Delta t}{2} \boldsymbol{R}^{n+1} + O\left(\Delta t^3 \right) , \tag{5.7}$$

where $\boldsymbol{R}^n$ is the shorthand for $\boldsymbol{R}(\boldsymbol{\psi}^n, t^n)$, *i.e.*, eq. (5.7) forms a semi-implicit scheme in the terms $\boldsymbol{R}(\boldsymbol{\psi}^{n+1}, t^{n+1})$.

For further details we refer the interested reader to Smolarkiewicz, Kühnlein, and Wedi (2014), where details are given about the integration of the perturbative system as well as the implicit-pressure scheme. Further, we note that we make use of the static grid refinement capability of EULAG, as we will explain in section 5.2.1 when giving details about the numerical grid.

---

[4]Note that, with suitable re-definitions of the components of $\boldsymbol{\psi}$ (and $\boldsymbol{R}$), EULAG offers a uniform approach to integrate the Euler equations under anelastic (Bannon 1996) and pseudo-incompressible constraints (Durran 1989, 2008), or in a fully compressible mode (Klein 2009; Smolarkiewicz, Kühnlein, and Wedi 2014).
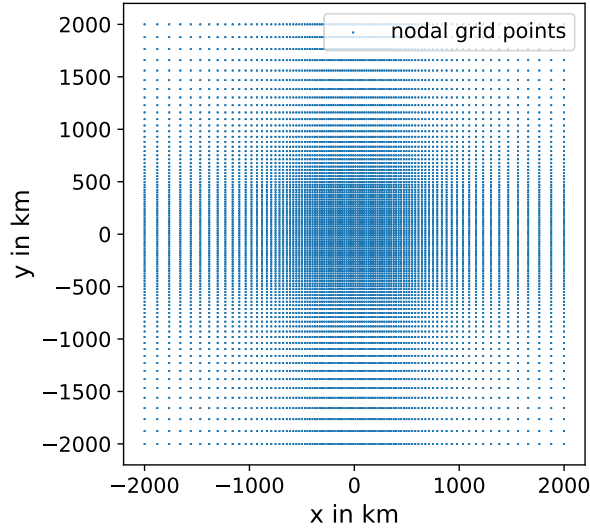
Figure 5.1.: Static grid refinement. For an example resolution of 192×192 grid points, the horizontal nodal grid positions are shown.

5.2. Numerical Setup and Initial Data

Päschke et al. (2012) and the derivations of chapter 2 provide a reduced model for the motion of a tropical cyclone with the *centerline* position $X(z, t)$ and the circumferentially averaged *mean tangential wind* $u_{\theta,0}$ as the dynamical degrees of freedom. The numerical experiments of chapter 6 are supposed to validate how well the system is represented by the given dynamical variables and the leading-order equations eqs. (3.1) and (3.34).

To this end, we shall construct initial data by prescribing X and u_θ and subsequently reconstructing the missing flow variables by the leading- and higher-order asymptotic balance relations derived in section 2.4.3. By satisfying the assumptions of the asymptotic analysis up to higher-order we shall be able to initialize three-dimensional simulations which exhibit certain symmetries at leading order (axisymmetric mean tangential velocity centered around X). Under the influence of external forcing by diabatic heating and/or shear these symmetries shall be maintained, as anticipated by the asymptotic theory. This allows us to compare the results of three-dimensional numerical experiments with reference simulations of the leading-order asymptotic equations. Although extended, the construction of the initial data follows essentially the ideas of the preceding work of Papke (2017). The setup as described in the upcoming sections matches the one used for creating the results of Dörffel et al. (2021).

5.2.1. Static Grid Refinement

EULAG provides the feature of computing solutions to the Euler equations on a non-uniform grid. Despite more advanced features, such as vertical and dynamic grid refinement, here, we make only use of the static grid refinement capability for the horizontal grid directions. The full horizontal domain, mapped to $[-1, 1]^2$ by an affine

transformation, is sampled equidistantly in the coordinates (x_c, y_c) and subsequently transformed to stretched coordinates x_p:

$$
\begin{pmatrix} x_p \\ y_p \end{pmatrix} = c_1 \begin{pmatrix} x_c \\ y_c \end{pmatrix} + c_2 \begin{pmatrix} x_c^\alpha \\ y_c^\alpha \end{pmatrix}
\tag{5.8}
$$

The parameters are chosen as $c_{1,2} = 1/2$ and $\alpha = 5$. The result is displayed for the example of 192×192 horizontal grid points by fig. 5.1.

5.2.2. Boundary Conditions

Boundary conditions arise in EULAG as a twofold problem: Firstly, the advection solver (MPDATA) needs information on the mass flux through the edges of the simulation domain. Secondly, the implicit pressure equation (see eq. (57) of Smolarkiewicz, Kühnlein, and Wedi (2014)) resembles a Helmholtz, *i.e.*, an elliptic problem that requires boundary conditions in order to characterize the problem and make statements on existence and uniqueness of solutions.

For the sake of reducing complexity in the presented implementation, boundary conditions are therefore imposed such that the normal component of velocity through the boundary interface $\mathbf{n} \cdot \mathbf{v}|_{\partial \Omega} = 0$. Note that $\mathbf{v}$ is the three-dimensional velocity vector measured the stretched coordinates (cf. section 5.2.1).

This, in particular, implies that there are no mass fluxes through the boundaries. Any further choice of boundary conditions for the advected variables therefore is obsolete, and by construction the pressure vanishes at the lateral boundaries: $p|_{\partial \Omega_L} = 0$. These boundary conditions translate in what is known in literature as "rigid lid, free slip".

5.2.3. Atmospheric Background State

Starting point of setting up the data is to define an atmospheric background state which is necessary for both, settling the asymptotic regime and defining the reference state against which EULAG integrates the dynamical variables as perturbations.

The background state is supposed to be a more or less trivial solution of the governing equations, in our case horizontally homogeneous and governed by the hydrostatic equation

$$
\frac{d\overline{p}}{dz} = -g\overline{\rho}
\tag{5.9}
$$

In analogy to the notation of section 3.1.3, $\overline{(\cdot)}$ symbolizes a time-independent, horizontally homogeneous variable, *i.e.*, only dependent on the vertical coordinate z. Prescribing $\overline{p}(0) = p_{\text{ref}}$, *i.e.*, the mean sea-level pressure, together with the equation of state eq. (2.1e), eq. (5.9) can be solved for a given vertical profile of potential temperature

$$
\overline{\Theta}(z) = T_{\text{ref}} \exp\left(\frac{N_{\text{ref}}^2}{g} z\right) .
\tag{5.10}
$$

See table 2.1 for the parameters p_{ref}, T_{ref}, N_{ref}, and g. For completeness, the resulting profiles for pressure and density are

$$\overline{p}(z) = p_{\mathrm{ref}} \left(\frac{gR}{c_p N_{\mathrm{ref}}^2 h_{\mathrm{sc}}} \left(\exp\left(-\frac{N_{\mathrm{ref}}^2}{g}z\right) - 1 \right) + 1 \right)^{c_p/R} \tag{5.11a}$$

$$\overline{\rho}(z) = \frac{p_{\mathrm{ref}}}{R\overline{\Theta}(z)} \left(\frac{\overline{p}(z)}{p_{\mathrm{ref}}} \right)^{1/\gamma} . \tag{5.11b}$$

5.2.4. Mean Tangential Velocity and Centerline

The assumptions leading to the regime under investigation settle ranges for both, spatial and time scales at which the quantities vary at leading order. In the present case, these are about $100\,\mathrm{km}$ spatial and $8\,\mathrm{h}$ of temporal extent under which solutions vary at $O(1)$ compared to the corresponding reference quantities. Although the two regimes with $\alpha = 0$ and $\alpha = 1/2$ are derived in section 2.4.3, we argued in section 3.4.3, that the prototypical heating pattern that cancels the adiabatic vertical velocity, causes problems in matching to the outer QG flow since the curvature term proportional to $\ln(r)\boldsymbol{M}_1$ does not find a matching counterpart. Nonetheless, this heating pattern is useful as it allows to investigate the effects adiabatic heating resulting in a linear first-order-in-time second-order-in-space PDE for the centerline that can be analyzed through the spectral properties of the operator $(1 + \exp(i\tilde{\theta}_0))\hat{H}$ (cf. eq. (3.70)). Therefore, we select the regime with $\alpha = 0$, i.e., a vortex core scale of $100\,\mathrm{km}$. Effects that are due to the interaction of the vortex core flow with the large-scale Coriolis force are present, as we will see, but separated in magnitude from the leading-order dynamics, at least on the present timescales.

As discussed before, the degrees of freedom are u_θ and $\boldsymbol{X}$, and we aim for them to vary "on a slow manifold", which means on a timescale that is large compared to small-scale oscillatory motions but short w.r.t. the timescale at which the background changes. To this end, initial data must as well satisfy the scaling regime that led to the asymptotic model and therefore, we construct the "simplest", physically meaningful data. Along the lines of observational studies, we initialize the wind field as leading-order symmetric tangential wind field corresponding to a barotropic[5] Gaussian vorticity profile

$$\zeta(r) = \zeta_m \exp\left(-\sigma^2 r^2\right) . \tag{5.12}$$

ζ_m and σ are constants determined by prescribing a value $u_{\theta,\mathrm{max}}$ at a given radius R_{mw}:

$$\max_r u_\theta = u_\theta(r = R_{\mathrm{mw}}) = u_{\theta,\mathrm{max}} , \tag{5.13}$$

i.e., imposing a value of maximum velocity at the radius of maximum wind (RMW). The resulting velocity profile reads

$$u_\theta(r) = q_m \frac{1 - \exp(-\sigma^2 r^2)}{2\sigma^2 r} \tag{5.14}$$

and is shown in fig. 5.2.

---

[5]The term "barotropic" refers to the fact, that the vorticity (velocity) does not depend on z in the centerline coordinates, but only on r, the distance from the centerline. Barotropy, in the strict sense, is satisfied if the tilt $\partial_z \boldsymbol{X}$ vanishes, rendering the coordinates (r,z) to usual cylindrical coordinates. Non-zero tilt, however, tilts the coordinate system and with that renders the velocity genuinely baroclinic.
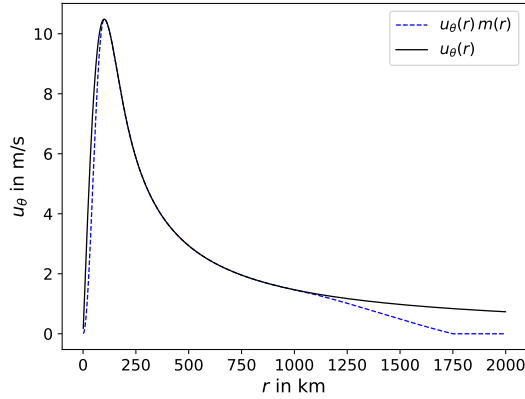
Figure 5.2.: Initial radial velocity profile associated to Gaussian vorticity profile 5.12. The black curve shows the unmodified profile of eq. (5.14). The dashed blue curve represents the mollified velocity profile as taken for initializing the three-dimensional simulations.

The analytical structure of the *centerline equation* (3.34), especially that of the *Hamiltonian $\hat{H}$*, governing adiabatic self-induced motions, provides information on the characteristics of solutions to the centerline motion. In section 3.3, we found evidence that $\hat{H}$ possesses properties of a Sturm-Liouville operator (SLO), in the present case that of a *regular SLO*, and therefore, solutions are represented by superpositions of discrete eigenmodes X_n, each precessing with a unique *eigenfrequency λ_n*. The theory on SLOs states, that these eigenfrequencies asymptotically follow a sequence with $\lambda_n \sim n^2$, *i.e.*, the nontrivial part of the spectrum of $\hat{H}$ imposes an upper bound on the timescale (inverse of λ_1) on which the solution can vary, but there is no lower bound ($1/\lambda_n \to 0$). Hence, the first non-trivial eigenmode determines the characteristic timescale at which *slow solutions* evolve which is that of the vortex-core timescale imposed *a priori* on the asymptotic theory. Thus, although general solutions populate the full spectrum of $\hat{H}$ (or at least that part numerically represented), we focus on the first (slowest) non-trivial eigenvalue λ_1 that exhibits a *cosine-like* eigenfunction $X_1(z)$.

Päschke et al. (2012) found an analytical expression for a simplified setting which required $\overline{\rho} = \text{const}$ or $\overline{\rho}(z) \sim \exp(-z/z_{\text{ref}})$. Covering more general, and more realistic settings as presented in section 5.2.3, however, eigenmodes are less feasible to handle analytically, and numerical approaches are required. The numerical scheme to solve eqs. (4.1) involves discretizing $\hat{H}$ (cf. section 4.4). The sparse eigenvalue problem can be efficiently solved by employing the numerical environment provided by SciPy (Virtanen et al. 2020).

In section 2.5 we have provided insights into the self-induced motion of a tropical cyclone caused by the fact that a non-vanishing large-scale circulation is presents. In both of the regimes $\alpha = 0$ and $\alpha = 1/2$ in section 2.4.3, the long-range velocity tail of the inner core, proportional to $1/r$, couples to the leading-order QG flow and induces a precessing motion. This long-range tail, however, causes complications in terms of the boundary conditions since non-vanishing contributions of it may interfere with the domain boundaries for limited-sized domains. For a numerical simulation

in general, however, and EULAG specifically, it is necessary to consistently comply with the boundary conditions. In EULAG, they are chosen to make the orthogonal velocity components vanish.[6] Even for comparably large radii, we cannot simply impose this condition with eq. (5.13) since this approach would lead to a jump discontinuity at the boundaries due to the $1/r$ velocity tail. To remedy, a domain large enough to establish the scaling regimes of the inner core ($\mathcal{O}(100\,\mathrm{km})$) as well as the QG flow ($\mathcal{O}(1000\,\mathrm{km})$) is employed for the numerical simulations. This approach allows for a precessing-centerline solution due to the two-scale coupling. Additionally, in the outer skirts of the QG far field, a smooth transition of the velocity field towards zero is achieved by the use of a *mollifier:*

$$
m(r) := \begin{cases} 1 & , \quad 0 \leq r < r_1 \\ \cos^2\left(\frac{\pi}{2}\frac{r-r_1}{r_1-r_\infty}\right) & , \quad r_1 \leq r < r_\infty \\ 0 & , \quad r \geq r_\infty \end{cases} \tag{5.15}
$$

The two radii of the outer suppression region are $r_1 = 1250\,\mathrm{km}$ and $r_\infty = 1750\,\mathrm{km}$. These radii are — somewhat arbitrarily — set on the basis of the sensitivity of tilt and the velocity field towards these parameters and for efficiency reasons, *i.e.*, such that we can limit the size of the simulation domain without too strong effects on the solution.[7] The resulting radial profile of mean tangential velocity as initialized is displayed in fig. 5.2 by the dashed blue curve.

The resulting initial data are presented in the three-dimensional visualization of fig. 5.3 showing vortex centerline and streamlines. Further details are discussed in section 5.2.5.

5.2.5. Higher-Order Perturbations

The balance relations derived in section 2.4.3 deliver higher-order corrections to all physical fields and allow to bring the initial data closer to a balanced state. Interestingly, in the adiabatic case all correction terms depend only on the leading-order of u_θ and X and are governed by diagnostic differential relations which can be evaluated at any given instance in time without prior knowledge of the tendency of the physical state.

Numerical experiments (omitted here) have shown that it is beneficial if not necessary to account for this additional information on the balanced state, since otherwise the solution exhibits oscillations obscuring the effects we are interested in. For several reasons, *e.g.*, the fact that we will parameterize the diabatic heating by local values of tilt and tangential velocity, we need to control local imbalances as they may lead to fast adjustments causing small-scale features. The parametrization, typically involving

---

[6]A more general treatment of velocity boundary conditions is technically possible but is not implemented in the author's version of EULAG. Note, that through the use of static or time-varying background states, however, it is possible to implement open or inflow boundary conditions. That would require an analytical expression of the background fields, and is thus impractical for our applications.

[7]In fact, with the three-dimensional simulation we want to approximate the situation where the vortex transitions smoothly into the environmental synoptic-scale flow. From a compact, or at least exponentially decaying vorticity profile, the $1/r$ decay of u_θ follows, that would actually require an infinite outer radius. Being unfeasible, we try to mimic this behavior by choosing a mollifier which allows to limit the simulation domain but still to capture the essential dynamics.
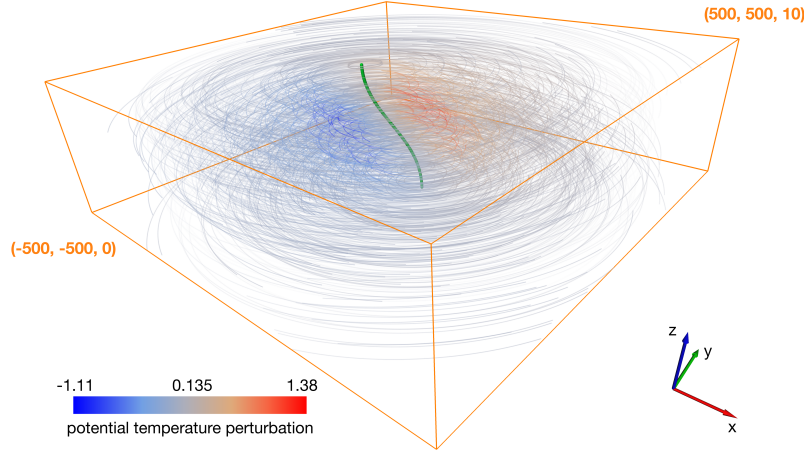
Figure 5.3.: Centerline (green) and streamlines of initial data. Streamlines are color-coded (see color bar) with the local value of the potential temperature perturbation. The figure is adopted from Dörffel et al. (2021) and courtesy of Natalia Mikula.

differential expressions, then may take on the gradients of these small scale features and amplify them, eventually causing the simulation to crash.

Given in section 2.4.3 in non-dimensional form, we will repeat those expressions important for the implementation of the high-order balances. All quantities will be given in dimensional form, and we follow the notation of $\phi = \overline{\phi} + \phi'$, where a quantity ϕ is expressed as a horizontal mean $\overline{\phi}$ and the perturbation ϕ'. The latter typically is small ($\phi' = o(\overline{\phi})$) and we often make use of the approximation $\overline{\phi} \approx \phi$. Occasionally, we will deviate from this convention and give individual definitions.

The first expression to evaluate is the *gradient wind balance* which dominates the horizontal momentum balance and reads

$$\frac{1}{\rho} \frac{\partial p'}{\partial r} = \frac{u_\theta^2}{r} + f u_\theta \,. \tag{5.16}$$

By straightforward numerical integration in the radial coordinate,

$$p' = \int_r^\infty \frac{\partial p'}{\partial r} \, dr \tag{5.17}$$

we obtain an expression for the perturbation pressure balancing radial and Coriolis forcing. Note, that for compactly supported u_θ the outer integration bound effectively shrinks to r_∞ (see eq. (5.15) for definition) rendering the integral convergent on a finite-sized simulation domain.

Next in line are corrections due to the hydrostatic balance which governs not only leading-order pressure and density, but also the respective perturbation quantities:

$$\frac{\partial p'}{\partial z} = -g \rho' \,. \tag{5.18}$$

Given p', this equation allows solving for ρ'.

With the equation of state eq. (2.1e), we finalize the correction terms for the thermodynamics quantities by expressing the potential temperature perturbation as

$$\Theta' = \Theta - \overline{\Theta} = \frac{p_{\text{ref}}}{R\rho}\left(\frac{\overline{p}+p'}{p_{\text{ref}}}\right)^{1/\gamma} - \overline{\Theta} \tag{5.19}$$

We could also directly make use of eq. (2.41). The difference to eq. (5.19), however, is of order $o(1)$, and the two variants are asymptotically equivalent. The resulting potential temperature perturbation is visualized in fig. 5.3 by color-codings of the streamlines.

Through the vertical coupling by hydrostatic balance, pressure troughs are translated into troughs in density and, via the equation of state, lead to perturbations of potential temperature. This is the cause for eq. (5.19). Misalignment of the troughs through the centerline tilt lead to Fourier-1 perturbations in density and potential temperature. Considering the circular motions initialized by eq. (5.14), fluid parcels need to follow paths of constant entropy, *i.e.*, potential temperature, (in the adiabatic case) on their way around the storm. For this reason, the vertical velocity has a non-trivial structure even in the adiabatic case. We account for that by using eq. (3.19c) in its dimensional form for the initialization of vertical velocity:

$$w_{\text{ad}} = \frac{1}{d\overline{\Theta}/dz}\frac{\overline{\Theta}}{g}\frac{u_\theta}{r}\frac{1}{\rho}\frac{\partial p'}{\partial r}\frac{\partial \boldsymbol{X}}{\partial z}\cdot\boldsymbol{e}_\theta \tag{5.20}$$

The corrections outlined above already provide substantial improvements in terms of preserving the initial balance. Numerical experiments, not shown here, unveil that these adjustments lead to a dramatic reduction of initial oscillations and help to maintain the structure of the initial flow, hence, the centerline tilt. Päschke et al. (2012, Section 4.4) and the discussions of sections 2.4.5 and 3.1.1, however, provide further insights by giving expressions for the streamfunction $\psi^{(2)}$ and the velocity potential $\phi^{(2)}$ associated to the asymptotic modes of $u_r^{(2)}$ and $u_\theta^{(2)}$, see eqs. (2.55). As discussed in the context of eq. (3.2), we subtract the far field tail of the higher-order velocity corrections to match to the outer solution (at rest) to account for the proper motion of the tilted centerline. With this additional information we initialize u_r and u_θ by

$$u_r = \delta u_{\text{ref}} u_r^{(2)} \tag{5.21}$$

$$u_\theta = q_m\frac{1 - \exp(-\sigma^2 r^2)}{2\sigma^2 r} + \delta u_{\text{ref}} u_\theta^{(2)} \tag{5.22}$$

The procedure above for constructing balanced data allows for initializing simulations which are close to balance and maintain tilt and maximum velocity to high-order of accuracy, at least in a sensible range of parameters. Still, there are imbalances present within the first several days of simulation, which is why we additionally make use of an *initialization phase* of 4 days which brings the data closer to a state which is balanced within the numerical scheme of EULAG. Disparity between analytical and numerical representation of differential balance relations may be the reason for this strategy to be necessary.

5.3. Reconstruction of the Leading-Order Quantities

In chapter 6, we will present results of numerical experiments showing the influence of a diabatic heating imposed on the flow field. In nature, diabatic heating would be the result of a number of physical processes, among them radiation, sensible heat fluxes between the (ocean) surface and the boundary layer, and latent heat release by phase transitions of moisture content (Houze 2010; Marks 2003; Montgomery and Smith 2017b). Here, however, the guiding question is how heat release is affecting the dynamics and structure of TCs, rather than vice versa. This question mainly concerns structures in the diabatic heating field that materialize on the meso-scale and cover the full depth of the free troposphere, thus being essentially the spatially averaged effect of latent heat release through moist cloud dynamics.

In NWP, physically motivated models accounting for the chemistry of cloud condensation and evaporation (*i.e.*, phase transitions and corresponding energy conversion rates) rely on the notion of *moisture content*. Typically, this involves transporting additional variables with the flow, whose spatial structure and the parametrization of conversion between the different constituents determine the latent heat release and consequently the feedback to structure and intensity of the TC. We are, however, mainly interested in how the spatial structure of diabatic heating is affecting the flow structure. Further, for the simplified asymptotic model, we do not have access to information concerning moisture variables.[8]

For this study, we want to investigate the response of the flow structure to a given (parameterized) diabatic heating pattern. The parametrization, as due to model limitations, needs to be in terms of the available flow variables (ρ, u, v, w, Θ), which are indirectly all determined by the leading-order quantities X and $u_{\theta,0}$ via the diagnostic relations of section 5.2.5. For this reason, in general we have to assume that the parametrization of the diabatic heating terms depends on X ($\partial_z X$, resp.) and $u_{\theta,0}$. To this end, and for the sake of directly comparing the simulation results of asymptotic and three-dimensional equations, we require a methodology to reconstruct mean tangential wind and the centerline position from the three-dimensional flow field for a given instance in time. $u_{\theta,0}$ and X, found by suitable methods, can then be taken as input for a reference simulation of the asymptotic model.

5.3.1. Reconstruction of the Vortex Centerline

Clearly, the definition of $u_{\theta,0}$ essentially depends on the choice of coordinates, which itself depend on the centerline position at each horizontal level. As a direct consequence of the assumption that, at leading order, u_θ is axisymmetric[9], the centerline position must be the position maximizing the symmetric component of u_θ.[10] For idealized simulations, *i.e.*, where we can assume a certain degree of symmetry in the flow field, we can approximate the centerline coordinates by computing the center of gravity of the

---

[8]It would in principle be possible to add information of advective scalar quantities, but requires substantial extensions to the asymptotic model exceeding the scope of this work.

[9]In fact, Mikusky (2007) found that the leading-order symmetry of u_θ is a consequence of the asymptotic scaling rather than an assumption.

[10]Note, that u_θ is the tangential velocity *relative* in the co-moving coordinate frame attached to the centerline.

vorticity distribution:

$$X(z, t) = \int_\Omega \begin{pmatrix} x \\ y \end{pmatrix} \zeta_n(x, y, z, t)\, d\Omega \tag{5.23}$$

$\Omega = \{(x, y) \in \mathbb{R}^2\}$ is a compact and convex two-dimensional domain over which the ζ is sufficiently regular (positive in our case) and $\zeta_n = \zeta/||\zeta||_\Omega$ is the normalized vorticity field with the measure

$$||\zeta||_\Omega = \int_\Omega \zeta\, d\Omega\,. \tag{5.24}$$

This approach requires a certain degree of regularity (symmetry) of the velocity field. There are other choices possible for the definition of the centerline based on statistical methods and other vorticity-based indicator fields. A more comprehensive discussion can be found in Mikula et al. (2021) and von Lindheim et al. (2021). In the former reference, an optimization approach is presented that maximizes the symmetric component of tangential velocity. That can be considered as ground truth, yet, it is computationally too expensive to implement as run-time evaluation within the three-dimensional simulation.

5.3.2. Reconstruction of the Mean Tangential Velocity

Having reconstructed the coordinate center X, and therefore the polar coordinate center per level, we could compute the tangential velocity by

$$u_\theta = \boldsymbol{u}_\parallel{}^{\mathrm{rel}} \cdot \boldsymbol{e}_\theta = -u \sin\theta + v \cos\theta \tag{5.25}$$

and subsequently average in the θ-direction:

$$u_{\theta,0}(r, z, t) := \frac{1}{2\pi r} \int\limits_0^{2\pi} u_\theta(r, \theta, z, t)\, d\theta \tag{5.26}$$

The fact, that the three-dimensional simulations are conducted on a Cartesian grid renders this approach somewhat cumbersome, and furthermore, expensive due to the mapping between two different grids at each horizontal level and instance in time.

Papke (2017) proposed an algorithm, in which the data is remapped before averaging. We will summarize this approach here and show a minor extension to achieve higher accuracy for medium-resolved grids. First, we define radial grid, centered at X and covering a sufficiently large region on top of the numerical Cartesian grid (see fig. 5.4). For each circle with radius r prescribes by the points on that grid, we compute the circulation Γ, defined as

$$\Gamma(r, z, t) = \int\limits_{B_X(r)} \zeta(x, y, z, t)\, d^2x = \int\limits_0^{2\pi} \int\limits_0^r \zeta(r', \theta, z, t)\, r'dr'\, d\theta \tag{5.27}$$

by integrating over the disk $B_X(r) := \{\boldsymbol{x} \in \mathbb{R}^2 : ||\boldsymbol{x} - \boldsymbol{X}|| \le r\}$. From the expression of vorticity in polar coordinates, $\zeta = \frac{1}{r}\partial_r(ru_\theta) - \partial_\theta u_r$, we get

$$\Gamma(r, z, t) = \int\limits_0^{2\pi} ru_\theta(r, \theta, z, t)\, d\theta = 2\pi r u_{\theta,0}\,. \tag{5.28}$$
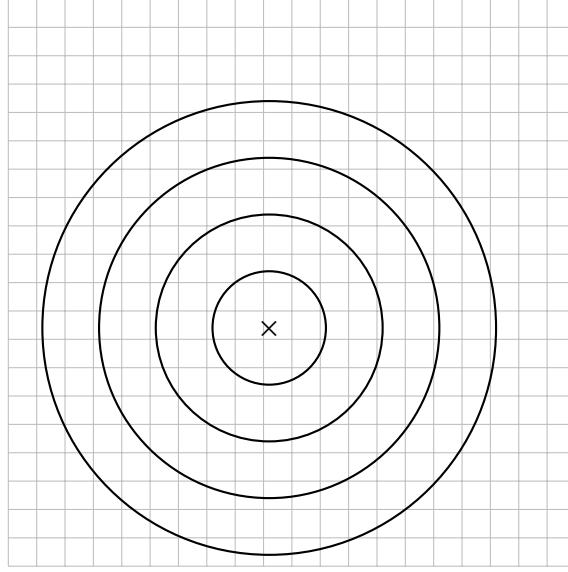
Figure 5.4.: Overlay of radial grid on Cartesian grid. "×" denotes the centerline position and each radius defines a disk over which to integrate eq. (5.27).

The first integral in eq. (5.27) is computed from vorticity values ζ_j, given on the nodes of a Cartesian grid, for a set of radii $\{r_i\}$ by means of numerical integration:

$$\Gamma(r_i, z, t) \approx \sum_j a_{j,i} \zeta_j \tag{5.29}$$

j symbolized the *multi-index* labelling the grid cells and i corresponds to the radius r_i. The *area weights* $a_{j,i}$ depend on the fact whether the cells, adjacent to the node j, are located within the circle with radius r_i, outside, or are intersected by it. Papke (2017) constructed an integration scheme to approximate eq. (5.27) by a *cut-cell* method accounting for the vertices' position relative to the intersecting circle arc.

In the following, we will consider grid cells as the volume delimited by the grid coordinate lines ($x = x_i$ and $y = y_j$, respectively) and dual cells as the control volume for the finite volume approximation of the nodal data, see fig. 5.5. The value, stored at the position (x_i, y_j), is interpreted as the volume average over the dual grid cell

$$\Omega_j = \{(x, y) \in \mathbb{R}^2 : x_{i-1/2} \leq x \leq x_{i+1/2}, \ y_{j-1/2} \leq y \leq y_{j+1/2} \text{ with } j = (i, j)\}. \tag{5.30}$$

The integral eq. (5.27) then is approximated by eq. (5.29) interpreting $a_{j,i}$ as the *effective volume* of cell j contributing to the integration, *i.e.*, the volume fraction of the cell inside the radius r_i. In the finite volume approximation $a_{j,i}\zeta_j$ is the contribution of a single cell to the approximate integral (5.29).

For a fixed integration radius r, Papke (2017) identified 5 distinct cases, depending on the radial distance of the vertices relative to the centerline positions:

(0) $r_i < r \quad \forall i = 1, \ldots, 4$

(1) $r_1 > r, r_i < r \quad \forall i = 2, 3, 4$
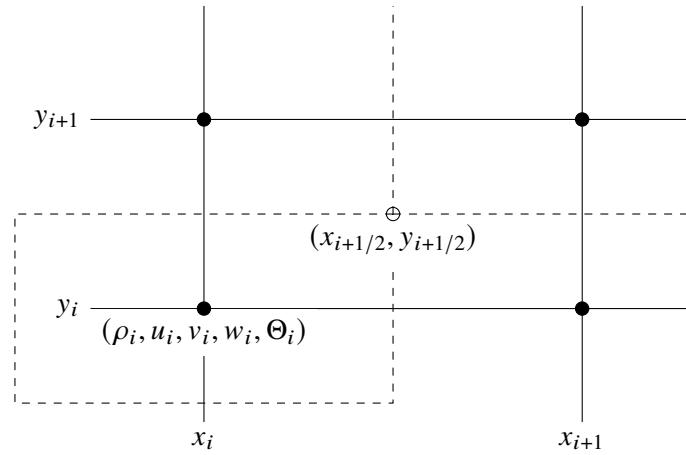
Figure 5.5.: Schematics of a grid cell. Integer-valued indexes denote data positions on an Arakawa A-grid (Arakawa and Lamb 1977) used by EULAG. Solid lines delimit the grid cell, while dashed lines indicate the dual control volume for which the stored values are interpreted as averages.
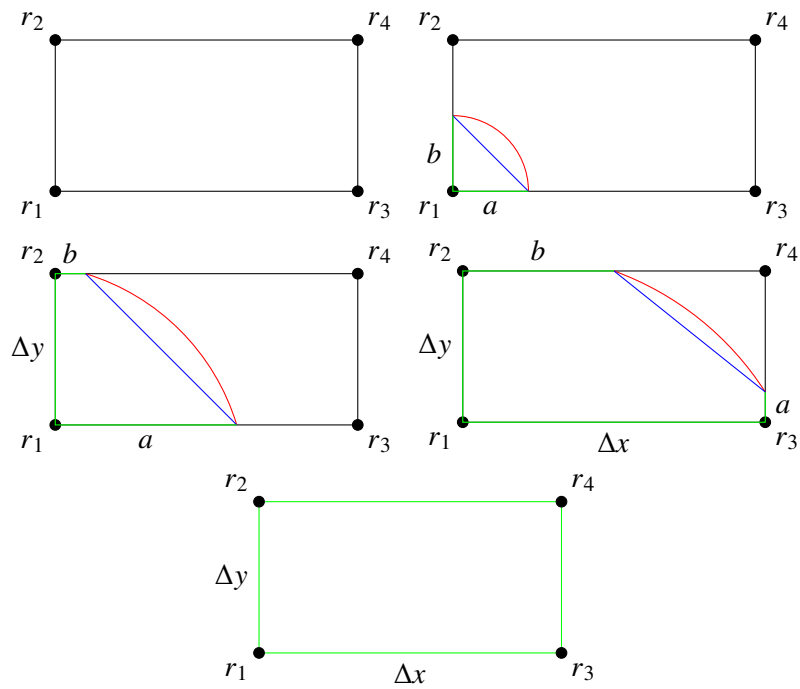
Figure 5.6.: Integration areas for intersecting circular arcs (figure adopted from Papke (2017)). Colored line segments enclose the area to be integrated. Cell vertices are numbered by their radial distance to the center of the circle.

(2) $r_i > r$ $\forall i = 1, 2,$
     $r_i < r$ $\forall i = 3, 4$

(3) $r_i > r$ $\forall i = 1, 2, 3, r_4 < r$

(4) $r_i > r$ $\forall i = 1, \ldots, 4$

This situation is also depicted in fig. 5.6 showing, that the dual cells' effective volume is accounted for by a three-, four-, or five-sided polygon plus a circular segment. Note that, in general, it is necessary to sort the vertices of a dual cell according to their radial distance in ascending order to meet the situation depicted in fig. 5.6. This involves mirroring the cell, as described in Papke's (2017) section 3.3.2.4. Given the length of the dual cells' lateral boundaries, Δx and Δy, the corresponding area fractions for the individual cases are given by

$$(0): \quad a_j = 0, \tag{5.31a}$$

$$(1): \quad a_j = \frac{ab}{2} + \frac{1}{2}r^2(\Delta\theta - \sin\Delta\theta), \tag{5.31b}$$

$$(2): \quad a_j = \Delta y b + \frac{(a-b)\Delta y}{2} + \frac{1}{2}r^2(\Delta\theta - \sin\Delta\theta), \tag{5.31c}$$

$$(3): \quad a_j = \Delta x \, \Delta y - \frac{(\Delta x - b)(\Delta y - a)}{2} + \frac{1}{2}r^2(\Delta\theta - \sin\Delta\theta), \tag{5.31d}$$

$$(4): \quad a_j = \Delta x \, \Delta y. \tag{5.31e}$$

a and b depend on the specific case and are given in fig. 5.6. $\Delta\theta$ is the arc length between the intersection points with the cell boundary. Amending the integration formulas eq. (5.31) by contribution according to the circular segments, in conjunction with the finite-volume integration on dual cells, marks the extension with respect to Papke original formulations. It allows for the exact[11] integration of the area of a disk with radius r,

$$A = \int_{B_X(r)} 1 \, d^2x = \pi r^2, \tag{5.32}$$

and further provides accurate results even on rather coarse grids.

Note, that the integration scheme involves determining the intersection points of a dual cell boundary with the circle. Papke (2017) outlined in section 3.3.2.1 how to solve this as a quadratic problem which we adopted without modifications. The case, where a circle is enclosed completely by a single grid cell, is ignored since we choose the radial grid spacing large enough to circumvent this particular issue.

---

[11]Up to machine precision.

6. Physical Test Cases

The asymptotic theory of TCs, originally derived by Päschke et al. (2012) and refined by Dörffel et al. (2021) and the present work, will be tested in comparison to unconstrained three-dimensional simulations of the equations of atmospheric fluid dynamics (2.1). The cited work provides insights on the "motion and structure of atmospheric [...] vortices" (sic!) in a sense that the theory prescribes the time evolution of atmospheric structures that resemble a TC under the influence of external shear and diabatic heating. More precisely, the theory provides tendency equations for the leading-order circumferential velocity, *i.e.*, the intensity, and the vertical structure, *i.e.*, centerline of the TC.

Clearly, the asymptotic model poses a problem much cheaper to solve numerically in comparison to the full three-dimensional model, which is one of the main motivational points for the subsequent assessment. Yet, the model needs to be validated against three-dimensional simulations to make sure the key assumptions are preserved throughout the time evolution of the vortex. To this end, we will present a collection of numerical experiments which compare the simulation results of the asymptotic model against the three-dimensional Euler equations with Coriolis- and gravitational forcing (cf. eqs. (2.1)). Next to standard procedures, necessary to efficiently integrate the equations under atmospheric conditions, there will be no further restriction towards the asymptotic regime of TCs in terms of symmetry or invariants, so we are able to attribute similarities between the results of the two approaches to the fact whether (or not) the asymptotic theory captures physical properties of TCs.

Extending the preliminary results of Papke (2017), we analyze a number of settings, each focussing on an isolated effect, and compare asymptotic and three-dimensional results. Of particular interest will be the question, how higher-order effects, truncated by the asymptotic model, may accumulate and impact its predictive quality. Ultimately, we want to outline possible pathways towards RI and RW, as it remains unclear, how weak TCs intensify under unorganized convection. The results of the following sections have been partially published in Dörffel et al. (2021).

6.1. Effects of Environmental Wind Shear

For the sake of completeness, we start the series of experiments by forcing a barotropic, vertically aligned vortex by sheared external wind. These results essentially resemble the findings of Reasor, Montgomery, and Grasso (2004), but we want to put special emphasis on the connection to the eigenstructure of the governing Hamiltonian, as discussed on an analytical level in section 3.4.1.

In fig. 6.1, the evolution of the TC centerline is shown as a result of externally imposed vertical wind shear for both, the asymptotic model and as a solution to three-dimensional Euler equations. The vortex is initially vertically aligned, and the forcing external velocity field resembles the first non-trivial eigenmode of the centerline Hamiltonian.

(a) Asymptotic   (b) 3D   (c) Asymptotic + damping
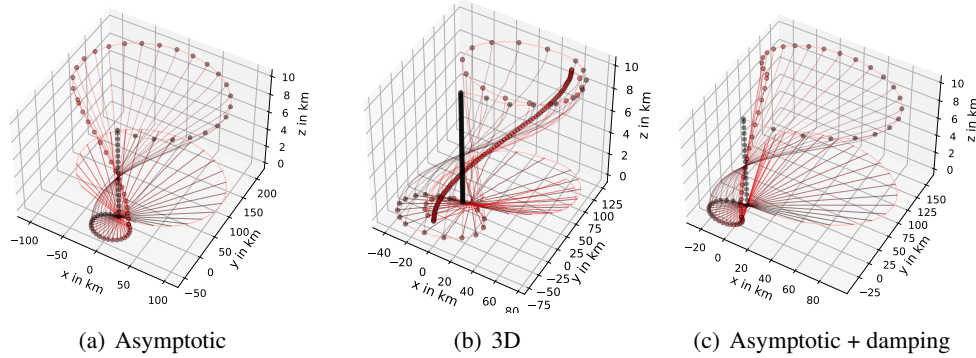
Figure 6.1.: Centerline evolution of initially barotropic vortex forced by external wind shear for an integration time of 8 d. Initial data is shown by dotted black lines, final data by dotted red lines, and the time evolution is encoded by the transition from black to red. Endpoint (top and bottom) at each time step are marked by circles and are connected by splines. On the bottom plane, the projection of the three-dimensional centerline is shown. Results are shown for the asymptotic model (a), the three-dimensional equations (b), and the asymptotic model including a damping term (c).

Thus, the external forcing excites that mode in the centerline (see eq. (3.55)). In the same manner, projections of the external wind shear onto other eigenmodes would excite the corresponding eigenmodes of the centerline, hence, in general, lead to small-scale oscillations (not shown here). Since these higher-order oscillation would obscure the clean picture of how external wind shear induced precession of the centerline, we restrict to the first eigenmode although in nature a superposition of all modes is present.

By comparing the left and middle panels of fig. 6.1, it becomes apparent, that the centerline time evolution of the two approaches, asymptotic and three-dimensional, differs in that the asymptotic result precesses undamped about a tilted mean state that corresponds to $-iu_1/\lambda_1$ (c.f. eq. (3.58)). The three-dimensional simulation, on the other hand, possesses a clear sign of damping within the eight days of time integration that, as Reasor, Montgomery, and Grasso (2004) argues, is due to the "dispersion of the vortex tilt asymmetry on the mean vortex [by] sheared VRWs". Longer integration times would eventually lead to a configuration where tilt becomes stationary. Although not directly captured by the asymptotic theory, we can partially mimic that behavior by introducing a damping term that is proportional to X, *i.e.*, we impose *Rayleigh damping*. The result of this approach with a damping term of $d = 0.035$ (c.f. eq. (3.59)) is plotted in the right panel of fig. 6.1. The observed damping is caused by the inevitable presence of a gradient of a Gaußian vorticity distribution at the critical radius. The damping rate of is comparable at least in terms of the order of magnitude to theoretical predictions (cf. Schecter, Montgomery, and Reasor 2002, Fig. 10). A precise state would require more insights into the core and skirt structure of the vortex and shall not be part of the present discussion.

For the remaining experiments of this chapter we draw the following conclusion: Damping by VRWs *is* present even in the well-prepared three-dimensional setting
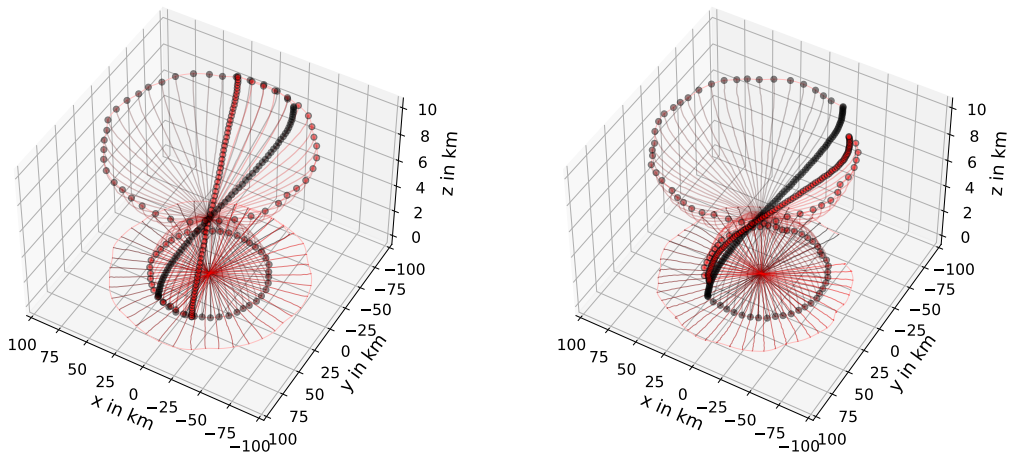
Figure 6.2.: Adiabatic time evolution of the centerline motion for asymptotic (left panel) and three-dimensional simulations (right panel). Both plots show the centerline from $t = 1$ d (black dotted line) to $t = 6$ d (red dotted line) with intermediate timesteps (thin lines) ranging from black to red. Material from: Dörffel et al. (2021)

of the initial data since there is a small but non-zero radial vorticity gradient at the critical radius[1]. This effect however, is on a timescale long compared to the precession timescale[2], as apparent by the fact that after 8 days the centerline has not yet become stationary but still exhibits precession. We therefore consider resonant damping by VRWs as a sub-dominant effect. As the experiments of section 6.2 will show, without external wind shear the damping becomes even less apparent.

6.2. Adiabatic Tilted Vortices

The initial data, outlined in sections 5.2.4 and 5.2.5, provide the setup for an initially tilted tropical cyclone that is balanced with respect to high-order asymptotic expansion modes. The centerline is initialized by the first non-trivial eigenmode of the Hamiltonian governing the adiabatic centerline motion. Hence, we expect precession of the vortex centerline about a vertical axis, constant tangential velocity, and maintaining the leading-order balances. Dominant motions are on the timescale of the precession, and motions attributed to small scale imbalances are on a faster timescale.

Left and right panels of fig. 6.2 in comparison show the time evolution of the vortex centerline for both, an asymptotic and a three-dimensional reference simulation, respectively. Precession time scales in the present case are approximately 5.5 days for the asymptotic model and 6.5 days for the three-dimensional reference simulation. This difference is well within the expected range as due to the fact that the asymptotic

---

[1]The radius where the primary circulation velocity is in resonance with the velocity due to precession (Reasor and Montgomery 2001)

[2]In the presented asymptotic experiment to mimic the behavior of the 3D solution the damping timescale is longer compared to the precession timescale by a factor of about 30, which corresponds to approximately 8 days. This damping timescale is of the same order of magnitude as theoretically predicted by the theory of critical layer stirring of Schecter and Montgomery (2004).
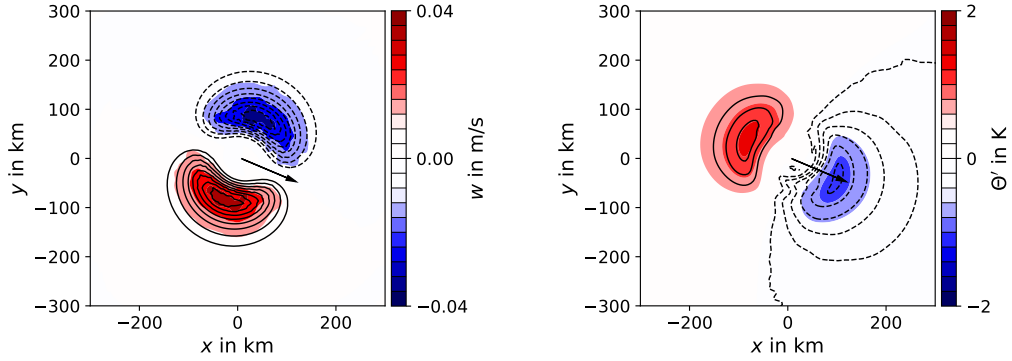
Figure 6.3.: Comparison of vertical velocity (left panel) and potential temperature perturbation (right panel) for asymptotic (contour lines) and three-dimensional simulation (color shading). Values are shown at $t = 1.5\,\mathrm{d}$ and $z = 5000\,\mathrm{m}$. w ranges from $-0.04\,\mathrm{m\,s^{-1}}$ to $0.04\,\mathrm{m\,s^{-1}}$ and Θ' from $-2\,\mathrm{K}$ to $-2\,\mathrm{K}$. Solid (dashed) contours indicate positive (negative) values. In both panels, the black arrow indicates the tilt vector $\partial_z X$. Material from: Dörffel et al. (2021)

expansion was carried out with the effective expansion parameter of $\varepsilon^{1/2} \approx 1/3$, and we truncated the centerline motion $\partial_t X$ at leading-order.

In section 5.2.5 we discussed how higher-order balance relations enter the picture. Both, vertical velocity w and potential temperature perturbation Θ', have non-trivial components which account for the fact that the vortex is vertically tilted, see fig. 6.3. Again, there is qualitative agreement between the asymptotic and the three-dimensional simulation with relative deviations of $O\!\left(\varepsilon^{1/2}\right)$.

These visualizations also highlight the structure of the balanced adiabatic flow: Due to the hydrostatic balance, which is maintained up to all considered asymptotic orders, the horizontal pressure gradient due to gradient-wind balance imprints perturbations to the variables ρ and Θ. Next to symmetric perturbations of ρ and Θ, which are associated to symmetric pressure gradient in the center of the storm, vertical misalignment of the centerline (the tilt $\partial_z X$) is the reason for the symmetric pressure gradient causing additional dipolar perturbations. For an adiabatic flow, however, potential temperature is materially conserved, i.e., the flow is along surfaces of constant potential temperature. Hence, the dipolar perturbation Θ' causes fluid parcels to ascend or descend on their orbit around the vortex core. Jones (1995) made the same findings in a setup where the storm is tilted by externally imposed shear.

6.3. Effects of Asymmetric Diabatic Heat Release

We argued in chapter 3 that there are two disjunct mechanisms of vortex intensity changes based on either symmetric or asymmetric diabatic heat release. For the latter one, and that is the mechanism of interest for this section, the orientation of the heating dipole with respect to the tilt of the centerline determines the dynamics of both, structure and intensity of the TC.

We completely neglect symmetric contributions to the diabatic heating as well as effects induced by sheared external wind. An asymmetric diabatic heating pattern is constructed from a prototype heating pattern that cancels the vertical velocity,

$$Q_{\Theta,\theta_0} = \frac{d\overline{\Theta}}{dz} w_{\text{dia}} \qquad (6.1)$$

with w_{dia} as constructed in eq. (3.68), the resulting equations are given by eqs. (3.65) and (3.70). In both equations, terms expressing the relative orientation of the diabatic heating dipole with respect to the centerline tilt, expressed by the angle θ_0, are key. We identify four neuralgic points:

- *Attenuation $\theta_0 = 0$*: Centerline tilt and tangential velocity decrease.

- *Stagnation $\theta_0 = \pi/2$*: Centerline tilt and tangential velocity remain constant, precession slows down.

- *Intensification $\theta_0 = \pi$*: Centerline tilt and tangential velocity increase.

- *Antistagnation $\theta_0 = -\pi/2$*: Centerline tilt and tangential velocity remain constant, precession speeds up.

For angles in between, the behavior smoothly transitions in a sense, that the asymmetric diabatic forcing of the centerline, iQ, (superposing the adiabatic motion) is rotated in the horizontal plane while the angular dependency of $u_{r,*}$ is captured by the factor $\cos\theta_0$.

In a series of subsequent experiments we will test the asymptotic theory and compare it against results of three-dimensional simulations where the diabatic heating pattern is constructed along the lines of section 3.4.3. Special emphasis will be put on the orientation of the diabatic heating dipole.

6.3.1. Stagnation

The experimental setting called *stagnation* in the further course of this work naturally arises from the construction in section 3.4.3, where we constructed a heating dipole that cancels the vertical velocity at leading order. The relative angle between tilt and heating dipole is $\theta_0 = \pi/2$. Although appealing, since leading-order tendency equations become elegantly simple (cf. eqs. (3.65) and (3.70)), this test undoubtedly shows the limitations of comparing three-dimensional simulations with leading-order asymptotic equations.

From a physical point of view a bit of a dull experiment, the stagnation test reveals how far we can go by forcing the vortex by an artificial diabatic heating dipole before driving the three-dimensional simulation into a regime where the flow is not well-represented by the asymptotic theory, anymore. The challenge of the present experiment is twofold: For once, as discussed in section 3.4.3, coupling between the inner-core and the outer QG flow suffers from the singularity of the outer point-vortex flow that does not find a matching counterpart in the inner-core flow when $w \equiv 0$. The situation becomes less severe through the scaling regime with $\alpha = 0$, *i.e.*, for a vortex whose core size is of $O(100\,\text{km})$. Nonetheless, the singularity remains unmatched even in that case, but the effect is shifted to higher asymptotic orders. Physically speaking: There is a forcing induced by the Coriolis force acting on the QG scale that the vortex does not translate

into a precessing motion of the centerline as the inner-core flow is forced to remain stationary. This induces a stress on the vortex structure that, on the long run, disrupts its integrity. Hence, we need to restrict the heating to a limited time interval. A consistent theory for that case would require including a weakly decaying heat source also in the QG far field regime, which is missing in the present state of the theory. In the context of QG flows, an asymptotic theory for this purpose has recently been published (Klein, Schielicke, et al. 2021). Combining it with the present TC model, however, is left to future research.

A second challenge consists in reconstructing the dynamical degrees of freedom of the asymptotic model, *i.e.*, the centerline and circumferentially averaged tangential velocity, and construct the asymmetric diabatic heating pattern from that. The solution space of the asymptotic model, however, is embedded into the three-dimensional solution space of the three-dimensional atmospheric equations, that clearly is of higher cardinality. Phrased abstractly, this means that a solution of the three-dimensional model has additional degrees of freedom which may be unintentionally excited, *e.g.*, by (inevitable) errors in the reconstruction procedure. As we will see, the asymptotic theory in fact reproduces the behavior of the three-dimensional simulation to a sufficient degree, if the solution remains close to an asymptotic state. Especially small scale oscillations of the centerline, thus strong local gradients, as part of the reconstruction, however, may lead to non-linear feedback loops eventually crashing the simulation.

These difficulties aside, for the sake of a quantitative comparison between the two different approaches we aim for numerical solutions of both, asymptotic and three-dimensional equations, which show the vortex behavior for $w \approx 0$. Computing the diabatic component of the vertical velocity involves a notion of the tilt that requires numerical reconstruction of the centerline position by means of eq. (5.23) and the subsequent numerical differentiation. The resulting diabatic heating then is injected as a source into the potential temperature equation, all together a process which involves the risk of suffering from numerical instabilities. To this end, the experiment needed to be fine-tuned to preserve the structure of both, vortex centerline and mean circumferential velocity. Here, we continue using a setup found sufficient to show the considered effects.

To limit the heating to a restricted period in time, we multiply the diabatic heating constructed in eq. (6.1) by an *amplitude factor* of the form

$$a(t) = a_0 \exp\left(\frac{(t - t_0)^2}{2\sigma^2}\right), \tag{6.2}$$

where we use $a_0 = 1$, $t_0 = 1.5\,\mathrm{d}$, and $\sigma = \frac{1\,\mathrm{d}}{2\sqrt{2\ln 300}}$, *i.e.*, a Gaussian profile centered a $t = t_0$ and approximately limited to the time interval $[1\,\mathrm{d}, 2\,\mathrm{d}]$. The expected negligible impact on the mean tangential velocity (5.26) is shown in fig. 6.4 by plotting its maximum for the three-dimensional simulation. The reference plot for the asymptotic simulation is omitted as the mean tangential velocity is trivially stationary.

At $t = 1.5\,\mathrm{d}$, $a(t) = 1$, hence the diabatic heating Q_Θ is such that the vertical velocity w is supposed to be suppressed at leading order. In fig. 6.5, Q_Θ and w (left and right panels, respectively) are plotted at that time and $z = 5000\,\mathrm{m}$. As expected, the diabatic heating pattern that is 90° rotated relative to the tilt (indicated by the arrow) leads to canceling the dominant mode of w (cmp. to fig. 6.3, left panel) leading to the residual on the right which is about one fifth in amplitude compared to the adiabatic vertical velocity.
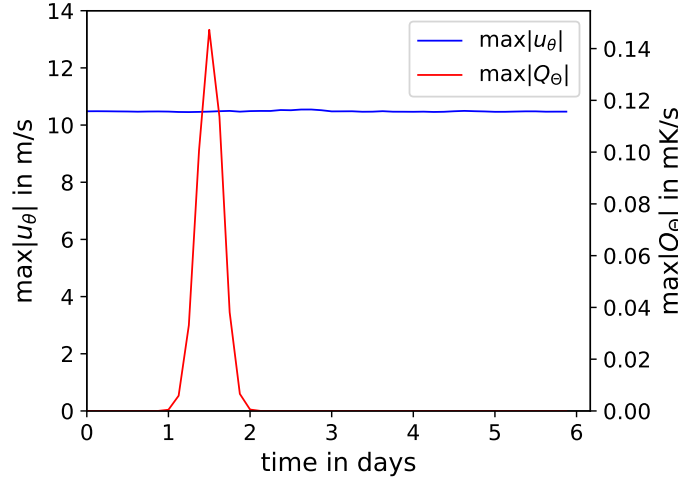
Figure 6.4.: Maximum of mean tangential velocity (blue) for stagnation test applying the heating (maximum amplitude shown in red) with $\theta_0 = \pi/2$ and $a(t)$ given by eq. (6.2). The figure shows the result of the three-dimensional reference simulation. Material from: Dörffel et al. (2021)

This is in perfect agreement, since the representation of w by the first asymptotic mode induces a relative error of order $O(\varepsilon^{1/2}) = O(1/3)$.

During the phase of active heating, in both panels of fig. 6.6 the centerline precession is slowed down. After shutting down the heating, the precession frequency is restored to its value before the heating was activated. In the three-dimensional reference experiment, however, higher-order oscillations become apparent which are most likely caused by projections of the diabatic term iQ in eq. (3.34) onto eigenmodes of the Hamiltonian $\hat{H}$ higher than the first. Higher-order eigenmodes thus activated are superimposed on the first eigenmode and oscillate with higher frequency. The reason for this behavior may be deviations of the estimated centerline reconstruction of eq. (5.23) in the three-dimensional simulation from the true one (recall the discussion above).

With the present stagnation experiment we found a stable setup that bypasses the issues that challenge the stability of the vortex as discussed above. In the further course of this section we can analyze the behavior of the tilted vortex under rotations of the heating dipole.

6.3.2. Intensification

We have shown that for a dipolar heating pattern, rotated by $\theta_0 = \pi/2$ relative to the tilt, tangential velocity (*i.e.*, intensity) remains constant since the positive and negative contributions of energy transfer cancel each other. In section 3.1.3 we discussed that for a given heating dipole the energy input depends on the correlation of diabatic heating and potential temperature perturbations.

To this end, we set up an experiment where both quantities are positively correlated. For the sake of comparison with the previous experiment, we construct the diabatic heating such that maximum heating rate is the same for both experiments, and it only differs in the phase shift $\theta_0 = \pi$. The prototype formulation of the heating dipole,
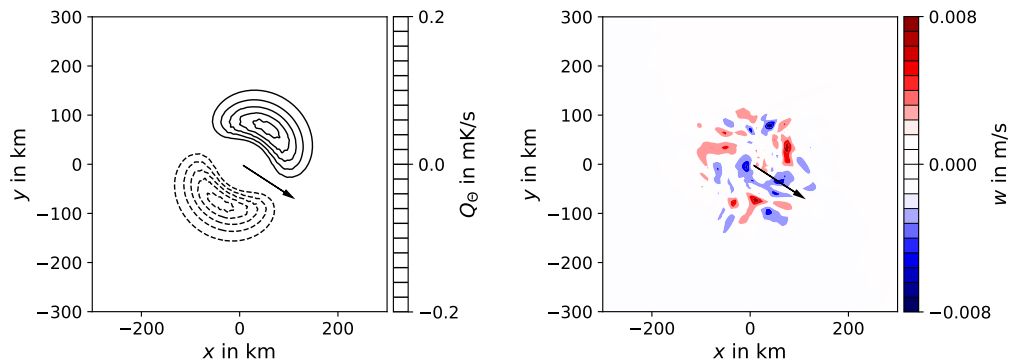
Figure 6.5.: Diabatic heat release (left) in stagnating configuration and response of vertical velocity (right). Both panels show horizontal slices at $z = 5000\,\text{m}$, positive contour lines in the left panel are solid, negative ones are dashed. In both plots, the centerline position is indicated by the base of the back arrow and tilt by its direction. Material from: Dörffel et al. (2021)
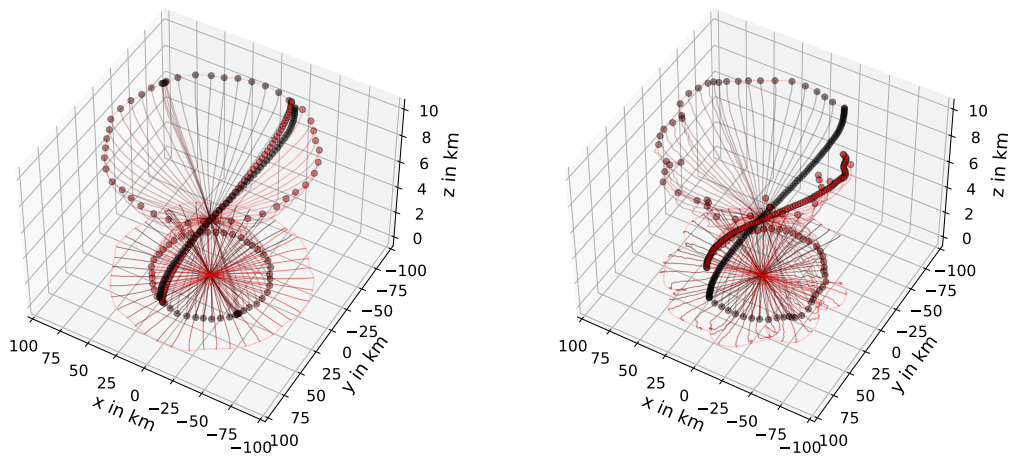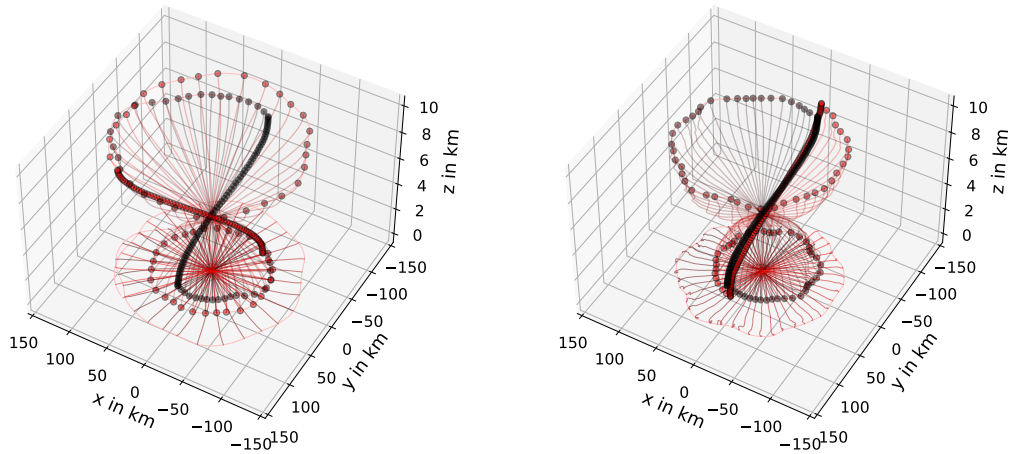

Figure 6.6.: Centerline of stagnation test. Similar to fig. 6.2, the centerline time evolution for the stagnation experiment is shown for both, asymptotic (left) and three-dimensional model equations (right). Material from: Dörffel et al. (2021)
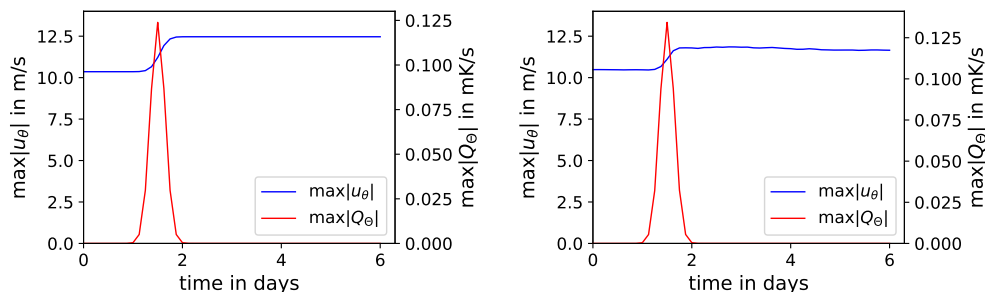
Figure 6.7.: Maximum tangential wind for intensification experiment (blue). Additionally, the amplitude of the heating dipole is plotted by the red curve. Material from: Dörffel et al. (2021)
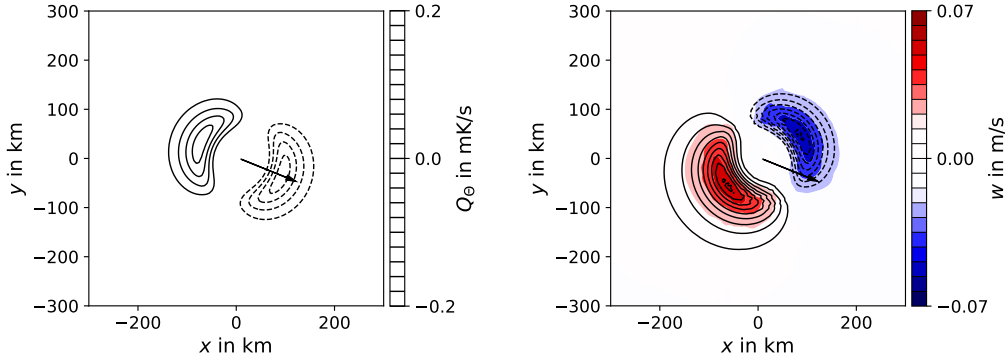
Figure 6.8.: Diabatic heat release in intensifying configuration and response of vertical velocity (cmp. with fig. 6.5). Material from: Dörffel et al. (2021)

given in eq. (6.1), involves the dependency on the tilt and thus modulations in the tilt amplitude would impact on the heating amplitude. Keeping the latter constant, when computing the heating dipole, we replace the dependency on the tilt by

$$
\frac{\partial \boldsymbol{X}}{\partial z} \rightarrow \left| \frac{\partial \boldsymbol{X}}{\partial z} \right|_{t=t_0} \frac{\partial_z \boldsymbol{X}}{|\partial_z \boldsymbol{X}|} \, ,
\tag{6.3}
$$

i.e., we fix the amplitude at time t_0 but follow its time-dependent orientation. Same as in the previous experiment, we constrain the heating in time by the factor given eq. (6.2). Probing the vortex by an asymmetric heating pattern constructed in that way leads to increased tangential wind speed as demonstrated in fig. 6.7 (compare with fig. 6.4 of the stagnation experiment).

As indicated in section 3.1.1, the intensification mechanism is traced back to circumferentially averaged radial motions $u_{r,*}$ that balance vertical mass fluxes through the surface of a tilted control volume (cf. fig. 3.2). Figure 6.8 confirms that antiparallel relative orientation of tilt (black arrow) and the diabatic heating dipole (contour lines in left panel) lead to a Fourier-1 mode configuration of the resulting vertical velocity (right panel) that is rotated by $\sim 135°$ relative to the tilt, *i.e.*, a phase shift of about $-45°$ in comparison to the adiabatic configuration (see fig. 6.3).

With fig. 6.9 we also want to highlight the influence of asymmetric heating on the dynamics of the centerline. For both, asymptotic (left panel) and three-dimensional simulations (right panel), the tilt increases with active heating and remains at an increased level after the heating is shut off.

The constraints on the heating dipole, discussed in section 6.3.1, yield a rather small impact on the tangential velocity when rotated into the uptilt direction, see fig. 6.7. To demonstrate the potential of asymmetric heating in intensifying we lift these constraints a little by increasing the duration of heating to 3 days. In fig. 6.10, we can observe a significantly larger response of the maximum tangential wind speed by the elongated heating period demonstrating the potential ability of this pathway to increase the intensity of the storm.

Figure 6.9.: Centerline of intensification test. Similarly to figs. 6.2 and 6.6, the centerline time evolution for the stagnation experiment is shown for both, asymptotic and three-dimensional model equations. Material from: Dörffel et al. (2021)
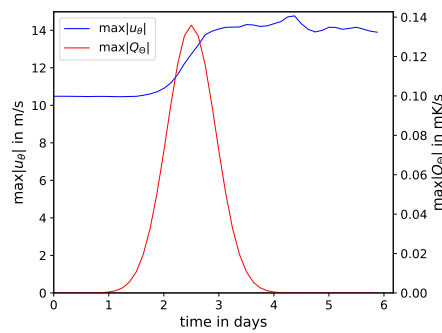

Figure 6.10.: Maximum tangential wind for strong intensification experiment. In comparison to fig. 6.7, the heating (indicated by the red curve) is applied for 3 days. Material from: Dörffel et al. (2021)
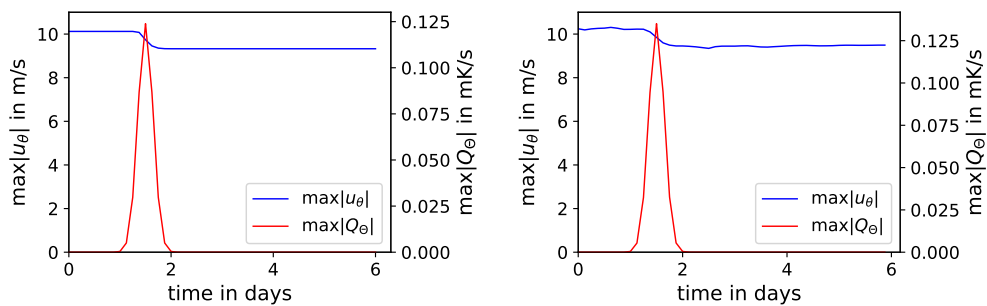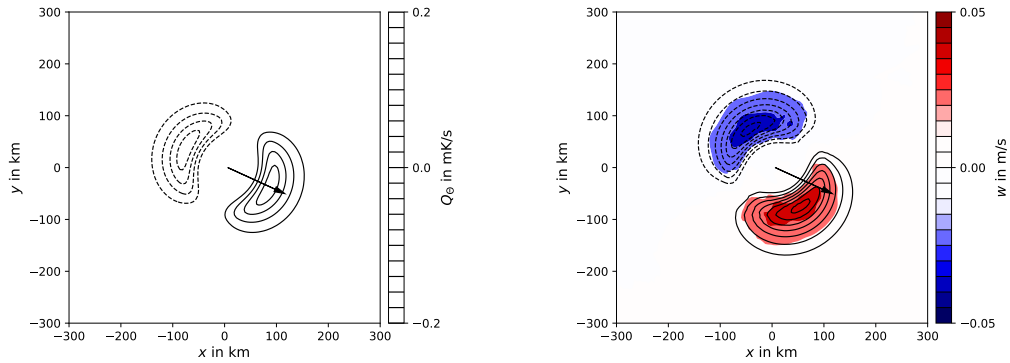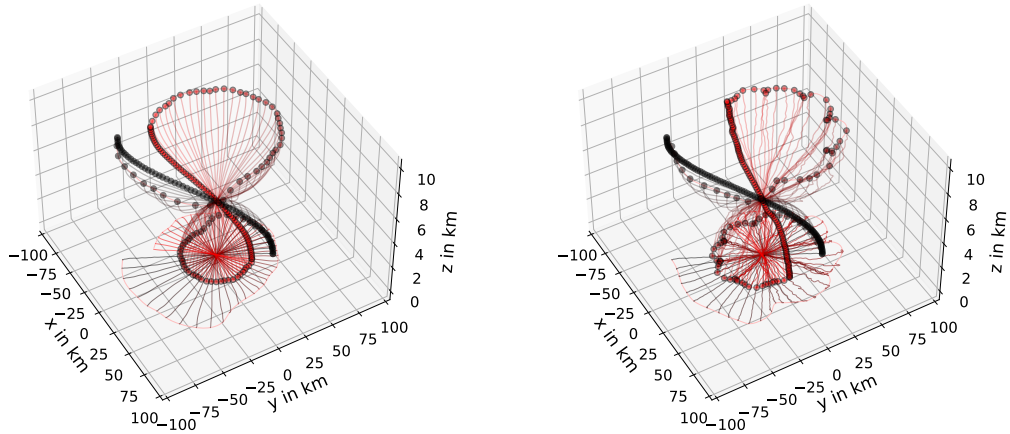

Figure 6.11.: Maximum tangential wind for intensification experiment. Plotted are the quantities $\min_z \max_r u_{\theta,0}$ (blue) and $\max Q_\theta$ (red). Material from: Dörffel et al. (2021)

Figure 6.12.: Diabatic heat release in attenuating configuration and response of vertical velocity (cmp. with fig. 6.5). Material from: Dörffel et al. (2021)

Figure 6.13.: Centerline of attenuation test. Similar to figs. 6.2 and 6.6, the centerline time evolution for the stagnation experiment is shown for both, asymptotic and three-dimensional model equations. Material from: Dörffel et al. (2021)

6.3.3. Attenuation

The heating (6.1) takes its maximum along the vertical axis where the tilt is the largest, *i.e.*, in the middle layers of the atmosphere. Thus, we expect the strongest impact on the velocity, which is initially uniform in the z-direction (in the tilted coordinated system), in the mid-levels of the atmosphere by slowing down the circulation there. To this end, we analyze the quantity $\min_z \max_r u_{\theta,0}$ that tracks the decrease of $u_{\theta,0}$ at the mid-levels. The result is plotted in fig. 6.11 confirming the weakening ability of the present heating configuration.

Similar to fig. 6.8, we show the dipolar vertical velocity field w at $z = 5000\,\mathrm{m}$ and $t = 1\,\mathrm{d}$ in fig. 6.12, right panel. The heating dipole, shown in the left panel, causes the vertical velocity dipole w_1 to align with an angle of $-45°$ relative to the tilt vector $\partial_z X$.

Finally, fig. 6.13 displays the time series of both, asymptotic and three-dimensional simulation. As expected, the tilt decreases due to the heating dipole oriented with $\theta_0 = 0$.
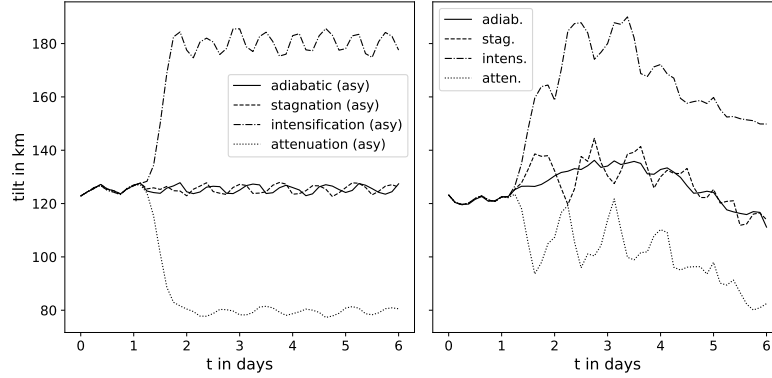
Figure 6.14.: Tilt dynamics of the individual experiments of section 6.3. Left and right panel show the results of the asymptotic (left) and three-dimensional simulations (right). Material from: Dörffel et al. (2021)

Though, the three-dimensional simulation result is affected by the same oscillations experienced in the previous experiments.

6.3.4. Summary of Tilt Dynamics

Here, we summarize the tilt dynamics of the experiments conducted in section 6.3. Figure 6.14 demonstrates the effects of the various configurations of asymmetric diabatic heating to the amplitude of the tilt, measured by the norm of the local tilt vector:

$$\left\|\frac{\partial X}{\partial z}\right\| := \int\limits_0^{z_{\text{top}}} \left(\sqrt{\frac{\partial X}{\partial z} \cdot \frac{\partial X}{\partial z}}\right) dz, \qquad z_{\text{top}} = 10\,\text{km} \tag{6.4}$$

The left and right panels of fig. 6.14 display the dynamics of the asymptotic and the three-dimensional simulation approaches, respectively. In all cases, heating is applied between $t = 1\,\text{d}$ and $t = 2\,\text{d}$. As a first general statement, we realize that the tilt dynamics correlates with the orientation of the dipole of the asymmetric diabatic heating. In case of the parallel alignment of the heating dipole and the tilt vector (both pointing in the same direction), the tilt decreases (dotted curves), whereas the situation turns around with the opposite direction (antiparallel orientation) of tilt and heating dipole, *i.e.*, the tilt increase (dash-dotted curves). These two setting are found in the previous subsections to attenuate (parallel orientation) and intensify (antiparallel orientation) the primary circulation. By comparing to the adiabatic experiment (solid curves), presented in section 6.2, we are able to confirm that the configuration of the heating dipole vector being rotated 90° counter-clockwise relative to the tilt vector (dashed curves) leads to no significant deviation from the adiabatic behavior, as also found for the mean tangential wind in section 6.3.1. There, we found that during the phase of active heating, the precession of the centerline slows down, which leads to the phase shift of the higher-order oscillations after the heating shut down, obvious in the left panel of fig. 6.14, between adiabatic and stagnation experiment.

  Albeit the qualitative agreement between the asymptotic model predictions and the three-dimensional simulations, in varying strength, the adiabatic reference experiments
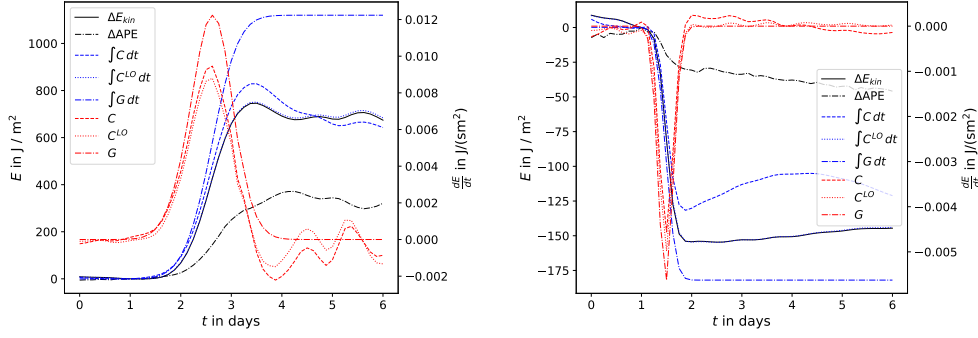
Figure 6.15.: Kinetic and available potential energy (solid and dashed black lines) of intensifying (left) and attenuating (right) vortices as presented in section 3.1 and section 6.3.3. Energy transfer rates according to Lorenz (1955) are given by the red curves and their corresponding integral expression by blue curves of the same style. More details are provided in the main text. Material from: Dörffel et al. (2021)

(black curves) exhibit oscillatory features of the centerline tilt in both simulation approaches. These are most likely the result of the excitation of higher-order eigenmodes of the centerline Hamiltonian. For the asymptotic simulations, all experiments feature an oscillation of approximately 1-day period. The three-dimensional results, however, add another mode of approximately 10 days (5 days for the half-wave). The effects of diabatic heating are superimposed on top of these oscillatory features. In case of the asymptotic experiments, we can conclude that the post-heating behavior correspond to the one before the heating, *i.e.*, stationarity with a small higher-order perturbation of period 1 day. The three-dimensional experiment, however, reveals more sever deviations between pre- and post-heating phases. There are rather substantial excitations of modes with 1-day period for all the experiments with diabatic heating activated. This may be a manifestation of the difficulty there is in aligning the heating dipole with the *effective* centerline in the three-dimensional experiments. In that approach, the centerline is not an explicitly given object but needs to be determined by approximate methods, and therefore it is likely to misplace the center of the heating dipole from what the "simulation sees as centerline". Approaches for more sophisticated and robust methods to determine the centerline are presented by Mikula et al. (2021). However, also for the three-dimensional simulations, the tilt dynamics follows the same trends as the asymptotic experiments after neglecting the excitation of higher-order modes.

6.4. Discussion on the Energetics of Tilted Vortices

Thus far, we analyzed intensity changes on the basis of changes of mean tangential wind. In addition to that we now want to inspect the time evolution of total kinetic energy, computed as

$$E_{\text{kin}} = \frac{1}{2} \int_{\Omega} \rho (\boldsymbol{u}_{\parallel}^2 + w^2) \, d\Omega \qquad (6.5)$$

with Ω the three-dimensional simulation domain.

To this end, along the lines of section 3.1.3, where we presented Lorenz's (1955) framework of available potential energy (APE) that provides analytical expressions for energy rates accounting for the *generation* of APE (G), the *conversion* between APE and kinetic energy (C), and dissipation of kinetic energy by friction (D), here we will analyze the three-dimensional simulation data and track these energy transitions. This approach shall provide a more profound understanding of the asymmetric mechanism of intensity change. In section 3.1.3, we reformulated the original equations of Lorenz (1955) to apply them to data given on Cartesian grid cells (see eqs. (3.17) and (3.18)). Further, we found that under the conditions of mean-zero diabatic heating (*i.e.*, especially in the case of purely asymmetric diabatic heating), the leading-order expressions of C and D take the same analytical expression (cmp. eqs. (3.9) and (3.17)). Below, we will discuss this statement on the basis of fig. 6.15.

In both panels of fig. 6.15, the energy quantities ΔE_{kin} and ΔAPE are plotted by black solid and dashed lines, respectively. Both quantities are computed against a reference state at $t = 1\,\text{d}$. C and G (according to eqs. (3.17) and (3.18)) are displayed by red dashed and dash-dotted lines, respectively. Integrals of G and C are depicted by blue lines of the same style, again. Additionally, we plot the expression eq. (3.9b) (labeled by C^{LO}, dotted lines) found to be identical for *generation* and *conversion* at leading-order in section 3.1.3. For all energy-like quantities the axis is plotted on the left, while for all energy rates of change, the corresponding axis is on the right.

In the left panel of fig. 6.15, we examine the simulation data of the *strong intensification experiment*, and we immediately conclude that changes in the energies E_{kin} and APE are correlated to amplitudes in the transitions rates and thus to the release of diabatic heating. Furthermore, we find that indeed, at leading order the energy transition rates coincide approximately. Considering the asymptotic truncation at first order, the relative discrepancy between all plotted energy rates is well within the relative error bound of $\varepsilon^{1/2} \approx 1/3$.

In addition to the rephrased version of Lorenz's (1955) equations for G and C, we plotted C^{LO} which coincides analytically with G assuming the WTG law to be satisfied, *i.e.*, when diabatic heating directly results in balanced vertical motions. It is remarkable, that the integral of C^{LO}, using the vertical velocity field as result of the three-dimensional simulation (eq. (3.9b)), is virtually identical with the time series of E_{kin}. It represents the kinetic energy time series even better than the original integral expression for C. We observe that G is higher in amplitude during the active phase of heating, while it becomes neutral before and after. C and C^{LO} on the other hand feature small amplitude oscillation after diabatic heating is turned off. Finally, we notice that the difference between G and C (or C^{LO}) approximately compares to the increase in APE.

Similarly, we present the energy analysis for the *attenuation* experiment (cf. section 6.3.3) in the right panel of fig. 6.15. We can observe the analogous behavior, *i.e.*, essentially negative conversion rates and decrease of E_{kin} and APE. In this configuration, the coincidence between the energy conversion rates is even closer which is to be expected, since the solution converges towards the trivial state of zero tilt and velocity, *i.e.*, is inherently more stable.

On the basis of the previous observations, we are able to draw the following conclusions: Our initial statement that at leading order APE, created by the correlation of perturbation potential temperature and diabatic heating (cf. eq. (3.17)), is directly

converted to kinetic energy via vertical motions and accumulates only at next-to-leading-order. This accumulation is due to deviations from the WTG law, since the evaluation of G equals that of C^{LO} except for the fact that in the latter the expression $\frac{Q_\theta}{\partial_z \Theta}$ is replaced by w. Since furthermore $\int C^{LO}\, dt$ follows the time series of E_{kin} almost identically, we infer that it is the correlation of potential temperature perturbation and vertical motion resulting from the diabatic heating that drives intensity changes. Although physically meaningful in the context of the presented setting for the sake of highlighting the physical mechanisms, dipolar diabatic heating pattern with areas of accentuated positive and negative diabatic heat exchange are not realistic for TCs. Nonetheless, the asymmetric patterns of vertical velocity that are caused by the asymmetric diabatic heating are what couples to the tilt asymmetry of the flow field and has the potential to steer the vortex towards intensity changes. Even after the heating is turned off, vertical motions (accounting for imbalances) further drive the conversion between APE and E_{kin}.

6.5. Interaction of Shear and Diabatic Heat Release

In the previous section, we discussed the intriguing effects of asymmetric diabatic heating as a driver for intensity and structural (*i.e.*, centerline) changes and compared solutions to the asymptotic with those of the unconstrained three-dimensional equations (2.1). We argued that there is qualitative and, up to the truncation order of the asymptotic expansion, quantitative agreement between the two approaches. This enables us to make further prediction on the basis of the asymptotic model. Here, we want to highlight the interaction of symmetric, asymmetric diabatic heating, and shear with the structure and intensity of the vortex aiming for a simple yet realistic scenario. To this end, we set up initial data for the tangential velocity by the profile depicted in fig. 5.2 but multiply it by the function

$$z \mapsto 1 - \frac{z}{z_{\text{max}}}\,. \tag{6.6}$$

The numerical grid covers the physical domain $(r, z) \in [0, 1000\,\text{km}] \times [0, 10\,\text{km}]$ (in rescaled coordinates) by 128×32 grid points.

The series of experiments presented here takes a parametrization of diabatic heating into account that possesses both, Fourier modes 0 and 1. Higher-order modes are discarded as being irrelevant at leading order. The heating itself is constructed on the principle that the tilted structure of the vortex modulates the thermodynamic state of the inner core region by a wavenumber-1 perturbation. Equation (2.52) connects the dipolar perturbation of potential temperature to the tilt of the centerline. For adiabatic motions, where particles follow isosurfaces of constant potential temperature (entropy), the dipole, *i.e.*, wavenumber-1 perturbation in azimuthal direction translates into lifting/lowering of particle trajectories as they circulate about the centerline. This dipolar potential temperature perturbation hence translates into the vertical lift

$$\Delta z = \frac{\Theta'}{d\overline{\Theta}/dz}\,. \tag{6.7}$$

We assume that a particle, lifted from below z_{LCL} (for *lifting condensation level*) and elevated above z_{LFC} (for *level of free convection*) is able to release heat due to
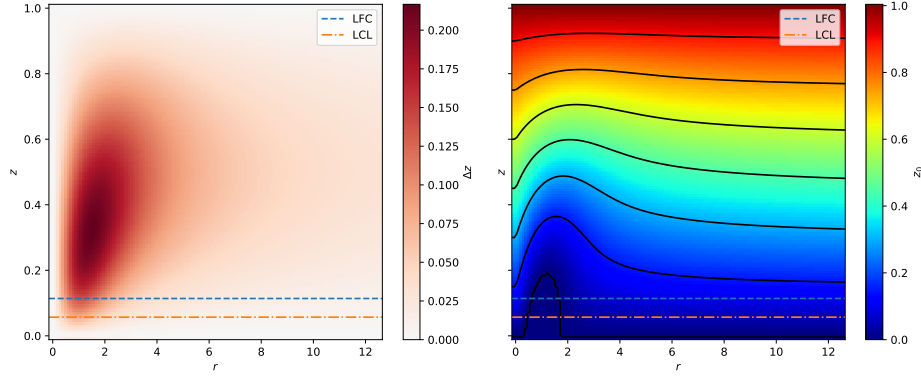
Figure 6.16.: Adiabatic lifting due to tilted centerline. The left panel shows the amplitude of adiabatic lifting Δz (cf. eq. (6.7)) of a particle orbiting around the centerline as result of the potential temperature perturbation $\Theta^{(4)}$ (cf. eq. (2.52)). In the right panel the origin height z_0 is shown from which a particle is lifted to $z = z_0 + \Delta z$. All quantities are in non-dimensional form.

condensation of moisture (cf. fig. 6.16) (cf. fig. 6.17, left panel). Hence, we allow for heating only where $z - z_{\mathrm{LCL}} < \Delta z$ and $z > z_{\mathrm{LFC}}$. This procedure induces a mask to Δz (fig. 6.17, right panel) that sets values to zero everywhere except where (adiabatically induced) updrafts are strong enough to break through the layer between z_{LCL} and z_{LFC}, an ad-hoc model of a CIN. In the unlifted case, we model moisture through a linear profile with the maximum at the surface and zero at z_{LCL}. The adiabatic lifting mechanism then transports moisture through the CIN and above z_{LFC} where moisture can evaporate and release heat. The amount of heat is proportional to the moisture content transported from below z_{LCL}. Free convection is modeled by convolving the so far constructed diabatic heat release by a one-sided kernel to smear out the concentrated peak above z_{LFC} smoothly into the deep troposphere.

The above construction of diabatic heating relies essentially on the fact that the vortex is tilted, since moisture is transported through the adiabatic lifting mechanism. In other words, without tilt, *i.e.*, for a symmetric vortex there is no adiabatic lift along the path lines of orbiting air parcels which would lead to no diabatic heating from the proposed mechanism. For this reason, we additionally add a purely symmetric component to the diabatic heating that depends on the tangential velocity in the sense of WISHE. This addition delivers a purely symmetric heating pattern that is present even in the case of no tilt.

Motivated by the construction of eq. (3.68), we have

$$Q_{\Theta}^{\mathrm{WISHE}} = \frac{u_\theta}{r} \left(\frac{u_\theta^2}{r} + f u_\theta \right) . \tag{6.8}$$

The total heating then is a superposition of both contributions where prefactors determine the relative strength.
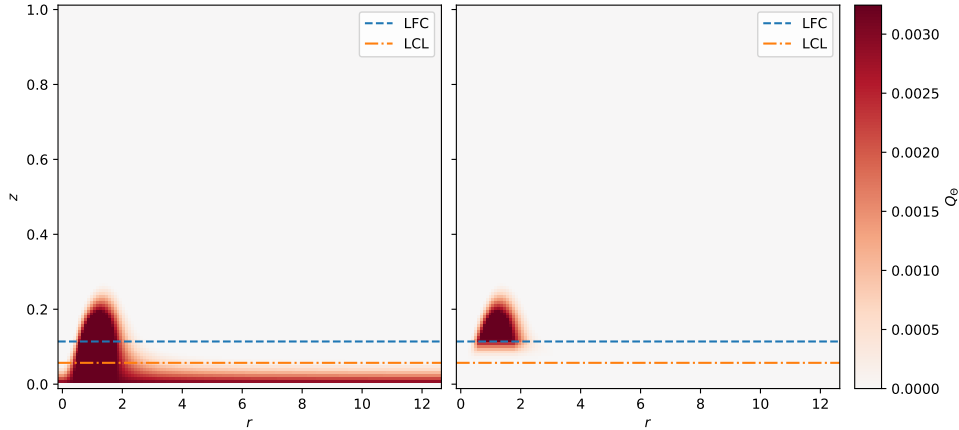
Figure 6.17.: Moisture transport due to adiabatic lifting. Adiabatic lifting (cf. fig. 6.16) caused moisture, modelled by a linear profile between 0 and z_{LCL} in the unperturbed atmosphere to be transported through the CIN layer between z_{LCL} and z_{LFC} (left panel). Parcels that are capable of passing through that layer are contributing to the heating (see right panel). All quantities are in non-dimensional form.

Shear, in the present series of experiments is induced by the external wind that takes the form

$$\boldsymbol{u} = \boldsymbol{u}_0 \cos(z/z_{\mathrm{max}}) \tag{6.9}$$

with the constant $\boldsymbol{u}_0$ determining the difference in wind speed between bottom and top of the simulation domain.

With the setup as outlined above, we first look into the effect symmetric heating has on the vortex structure and intensity. To this end, shear and asymmetric contributions are set to zero. Figure 6.18 (left and top right panel) show the ability of purely symmetric heating to align the centerline via the vertical advection term $A\partial_z X$ in eq. (3.34) that is due to symmetric diabatic heating and the resulting symmetric vertical velocity. The lower right panel of fig. 6.18 demonstrates the intensification connected to the purely symmetric heating.

On the other hand, when deactivating shear and symmetric heating and leaving only asymmetric heating active, fig. 6.19 demonstrates how the vortex undergoes vertical alignment by parallel orientation of diabatic heating and the tilt vector (cf. section 6.3.3) while in that setting the effecting intensity changes are negligible due to the fact that tilt decreases so fast that the coupling of the diabatic asymmetry to the tilt vanishes.

Finally, with shear, symmetric and asymmetric heating active, fig. 6.20 highlights a scenario, where shear and aligning forcings by symmetric and asymmetric diabatic heating compete with each other eventually leading to a configuration where the tilt (both, in orientation and amplitude) changes only slowly. However, the behavior of the maximum tangential velocity essentially follows that of fig. 6.18, although even between $t \approx 1\,\mathrm{d}$ and $t \approx 2\,\mathrm{d}$ the asymmetric diabatic heating extracts more energy from the system than the symmetric heating injects. The observed ongoing increase of u_θ may appear as a contradiction. Maximum wind speed, however, is a local quantity, while the integrated energy tendencies are global. We expect that, for a more realistic
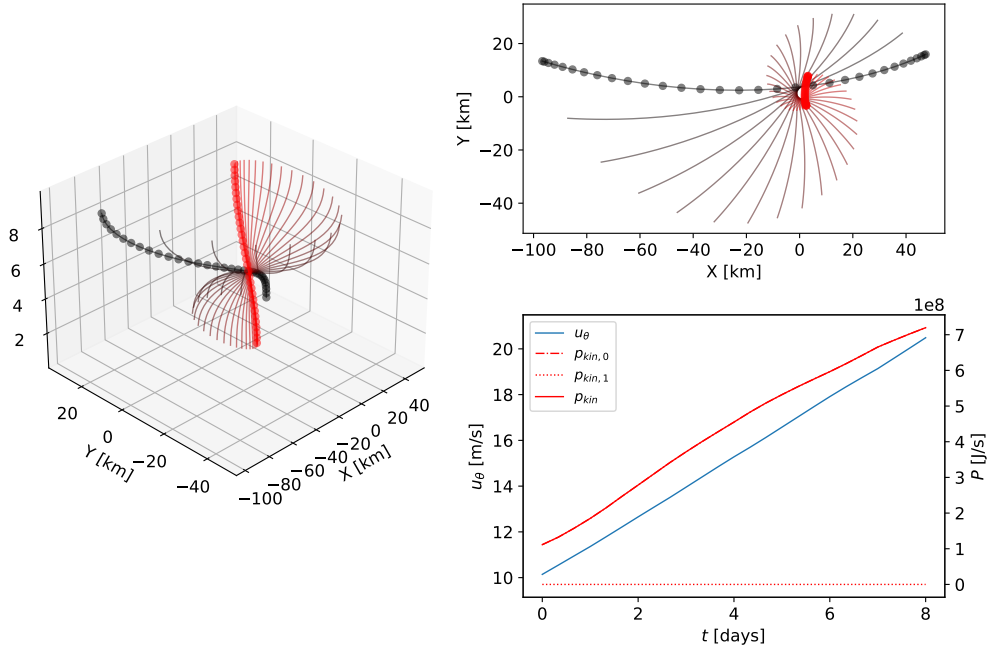
113

Figure 6.18.: Centerline evolution and kinetic energy budget under symmetric diabatic heating without shear. Left and top right panel show the centerline time evolution (perspective view and projection on the surface plane), while the lower right panel depict the time series of max u_θ (blue) and the integrated energy tendencies (red, cf. eq. (3.9)) due to symmetric ($p_{\text{kin},0}$, dashed, hidden by solid line), asymmetric ($p_{\text{kin},1}$, dotted) adiabatic heating, and the sum of both (p_{kin}, solid).

setting, this cancelation may lead to stagnation also in the tangential velocity. Further investigations are subject to future research. Anyway, for the present setting we conclude that the asymmetric component of diabatic heating efficiently leads to stabilization of the orientation of the centerline but does not affect the intensity to a strength that suffices to counteract the symmetric contribution of diabatic heating.

The above results need to be interpreted under the assumption made by the asymptotic theory. The leading-order equations were derived for the bulk flow of the vortex, where frictional dissipation does not play a major role. In real TCs, however, the most dynamical changes of intensity happen in the boundary layer, where friction *does* play a major role. Thus, there is a counteracting mechanism that would lead to balancing of intensifying and attenuating forcings. Due to the present lack of a suited extension of the asymptotic model that would incorporate the boundary layer, we leave this discussion open and refer to future work.
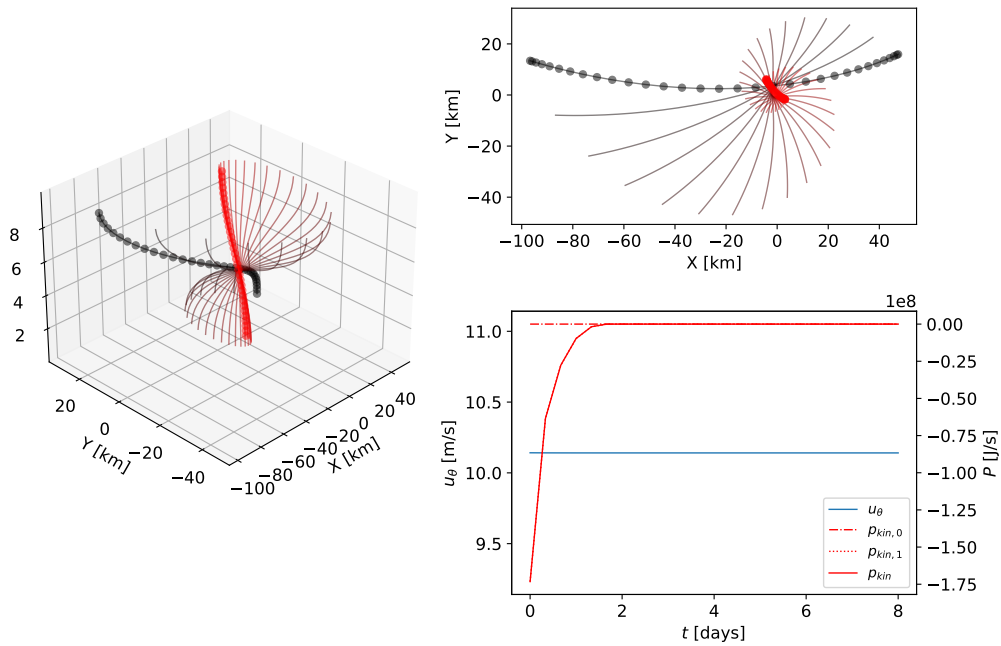
Figure 6.19.: Same as fig. 6.18 but with purely asymmetric diabatic heating and without shear.
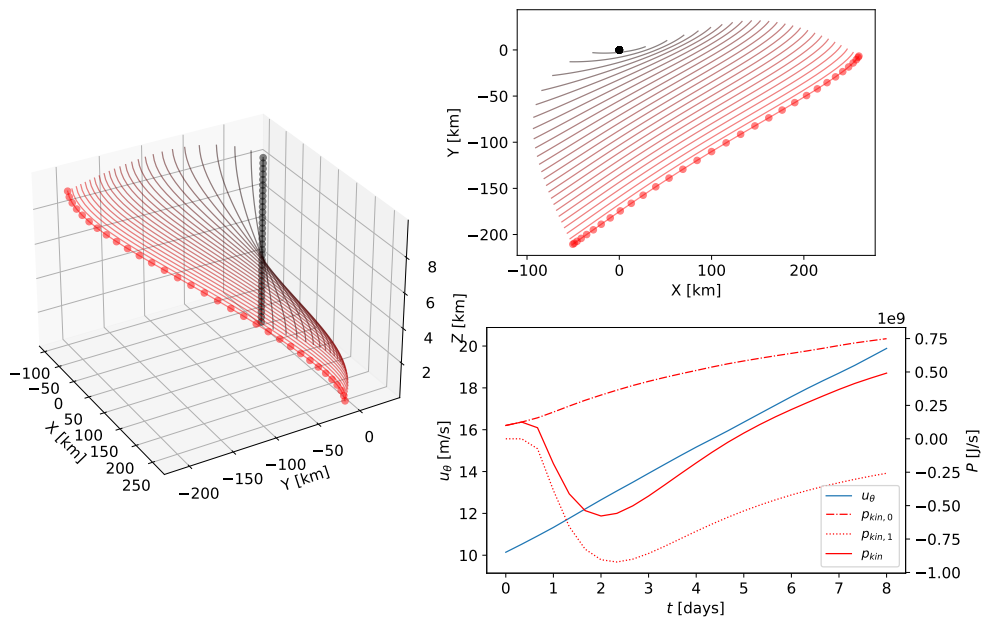

Figure 6.20.: Same as fig. 6.18 but with shear, symmetric, and asymmetric diabatic heating.

115

7. Summary and Outlook

This thesis is a continuation of the findings conducted by the preceding works of Mikusky (2007), Papke (2017), and Päschke et al. (2012). The main motivation was to test the asymptotic theory of Mikusky (2007) and Päschke et al. (2012) under various settings and find evidence for the applicability in the context of modelling TCs and further insights by comparing solutions to the asymptotic model with three-dimensional simulations.

To this end, we extended the asymptotic theory, originally derived for the interaction of the synoptic scale with the vortex core scale of $L_{\mathrm{meso}} = O(300\,\mathrm{km})$, to a vortex core scale of $L_{\mathrm{meso}} = O(100\,\mathrm{km})$ and showed that the leading-order reduced model equations are uniformly valid through both of these regimes. We identified the governing regimes as *gradient wind* and *cyclostrophic* and argued that with the asymptotic model we are well within the regime that describes TCs from the incipient phase to weak hurricane strength. We have also pointed out that for slender vortices embedded into a QG far-field the circulation-free limit essentially means that there is no coupling of the inner-core solution to the QG far-field, at least locally, *i.e.*, on horizontal levels where the circulation is vanishing. Hence, in this situation the inner core is driven by the forcing of external wind (shear) but there is no self-induced motion (precession) as a net effect of in vortex filament's circulation.

Furthermore, we analyzed the structure of the equation with special emphasis on the ability to structural and intensity changes. By analyzing linear and angular momentum budgets, we pinpointed intensity changes to two major factors: (i) Symmetric diabatic heating causes air parcels to redistribute in the r-z-plane. In this setting, angular momentum is materially conserved in the centerline-coordinate system, *i.e.*, constant along trajectories. Intensification (attenuation) are the result of decreasing (increasing) the radial distance of a fluid parcel relative to the vortex center. Depending on the radial (and vertical) distribution of angular momentum, the local velocity increases if higher angular momentum from larger radii replaces the residing fluid parcels. Similarly, lower angular momentum can be transported inwards, increasing the tangential velocity of the transported fluid parcels but ultimately, by replacing higher angular momentum parcels, lead to (local) attenuation. This is in complete agreement with preexisting findings studying axisymmetric TC models (Charney and Eliassen 1964; Emanuel 1986; Montgomery and Smith 2017a).

(ii) In addition to the symmetric mechanism, the asymptotic theory provides a pathway for intensity changes by asymmetric diabatic heating. With the tangential momentum budget, we traced intensity changes back to radial mass fluxes that are due to vertical motions causing in- or outflux through the boundaries of a tilted control volume that is based on the tilted centerline coordinate system. The angular momentum budget revealed that this intensification (attenuation) is connected to a source term that breaks angular momentum conservation in that particular coordinate system by breaking rotational invariance.

Further examination of the energy budget led to the following conclusions: Intensity changes are due to the correlation of diabatic heat release and perturbations of the potential temperature. Symmetric and asymmetric diabatic heating contribute at the same asymptotic order to the energy budget. It is, however, the vortex tilt that modulates the thermodynamic balance causing asymmetric perturbations of potential temperature and, by that, opening the "window" to the asymmetric pathway. In the context of Lorenz's (1955) theory of APE, this consideration led us to conclude that it is ultimately the vertical velocity resulting from the diabatic heating that drives the both, symmetric and asymmetric intensity changes. By numerical experiments, we demonstrated that for zero-mean heating, APE generated by diabatic heating is instantaneously converted into kinetic energy at leading order.

En route to solving the asymptotic equations numerically, by constructing formal solutions to the time-dependent problem, we were able to design a consistent, second-order time integration scheme. That enabled us to split the non-linear problem into building blocks of equation archetypes that were identified as archetypical PDE problem, each treated quasi-linearly and quasi-independently. This approach ultimately allowed solving Mikusky's (2007) asymptotic model by a robust and accurate second-order scheme in space and time. With the numerical framework at hand, we were able to show that, besides the specialized analytical solutions presented by Päschke et al. (2012), a wide range of time-dependent solution exists.

In a subsequent step, and in continuation to Papke (2017), we found, that for a variety of settings, the solutions to the asymptotic model correspond to those of the three-dimensional, unconstrained equations of atmospheric fluid dynamics. With special emphasis to the interaction between the tilt asymmetry of the flow field and asymmetries in the diabatic heating, we found that there is qualitative, and to the degree of the asymptotic approximation, quantitative agreement of the two approaches.

In a series of numerical experiments we outlined the interactions of the different forcings by both, symmetric and asymmetric diabatic heating, as well as external wind shear. We demonstrated that symmetric heating causes vertical alignment due to vertical advection of momentum, while asymmetric heating steers the vortex centerline depending on the relative orientation of the tilt and the heating dipole. For the parallel orientation of both, we found an additional pathway to vertical alignment of the vortex. This may be of special interest for explaining vortex resiliency against vertical wind shear in weak TC where organized, *i.e.*, symmetric convection is not yet strong enough to explain a counteracting force. In such a scenario, both, symmetric and asymmetric heating components, cause the flow to withstand shear forcing, while their contribution to the intensity of the TC may cancel each other, at least locally.

Further work may contribute to the question of rapid intensification. With the above mechanisms it is plausible that a stationary phase, as observed and described abundantly in the literature, may be the result of a balance of all the above forces. Rapid intensification (or weakening) could be the response towards a change of environmental conditions that directly or indirectly affect the established balance. The adjustment towards a new balance may be established within the timescale as considered for the asymptotic analysis, *i.e.*, in the order of one day. Nonetheless, there are model extensions likely to be necessary. We did not account for the stabilization mechanism due to VRW resonant damping. The timescale of this process is, as (Reasor and Montgomery 2001) pointed out, asymptotically speaking an order in ε faster than the present model.

By asymptotic matching, it would be possible to consider the long-term limit of a solution affected by resonant damping as the initial condition to the present asymptotic model. Since resonant damping, if present, leads to a stationary solution for constant background conditions, this task appears to be trivial. Thorough examinations of this mechanism and further implications w.r.t. the time evolution of TCs, however, are subject to future research.

Another question arose from the findings of this thesis, that is about the self-induced motions of the vortex. We found that the streamfunction at next-to-leading order of the inner-core solution induces motions of the centerline. That forcing, however, is composed of an adiabatic contribution, leading to precession, and another one caused by diabatic heating. The latter one itself splits into two contributions due to symmetric and asymmetric heating, respectively. While the symmetric component leads to vertical alignment of the vortex structure due to vertical advection, the asymmetric forcing term depends on the Fourier-1 modes of the diabatic contribution to vertical velocity. It is not yet fully understood, how the tilted vortex structure affects asymmetries in the vertical velocity field, but in general, it is easily conceivable, that the asymmetric forcing term to the centerline equation, iQ (cf. eq. (3.34)), is such that the vortex is shifted as whole. Mathematically speaking, a projection onto the zeroth (constant) eigenmode of the centerline Hamiltonian $\hat{H}$ would cause such a forcing. From a physical perspective, this touches upon the question of the extent to which the vortex generates its own background in which it is transported horizontally. That, again, is subject to ongoing and future research.

Appendices

A. Convergence Results of SHARPIE

In the course of solving the asymptotic equations as outlined in chapters 2 and 4, the model Scheme for Hamiltonian-Advection equations on Radial geometry by Pseudo-linear Implicit-Explicit integration (SHARPIE) was developed. Here, we want to present the results of a convergence test. For a convergence test covering the full dynamics of the asymptotic model, we initiated a simulation with zero-tilt centerline and tangential velocity

$$u_\theta(r, z, t = 0) = \frac{1 - \exp(-r^2)}{2r} \exp\left(-z/2\right) . \qquad (A.1)$$

r and z are given in non-dimensional units. The centerline is forced externally by the wind field

$$u_s = \cos(2\pi z) . \qquad (A.2)$$

In addition, the dynamics is forced by the diabatic heating computed from eq. (6.1) with $\theta_0 = 0$ and constant amplitude prefactor $a = 0.1$. The numerical grid extends to $(r, z) \in [0, 12.5] \times [0, 1]$ and the time integration stops at $T = 0.01$. The restriction on the ending time is necessary to avoid shock-like solution that eventually arise due to the non-linear advection. The lowest-resolved run has a resolution of 32 grid points in each spatial direction and takes two time steps, $i.e.$, $\Delta t = 0.01$. For each subsequent run, the resolution in each direction, as well as in time, is doubled. The highest number of grid points is 256. For all runs, the slope limiter is deactivated as to achieve full second-order reconstruction even in the vicinity of local maxima.

The error is computed between two subsequent runs by first averaging the solution from the cell-centered grid points of the grid with double the resolution to the locations of the cell-centers of the reference grid. The error is then taken as the modulus of maximum difference (l_∞-norm) between the two runs.

For reference, the solution of the simulation with 1024 grid points in each direction is displayed in fig. A.1. Both, the centerline X and the tangential velocity u have evolved throughout the integration time, but due to the short time interval only slightly. This is necessary because of the shock formation caused by the fully non-linear coupling of the system of eqs. (4.1). Time integration time T is chosen such to avoid shock formation within that interval based on heuristic experiments, which have shown that the convergence order diminishes shortly after. Nevertheless, the absolute (non-normalized) error for 64 grid points is $4.504 \cdot 10^{-4}$ for X and $2.785 \cdot 10^{-3}$ for u_θ, hence we consider the signal strong enough for a reliable error convergence analysis.

Figure A.2 displays the error convergence for both, the centerline X (dots) and the tangential velocity u (crosses). For both, comparison against a second-order reference, depicted by the solid line, shows that the error convergence is close to second order.
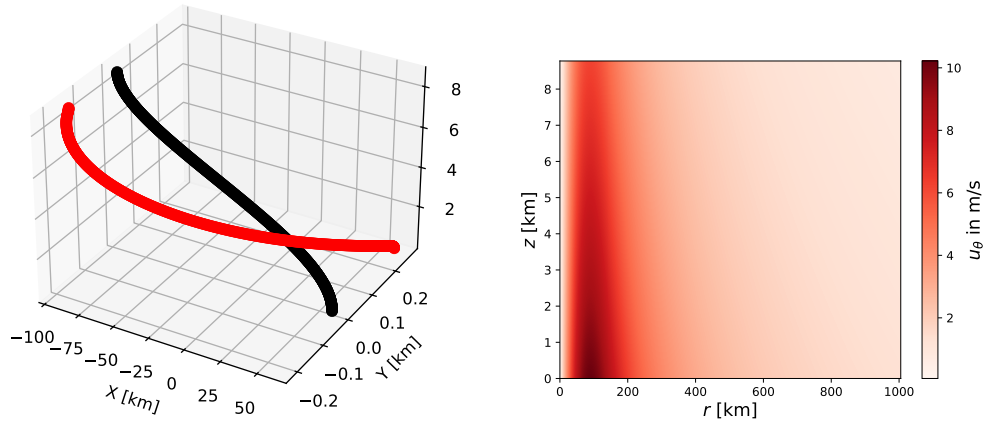
Figure A.1.: Solution of convergence test at final time $t = 0.025$. The centerline is shown at initial (black) and final time (red) in the left panel. The right panel shows the tangential velocity u at final time.
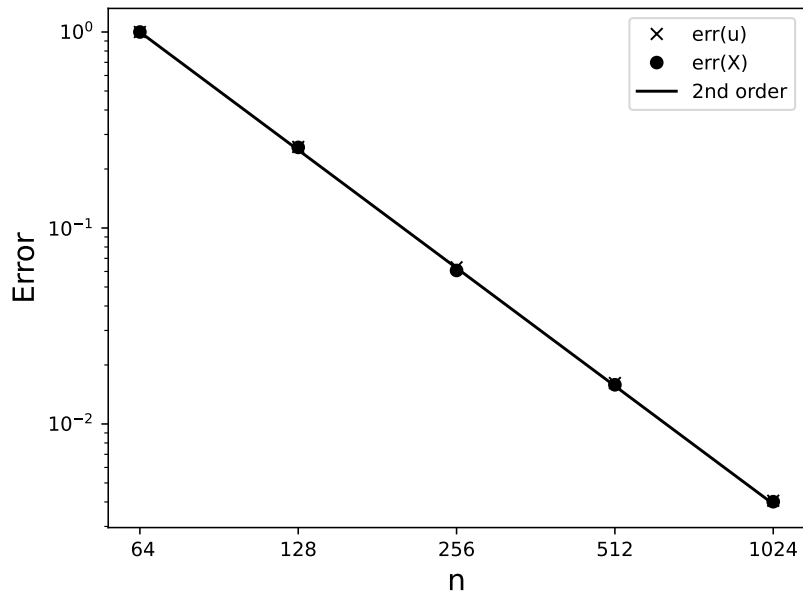

Figure A.2.: Normalized error convergence of SHARPIE. Each of the plotted errors of the tangential velocity (u) and the centerline (X) at the respective resolution are computed against a reference run with half the resolution. The errors of each variable are scale with respect to the errors at the coarsest resolution. The solid black line represents a second-order reference.

Zusammenfassung

Die vorliegende Arbeit untersucht das asymptotische Model, welches in seiner ursprünglichen Form von Päschke u. a. (2012) hergeleitet und veröffentlicht wurde. Es beschreibt die troposphärische Strömung eines stark geneigten tropischen Wirbelsturms oberhalb der planetaren Grenzschicht unter den Einflüssen von vertikaler Windscherung und diabatischer Wärmefreisetzung.

Wir beginnen mit der Herleitung der reduzierten Modellgleichungen, wobei wir im Wesentlichen den Ausführungen von Päschke u. a. (2012) folgen. Dabei zeigen wir eine Erweiterung auf, die es zulässt, das reduzierte Modell auch auf Stürme mit kleinerer räumlicher Ausdehnung anzuwenden, die sich im ursprünglich nicht berücksichtigten zyklostrophischen Regime befinden. Im Folgenden stellen wir analytische Untersuchungen der Gleichungen an, die als Resultat der asymptotischen Betrachtungen die Bewegung eines tropischen Sturms in führender Ordnung beschreiben. Darauf aufbauend treffen wir Aussagen über die Energiebilanz und die Veränderungen der Struktur des Strömungsfeldes im Zusammenhang von Intensitätsveränderungen, die durch symmetrische und asymmetrische Wärmefreisetzung hervorgerufen werden. Des Weiteren gehen wir auf die analytische Struktur der Gleichungen ein, was es uns erlaubt ein adaptiertes numerisches Schema zu konstruieren, das mithilfe von Finite-Volumen-Verfahren die asymptotischen Gleichungen effizient und robust integriert. Wir legen dabei besonderes Augenmerk auf die gekoppelte, semi-implizite Zeitintegration zweiter Ordnung.

Der verbleibende Teil dieser Arbeit wird numerischen Experimenten sowie der Darstellung und Interpretation der Ergebnisse gewidmet. Dabei werden Mechanismen, die im Zusammenhang mit rapider Verstärkung oder Abschwächung stehen und die Einfluss auf die Wirbelstruktur haben, sowohl isoliert als auch in kombinierter Weise untersucht. Die Experimente werden mithilfe der numerischen Implementierung der asymptotischen Gleichungen untersucht, sowie anhand von dreidimensionalen Referenzlösungen der Gleichungen der atmosphärischen Fluiddynamik. Wir zeigen mögliche Wege zur Intensitätsveränderung auf, die auf Interaktionen des Wirbels mit der Scherung des externen Windfeldes und einer Kombination aus symmetrisch-asymmetrischer diabatischer Wärmefreisetzungen zurückzuführen sind. Von großem Interesse ist dabei die Interaktion der asymmetrische Komponente der Wärmefreisetzung mit der Sturmstruktur, die wiederum die Intensität und Struktur selbst beeinflusst. Rückschlüsse in Bezug auf die Anwendbarkeit der asymptotischen Theorie im Zusammenhang mit rapider Verstärkung/Abschwächung werden als abschließender Beitrag dieser Arbeit gezogen.

Acknowledgments

Bibliography

Alvey III, G. R., J. Zawislak, and E. Zipser (2015). „Precipitation Properties Observed during Tropical Cyclone Intensity Change". In: *Monthly Weather Review* 143.11, pp. 4476–4492.

Arakawa, A. K. I. O. and V. R. Lamb (1977). „Computational Design of the Basic Dynamical Processes of the UCLA General Circulation Model". In: *Methods in Computational Physics: Advances in Research and Applications*. Ed. by J. U. L. I. U. S. Chang. Vol. 17. General Circulation Models of the Atmosphere. Elsevier, pp. 173–265.

Bannon, P. R. (1996). „On the Anelastic Approximation for a Compressible Atmosphere". In: *Journal of the Atmospheric Sciences* 53.23, pp. 3618–3628.

Barenblatt, G. I. (1996). *Scaling, Self-Similarity, and Intermediate Asymptotics: Dimensional Analysis and Intermediate Asymptotics*. Cambridge Texts in Applied Mathematics. Cambridge: Cambridge University Press.

Beam, R. M. and R. F. Warming (1976). „An Implicit Finite-Difference Algorithm for Hyperbolic Systems in Conservation-Law Form". In: *Journal of Computational Physics* 22.1, pp. 87–110.

Benacchio, T. and R. Klein (2019). „A Semi-Implicit Compressible Model for Atmospheric Flows with Seamless Access to Soundproof and Hydrostatic Dynamics". In: *Monthly Weather Review* 147.11, pp. 4221–4240.

Berger, M. J. and J. Oliger (1984). „Adaptive Mesh Refinement for Hyperbolic Partial Differential Equations". In: *Journal of Computational Physics* 53.3, pp. 484–512.

Bhalachandran, S. et al. (2020). „Characterizing the Energetics of Vortex-Scale and Sub-Vortex-Scale Asymmetries during Tropical Cyclone Rapid Intensity Changes". In: *Journal of the Atmospheric Sciences* 77.1, pp. 315–336.

Boussinesq, J. (1897). *Théorie de l'écoulement Tourbillonnant et Tumultueux Des Liquides Dans Les Lits Rectilignes a Grande Section*. Vol. Vol. 1. Paris: Gauthier-Villars.

Buckingham, E. (1914). „On Physically Similar Systems: Illustrations of the Use of Dimensional Equations". In: *Physical Review* 4.4, pp. 345–376.

Callaghan, J. (2017). „Asymmetric Inner Core Convection Leading to Tropical Cyclone Intensification". In: *Tropical Cyclone Research and Review* 6.3, pp. 55–66.

Callegari, A. J. and L. Ting (1978). „Motion of a Curved Vortex Filament with Decaying Vortical Core and Axial Velocity". In: *SIAM Journal on Applied Mathematics* 35.1, pp. 148–175.

Charney, J. G. and A. Eliassen (1964). „On the Growth of the Hurricane Depression". In: *Journal of Atmospheric Sciences* 21, pp. 68–75.

Chen, H. and S. G. Gopalakrishnan (2015). „A Study on the Asymmetric Rapid Intensification of Hurricane Earl (2010) Using the HWRF System". In: *Journal of the Atmospheric Sciences* 72.2, pp. 531–550.

Chen, J.-H. et al. (2019). „Advancements in Hurricane Prediction With NOAA's Next-Generation Forecast System". In: *Geophysical Research Letters* 46.8, pp. 4495–4501.

Craig, G. C. and S. L. Gray (1996). „CISK or WISHE as the Mechanism for Tropical Cyclone Intensification". In: *Journal of Atmospheric Sciences* 53.23, pp. 3528–3540.

Davis, C. A., S. C. Jones, and M. Riemer (2008). „Hurricane Vortex Dynamics during Atlantic Extratropical Transition". In: *Journal of the Atmospheric Sciences* 65.3, pp. 714–736.

Dörffel, T. et al. (2021). „Dynamics of Tilted Atmospheric Vortices under Asymmetric Diabatic Heating". In: *Theoretical and Computational Fluid Dynamics*.

Dumbser, M. and C.-D. Munz (2005). „ADER Discontinuous Galerkin Schemes for Aeroacoustics". In: *Comptes Rendus Mécanique*. Computational AeroAcoustics: From Acoustic Sources Modeling to Farfield Radiated Noise Prediction 333.9, pp. 683–687.

Dunkerton, T. J., M. T. Montgomery, and Z. Wang (2009). „Tropical Cyclogenesis in a Tropical Wave Critical Layer: Easterly Waves". In: *Atmos. Chem. Phys.*, p. 60.

Durran, D. R. (1989). „Improving the Anelastic Approximation". In: *Journal of the Atmospheric Sciences* 46, pp. 1453–1461.

– (2008). „A Physically Motivated Approach for Filtering Acoustic Waves from the Equations Governing Compressible Stratified Flow". In: *Journal of Fluid Mechanics* 601, pp. 365–379.

Eckhaus, W. (1979). *Asymptotic Analysis of Singular Perturbations*. Vol. v. 9. Amsterdam: North-Holland Pub. Co.

Eliassen, A. (1952). „SYMPOSIUM ON NUMERICAL FORECASTING: Simplified Dynamic Models of the Atmosphere, Designed for the Purpose of Numerical Weather Prediction". In: *Tellus* 4.3, pp. 145–156.

Emanuel, K. A. (1986). „An Air-Sea Interaction Theory for Tropical Cyclones. Part I: Steady-State Maintenance". In: *Journal of the Atmospheric Sciences* 43.6, pp. 585–605.

– (1991). „The Theory of Hurricanes". In: *Annu. Rev. Fluid. Mech.* 23, pp. 179–196.

Erdélyi, A. (1956). *Asymptotic Expansions*. Courier Corporation. 118 pp.

Farwig, R. (2014). „On Regularity of Weak Solutions to the Instationary Navier–Stokes System: A Review on Recent Results". In: *ANNALI DELL'UNIVERSITA' DI FERRARA* 60.1, pp. 91–122.

Frank, W. M. and E. A. Ritchie (1999). „Effects of Environmental Flow upon Tropical Cyclone Structure". In: *Monthly Weather Review* 127, pp. 2044–2061.

Friedrichs, K. O. (1955). „Asymptotic Phenomena in Mathematical Physics". In: *Bulletin of the American Mathematical Society* 61, pp. 485–504.

Grabowski, W. and P. K. Smolarkiewicz (1996). „Two-Time-Level Semi Lagrangian Model for Preciptating Clouds". In: *Monthly Weather Review* 124, pp. 487–497.

Grooms, I. and K. Julien (2018). „Multiscale Models in Geophysical Fluid Dynamics". In: *Earth and Space Science* 5.11, pp. 668–675.

Grooms, I., K. Julien, and B. Fox-Kemper (2011). „On the Interactions between Planetary Geostrophy and Mesoscale Eddies". In: *Dynamics of Atmospheres and Oceans* 51.3, pp. 109–136.

Gutzwiller, M. C. (1998). „Moon-Earth-Sun: The Oldest Three-Body Problem". In: *Reviews of Modern Physics* 70.2, pp. 589–639.

Hack, J. J. and W. H. Schubert (1986). „Nonlinear Response of Atmospheric Vortices to Heating by Organized Cumulus Convection". In: *Journal of the Atmospheric Sciences* 43.15, pp. 1559–1573.

Hairer, E., G. Wanner, and C. Lubich (2006). *Geometric Numerical Integration*. Vol. 31. Springer Series in Computational Mathematics. Berlin/Heidelberg: Springer-Verlag.

Harris, C. R. et al. (2020). „Array Programming with NumPy". In: *Nature* 585.7825 (7825), pp. 357–362.

Hazelton, A. T., R. E. Hart, and R. F. Rogers (2017). „Analyzing Simulated Convective Bursts in Two Atlantic Hurricanes. Part II: Intensity Change Due to Bursts". In: *Monthly Weather Review* 145.8, pp. 3095–3117.

Hazelton, A. T., R. F. Rogers, and R. E. Hart (2017). „Analyzing Simulated Convective Bursts in Two Atlantic Hurricanes. Part I: Burst Formation and Development". In: *Monthly Weather Review* 145.8, pp. 3073–3094.

Hittmeir, S. and R. Klein (2017). „Asymptotics for Moist Deep Convection I: Refined Scalings and Self-Sustaining Updrafts". In: *Theor. & Comput. Fluid Dyn.* submitted April 2017.

Holton, J. R. (2004). *An Introduction to Dynamic Meteorology*. 4th ed. Burlington, San Diego, London: Elsevier Academic Press.

Houze, R. A. (2010). „Clouds in Tropical Cyclones". In: *Monthly Weather Review* 138.2, pp. 293–344.

IPCC (2021). *Climate Change 2021: The Physical Science Basis. Contribution of Working Group I to the Sixth Assessment Report of the Intergovernmental Panel on Climate Change*. IPCC.

Jiang, G.-S. and C.-W. Shu (1996). „Efficient Implementation of Weighted ENO Schemes". In: *Journal of Computational Physics* 126.1, pp. 202–228.

Jones, S. C. (1995). „The Evolution of Vortices in Vertical Shear. I: Initially Barotropic Vortices". In: *Quarterly Journal of the Royal Meteorological Society* 121.524, pp. 821–851.

– (2000). „The Evolution of Vortices in Vertical Shear II: Large-scale Asymmetries". In: *Q.J.R. Meteorol. Soc.* 126, pp. 3137–3159.

– (2004). „On the Ability of Dry Tropical-Cyclone-like Vortices to Withstand Vertical Shear". In: *Journal of Atmospheric Sciences* 61, pp. 114–119.

Klein, R. (2000). „Asymptotic Analyses for Atmospheric Flows and the Construction of Asymptotically Adaptive Numerical Methods". In: *Zeitschrift fur Angewandte Mathematik und Mechanik* 80, pp. 765–777.

– (2004). „An Applied Mathematical View of Theoretical Meteorology (Invited Lecture ICIAM 2003)". In: *Applied Mathematics Entering the 21st Century; Invited Talks from the ICIAM 2003 Congress*. ICAM 2003 Congress. Vol. 116. SIAM Proceedings in Applied Mathematics. SIAM, p. 44.

– (2005). „Multiple Spacial Scales in Engineering and Atmospheric Low Mach Number Flows". In: *ESAIM: Mathematical Modelling and Numerical Analysis (M2AN)* 39, pp. 537–559.

– (2008). „An Unified Approach to Meteorological Modelling Based on Multiple-Scales Asymptotic". In: *Advances in Geosciences* 15, pp. 22–33.

– (2009). „Asymptotics, Structure, and Integration of Sound-Proof Atmospheric Flow Equations". In: *Theoretical and Computational Fluid Dynamics* 23.3, pp. 161–195.

Klein, R. (2010). „Scale-Dependent Models for Atmospheric Flows". In: *Annual Review of Fluid Mechanics* 42.1, pp. 249–274.

– (2017). „Scale Analysis of Compressible Flows from an Application Perspective". In: *Handbook of Mathematical Analysis in Mechanics of Viscous Fluids*. Ed. by Y. Giga and A. Novotny. Cham: Springer International Publishing, pp. 1–42.

– (2022). *On the Distinction between Distinguished and Rich Limits*. Private communication.

Klein, R. and A. J. Majda (2006). „Systematic Multiscale Models for Deep Convection on Mesoscales". In: *Theoretical and Computational Fluid Dynamics* 20.5-6, pp. 525–551.

Klein, R., L. Schielicke, et al. (2021). „Dynamics of a Diabatic Layer in the Quasi-Geostrophic Framework". In: EGU21–7377.

Kruskal, M. (1963). „Asymptotology". In: *Proceedings of the Conference at the University of Notre Dame, 1962*. Englewood Cliffs, New Jersey: Prentice-Hall, pp. 17–48.

Kutz, J. N. (2020). „Advanced Differential Equations: Asymptotics & Perturbations". arXiv: `2012.14591 [nlin]`.

Lee, M. and T. Frisius (2018). „On the Role of Convective Available Potential Energy (CAPE) in Tropical Cyclone Intensification". In: *Tellus A: Dynamic Meteorology and Oceanography* 70.1, pp. 1–18.

Leighton, H. et al. (2018). „Azimuthal Distribution of Deep Convection, Environmental Factors, and Tropical Cyclone Rapid Intensification: A Perspective from HWRF Ensemble Forecasts of Hurricane Edouard (2014)". In: *Journal of the Atmospheric Sciences* 75.1, pp. 275–295.

LeVeque, R. J. (1992). *Numerical Methods for Conservation Laws*. Lectures in Mathematics. Basel, Boston, Berlin: Birkhäuser.

Li, Q. and Y. Dai (2020). „Revisiting Azimuthally Asymmetric Moist Instability in the Outer Core of Sheared Tropical Cyclones". In: *Monthly Weather Review* 148.3, pp. 1297–1319.

Ling, G. and L. Ting (1988). „Two-Time Scales Inner Solutions and Motion of a Geostrophic Vortex". In: *Scienta Sinica* XXXI.7.

Lipps, F. B. and R. S. Hemler (1982). „A Scale Analysis of Deep Moist Convection and Some Related Numerical Calculations". In: *Journal of the Atmospheric Sciences* 39.10, pp. 2192–2210.

Lorenz, E. N. (1955). „Available Potential Energy and the Maintenance of the General Circulation". In: *Tellus* 7.2, pp. 157–167.

Magnusson, L. et al. (2021). „Tropical Cyclone Activities at ECMWF". In: 888.

Majda, A. J. and I. Grooms (2014). „New Perspectives on Superparameterization for Geophysical Turbulence". In: *Journal of Computational Physics*. Frontiers in Computational Physics 271, pp. 60–77.

Marks Jr., F. D. (2003). „Hurricanes". In: *Handbook of Weather, Climate, and Water: Dynamics, Climate, Physical Meteorology, Weather Systems, and Measurements*. John Wiley & Sons, Inc.

Marks Jr., F. D., P. G. Black, et al. (2008). „Structure of the Eye and Eyewall of Hurricane Hugo (1989)". In: *Monthly Weather Review* 136.4, pp. 1237–1259. eprint: `https://journals.ametsoc.org/mwr/article-pdf/136/4/1237/4235240/2007mwr2073\_1.pdf`.

Marks Jr., F. D., R. A. Houze Jr., and J. F. Gamache (1992). „Dual-Aircraft Investigation of the Inner Core of Hurricane Norbert. Part I: Kinematic Structure". In: *Journal of the Atmospheric Sciences* 49.11, pp. 919–942. eprint: `https://journals.ametsoc.org/jas/article-pdf/49/11/919/3425944/1520-0469(1992)049\_0919\_daioti\_2\_0\_co\_2.pdf`.

Marschalik, P. (2015). „Asymptotisch Schnelle Übergänge Und Der Steifheitsbegriff Bei Gewöhnlichen Differentialgleichungen".

Mikula, N. et al. (2021). *An Interactive Approach for Identifying Structure Definitions*. arXiv: `2112.09066 [physics.ao-ph]`. preprint.

Mikusky, E. (2007). „On the Structure of Concentrated Atmospheric Vortices in a Gradient Wind Regime and Its Motion on Synoptic Scales". Universität Hamburg, Fachbereich Geowissenschaften.

Miyamoto, Y. and D. S. Nolan (2018). „Structural Changes Preceding Rapid Intensification in Tropical Cyclones as Shown in a Large Ensemble of Idealized Simulations". In: *Journal of the Atmospheric Sciences* 75.2, pp. 555–569.

Montgomery, M. T. and R. K. Smith (2017a). „On the Applicability of Linear, Axisymmetric Dynamics in Intensifying and Mature Tropical Cyclones". In: *Fluids* 2.4, p. 69.

– (2017b). „Recent Developments in the Fluid Dynamics of Tropical Cyclones". In: *Annual Review of Fluid Mechanics* 49.1, pp. 541–574.

Nandy, A. K. and C. S. Jog (2014). *Conservation Properties of the Trapezoidal Rule in Linear Time Domain Analysis of Acoustics and Structures*. arXiv: `1401.0991 [physics.comp-ph]`.

Noether, E. (1918). „Invariante Variationsprobleme". In: *Nachr. D. König. Gesellsch. D. Wiss. Zu Göttingen, Math-phys. Klasse, S.* Göttingen: Weidmannsche Buchhandlung, pp. 235–257.

Nolan, D. S. and L. D. Grasso (2003). „Nonhydrostatic, Three-Dimensional Perturbations to Balanced, Hurricane-Like Vortices. Part II: Symmetric Response and Nonlinear Simulations". In: *JOURNAL OF THE ATMOSPHERIC SCIENCES* 60, p. 29.

Nolan, D. S. and M. T. Montgomery (2002). „Nonhydrostatic, Three-Dimensional Perturbations to Balanced, Hurricane-like Vortices. Part I: Linearized Formulation, Stability, and Evolution". In: *JOURNAL OF THE ATMOSPHERIC SCIENCES* 59, p. 32.

Ooyama, K. V. (1964). „A Dynamical Model for the Study of Tropical Cyclone Development". In: *Geofísica Internacional* 4, pp. 187–198.

– (1969). „Numerical Simulation of the Life Cycle of Tropical Cyclones". In: *Journal of Atmospheric Sciences* 26, pp. 3–40.

– (1982). „Conceptual Evolution of the Theory and Modeling of the Tropical Cyclone". In: *Journal of the Meteorological Society of Japan* 60, pp. 369–380.

Owinoh, A. Z., B. Stevens, and R. Klein (2011). „Multiscale Asymptotics Analysis for the Mesoscale Dynamics of Cloud-Topped Boundary Layers". In: *Journal of the Atmospheric Sciences* 68.2, pp. 379–402.

Papke, A. (2017). „Atmospheric Vortex Stability under Vertical Shear". Berlin: Freie Universität Berlin. 121 pp.

Parkins, C., P. Blythe, and D. Crighton (2000). „Hot Spot Ignition: The Newtonian Limit". In: *Proceedings of the Royal Society of London. Series A: Mathematical, Physical and Engineering Sciences* 456.2004, pp. 2857–2882.

Päschke, E. et al. (2012). „Motion and Structure of Atmospheric Mesoscale Baroclinic Vortices: Dry Air and Weak Environmental Shear". In: *Journal of Fluid Mechanics* 701, pp. 137–170.

Pauluis, O. M. and F. Zhang (2017). „Reconstruction of Thermodynamic Cycles in a High-Resolution Simulation of a Hurricane". In: *Journal of the Atmospheric Sciences* 74.10, pp. 3367–3381.

Pedlosky, J. (1984). „The Equations for Geostrophic Motion in the Ocean". In: *Journal of Physical Oceanography* 14.2, pp. 448–455.

Persing, J. and M. T. Montgomery (2003). „Hurricane Superintensity". In: *Journal of the Atmospheric Sciences* 60.19, pp. 2349–2371.

Pope, S. B. (2011). *Turbulent Flows*. Cambridge: Cambridge Univ. Press.

Prusa, J. M. and P. K. Smolarkiewicz (2003). „An All-Scale Anelastic Model for Geophysical Flows: Dynamic Grid Deformation". In: *Journal of Computational Physics* 190.2, pp. 601–622.

Prusa, J. M., P. K. Smolarkiewicz, and A. A. Wyszogrodzki (2008). „EULAG, a Computational Model for Multiscale Flows". In: *Computers & Fluids* 37.9, pp. 1193–1207.

Reasor, P. D., M. T. Montgomery, F. D. Marks Jr., et al. (2000). „Low-Wavenumber Structure and Evolution of the Hurricane Inner Core Observed by Airborne Dual-Doppler Radar". In: *Monthly Weather Review* 128, pp. 1653–1680.

Reasor, P. D. and M. T. Montgomery (2001). „Three-Dimensional Alignment and Corotation of Weak, TC-like Vortices via Linear Vortex Rossby Waves". In: *JOURNAL OF THE ATMOSPHERIC SCIENCES* 58, p. 25.

Reasor, P. D., M. T. Montgomery, and L. D. Grasso (2004). „A New Look at the Problem of Tropical Cyclones in Vertical Shear Flow: Vortex Resiliency". In: *JOURNAL OF THE ATMOSPHERIC SCIENCES* 61, p. 20.

Riemer, M., M. T. Montgomery, and M. E. Nicholls (2010). „A New Paradigm for Intensity Modification of Tropical Cyclones: Thermodynamic Impact of Vertical Wind Shear on the Inflow Layer". In: *Atmos. Chem. Phys.*, p. 26.

Rios-Berrios, R. (2020). „Impacts of Radiation and Cold Pools on the Intensity and Vortex Tilt of Weak Tropical Cyclones Interacting with Vertical Wind Shear". In: *Journal of Atmospheric Sciences* 77, pp. 669–689.

Robinson, J. C. (2020). „The Navier–Stokes Regularity Problem". In: *Philosophical Transactions of the Royal Society A: Mathematical, Physical and Engineering Sciences* 378.2174, p. 20190526.

Rogers, R. F., P. D. Reasor, and J. F. Zhang (2015). „Multiscale Structure and Evolution of Hurricane Earl (2010) during Rapid Intensification". In: *Monthly Weather Review* 143, pp. 536–562.

Rotunno, R. and K. A. Emanuel (1987). „An Air–Sea Interaction Theory for Tropical Cyclones. Part II: Evolutionary Study Using a Nonhydrostatic Axisymmetric Numerical Model". In: *Journal of the Atmospheric Sciences* 44.3, pp. 542–561.

Rousseau-Rizzi, R., T. Merlis, and N. Jeevanjee (2021). *The Connection between Carnot and CAPE Formulations of TC Potential Intensity*. preprint. Atmospheric Sciences.

Ryglicki, D. R. et al. (2018). „The Unexpected Rapid Intensification of Tropical Cyclones in Moderate Vertical Wind Shear. Part I: Overview and Observations". In: *Monthly Weather Review* 146.11, pp. 3773–3800. eprint: `https://journals.ametsoc.org/mwr/article-pdf/146/11/3773/4371181/mwr-d-18-0020\_1.pdf`.

Schecter, D. A. (2015). „Response of a Simulated Hurricane to Misalignment Forcing Compared to the Predictions of a Simple Theory". In: *Journal of the Atmospheric Sciences* 72.3, pp. 1235–1260.

Schecter, D. A., M. T. Montgomery, and P. D. Reasor (2002). „A Theory for the Vertical Alignment of a Quasigeostrophic Vortex". In: *JOURNAL OF THE ATMOSPHERIC SCIENCES* 59, p. 19.

Schecter, D. A. and M. T. Montgomery (2003). „On the Symmetrization Rate of an Intense Geophysical Vortex". In: *Dynamics of Atmospheres and Oceans* 37.1, pp. 55–88.

– (2004). „Damping and Pumping of a Vortex Rossby Wave in a Monotonic Cyclone: Critical Layer Stirring versus Inertia–Buoyancy Wave Emission". In: *Physics of Fluids* 16.5, pp. 1334–1348.

– (2007). „Waves in a Cloudy Vortex". In: *Journal of the Atmospheric Sciences* 64.2, pp. 314–337.

Schubert, W. H. and J. J. Hack (1982). „Inertial Stability and Tropical Cyclone Development". In: *Journal of the Atmospheric Sciences* 39, pp. 1687–1697.

– (1983). „Transformed Eliassen Balanced Vortex Model". In: *Journal of Atmospheric Sciences* 39, pp. 1687–1697.

Smith, R. K., M. T. Montgomery, and S. Vogl (2008). „A Critique of Emanuel's Hurricane Model and Potential Intensity Theory". In: *Quarterly Journal of the Royal Meteorological Society* 134.632, pp. 551–561.

Smolarkiewicz, P. K. (1984). „A Fully Multidimensional Positive Definite Advection Transport Algorithm with Small Implicit Diffusion". In: *Journal of Computational Physics* 54.2, pp. 325–362.

– (2006). „Multidimensional Positive Definite Advection Transport Algorithm: An Overview". In: *International Journal for Numerical Methods in Fluids* 50.10, pp. 1123–1144.

Smolarkiewicz, P. K. and P. Charbonneau (2013). „EULAG, a Computational Model for Multiscale Flows: An MHD Extension". In: *Journal of Computational Physics* 236, pp. 608–623.

Smolarkiewicz, P. K., C. Kühnlein, and W. W. Grabowski (2017). „A Finite-Volume Module for Cloud-Resolving Simulations of Global Atmospheric Flows". In: *Journal of Computational Physics* 341, pp. 208–229.

Smolarkiewicz, P. K., C. Kühnlein, and N. P. Wedi (2014). „A Consistent Framework for Discrete Integrations of Soundproof and Compressible PDEs of Atmospheric Dynamics". In: *Journal of Computational Physics* 263, pp. 185–205.

Smolarkiewicz, P. K. and L. G. Margolin (1993). „On Forward-in-Time Differencing for Fluids: Extension to a Curvilinear Framework". In: *Monthly Weather Review* 121.6, pp. 1847–1859.

– (1998). „MPDATA: A Finite-Difference Solver for Geophysical Flows". In: *Journal of Computational Physics* 140.2, pp. 459–480.

Stevens, B. et al. (2020). „The Added Value of Large-eddy and Storm-resolving Models for Simulating Clouds and Precipitation". In: *Journal of the Meteorological Society of Japan. Ser. II* 98.2, pp. 395–435.

Stevenson, S. N., K. L. Corbosiero, and J. Molinari (2014). „The Convective Evolution and Rapid Intensification of Hurricane Earl (2010)". In: *Monthly Weather Review* 142.11, pp. 4364–4380.

Strang, G. (1968). „On the Construction and Comparison of Difference Schemes". In: *SIAM Journal on Numerical Analysis* 5.3, pp. 506–517.

Süli, E. and D. Mayers (2003). *An Introduction to Numerical Analysis*. Cambridge University Press.

Sweby, P. K. (1984). „High Resolution Schemes Using Flux Limiters for Hyperbolic Conservation Laws". In: p. 19.

Tadmor, E. (2012). „A Review of Numerical Methods for Nonlinear Partial Differential Equations". In: *Bulletin of the American Mathematical Society* 49.4, pp. 507–554.

Tang, C. K., J. C. L. Chan, and M. Yamaguchi (2021). „Large Tropical Cyclone Track Forecast Errors of Global Numerical Weather Prediction Models in Western North Pacific Basin". In: *Tropical Cyclone Research and Review* 10.3, pp. 151–169.

Teschl, G. (2012). *Ordinary Differential Equations and Dynamical Systems*. Graduate Studies in Mathematic 140. Providence: Amer.Math.Soc.

Van Leer, B. (1974). „Towards the Ultimate Conservative Difference Scheme. II. Monotonicity and Conservation Combined in a Second-Order Scheme". In: *Journal of Computational Physics* 14.4, pp. 361–370.

Van Dyke, M. (1975). *Perturbation Methods in Fluid Mechanics*. Second Printing 1978. The Parabolic Press.

Veldman, A. E. P. (2001). „Matched Asymptotic Expansions and the Numerical Treatment of Viscous-Inviscid Interaction". In: *Practical Asymptotics*. Ed. by H. K. Kuiken. Dordrecht: Springer Netherlands, pp. 189–206.

Vigh, J. L. and W. H. Schubert (2009). „Rapid Development of the Tropical Cyclone Warm Core". In: *Journal of the Atmospheric Sciences* 66.11, pp. 3335–3350.

Virtanen, P. et al. (2020). „SciPy 1.0: Fundamental Algorithms for Scientific Computing in Python". In: *Nature Methods* 17.3 (3), pp. 261–272.

Von Lindheim, J. et al. (2021). *Definition, Detection, and Tracking of Persistent Structures in Atmospheric Flows*. arXiv: `2111.13645` [`physics.ao-ph`]. preprint.

Wadler, J. B. et al. (2021). „The Rapid Intensification of Hurricane Michael (2018): Storm Structure and the Relationship to Environmental and Air–Sea Interactions". In: *Monthly Weather Review* 149.1, pp. 245–267.

Wang, Y. and G. J. Holland (1996). „Tropical Cyclone Motion and Evolution in Vertical Shear". In: *Journal of Atmospheric Sciences* 53.22, pp. 3313–3332.

Weber, T. (2011). „Analyse Und Numerische Berechnung Atmosphärischer Wirbel Im Regime Tropischer Stürme". Berlin, Germany: Freie Universität Berlin, FB für Mathematik und Informatik.

Yu, H. et al. (2021). „Are We Reaching the Limit of Tropical Cyclone Track Predictability in the Western North Pacific?" In: *Bulletin of the American Meteorological Society* -1 (aop), pp. 1–46.

Ziemiański, M. Z. et al. (2021). „Compressible EULAG Dynamical Core in COSMO: Convective-Scale Alpine Weather Forecasts". In: *Monthly Weather Review* 149.10, pp. 3563–3583.

Der Lebenslauf ist in der Online-Version aus Gründen des Datenschutzes nicht enthalten.

Selbstständigkeitserklärung

Hiermit erkläre ich, dass ich zur Anfertigung dieser Dissertation keine weiteren als die angegebenen Hilfsmittel und Hilfen verwendet habe. Ich versichere, dass diese Arbeit nicht bereits in einem früheren Promotionsverfahren eingereicht wurde.

Berlin, den 30.10.2023

_____

Tom Dörffel